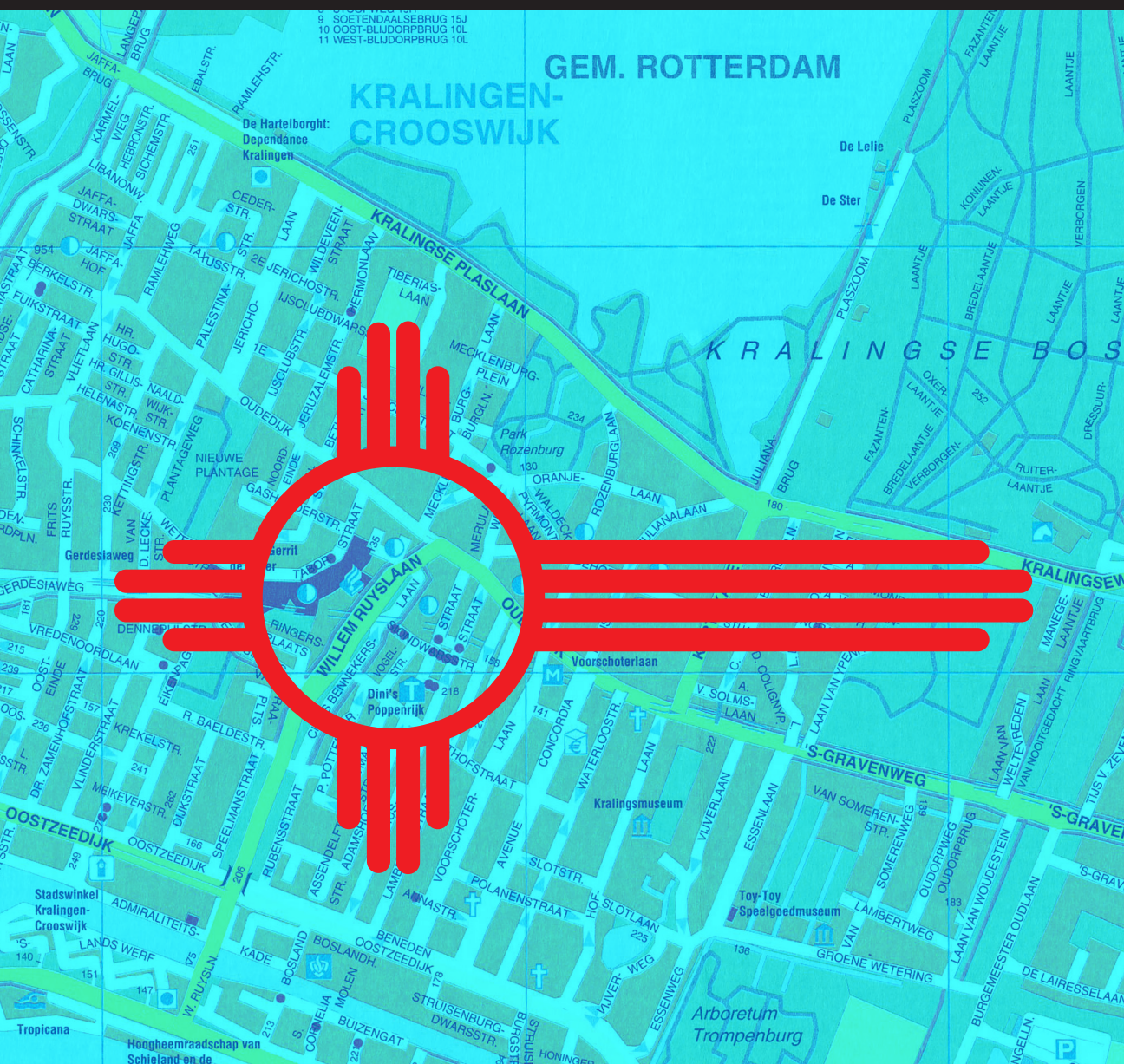


Novel Strategies to Optimize Targeted Molecular Imaging and Therapy

— Jeffrey Norenberg —



Novel Strategies to Optimize Targeted Molecular Imaging and Therapy

*Nieuwe Strategieën voor Optimalisatie van
Targeted Moleculaire Imaging en Therapie*

Jeffrey Norenberg

Novel Strategies to Optimize Targeted Molecular Imaging and Therapy

*Nieuwe Strategieën voor Optimalisatie van
Targeted Moleculaire Imaging en Therapie*

Proefschrift

ter verkrijging van de graad van doctor aan de
Erasmus Universiteit Rotterdam
op gezag van de
rector magnificus

Prof.dr. H.G. Schmidt

en volgens besluit van het College voor Promoties.

De openbare verdediging zal plaatsvinden op
woensdag 29 mei 2013 om 13.30 uur

door

Jeffrey Paul Norenberg

geboren te Wahoo, Nebraska, VS

ISBN:

Printed by: Ipskamp Drukkers
<http://www.ipskampdrukkers.nl/>
Cover design by: Jeffrey Norenberg and Ton Everaers
Lay-out by: Ton Everaers

© 2013 Jeffrey Norenberg

All rights reserved. No part of this thesis may be reproduced or transmitted in any form or by any means, electronic or mechanical, including photocopying, recording, or any information storage and retrieval system, without prior written permission from the copyright owner.



Promotoriecommissie

Promotoren	Prof.dr. M. de Jong Prof.dr. E. P. Krenning
Co-promotor	Dr. W. A. P. Breeman
Overige leden	Prof.dr. T. J. Visser Prof.dr. J. F. Verzijlbergen Prof.dr. W.W. de Herder

Contents

Chapter 1: Introduction	11
Chapter 2: PRRT Using High-LET Radionuclides	51
2.1 A Comparison Of High-Versus Low-Linear Energy Transfer Somatostatin Receptor Targeted Radionuclide Therapy In Vitro. <i>Cancer Biotherapy And Radiopharmaceuticals</i> , 2005;20(1):52-57.	53
2.2 Somatostatin-Receptor Targeted α -Emitting ^{213}Bi Is Therapeutically More Effective Than β -Emitting ^{177}Lu In Chemoresistant Human Pancreatic Adenocarcinoma Cells. <i>Nuclear Medicine Biology</i> 2007; 34(2):185-193.	65
2.3 ^{213}Bi -[DOTA ⁰ ,Tyr ³] Octreotide Peptide Receptor Radionuclide Therapy Of Pancreatic Tumors In A PreClinical Animal Model. <i>Clinical Cancer Research</i> 2006;12(3) February 1:897-903.	83
2.4 Radiation Absorbed Dose Estimates For Intravenously Injected ^{213}Bi -[DOTA]Tyr ₃ -Octreotide In Peptide Receptor Radionuclide Therapy. Manuscript in preparation for submission to <i>JNM or EJNM</i> 2013.	99
Chapter 3: Modulation of Somatostatin Receptor Expression and Implications for Improved PRRT	109
Enhancement Of Somatostatin-Receptor-Targeted ^{177}Lu -[DOTA ⁰ -Tyr ³]-Octreotide Therapy By Gemcitabine Pre-Treatment-Mediated Receptor Uptake Up-Regulation And Cell Cycle Modulations. <i>Nuclear Medicine And Biology</i> , 2008;35(6):673-678.	
Chapter 4: Development of Molecular Imaging Probe Targeting Lymphocyte-Functional Antigen-1	123
Characterization of ^{177}Lu -Labeled Small Molecule For Non-Invasive Tumor Imaging And Radiotherapy. <i>Cancer Biotherapy and Radiopharmaceuticals</i> , 2006;21 (5): 418-426.	

Chapter 5: Development Molecular Imaging Probes Targeting the Glycoprotein Receptor GPR-30	137
---	------------

Pre-Clinical Development Of A Neutral, Estrogen Receptor-Targeted, Tridentate $^{99\text{m}}\text{Tc}$ (I) Estradiol Pyridin-2-yl Hydrazine Derivative For Imaging Of Breast And Endometrial Cancers.
Journal of Nuclear Medicine 2008;49(6):978–986.

Chapter 6: Evaluating Drug Delivery to the Lung in Rodents and Man	157
---	------------

6.1 Implementation Of A 3D Topographic Thinning Model For Assessing Aerosol Deposition Of Radioactive Assays In Small-Animal CT/SPECT Imaging. IEEE Nuclear Science Symposium Conference Record (NSS/MIC) 2009;3705-3709.	159
6.2 Regional Particle Size Dependent Deposition Of Inhaled Aerosols In Rats And Mice. <i>Inhalation Toxicology</i> 2012; 24(1):27-35.	171
6.3 Characterization Of Respiratory Deposition Of Fluticasone-salmeterol Hydrofluoroalkane-134a And Hydrofluoroalkane-134a Beclomethasone In Asthmatic Patients. <i>Annals of Allergy, Asthma & Immunology</i> , 2012 Mar;108(3):195-200.	191

Chapter 7: Metrology in Nuclear Medicine	205
---	------------

A Performance Evaluation Of 90Y Dose Calibrator Measurements In Nuclear Pharmacies And Clinics In The United States.
Applied Radiation And Isotopes, 2008;66(2):252-60.

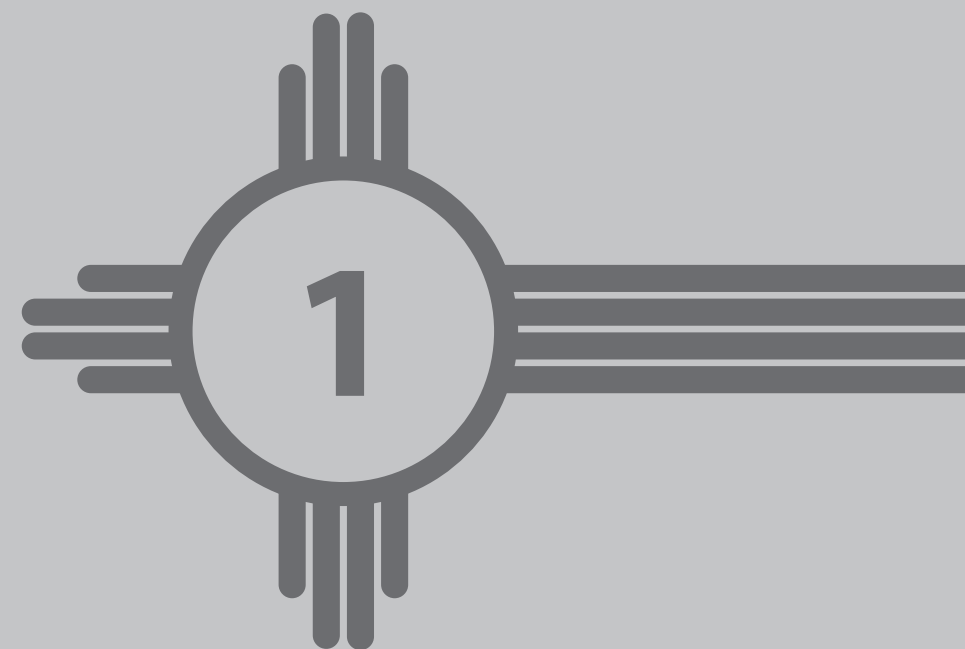
Appendixes:

Patent: Non-invasive diagnostic agents of cancer and methods of diagnosing cancer, especially leukemia and lymphoma.
United States Patent No. 8,097,237, issued January 17, 2012.

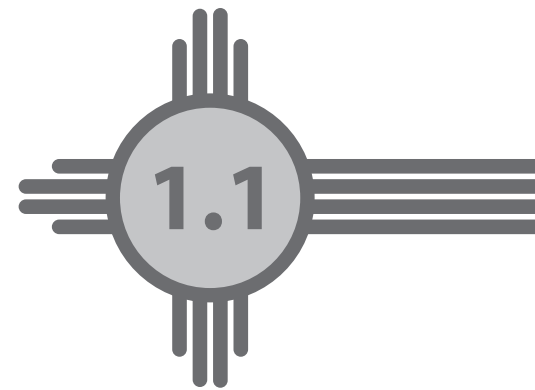
Patent: Non-invasive diagnostic agents of cancer and methods of diagnosing cancer, especially leukemia and lymphoma.
United States Patent Application No. 13/309,972 Notice of Allowance received January 9, 2013; Patent to issue April 9, 2013.

Dutch Summary	231
PhD Portfolio: 60 ECTs	235
Acknowledgements	241
Curriculum vitae	247

Preface



General Introduction and Outline of Thesis



Introduction

Improving patients' clinical outcomes requires many levels of examination, owing to the enormous complexities of human disease and healthcare delivery. Our understanding of disease also requires many different levels of observation. The human experience preconditions us to see the whole person and to relate to them as individuals, each with their own unique set of circumstances. Modern medicine seeks to apply many forms of intervention, including surgical resection, radiation and chemotherapy, and more recently, targeted drug therapy. In this forum, we are concerned with disease and pathophysiology, and how best to reach the site or sites of disease with targeted therapies. Monoclonal antibodies and their fragments have long held promise in targeting epitopes unique to diseased cells, e.g. cancer. Peptides and small molecule ligands that are capable of binding unique expressions of disease are increasingly the focus of drug discovery and development. This thesis focuses on development of radioligands for molecular imaging and therapy and novel strategies to improve their application to achieve greater success. These efforts are pursued in order to improve patient outcomes through more accurate and timely diagnosis, staging, and monitoring of treatment interventions using molecular imaging, and to more effectively treat disease using highly targeted therapies.

While we see patients as people, our scientific knowledge seeks to reduce and sometimes disassemble the human body into more objective and manageable units of understanding, e.g. organs, tissues, cells, or biochemical pathways. Medical specialties largely follow these same levels of organization to diagnose and treat patients' diseases. Cardiologists diagnose and treat patients with cardiac disease. Endocrinologists focus on patients with diseases involving the endocrine organs and tissues producing hormones. Similarly, this reductionist approach leads one to believe that more focused interventions are capable of producing more discrete and possibly better results. The concept of the magic bullet was first professed in the 14th century whereby the Freischütz, or "free shooter" in German folklore, was a marksman who, through a contract with the devil, obtained a certain number of bullets destined to hit without fail whatever object desired.

A more contemporary example was provided in the 19th century through Dr. Paul Ehrlich's work to target bacterium with staining techniques for the diagnosis of tuberculosis, leading to the first targeted treatment of syphilis¹. Ehrlich and his colleagues were also the first to recognize that when tumors are cultivated by transplanting tumor cells, their malignancy increases from generation to generation, and that if the primary tumor is removed, then metastasis increase precipitously. Ehrlich also applied bacteriological methods to cancer research, resulting in the introduction of a new technology of in vivo staining. Ehrlich injected the dyes alizarin blue and indophenol blue into laboratory animals and established that after their death various organs had been colored to different degrees. In organs with high oxygen saturation indophenol was retained, in organs with medium saturation indophenol blue was reduced, but not alizarin blue. In areas with low oxygen

saturation both pigments were reduced. From these observations, Ehrlich developed the side-chain or receptor theory. The differential staining of tissue sections with a broad spectrum of chemical dyes establish the roots of his 'targeted therapy concept'. From this work, Ehrlich formulated the conviction that all life processes can be traced to processes of physical chemistry occurring in the cell. Ehrlich's 'magic bullet concept' of targeted drug delivery, posits that drugs should be designed such that they go straight to their intended cell-structural targets. Ehrlich was the first to propose that targeted medicines should in theory efficaciously attack pathogens yet remain harmless in healthy tissues.

Nearly 100 years later (circa 1980), scientists posed that a small amount of toxin could be paired with an antibody, chemical, or enzyme that could preferentially bind to cancer cells. In that way the toxin would be delivered to kill the cancer cells with precision, resulting in far less collateral damage to healthy tissues than patients commonly endured with standard chemotherapies. However, the promise of targeted drug delivery that begun in the days of Ehrlich remains largely unfulfilled.

In the modern era, techniques in targeted molecular imaging and therapy are being used in patient care (Figure 1). This thesis describes novel strategies to improve targeted mo-

lecular imaging and therapy, extending the 19th century concept of the magic bullet by engaging 21st century knowledge and technology to advance our understanding of human disease and realize improved patient outcomes.

Introduction to targeted molecular imaging

As a result of the tremendous advances in our understanding of molecular biology, genomics, and proteomics, efforts to apply these advances to personalized molecular medicine have greatly increased. In turn, these advances have fueled a growing emergence of targeted molecular imaging and therapy using radioligands. In order to harness the tremendous promise of these applications, increased efforts are necessary to more effectively translate novel probes from pre-clinical to clinical applications. The work presented herein, describes novel strategies to improve targeted molecular imaging and therapy.

There exists something of a paradox in the field of targeted molecular imaging and therapy. In order to successfully translate novel radioligands to clinical applications, our understanding of the most basic factors that influence targeted molecular imaging and therapy must improve. These factors include the target, probe, radionuclide, and applications in both targeted molecular imaging and radionuclide therapy. There is a mandate to re-examination the factors that are capable of influencing the safety and effectiveness of these targeted probes. Some of these factors have been known for over 60 years, while others are only now being illuminated or applied in this setting. This re-examination is something of a return to first principles that is necessary in order to ensure that scientists seeking to discover and/or develop molecular-targeted probes for imaging and therapy apply the principles in a logical manner, consistent with their true meaning, and in harmony with others seeking to advance the cause. A more disciplined approach using harmonized methods and common endpoints may speed translation to the clinic to more greatly benefit patients. Thus, it is necessary to identify those factors that may benefit from efforts to optimize their impact on molecular imaging and therapy. The critical parameters for the pre-clinical characterization of PET and SPECT imaging probes are presented in Table 1.

High sensitivity ($1/[probe]$) targeted molecular imaging requires the use of a radioligand and an appropriate imaging system in order to image an object of interest, a disease in patients or a disease model in animals. High sensitivity ($1/[probe]$) refers to the ability to perform in vivo imaging using a very low concentration (mass dose) of probe or ligand. The tracer dose of radioligand administered for in vivo targeted molecular imaging is often less than 1 $\mu g/kg$. The imaging trilogy shown in Figure 2 allows one to ask and answer relevant biological questions, with the aim of translating results from small-animal studies to some clinical application. High sensitivity targeted molecular imaging can utilize sin-

Targeted Molecular Imaging and Therapy

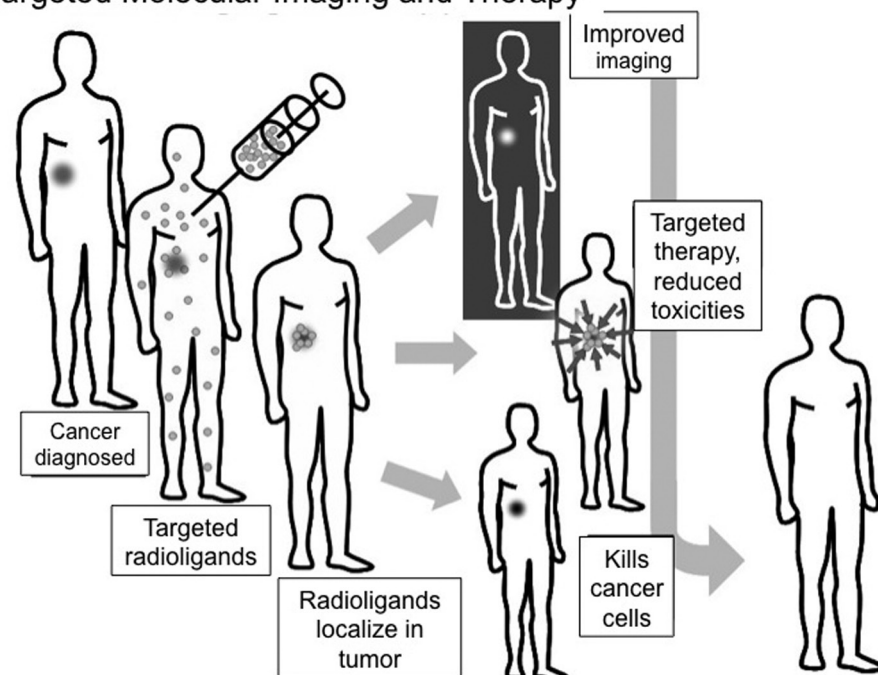


Figure 1. Targeted molecular imaging and therapy

Table 1. Critical parameters for the pre-clinical characterization of PET and SPECT imaging probes

Quality parameter	Criteria
Precursor	
Product yield	% of product formed from the primary chemical, peptide, protein, etc.
Chemical purity	Determined by HPLC, MS or composition analysis (e.g., H, O and C content)
Structure/Isomers	Crystallographic or spectroscopic analysis
# Tracer binding sites	Chelators, ligands, etc., conjugated to each PET or SPECT probe entity (e.g., small molecule, peptide, protein, nanoparticles, etc.)
Radiolabeled probe	
Synthesis time	Total time for labeling reaction, from addition of precursor to final purification of probe
Chemical purity	% of product formed based on the total amount of nonradioactive precursor and products after labeling reaction (determined by HPLC, UV analysis, etc.)
Incorporation yield	% of radionuclide incorporated into product, expressed as % bound, % unbound
Radiochemical yield	% of product (probe) formed based on the total amount of radionuclide added
Radiochemical purity	% of probe formed based on the total amount of all radioactive products formed
% Occupied sites	% of total binding sites occupied by tracer
Specific activity	Presented as GBq or Ci/mmol (or as GBq or Ci/mg with molecular weight)
Volatiles	In ppm as described in the United States or European Pharmacopeia
In vitro studies	
Stability of probe	In animal (e.g., mouse, rat, primate) and human serum at 37°C (analyzed by HPLC)
Lipophilicity	Solvent partition coefficient or theoretical log P
Cell line(s)	Describe generation or source and oncological origin
Characterization of cell line(s)	Determine expression of receptor, antigen or binding site (using Western blots, ELISA or biosensor techniques)
Binding characteristics	Comparison of Bmax, Ka, Kd obtained with nonradiolabeled and radiolabeled probe
Cell labeling efficiency	% of labeled cells; uptake by cells

Animal studies	
Animal description	Strain(s), e.g., for mice and rats; details of disease model; origin, generation, location and size of xenograft tumors
Number of animals	The use of five animals in a group or per data point is recommended
Quantitative biodistribution	Presented as %ID/g wet weight tissue or %ID/organ
PET or SPECT equipment	Description and specifications of scanning equipment
Imaging protocol	Quantity and route of radioactivity injected; composition and type of anesthetic used (gas or injectable); time, duration (of each scan) and number of scans performed at each time point
Input function	Description of measurement methods to assign radioactivity value of injectate, including: equipment and performance qualification, precision, accuracy
Quantitative PET or SPECT images	Detail method used to convert images to %ID/g or %ID/organ

Adapted from: A. Chopra, et al. Nuclear Medicine and Biology 2011;38:1079-1084

gle-photon computed emission tomography (SPECT) or positron emission tomography (PET) to render functional images of radioligand distribution patterns in vivo. Both SPECT and PET functional imaging modalities are increasingly combined with anatomic images obtained using x-ray computed tomography (CT) or magnetic resonance imaging (MRI), in hybrid imaging systems. This allows multiple-modality imaging to be performed in a single session, to produce co-registered data sets with increased diagnostic utility.

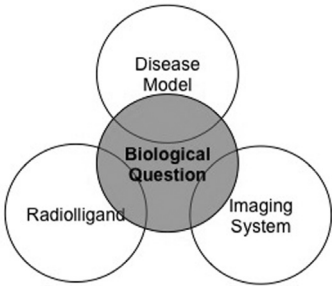
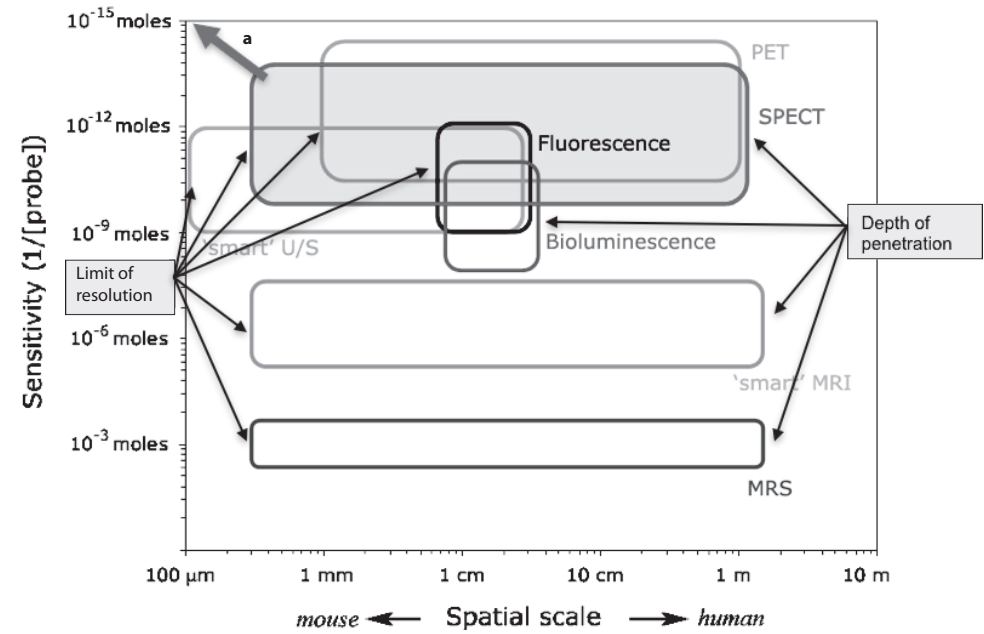


Figure 2. Preclinical targeted molecular imaging trilogy

Targeted molecular imaging using tracer doses of radioligands may be used to gather data regarding ligand pharmacokinetics and pharmacodynamics without disrupting the body’s biochemistry and physiology, or pathophysiology. The unique ability to visualize target expression non-invasively, in vivo and under naïve conditions is a distinct advantage of nuclear imaging modalities. Both PET and SPECT imaging employ radioligands administered in tracer quantities, at very low mass doses, typically well below the thresholds for pharmacologic activity. The concentration of PET and SPECT radioligands at their intended target has been reported as <0.1 nM and <0.03nM, respectively, far below the pharmacologic mass threshold for many compounds². Thus, the availability of high sensitivity (1/[probe]) radioligands for PET and SPECT is a tremendous advantage, allowing interrogation of the naïve biological milieu.

This compares to 10-100 μM of gadolinium used in MRI, concentrations nearly 10,000 times higher. A comparison of the characteristics of various imaging modalities is shown in Figure 3 and Table 2.

Figure 3. Probe sensitivity versus spatial resolution for various imaging modalities



Adapted from: Meikle et al., Phys. Med. Biol. 50 (2005) R45-R61
a: Increased probe sensitivity is possible, but limited by achievable specific activity

The molecular imaging matrix indicating the position of SPECT relative to other noninvasive in vivo imaging technologies. Here, we represent the matrix using sensitivity and spatial scale as the orthogonal axes. Sensitivity refers to the in vivo concentration of the labelled contrast agent (probe) required to elicit a certain signal-to-noise ratio. The spatial scale is the domain bounded by the limiting resolution (left limit) and the depth of penetration of the signal-generating radiation (right limit) for a given technology. 'Smart' U/S refers to high frequency (20–60 MHz) ultrasound imaging using echogenic, potentially activatable, contrast agents, such as microbubbles. 'Smart' MRI refers to MRI using targeted activatable contrast agents. MRS refers to magnetic resonance in vivo spectroscopy using ^{19}F - and ^{13}C -labelled molecules. SPECT is among the most sensitive of the molecular in vivo imaging technologies and its spatial scale spans the resolution required for imaging small laboratory animals and the depth penetration required for imaging humans.

The probe sensitivity of SPECT and PET imaging allow receptor-based assays to be conducted using non-invasive molecular imaging. This ability to interrogate the naïve tissue is a unique capability of nuclear medicine imaging. This is particularly useful when considering opportunities for molecular imaging to inform regarding subsequent targeted therapy. Using a very limited mass dose, even sites of low-density target expression ($<20\text{ nM}$) can be effectively targeted and visualized². This is particularly useful for ligands which may act as agonists at the target producing other downstream biochemical events, e.g.

Table 2. Advantages of radioligands in molecular imaging in vivo, especially for low density sites of target expression ($<20\text{ nM}$)

Imaging modality	Probe sensitivity at target	Spatial resolution Animal : Human	Depth of penetration
SPECT	$<0.03\text{ nM}$	0.5 – 2 mm : 4-12 mm	1 m
PET	$<0.1\text{ nM}$	1 – 2 mm : 4-6 mm	1 m
Ultrasound ^a	10 – 100 pM	100 μm	$<5\text{ cm}$
Fluorescence	10 – 100 pM	5 mm	$<5\text{ cm}$
Bioluminescence	$<1\text{ nM}$	5 mm	$<5\text{ cm}$
MRI ^b	1-100 μM	25 – 100 μM : 0.5-2 mm	1 m
MRS	10-1000 mM	25 – 100 μM : 0.5-2 mm	1 m

SPECT: Single-photon computed tomography; PET: Positron emission tomography; MRI: Magnetic resonance imaging; MRS: Magnetic resonance spectroscopy; a: Contrast-enhanced; b: Intraluminal, high-frequency transducer

signal-transduction. Using such a very low mass dose, it is also thought that target expression is largely unaffected by the radioligand-target binding. However, in the case of some agonists, caution must be used as the pharmacologic threshold has been shown to be in the nanomolar range for regulatory peptides, including bombesin analogs, substance P, VIP, etc.^{3,4}.

Prior to in vivo imaging, many parameters of SPECT and PET radioligands must be validated (Table 3). Because scintigraphic imaging records gamma rays rather than chemical structure, novel radioligands must be validated as binding to their intended target in vitro with specificity and selectivity representative of the parent compound such that recorded gamma rays reflect the biodistribution of the parent compound at the target receptor, antigen, or protein. The validation methods employed should characterize the properties of the radioligand, demonstrate all resultant radiochemical structures of the radioligand, and any significant radioactive metabolites encountered in vivo. This is necessary in order to confirm the degree to which the gamma ray signal represents the parent compound. This validation maybe accomplished using both in vitro and in vivo methods including, incubation in serum or hepatic microsomes, and collection of blood and urine, followed by HPLC analysis of radioactive metabolites. Mass spectroscopy may also aid in the identification of metabolites. It is also necessary to validate the in vivo fate of the radioligand and its radioactive metabolites using biodistribution studies, and autoradiography (or microautoradiography) in conjunction with immunohistochemistry.

Details of the precursor synthesis, purification, and yield of both the final precursor and any intermediate compounds should be described and validated against reference standards, whenever possible. The radiolabeling methods and radionuclide incorporation and

Table 3. Maximum specific activity and physical characteristics of a selected radionuclides

	⁶⁷ Ga	⁶⁸ Ga	⁹⁰ Y	¹¹¹ In	¹⁷⁷ Lu
Production Method	Cyclo- tron	Generator	Generator	Cyclotron	Reactor
	(p, 2n)			(p, 2n)	(n, g)
Target/Parent	⁶⁸ Zn	⁶⁸ Ge	⁹⁰ Sr	¹¹² Cd	¹⁷⁶ Lu or ¹⁷⁶ Yb
Decay Product	⁶⁷ Zn	⁶⁸ Zn	⁹⁰ Zr	¹¹¹ Cd	¹⁷⁷ Hf
t½ [days]	3.2617	4.702E-2	2.6667	2.8047	6.647
nmol metal per GBq	0.68	0.01	0.55	0.58	1.39
Maximal Specific Activity [GBq.nmol ⁻¹]					
In Theory ^a	1.48	102	1.81	1.72	0.72
In Practice	0.37	>1.0	0.5	1.7 ^b ; 0.82 ^c	0.15 ^d , 0.5 ^e , 0.42 ^f

Adapted from Breeman WAP, Correspondence Continuing Education Courses For Nuclear Pharmacists And Nuclear Medicine Professionals, 2012:16 (5). University of New Mexico Health Sciences Center, Albuquerque, New Mexico.

a: In theory, 1 nmol of a DTPA- or DOTA-peptide can incorporate 1 nmol radionuclide. This number indicates the maximal theoretical specific activity of the radiolabeled DTPA- or DOTA-peptides, expressed in [GBq.nmol⁻¹].

b: 1.7 GBq per nmol DTPA-peptide.

c: 0.82 GBq per nmol DOTA-peptide.

d: Reactor produced: ¹⁷⁶Lu (n, g) ¹⁷⁷Lu [40].

e: Reactor produced: ¹⁷⁶Lu (n, g) ¹⁷⁷Lu from High Flux Isotope Reactor at Oak Ridge National Laboratory using high thermal neutron flux (1.5 10¹⁵ neutrons cm⁻² s⁻¹) 80% of all the Lu atoms can be in the form of ¹⁷⁷Lu [40].

f: Reactor produced: ¹⁷⁶Yb (n, g) ¹⁷⁷Lu

radiochemical yields should be thoroughly described and validated. The strength, identity, and purity of the resultant radioligand should be well characterized, and validated against reference standards whenever possible. All components should be specified in precise detail, including: source, product name, reference number, batch or lot number, and expiry, if available. The components should also be sourced from a qualified supplier, as described elsewhere in this chapter.

When diagnostic and therapeutic radioligands demonstrate the same affinity for the target, a properly validated molecular imaging probe is able to predict the amount of the therapeutic entity that will reach the target. This strategy can be employed to optimize the amount of therapeutic radioligand that reaches the target while minimizing the amount that distributes or is retained by non-target tissues, where undesirable drug action and toxicities are thought to be more likely to occur. There are also opportunities to use the same ligand for both diagnosis and therapy. Such ligands are sometimes called “theranostics.”

Targets

The successful development of a targeted probe for molecular imaging or therapy is highly dependent upon the choice of a relevant target. Candidates for targeting include signals associated with disease control points. Control points can be disease specific or more general e.g. proliferation, metabolism, angiogenesis, genomic instability, etc.^{5,6}. Somatostatin receptors (SSTr) expressed by neuroendocrine tumors and glycoprotein receptor 30 (GRP30) expressed by breast cancers are examples of disease specific control points discussed further in this thesis. Leukocyte function-associated antigen-1 (LFA-1) is an example of a general control point in inflammation and immune cell mediated diseases discussed further in this thesis. Some candidates for targeting may be established biomarkers of disease whose anatomic, physiologic, biochemical or molecular parameters associate with the presence or severity of specific disease states (Table 4). Viable targets for molecular imaging and therapy must be measurable characteristics that reflect physiological, pharmacological, or disease processes in animals or humans, which can

Table 4. Biomarker Pros and Cons

Pros:
Objective
Change more rapidly than other endpoints
Faster detection of potential drug candidates
May reduce drug development costs
May speed time to market
Cons:
Validation – can be complicated (new assays, new models) and costly
Few validated biomarkers known

be objectively measured and evaluated as an indicator of normal biologic or pathogenic processes, or pharmacological responses to a therapeutic intervention. Typically, imaging targets must be detectable and measurable by at least one method other than medical imaging, such as a tissue biopsy, laboratory assay, or physical exam in order to validate the in vivo imaging ligand:target relationship against some objective or “truth” standard. In vitro binding affinity constants are often used to screen novel candidate in vivo molecular imaging and therapy probes. This is sometimes difficult, as the affinity constant cannot be evaluated without considering the target density in vivo. The association constant K_a (in nM⁻¹), or the reciprocal of K_d, the dissociation constant K_d (in nM) must be combined with the target density (in nM) to obtain a valid prediction. This is particularly difficult in vivo owing to the difficulties of obtaining information regarding target density, and the lack of

a comparison truth standard. Further complicating this scenario, are the heterogeneity of the tumor, irregular vascular supply, the rapidly changing microenvironment within and surrounding the tumor, and the evolution of the tumor toward increasing genomic instability, dysplasia, and more rapid tumor progression. Thus, the *in vivo* target expression is known to be heterogeneous and continuously evolving. This dynamic is itself yet another opportunity to employ molecular imaging to optimize targeted therapy, as evidenced herein by the work reporting the modulation of SSTR expression following gemcitabine exposure *in vitro*.

The largest challenge in targeted molecular imaging and therapy of cancer is presented by the spatial and temporal heterogeneity of tumor vasculature^{7,8}, this includes vessel diameter, length, permeability, integrin expression, density, and spatial distribution. Some of these attributes are dependent upon tumor size, such as the necrotic cores of tumors that result from high interstitial pressure and lack adequate vasculature and blood supply. While increased blood flow to tumors serves as a diagnostic marker in nuclear medicine imaging⁹, blood flow within a tumor is dependent upon the vessel network, pressure, and blood viscosity. Overall, blood flow within a tumor is more disorganized and less than that found in other more normal tissues. Tumor vasculature is tortuous and unpredictable, and as a consequence, it must be considered when developing molecular imaging and therapy strategies. One approach to improve therapeutic delivery is priming the tumor tissue with a course of treatment that changes tumor properties, such as interstitial pressure, to favor diffusion and convection to carry the therapeutic payload to its destination⁷. While this may seem counter-intuitive, a pretreatment of anti-angiogenic therapy or nutrient gradient based therapy was designed to improve or normalize blood flow and hence convective transport of a drug into a tumor. This technique has been used with some success, which has been attributed to a pruning effect whereby inefficient and immature blood vessels are shut down leaving behind the relatively mature vessels to flourish and become more efficient in transporting drug molecules into the tumor¹⁰⁻¹².

Mathematical models also provide insight into the relationships between various tumor parameters and drug delivery to solid tumors^{10,13}. Among the modeled attributes of tumors that pose challenges in delivery are limited diffusion and convection. Tumor size has also been shown to play a role in the outcome of various treatments¹⁴. It is more difficult to treat large tumors possibly due to the increased interstitial pressure and lack of vasculature in the necrotic core. The increased interstitial fluid pressure resulting from poor lymphatic clearance hinders extravasation, as well as limiting transport into the interstitium. In some cases, this can also be an advantage, as tumors may retain macromolecules due to limited lymphatic clearance of interstitial fluid¹⁵. Therefore, in addition to the factors influencing target expression, there are also many challenges in delivering radioligands for imaging and therapy. The dynamic nature of tumors greatly influences the effectiveness of targeted molecular imaging and therapy and should be assessed when designing schedules for both diagnostic and therapeutic interventions.

Candidate radioligands for targeted molecular imaging and therapy

Potential candidates for molecular imaging and therapy include radioligands which target specific protein expression products such as receptors, enzymes, and proteins. Radioligand discovery metrics must also include criteria related to disease and target selection, and biomarker development and validation (Table 5). These metrics include disease frequency or prevalence, the impact of the radioligand imaging results on treatment outcomes, and the path to biomarker development and validation. In this work, novel probes and methods were used to reach three targets for molecular imaging and therapy: SSTR, LFA-1, and GRP30.

Table 5. Radioligand Discovery Metrics

Disease Selection
High impact disease
Imaging can influence diagnosis, treatment strategy
Target Selection
Altered in disease state
Specific
Well characterized/validated
Biomarker development and validation
Optimize <i>in vitro</i>
Pre-Clinical
Clinical

Somatostatin is a 14-amino acid peptide hormone found on many cells of neuroendocrine origin that acts as a neurotransmitter in the central nervous system¹⁶. Somatostatin receptors have been demonstrated on the surface of human tumor cells which includes the cells with amine precursor uptake and decarboxylation (APUD) properties such as pituitary tumors, endocrine pancreatic tumors, carcinoids, paragangliomas, small cell lung cancers, medullary thyroid carcinomas and pheochromocytomas^{17,18}. Analogs of somatostatin were developed because human somatostatin has a very short half-life in circulation (2-3 minutes) and is easily broken down by endogenous peptidases¹⁹. These analogs preserved two important molecular features of somatostatin, i.e., its cyclic form and the 4 amino acids involved in the binding to the receptor. One somatostatin analog that has been studied *in vitro* and *in vivo* extensively is octreotide which has been used as a hormonal treatment in patients with carcinoid syndrome²⁰. The presence of SSTR has been used to detect and localize carcinoid, islet cell tumors²¹ and small-cell lung cancer²⁰.

Despite good imaging and diagnostic results with ^{111}In labeled [DTPA⁰] octreotide (Octreoscan®) in the last few years, there have been numerous reports describing new somatostatin radioligands for studying SSTR expression²². Two such ligands, [DOTA⁰, Tyr³] octreotide (DOTATOC) and octreotate (DOTATATE) labeled with ^{90}Y and ^{177}Lu continue to be evaluated for use in Peptide Receptor Radionuclide Therapy (PRRT) of neuroendocrine tumors²³⁻²⁶. Experience using radioligands targeting SSTR expression to effect PRRT have achieved tumor responses in the majority of patients, but have also posed problems with renal and hematological toxicities, and incomplete treatments, especially in radio-resistant tumors. The work presented herein shows that ^{213}Bi -DOTATOC is effective in treating SSTR-expressing tumors with a total absence of any significant toxicities in a preclinical model²⁷.

Leukocyte function-associated antigen-1 is a constitutively expressed integrin found on leukocytes (T-cells, B-cells, macrophages and neutrophils) that is highly overexpressed on lymphomas and leukemias. LFA-1 is involved in recruitment to the site of infection. It binds to intracellular adhesion molecule 1 (ICAM-1, also known as CD54) on antigen-presenting cells and functions as an adhesion molecule. LFA-1 is the first to bind T-cells to antigen-presenting cells and initially binds weakly. A signal from the T-cell receptor and/or the cytokine receptor changes the LFA-1 conformation and prolongs the cell contact, allowing the T-cell to proliferate. LFA-1 is part of the family of leukocyte integrins that are recognised by their common β -chains (CD18) and a distinct α -chain (CD11a), making it a heterodimer. The restricted expression of LFA-1 and its pivotal role in inflammation and immune diseases has created great interest in LFA-1 as a target of drug therapy. This has also provided opportunities for targeted molecular imaging and therapy using radioligands, as described in Chapter 4 of this work.

The G protein-coupled receptor 30 (GPR30) is a member of the rhodopsin-like family of G protein-coupled receptors. The protein binds estrogen, resulting in intracellular calcium mobilization and synthesis of phosphatidylinositol^{3,4,28}-trisphosphate in the nucleus. This protein therefore plays a role in the rapid nongenomic signaling events widely observed following stimulation of cells and tissues with estrogen. The ability to target GPR30 expression in vivo is thought to be an opportunity for targeted molecular imaging of this atypical estrogen-like receptor to provide diagnostic and prognostic information in patients with breast cancer. Efforts to develop a novel radioligand targeting GPR30 are described below and in Chapter 5.

Probes

In directing targeted molecules to tumors, it has been determined that three major limiting factors must be overcome on a systematic scale. The first of these factors is an uneven

distribution of a drug molecule in the organs of the body, where a large amount of a drug is delivered to highly vascular organs such as the kidney and liver, in proportion to blood flow. Secondly, small molecules and peptides are often rapidly excreted, and therefore have short circulation times. The third factor is drug inactivation by irreversible binding to proteins, whereby larger drug molecules (proteins, antibodies) and protein-drug complexes may exhibit prolonged circulation times and be retained in the spleen and bone marrow¹⁵.

Probes As Companion Diagnostics

There are many opportunities to develop radioligand probes for targeted molecular imaging and therapy, perhaps none more exciting than those designed as companion diagnostics, whereby molecular assays that measure levels of proteins, genes or specific mutations are used to provide a specific therapy for an individual's condition by stratifying disease status, selecting the proper medication and tailoring dosages to that patient's specific needs. There are opportunities to use non-invasive companion diagnostic imaging probes throughout the clinical evaluation of novel drugs. First, to aid in the accrual of subjects by using the companion diagnostic as a tool to screen for target expression. This allows trials of targeted therapeutics to be conducted in specific patient populations, which can decrease the size and costs of these studies. Then to monitor target expression within each subject throughout the study. Because patients' expression of a biomarker or target can and often does change over time, this provides additional advantages over conventional biopsy and immunohistochemistry that is typically employed only once prior to enrollment. There are also benefits derived through the use of the companion diagnostic for whole-body imaging, to provide information beyond the primary tumor and individual sites of biopsy-proven disease. And, finally to observe target behavior in response to a therapeutic ligand directed toward the same target. The ability to employ the companion diagnostic imaging probe as a validated biomarker to objectively measure the pharmacologic response to therapy, may sometimes be used as a surrogate end-point. In this manner, the companion diagnostic imaging probe for molecular imaging can be used to screen, monitor, and evaluate the target/tissue response throughout the course of a clinical study to evaluate the safety or efficacy of a targeted therapeutic. Pharmaceutical companies have recognized the considerable power companion diagnostics can bring to the resultant dataset.

There are currently four main themes in the development of radioligands for molecular imaging for use as companion diagnostics in the evaluation of targeted drugs:

1. Monitoring general disease control points such as metabolism, proliferation, hypoxia, apoptosis, angiogenesis, inflammation, and metastasis, e.g. ^{18}F -fluorodeoxyglucose, ^{18}F -Fluorothymidine, $^{99\text{m}}\text{Tc}$ -Annexin V;

2. Monitoring the targeting of a therapeutic radiopharmaceutical with a radioligand directed at the same target, e.g. ^{111}In -Pentetreotide and ^{90}Y -DOTA-Tyr³-octreotide, or more recently ^{68}Ga -DOTA-Tyr³-octreotate;
3. Using external imaging to monitor the same control point that the candidate therapeutic drug is targeting using a radiolabeled drug or drug surrogate, e.g. ^{18}F -fluorodopa;
4. Monitoring a downstream biochemical process that are known to be affected by the drug.

The first approach is analogous to a broad-acting “blockbuster” new angiotensin-receptor blocker (ARB) or a statin to reduce cholesterol which are effective in a variety of diseases in a wide range of patients, as opposed to seeking to develop a targeted drug that is effective in a small subpopulation of patients with disease. The later three themes are representative of more individualized, personalized medicine that holds the promise of higher therapeutic effectiveness. In the postgenomic era, the recognition of a single disease control point as a drugable target may guide the development of probes for molecular imaging and therapy. In the work presented herein, SSTR and GPR30 are examples of single disease control points that are targets of molecular imaging and therapy. Whereas, LFA-1 is an example of a general control point that is operative in a variety of diseases.

Targeted therapeutic drugs seek to exploit subtle phenotypic and pharmacogenomic differences in the pathogenesis of diseases such as breast cancer. For example, the expression of estrogen and progesterone receptors in breast cancer cells are recognized as important biomarkers used to guide treatment. Those patients who do not test positive for these specific receptors will not be able to respond to hormone modulation therapy, which may affect their chance of survival depending upon what treatment options remain, the exact type of the cancer, and the stage of the disease. In addition to hormone receptors, there are other cell surface proteins that may affect prognosis and treatment. For example, patients whose breast cancer cells express HER2 (Human Epidermal Growth Factor Receptor 2) have more aggressive disease and may be treated with the ‘targeted therapy’, trastuzumab (Herceptin®), a monoclonal antibody (MoAb) that targets the HER2 protein and has been shown to improve the prognosis significantly. In 1998, when the drug Herceptin® (trastuzumab) was evaluated for market approval by the U.S. Food and Drug Administration, the pharmacology of trastuzumab was not established²⁹. Rather, the presence of shed (circulating) HER2 was shown to increase the clearance of trastuzumab, presumably evidence of this MoAb binding the HER2 target. As a single agent, Herceptin® produced sustained objective tumor responses in only 14% of patients who had received one or more prior chemotherapies plus hormonal therapy for their metastatic disease studied in clinical trial H0649g (N = 222). In combination, the targeted therapy showed only modest improvement. Patients who were treated with trastuzumab in combination with AC chemotherapy (AC = doxorubicin 60 mg/m² or epirubicin 75 mg/m² plus cyclophosphamide 600 mg/m²) experienced a longer time to progression by 2.1 months ($p <$

0.001), a higher response rate (50% vs 38%), and improved short term 1-year survival, but no difference in median overall survival when compared to AC alone (AC+Herceptin®, N = 143; AC, N = 138). Patients treated with trastuzumab in combination with T chemotherapy (T = paclitaxel 175 mg/m² infused over 3 hours) experienced a longer time to progression by 4.2 months ($p < 0.001$), a higher response rate (35% vs 14%), improved short term 1-year survival, but no difference in median survival when compared to T alone (T+trastuzumab, N = 92; T, N = 96)²⁹. At that time, there were no molecular imaging probes available to aid in the phenotypic assessment of patients with breast cancer. Patients’ HER2 status was available only via immunohistochemistry of tissue biopsies, limited to 1-2 per patient. Thus, the HER2 expression, while documented at the time of patient enrollment, was left unchecked throughout the duration of the trials. Although the presence of satellite metastatic disease was known in many cases, the HER2 status was not known for all sites of disease. Thus, the inability to evidence the HER2 target of trastuzumab at all sites of known disease, coupled with the spatial and temporal heterogeneity of HER2 expression within the tumors, illustrates the need for molecular imaging agents to be used as companion diagnostics in the evaluation of targeted drugs. Such companion diagnostics would have several benefits to drug evaluation and, if marketed as stand-alone diagnostic, to patients who are candidates for targeted therapy.

Radionuclides

Choosing a radionuclide for targeted molecular imaging or therapy is somewhat complex and requires simultaneous analysis of many factors, including: radioactive decay emissions, half-life, chemical properties, production methods, and availability. The ideal radionuclides for molecular imaging and therapy must be readily available. This implies that the radionuclide in the desired chemical form and specific activity is available when needed. The clinical use of molecular imaging and therapy requires that the radionuclide is available Monday through Friday (and perhaps Saturday) to facilitate patient care and to avoid delays in diagnosis and/or treatment. The logistics of the supply chain must also be considered. In some cases, the desired radionuclide may be in limited supply, or available only from a single source. It is prudent to understand the details of the logistics, including: sites of production and target processing, means of shipment, intermediate points in-transit, and other details. This allows one the ability to understand how weather, natural disasters, terrorist acts, and other unforeseeable activities may influence the timely delivery of the radionuclide shipment. The shipping and receipt of the radionuclide should be monitored to maintain awareness of the progress of the radionuclide shipment. This vigilance will allow one to be aware of potential delays and to react appropriately to modify the schedule as necessary. Because time, tide, and radionuclides wait for no man, the schedule of diagnostic or therapeutic administrations must be closely monitored to match the radionuclide and radioligand availability.

The radionuclide must also be available in the desired chemical form, with well-characterized and reliable purity and impurities, and at a cost (including shipping and receiving) that is not prohibitive. The chemical form of the radionuclide is important to facilitate subsequent radiolabeling reactions. The ideal chemical form of the radionuclide is as a simple salt e.g. $^{68}\text{GaCl}_3$, although more complex chemical forms may also be acceptable. Because the radiolabeling reactions are conceived and validated using very precise radiochemistry and stoichiometry, alterations in the chemical form and variations in pH, specific concentration, or impurities may lead to radiolabeling problems that can be quite vexing. This is particularly true when attempting to label compounds with radiometals at high specific activities where non-essential metal ion impurities are known to cause interference.

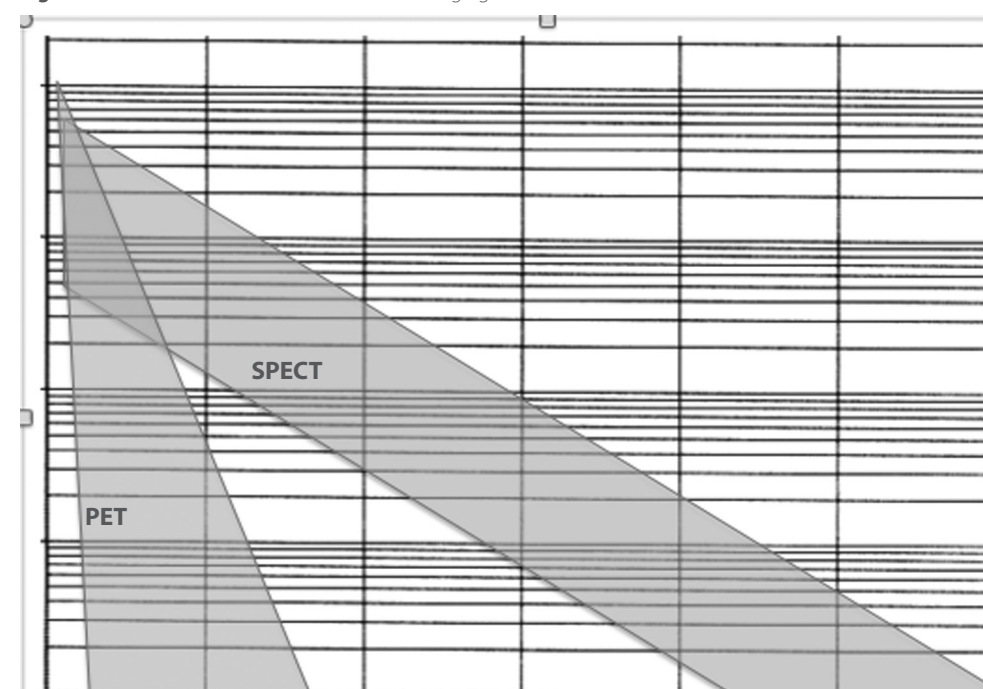
Many physical factors influence the maximum achievable specific activity of radioligands (Table 3). For example, ^{177}Lu -DOTATATE can be radiolabeled, in theory, at 0.72 GBq ^{177}Lu per nmol DOTA-peptide. However, contaminants inherent in the production reduce the maximum achievable specific activity to 0.15 GBq ^{177}Lu per nmol DOTA-peptide. Reactor-produced ^{177}Lu is obtained following (n, γ) reaction on enriched ^{176}Lu , yielding ^{177}Lu with ^{176}Lu and ^{175}Lu contaminants. Because all isotopes of Lu will participate in radiolabeling reactions, the presence of ^{176}Lu and ^{175}Lu will reduce the maximum achievable specific activity. Thus, variability in ^{177}Lu production yields and in the amounts of ^{176}Lu and ^{175}Lu contaminants will produce variability in maximum achievable specific activity. In practice, ^{177}Lu -DOTATATE is often labeled at a specific activity of 40 - 80 MBq per nmol DOTA-peptide. Much higher specific activities have been reported using 0.5 GBq ^{177}Lu per nmol DOTA-peptide prepared using high-specific activity ^{177}Lu , such as that obtained from the High Flux Isotope Reactor at Oak Ridge National Laboratory³¹. Recently, reactor-produced ^{177}Lu from (n, γ) on an enriched ^{176}Yb target has demonstrated much higher achievable specific activity of 0.42 GBq ^{177}Lu per nmol DOTA-peptide³². High specific activities of 0.5 GBq ^{90}Y per nmol DOTA-peptide have also been achieved. In order to achieve higher specific activities, the rigorous elimination of metal impurities is necessary, not only during radiolabeling, but also during synthesis of the DTPA- and DOTA-conjugated peptides^{31,33}.

The radionuclide must be sourced from a previously qualified or "trusted supplier", meaning the supplier has provided evidence of licensure and documentation of appropriate compliance programs to support their production of the radioactive material. The supplier should provide a certificate of analysis accompanying each shipment stating the radionuclide, specific activity, specific concentration, and all radionuclidic and chemical impurities of the batch or lot produced. In the case of radiometals destined for incorporation in multidentate chelates such as DTPA, DOTA, NOTA, TETA, HEHA, etc. it may also be necessary to characterize the metal impurities that may cause interference. Metal impurities in the parts per million (ppm) range are commonly found in radionuclides as a result of their production, and may interfere with radiolabeling reactions. The presence of metal ions of each production batch should be characterized using inductively coupled plasma mass spectroscopy (ICP-MS) and reported at the time of receipt.

Radionuclides for imaging or therapy must also be selected based upon their different properties owing to their intended purpose. Radionuclides intended for molecular imaging should have a relatively short half-life, lack particulate emissions, and have imageable photons. The half-life should also be matched to the timeframe of the biological phenomenon of interest (Figure 4). This ideal half-life could be seconds if intended to measure blood flow or enzyme activity, or minutes to reflect receptor occupancy, or even hours if intended to reflect protein synthesis. The time to target and blood clearance half-time of the candidate probe are also important when selecting radionuclides for imaging and therapy. In general, smaller molecules clear more rapidly, while larger proteins and antibodies exhibit prolonged blood clearance due to interactions with cells and proteins found within the blood and serum.

In order to keep the radiation dose to the patient as low as reasonably achievable, the ideal radionuclides for imaging should have a relatively short half-life, typically minutes to hours. Radionuclides for targeted molecular imaging should also lack particulate emissions, e.g. alpha, beta, or electrons, as they impart significant radiation dose with no ben-

Figure 4. Observation time for PET and SPECT imaging



Adapted from: Meikle et al., Phys. Med. Biol. 50 (2005) R45-R61

Observation time windows of PET and SPECT for measuring the fate of radioligands in vivo. Although the sensitivity of SPECT for detecting minute concentrations of radioligands maybe lower than that of PET, SPECT extends the observational time window to hours, days, or even weeks using tracer-based molecular imaging.

efit for imaging. The biodistribution or pharmacokinetics of the radioligand will also inform regarding the residence time in organs and tissues of interest. This data is useful in estimating the radiation absorbed dose to both target and non-target organs or tissues. Owing to their short half-life, imaging radionuclides must also have chemical properties that allow rapid and complete incorporation into biologically-active compounds of interest.

The imaging modality may also influence the choice of the radionuclide, e.g. SPECT versus PET, and must be matched to the intended observation. If the biological phenomenon is rapid or of short duration PET imaging may have advantages as PET employs short-lived radionuclides. In the case of measurements of blood flow, the tracer $^{15}\text{O}-\text{H}_2\text{O}$ has the distinct advantage that multiple observations are possible owing to the ultra-short half-life of ^{15}O ($t_{1/2} = 2.0$ m). For example, this allows multiple measurements of brain blood flow to be made in a single session, and under a variety of conditions, in order to observe patients' dynamic response to stimuli. Such rapid measurements are only possible with PET. Conversely, if one is interested in observing thyroperoxidase iodination of the tyrosyl residues of the thyroglobulin, a much longer observation time is necessary, so SPECT imaging using ^{123}I ($t_{1/2} = 13$ h) or ^{131}I ($t_{1/2} = 8$ d) or PET imaging using ^{124}I ($t_{1/2} = 4$ d)

maybe useful. In mice, it is also possible to image ^{125}I ($t_{1/2} = 59.4$ d) to observe the in vivo metabolic fate of iodinated radioligands for weeks following administration.

The physical characteristics of the radionuclide are a very important consideration. Radionuclides for imaging must have radioactive decay emissions that include gamma- and/or x-rays to allow PET or SPECT imaging. Positron emitting radionuclides produce two 511 keV gamma photons following the collision of the positron (e^+) with an electron. However, the kinetic energy of the positron must be dissipated before it collides with a relatively low-energy electron. The distance necessary for the positron to release its kinetic energy, the mean free path, is an intrinsic property of each PET radionuclide. This distance is typically 1-4 mm for medically-useful PET radionuclides, and may diminish spatial resolution as the photons are emitted from the point of collision between the positron and the electron, rather than from the nucleus. This limits spatial resolution of each PET radionuclide to its mean free path (≥ 1 -4 mm), which maybe significant in small-animal PET imaging. Upon radioactive decay, radionuclides for SPECT imaging emit gamma photons directly from the nucleus, providing opportunities for increased spatial resolution (0.5-1 mm). Thus, the maximum spatial resolution of SPECT is superior to PET. This is more relevant to small-animal imaging than in humans (Figure 5). In human imaging, where the body habitus is much larger and the resultant tissue attenuation is much greater, the resolution of PET is typically superior to SPECT. PET imaging also has the advantage derived from the increased sensitivity of the detectors used in PET cameras and the higher photon flux of PET radionuclides. The most commonly available radionuclide for PET molecular imaging is ^{18}F . The physical characteristics of cyclotron-produced PET radionuclides are shown in Table 6. There are also a number of generator-produced PET radionuclides available including ^{82}Rb and ^{68}Ga . The physical characteristics of generator-produced PET radionuclides are shown in Table 7.

Gamma cameras for SPECT imaging have been optimized to image 100-200 keV photons. This is a result of the ubiquity of $^{99\text{m}}\text{Tc}$, which has a primary gamma-ray photo-peak of 140 keV. However, it is useful to be reminded that SPECT imaging is possible with many other photon-emitting radionuclides (see Table 8). It is not uncommon to image ^{111}In and ^{123}I radioligands in patients, as both radionuclides are present in radiopharmaceuticals approved for clinical use. In small-animal SPECT many other radionuclides are also employed. In small-animal SPECT imaging, radiation absorbed dose is less of a concern. This allows the use of much longer lived radionuclides that may include particulate emissions in their radioactive decay. The ability to image ^{125}I -labeled radioligands is a unique capability of small-animal SPECT. Radioactive decay of ^{125}I results in the emission of relatively low energy x-rays (see Table 8). While these photons are not useful in human imaging due to their attenuation by overlying tissues, they are imageable in small-animals where the photon attenuation is greatly reduced or negligible. Thus, the imaging modality and radionuclide should be carefully considered when designing radioligands for targeted molecular imaging.

Figure 5. Volumetric resolution of SPECT and PET imaging systems

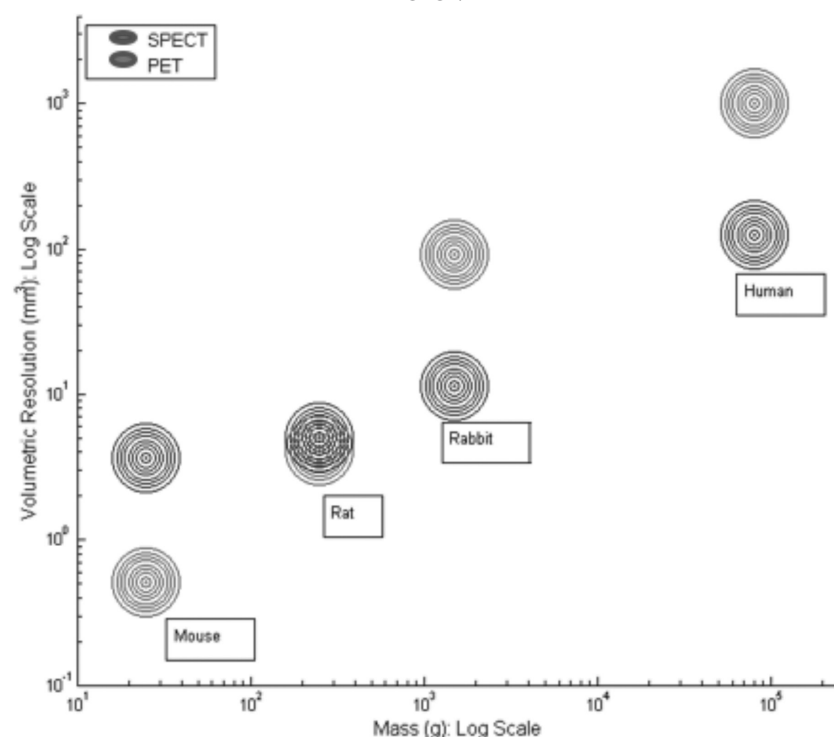


Table 6. Physical characteristics of cyclotron-produced radionuclides for use in PET molecular imaging

Radionuclide	Half-life	Decay mode (% branching ratio)	Production route	E _{β+} keV	β+ End-point energy keV	Abundance, I _{β+} %	E _γ keV (Intensity, I _γ %)
¹¹ C	20.385 m	β ⁺ (100)	¹⁴ N(p,α) ¹¹ C	385.6 (4)	960.2 (9)	99.759 (15)	511.0 (199.5)
¹³ N	9.965 m	β ⁺ (100)	¹⁶ O(p,α) ¹³ N	491.82 (12)	1198.5 (3)	99.8036 (20)	511.0 (199.6)
¹⁵ O	2.0373 m	β ⁺ (100)	¹⁵ N(p,n) ¹⁵ O ¹⁴ N(d,n) ¹⁵ O	735.28 (23)	1732.0 (5)	99.9003 (10)	511.0 (199.8)
¹⁸ F	109.77 m	β ⁺ (100)	¹⁸ O(p,n) ¹⁸ F ²⁰ Ne(d,α) ¹⁸ F	249.8 (3)	633.5 (6)	96.73 (4)	511.0 (193.5)
⁶⁴ Cu	12.701 h	ε + β ⁺ (61.5) β ⁺ (17.60) β ⁻ (38.5)	⁶⁴ Ni(p,n) ⁶⁴ Cu ⁶⁷ Zn(p,α) ⁶⁴ Cu	278.21 (9)	653.03 (20)	17.60 (22)	511.0 (35.2)
⁷⁴ As	17.77 d	ε + β ⁺ (66) β ⁺ (29) β ⁻ (34)	⁷⁴ Ge(p,n) ⁷⁴ As ⁷³ Ge(d,n) ⁷⁴ As	408.0 (8)	944.6 (17)	26.1 (22)	511.0 (58) 595.8 (59) 634.8 (15.4)
⁷⁶ Br	16.2 (2) h	ε + β ⁺ (100) β ⁺ (55)	⁷⁶ Se(p,n) ⁷⁶ Br ⁷⁵ As(α,3n) ⁷⁶ Br	1,532 (8)	3,383 (9)	25.8 (19)	511.0 (109) 559.1 (74) 657.0 (15.9) 1,853.7 (14.7)
⁸⁶ Y	14.74 h	ε + β ⁺ (100) β ⁺ (31.9)	⁸⁶ Sr(p,n) ⁸⁶ Y	535 (7)	1,221 (14)	11.9 (5)	443.1 (16.9) 511.0 (64) 627.7 (36.2) 703.3 (15) 777.4 (22.4) 1,076.6 (82.5) 1,153.0 (30.5) 1,854.4 (17.2) 1,920.7 (20.8)

⁸⁹ Z	78.41 h	ε + β ⁺ (100) β ⁺ (22.74)	⁸⁹ Y(p,n) ⁸⁹ Z	395.5 (11)	902 (3)	22.74 (24)	511.0 (45.5) 909.2 (99.0)
^{94m} Tc	52.0 m	ε + β ⁺ (100) β ⁺ (68.2)	⁹⁴ Mo(p,n) ^{94m} Tc	1,094	2,439 (5)	67.6 (4)	511.0 (140.3) 871.1 (94.2)
¹²⁴ I	4.1760 d	ε + β ⁺ (100) β ⁺ (22.7)	¹²⁴ Te(p,n) ¹²⁴ I	687.04 (85) 974.74 (85)	1,534.9 (19) 2,137.6 (19)	11.7 (10) 10.7 (9)	511.0 (45) 602.7 (62.9) 722.8 (10.4) 1,691.0 (11.2)

Adapted from: Holland JP, Williamson MJ, Lewis JS. Mol Imaging. 2010 Feb;9(1):1-20.
ε = electron capture; m = minutes; h = hours; d = days
Standard deviations given in parentheses, unless otherwise stated

Table 7. Physical characteristics of generator-produced radionuclides for use in PET molecular imaging

Radionuclide	Half-life	Decay mode (% branching ratio)	Production route	E _{β+} keV	β+ End-point energy keV	Abundance I _{β+} %	E _γ keV (Intensity, I _γ %)
⁶² Cu	9.673 m	ε + β ⁺ (100) β ⁺ (97.430)	⁶² Zn/ ⁶² Cu	1,316.0 (24)	2,926 (4)	97.200 (20)	511.0 (194.9)
⁶⁸ Ga	67.71 m	ε + β ⁺ (100) β ⁺ (89.14)	⁶⁸ Ge/ ⁶⁸ Ga	836.02 (56)	1,899.1 (12)	87.94 (12)	511.0 (178.3)
⁷² As	26.0 h	ε + β ⁺ (100) β ⁺ (87.8)	⁷² Se/ ⁷² As	1,117.0 (19) 1,528.5 (19)	2,500 (4) 3,334 (4)	64.2 (15) 16.3 (17)	511.0 (176) 834.0 (79.5)
⁸² Rb	1.273 m	β ⁺ (95.43)	⁸² Sr/ ⁸² Rb	1,167.6 (33) 1,534.6 (34)	2,601 (7) 3,378 (7)	13.13 (14) 81.76 (17)	511.0 (190.9) 776.52 (15.1)
^{110m} In	69.1 m	ε + β ⁺ (100) β ⁺ (63)	¹¹⁰ Sn/ ^{110m} In	1,043 (6)	2,260 (12)	62 (4)	511.0 (125) 657.8 (98)

Adapted from: Holland JP, Williamson MJ, Lewis JS. Mol Imaging. 2010 Feb;9(1):1-20.
ε = electron capture; m = minutes; h = hours
Standard deviations given in parentheses, unless otherwise stated

Table 8. Physical characteristics of γ -ray emitting radionuclides for use in SPECT molecular imaging

Radionuclide	Half-life	Decay mode (% branching ratio)	Production route	E_{np} (keV)	Abundance I_{np} %	E_{γ} keV	Intensity I_{γ} %
^{67}Ga	3.2617 d	ϵ (100)	$^{nat}\text{Zn}(p,\chi)^{67}\text{Ga}$ $^{68}\text{Zn}(p,2n)^{67}\text{Ga}$	Auger L (0.99) Auger K (7.35) CE – K (83.606)	168.3 (21) 60.7 (9) 29.1 (9)	91.265 (5) 93.310 (5) 184.576 (10) 208.950 (10) 300.217 (10) 393.527 (10)	3.11 (4) 38.81 (3) 21.410 (10) 2.460 (10) 16.64 (12) 4.56 (24)
^{99m}Tc	6.01 h	β^- (0.0037) IT (99.9963)	$^{99}\text{Mo}/^{99m}\text{Tc}$	CE – K (1.6286) Auger L (2.17)	74.595 10.32 (6)	140.511 (1)	89.06
^{111}In	2.8047 d	ϵ (100)	$^{111}\text{Cd}(p,n)^{111m}\text{In}$ $^{112}\text{Cd}(p,2n)^{111m}\text{In}$	Auger L (2.27) Auger K (19.3) CE – K (144.57) CE – K (218.64)	100.4 (4) 15.5 (4) 8.07 (8) 4.95 (5)	171.28 (3) 245.35 (4)	90.7 (9) 94.1 (10)
^{123}I	13.2234 h	ϵ (100%)	$^{124}\text{Xe}(p,2n)^{123}\text{Cs}$ $\rightarrow^{123}\text{Xe} \rightarrow^{123}\text{I}$ $^{124}\text{Xe}(p,pn)^{123}\text{I}$ $^{123}\text{Te}(p,n)^{123}\text{I}$	Auger L (3.19) Auger K (22.7) CE – K (127.16)	95.1 (6) 12.4 (4) 13.612	158.97 (5) 528.96 (5)	83.3 1.39 (4)
$^{125}\text{I}^*$	59,400 d	ϵ (100%)		Auger L (3.19) CE – K (3.68) Auger K (22.7) CE – L (30.55)	156.5 (18) 78.1 (19) 19.8 (7) 10.7 (3)	3.77 27.202 (6) 27.472 30.995 (6)	14.8 (6) 39.6 (11) 73.1 (19) 13.0 (3)

Adapted from: Holland JP, Williamson MJ, Lewis JS. Mol Imaging. 2010 Feb;9(1):1–20.
*SPECT imaging with ^{125}I is relevant to animal studies only; ϵ = electron capture; IT = isomeric transition; h = hours; d = days
Standard deviations given in parentheses, unless otherwise stated

Radionuclides for therapy must have a combination of half-life and radioactive decay emissions such that they deliver sufficient radiation dose to damage the cells and/or tissues in which they are localized. The physical characteristics of beta- and alpha-emitting radionuclides used to deliver targeted therapy are shown in Tables 10 and 11.

The relative biological effectiveness (RBE) of radiation is the ratio of biological effectiveness of one type of ionizing radiation relative to another, given the same amount of absorbed energy. The RBE is an empirical value that varies depending on the type of particles

Table 9. Physical characteristics of radionuclides used in targeted radiotherapy

Radionuclide	Decay mode (% branching ratio)	E_{α} keV (% abundance)	Maximum range in tissue (# cell diameters*)	Half-life (days)
^{90}Y	β (100)	2,280.1 (99.9885)	12 mm (>500)	2.6667
^{111}In	ϵ (100)	Auger L 2.27 (100.4) Auger K 19.3 (15.5) CE – K 144.57 (8.07) CE – K 218.64 (4.95)	10 μm (<1)	2.8047
^{177}Lu	β^-	177.0 (11.61) 385.3 (9.0) 498.2 (79.4)	2 mm (>100)	6.647
^{213}Bi	α (2.20) β^- (97.80)	5,549 (0.15) 5,869 (1.94)	50 μm (2)	3.166E-2
^{225}Ac	α (100)	5,637 (4.4) 5,724 (3.1) 5,732 (8.0) 5,790.6 (8.6) 5,792.5 (18.1) 5,830(50.7)	50 μm (2)	10.0

*Assuming an average tumor cell diameter of 20 μm

and energies involved. It is a set of experimental measurements. In radiation dosimetry, the RBE is represented in regulations by the radiation weighting factor, (W_R) or sometime the quality factor. The weighting factors convert absorbed dose (measured in units of grays or rads) into biological equivalent dose for radiation exposure (measured in units of sieverts or rem). The higher the RBE for a type of radiation, the more damaging the type of radiation is, per unit of energy deposited in biological tissues. Different types of radiation have different biological effectiveness mainly because they transfer their energy to the tissue in different ways. Photons and beta particles have a low LET coefficient (RBE = 1), meaning that they ionize atoms in the tissue that are spaced by several thousand angstroms apart along their path. Photons, which lack mass and charge, travel the great-

Table 10. Physical characteristics of β-emitting radionuclides for potential use in molecular targeted therapy

Radionuclide	Half-life	Decay mode (% branching ratio)	Enp keV	Abundance Inp %	EY keV	Intensity IY %
³² P	14.263 d	β ⁻ (100)	1,710.48 (22)	100	—	—
⁴⁷ Sc	3.3492 d	β ⁻ (100)	440.9 (19) 600.3 (19)	68.4 (6) 31.6 (6)	159.381 (15)	68.3 (4)
⁶⁶ Cu	5.120 m	β ⁻ (100)	1,602.8 (12) 2,642.0 (12)	9.01 (9) 90.77 (9)	1,039.2 (2)	9.23
⁶⁷ Cu	61.83 h	β ⁻ (100)	168.2 (15) 377.1 (15) 468.4 (15) 561.7 (15)	1.10 (11) 57 (6) 22.0 (22) 20.0 (22)	91.266 (5) 93.311 (5) 184.577 (10)	7.00 (10) 16.10 (20) 48.7 (3)
⁸⁹ Sr	50.53 d	β ⁻ (100)	1,495.1 (22)	99.99036 (5)	—	—
⁹⁰ Y	64.00 h	β ⁻ (100)	2,280.1 (16)	99.9885 (14)	—	—
¹⁰⁵ Rh	35.36 h	β ⁻ (100)	248 (3) 261 (3) 567.2 (25)	19.7 (5) 5.2 (4) 75.0 (6)	306.1 (2) 318.9 (1)	5.1 (3) 19.1
¹¹¹ Ag	7.45 d	β ⁻ (100)	694.7 (14) 1,036.8 (14)	7.1 (5) 92 (5)	343.12 (2)	6.7
^{117m} Sn	13.60 d	IT (100)	Auger L (2.95) Auger K (21.0) CE – K (126.82) CE – K (129.36) CE – L (151.56)	91.8 (5) 10.7 (3) 64.9 (4) 11.699 26.16 (14)	156.02 (3) 158.56 (2)	2.114 (12) 86.4
¹³¹ I	8.0252 d	β ⁻ (100)	333.8 (6) 606.3 (6)	7.23 (10) 89.6 (8)	284.305 (5) 364.489 (5) 636.989 (4)	6.12 (6) 81.5 (8) 7.16 (10)

¹⁴⁹ Pm	53.08 h	β ⁻ (100)	785 1,048	3.40 24	285.95	3.10
¹⁵³ Sm	46.50 h	β ⁻ (100)	634.7 (7) 704.4 (7) 807.6 (7)	31.3 (9) 49.4 (18) 18.4 (17)	103.18	29.25
¹⁶⁶ Ho	26.80 h	β ⁻ (100)	1,773.3 (11) 1,853.9 (11)	48.7 (21) 50.0 (21)	80.574 (8)	6.71 (8)
¹⁷⁷ Lu	6.647 d	β ⁻ (100)	177.0 (8) 385.3 (8) 498.2 (8)	11.62 (11) 9.0 (5) 79.4 (5)	112.9 208.4	6.17 (7) 10.36
¹⁸⁶ Re	3.7183 d	ε (7.47) β (92.53)	Auger L (6.53) 932.3 (9) 1,069.5 (9)	4.96 (10) 21.54 (11) 70.99 (14)	137.157 (8)	9.47 (3)
¹⁸⁸ Re	17.0040 h	β ⁻ (100)	1,965.4 (4) 2,120.4 (4)	26.3 (5) 70.0 (5)	155.041 (4)	15.61 (18)
^{195m} Pt	4.010 d	IT (100)	Auger L (7.24) Auger K (51.0) CE – L (17.01) CE – K (20.505) CE – M (27.59) CE – K (51.11) CE – L (85.02) CE – L (115.62) CE – M (126.20)	140 (4) 3.3 (4) 69 (6) 65 (5) 16.0 (13) 13.4 (9) 11.5 (8) 61 (4) 19.3 (14)	98.90 (2) 129.5 (2)	11.7 (8) 2.90 (21)
²⁰³ Pb	51.92 h	ε (100)	Auger L (7.78) CE – K (193.6648)	62.8 (15) 17.5	70.832 72.873 82.574 279.1952 (10)	26.4 (6) 44.2 (9) 10.22 (21) 80.9
²⁰⁹ Pb	3.253 h	β ⁻ (100)	197.5	100	—	—

Adapted from: Holland JP, Williamson MJ, Lewis JS. Mol Imaging. 2010 Feb;9(1):1-20.
ε = electron capture; IT = isomeric transition; m = minutes; h = hours; d = days
Standard deviations given in parentheses, unless otherwise stated

Table 11. Physical characteristics of α -emitting radionuclides for potential use in molecular targeted therapy

Radionuclide	Half-life	Decay mode (% branching ratio)	E_{α} keV	Abundance, I_{α} %	E_{γ} keV	Intensity, I_{γ} %
$^{211}\text{At}^*$	7.214 h	α (41.80) ϵ (58.20)	5,869.5 (22)	41.80	76.863 79.29	12.4 20.7
^{212}Bi	60.55 m	α (35.95) β^- (64.06)	6,050.78 (3) 6,089.88 (3)	25.13 (7) 9.75 (5)	727.330 1,620.50	6.67 ^a 1.47 ^a
$^{213}\text{Bi}^*$	45.59 m	α (2.20) β^- (97.80)	5,549 (10) 5,869 (10)	0.15 (3) 1.94 (4)	440.45	25.94 ^b
^{225}Ac	10.0 d	α (100)	5,637 (2)	4.4 (3)	See ^{213}Bi	See ^{213}Bi
			5,724 (3)	3.1 (5)		
			5,732 (2)	8.0 (5)		
			5,790.6 (22)	8.6 (9)		
			5,792.5 (22)	18.1 (20)		
^{230}U	20.8 d	α (100)	5,817.5 (7)	32.00 (20)	—	—
			5,838.4 (7)	67.4 (4)		

Adapted from: Holland JP, Williamson MJ, Lewis JS. Mol Imaging. 2010 Feb;9(1):1-20.
* Radioactive decay produces imageable photons; ϵ = electron capture; m = minutes; h = hours; d = days
Standard deviations given in parentheses, unless otherwise stated
a = insufficient abundance/intensity for imaging, but a radiation safety hazard
b = sufficient abundance/intensity to allow imaging

est distances (up to 1 m) in mater, and thus deposit their energy over the longest distance. Beta particles have mass and charge and travel less distance (2-12 mm), over which they must dissipate their energy. Hence, the lower LET coefficient (RBE = 1) for photons and beta particles. In contrast, alpha particles (RBE = 20), comprised of two protons and two neutrons, have considerably greater mass (1,000 times that of beta) and charge (2+), travel only very short distances (<80 μm) in any medium, and leave a much denser trail of ionized atoms in their wake, spaced about one angstrom apart. This makes alpha particles particularly lethal to the cell(s) with which they interact. However, the ultra short-range of alpha particles in tissue (50 μm) also limits the radiation dose to only 1-2 cell diameters. This is in contrast to beta emitters, which have significantly greater range in tissue (2-12 mm) capable of reaching 100-600 cell diameters. A comparison of the maximum range in tissue of radionuclides commonly used in targeted therapy is shown in Table 9.

The radionuclide range in tissue has an impact on both cell killing and off-target effects. Targeted cell killing using beta-emitting radionuclides capable of traveling great distances in tissue provide the opportunity to deliver radiation dose beyond the target. This so called “cross-fire effect” may allow targeted therapy of tumors in which blood flow or target expression is heterogeneous, such as large solid tumors (Figure 6). However,

the cross-fire radiation dose may reach other non-targeted organs or tissues, resulting in toxicity. The radiation emitted from shorter-ranged particles such as Auger electrons and alpha-emitters may reach only a single targeted cell, limiting greatly the radiation dose to surrounding cells and tissues. This may have an advantage in targeting single-cell disease such as leukemia, and micro-satellite disease. The ideal targeted therapy may involve a radionuclide cocktail, some combination of long- and short-range radioactive decay particles to treat both bulky disease and microscopic disease (Figure 7).

The most time-honored radionuclide for therapy is ^{131}I , with a half-life of 8 days, which decays emitting both gamma photons and beta particles. Therapeutic radionuclides that also emit imageable photons provide the advantage of allowing molecular imaging of the targeted therapy itself.

The radiation dose resulting from the type and energy of the particulate emissions from candidate therapeutic radionuclides can be evaluated using cellular and whole-organism models of radiation dosimetry. Cellular and even sub-cellular models of radiation dose are relevant to short ranged emissions such as alpha particles. Estimates of radiation dosimetry seek to integrate the radiation dose imparted by the radionuclide of interest, through its characteristic radioactive decay emissions, with the organ or tissue residence times (pharmacokinetic data) of the radioligand probe. Medical internal radiation dose estimates also model the radiation dose imparted to an object organ from other adjacent organs nearby. By modeling the radiation dose estimate to both target and non-target tissues, therapeutic radionuclides with desirable radioactive decay emissions and half-life can be selected and/or prioritized for evaluation in animal models.

In addition to the physical characteristics of radionuclides that are candidates for targeted therapy, one must also understand their biological and chemical properties. The in vivo fate of therapeutic radionuclides and their resultant decay products must be considered. This is particularly true for radionuclides which decay emitting other, daughter radionuclides which themselves maybe capable of imparting significant radiation absorbed

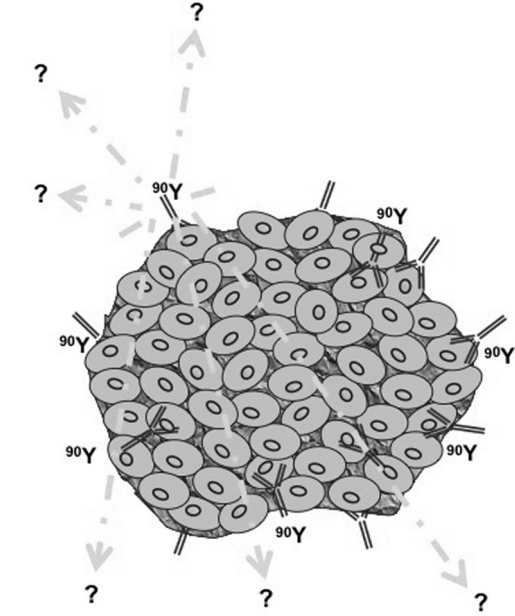


Figure 6. Radiation Cross-fire dose from the decay of the high-energy beta-emitter ^{90}Y

dose, e.g. ^{225}Ac . The biological fate of radionuclides with longer half-lives is also important. In vivo, therapeutic radioligands may deliver their radionuclide payload to the target, but what happens to the radionuclide following target localization? If the radionuclide is internalized within a cell, it may bind to elements within the cytoplasm and become trapped within the cell. Such is case for cationic, polyvalent radiometals that readily associate with elements within the cytoplasm. On the other hand, radiohalogens such as ^{211}At do not readily associate with cytoplasmic elements and maybe released from cells to re-circulate. Some alpha emitters (e.g. ^{225}Ac) have branched decay, resulting in multiple daughters, each with their own physical and chemical properties. The presence of multiple daughter radionuclides presents a challenge to the radioligand in that one radioatom is typically associated with each ligand. If decay results in more than one daughter, what is the fate of the other daughter(s)? Again, if the radionuclide were a cationic radiometal that is internalized within a cell, the daughters would likely be trapped within the cell. Consider also the fate of dead and dying cells whereby, following disruption of the cell membrane, the contents of the cytoplasm are spilled into the surrounding tissue. This is also a concern, particularly for long-lived therapeutic radionuclides such as ^{177}Lu and ^{225}Ac . Thus, the metabolic path of the radioligand must be carefully considered when choosing radionuclides for targeted therapy.

Minimizing off-target effects

Efforts to minimize the non-specific or off-target localization of targeted radioligands have taken many forms. In some instances efforts to modify the radioligand have resulted in changes in off-target localization. Such efforts to optimize target-to-background are aimed at improving the signal-to-noise ratio in molecular imaging, or safety in the case of targeted therapeutics. Some of these approaches to optimize probe targeting are described elsewhere in this chapter. In this section, efforts to modify radioligand localization or retention in, and clearance from, off-target sites of localization will be discussed.

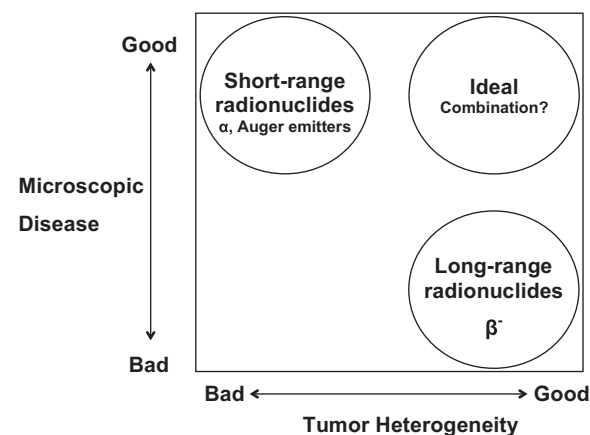


Figure 7. Advantages and disadvantages of short- and long-range radionuclides in therapy

The non-specific renal retention of peptide-based radioligands has proven to be a barrier to the development of targeted therapeutics, fueling efforts to minimize the localization and retention of radioligands in the kidneys. Several studies have reported that the radiation absorbed dose to the kidney is the limiting factor in peptide-receptor radionuclide therapy (PRRT). The first report of late-effects of radiation causing renal damage following ^{90}Y -DOTA, Tyr³-octreotide PRRT was published in 1999²⁸. For over 60 years, it has been known that high radiation doses to the kidney may cause nephropathies several months after exposure³⁴. The current dogma on safe radiation dose to the kidneys extrapolates the threshold tolerated from experience with external beam radiation therapy (XRT). Following XRT, the 5-year risk of developing nephropathy is 5% following a cumulative renal radiation absorbed dose of 23 Gy, increasing to 50% after a 28 Gy dose³⁵. This limit is a challenge for PRRT using beta-emitters such as ^{90}Y and (to a lesser extent) ^{177}Lu . The reduction of the renal uptake of peptide-based radioligands has been a major focus of efforts to minimize off-target localization in efforts to improve safety. These efforts have included interventions that can be categorized as general and specific. The most general intervention has been the co-infusion of large volumes of fluid to expand the plasma and encourage renal clearance of the radiopeptide. Co-infusions of lysine and arginine have been shown to partially prevent reabsorption of radiopeptides and have become a common practice in PRRT, resulting in approximately 40% reduction in renal retention^{26,36-39}. The plasma expander glofusine has also shown a similar ability to reduce renal retention of radiopeptides by 40% in both rats and humans^{40,41}, possibly by blocking megalin-mediated reabsorption in the kidneys^{42,43}. Co-injections of fragments of the megalin ligand albumin have also shown the ability to effectively reduce renal retention of various radiopeptides^{44,45}.

Other interventions aimed at mitigating the nephrotoxicity frequently observed following PRRT have targeted the inhibition of renal fibrosis, a late effect of radiation exposure, employing antioxidants such as amifostine, and inhibitors of angiotensin II. The application of antioxidants has been shown to inhibit the effects of free-radical oxygen species that result from radiation exposure. The free-radical scavenger amifostine is FDA-approved as a cytoprotector during XRT and chemotherapy⁴⁶⁻⁴⁹ and has demonstrated renal protective effects without interfering with the tumoricidal effects of PRRT⁵⁰. Angiotensin II is known to be an important mediator in the progression of renal disease⁵¹⁻⁵⁵. Interventions using angiotensin-converting enzyme inhibitor and angiotensin II receptor blocker have shown the ability to minimize such off-target effects, providing renal protection⁵⁶⁻⁵⁹.

Outline of the thesis

The introduction of this thesis (Chapter 1) focuses on the factors that influence targeted molecular imaging and therapy. Subsequent chapters present novel strategies to optimize targeted molecular imaging and therapy. Chapter 2 consists of several studies comparing high linear-energy transfer (LET) to lower-LET SSTR-targeted radionuclide therapy in vitro and in vivo. The SSTR has been targeted for molecular imaging and therapy for over 20 years, first using octreotide and later using radioligand derivatives thereof. In this work, the safety and efficacy of peptide-receptor radionuclide therapy (PRRT) using the high-LET alpha particle emitting radionuclide ^{213}Bi has been demonstrated both in vitro and in vivo. This safety and efficacy profile is uniquely enabled by combining the short-lived alpha emitter with a very rapidly localizing targeting peptide, ^{213}Bi -DOTATOC. It has been previously shown that the alpha particle resulting from the radioactive decay of ^{213}Bi emits 20% of the total alpha emissions within 15 minutes after injection, and that only 6% of the total alpha emissions remain 3 hours post-injection^{27,60}. This property of ^{213}Bi makes this cytotoxic radionuclide an attractive candidate for SSTR-targeted radionuclide therapy, as the octreotide-based somatostatin analogues are known to localize in tumor within a few minutes after intravenous injection^{27,61,62}. The thesis also contains the first report of the safety and efficacy of ^{213}Bi -DOTATOC used for PRRT of SSTR-expressing neuroendocrine tumors (Chapter 2.4).

The ability to increase the expression of SSTR in vitro following gemcitabine exposure is discussed in Chapter 3⁶³. This strategy provides an opportunity to improve the delivery of PRRT through chronotherapy, timing the administration of PRRT to coincide with increased SSTR expression, thus potentially increasing the amount of radioligand delivered to the target.

Chapter 4 describes novel strategies for targeted molecular imaging and therapy directed at LFA-1. In this work, a novel derivative of an allosteric inhibitor of LFA-1 (BIRT 377) was modified to form butylamino-NorBIRT. This probe was subsequently conjugated with a fluorophore and a bifunctional chelate while maintaining selectivity and specificity for the LFA-1 receptor, illustrating its potential as a radioligand for molecular imaging and targeted therapy⁶⁴.

In Chapter 5, a new structural class of neutral tridentate $^{99\text{m}}\text{Tc}(\text{I})$ -estradiol-pyridin-2-yl hydrazine derivatives is described. This novel GPR30-targeted radioligand was evaluated for potential use in molecular imaging of breast and endometrial cancers⁶⁵.

Pulmonary drug delivery has long held promise in the delivery of drugs targeting the airways and parenchyma of the lung, and also as a means of achieving systemic distribution while avoiding the first-pass effects of the liver encountered with oral dosing. The development of novel imaging strategies to evaluate pulmonary drug delivery are presented in

Chapter 6. In these studies, novel 3D topographic image analysis techniques were developed to allow quantitative assessment of aerosol deposition using small-animal SPECT/CT imaging⁶⁶. These methods were subsequently validated in rats and mice, and then translated to humans^{67,68,68}.

These optimized and validated quantitative techniques allowed SPECT/CT imaging in asthmatic patients to clearly demonstrate the decreased peripheral airway deposition and increased oropharyngeal deposition of fluticasone/salmeterol HFA was a result of its larger particle size. While the smaller particle size of HFA beclomethasone allowed a greater proportion of lung deposition with a concomitant decrease in oropharyngeal deposition⁶⁷.

Efforts to provide quantitative in vivo imaging of radioligand distribution have allowed characterization of the expression of several important single disease control points described above. This work is only possible through rigorous metrology efforts, both scientific and fundamental. Efforts to accurately measure ^{90}Y , a pure beta emitter, using a gas-filled ionization chamber (or radioactivity dose calibrator) are reported in Chapter 7. This work to improve the measurement of ^{90}Y is critical to enable understanding of the potential dose-effects of ^{90}Y -labeled targeted therapies⁶⁹. Many of these techniques also inform regarding best practices in the science of measurement and the need for more rigorous approaches to metrology. The accurate characterization of the input function, e.g. administered radioactivity, is paramount to quantitative in vivo molecular imaging and therapy.

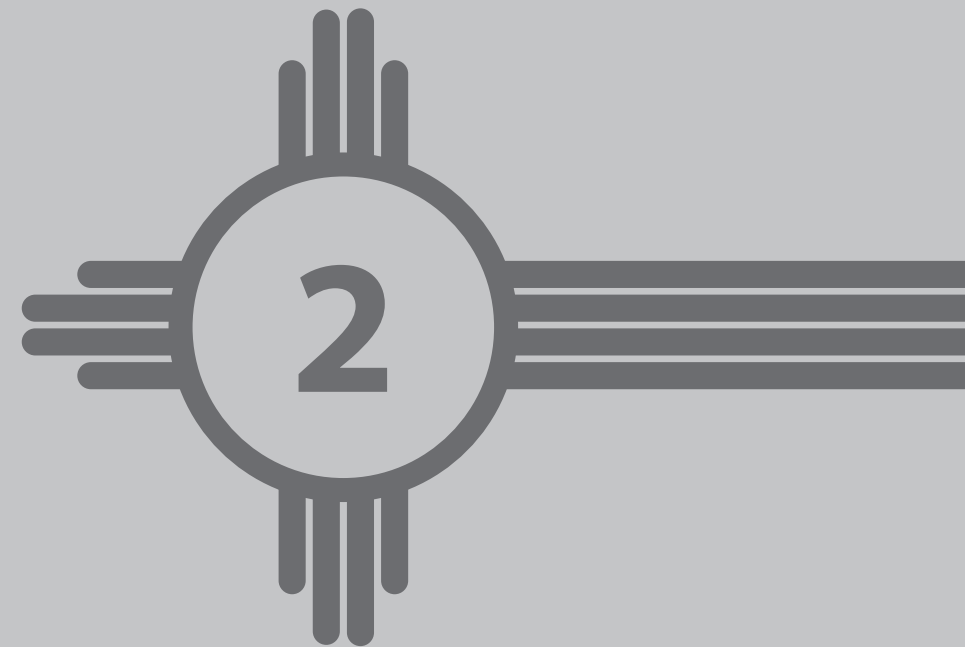
This thesis concludes with the Summary and Discussion Chapter, where the results of studies are summarized and discussed further. A final statement on the clinical relevance of these novel strategies to optimize targeted molecular imaging and therapy is given in order to provide the reader with greater recognition of the opportunities and the necessity to improve targeted molecular imaging and therapy.

References

1. Strebhardt K, Ullrich A. Paul Ehrlich's magic bullet concept: 100 years of progress. *Nat Rev Cancer*. 2008;8(6):473-480.
2. Eckelman WC, Reba RC, Kelloff GJ. Targeted imaging: An important biomarker for understanding disease progression in the era of personalized medicine. *Drug Discov Today*. 2008;13(17-18):748-759.
3. Teunissen JJM. Endocrine tumours - molecular radiation on target: Peptide receptor radionuclide therapy with lutetium-octreotate. The Author; 2008. <http://books.google.com/books?id=s1KtXwAACAAJ>.
4. Reubi JC. Regulatory peptide receptors as molecular targets for cancer diagnosis and therapy. *Q J Nucl Med*. 1997;41(2):63-70.
5. Hanahan D, Weinberg RA. The hallmarks of cancer. *Cell*. 2000;100(1):57-70.
6. Hanahan D, Weinberg RA. Hallmarks of cancer: The next generation. *Cell*. 2011;144(5):646-674.
7. Jang SH, Wientjes MG, Lu D, Au JL. Drug delivery and transport to solid tumors. *Pharm Res*. 2003;20(9):1337-1350.
8. Reddy LH. Drug delivery to tumours: Recent strategies. *J Pharm Pharmacol*. 2005;57(10):1231-1242.
9. Ponto LL, Madsen MT, Hichwa RD, et al. Assessment of blood flow in solid tumors using PET. *Clin Positron Imaging*. 1998;1(2):117-121.
10. Jain RK. Normalizing tumor vasculature with anti-angiogenic therapy: A new paradigm for combination therapy. *Nat Med*. 2001;7(9):987-989.
11. Padera TP, Stoll BR, Tooredman JB, Capen D, di Tomaso E, Jain RK. Pathology: Cancer cells compress intra-tumour vessels. *Nature*. 2004;427(6976):695.
12. Kashiwagi S, Tsukada K, Xu L, et al. Perivascular nitric oxide gradients normalize tumor vasculature. *Nat Med*. 2008;14(3):255-257.
13. Au JL, Jang SH, Wientjes MG. Clinical aspects of drug delivery to tumors. *J Control Release*. 2002;78(1-3):81-95.
14. Gabizon AA. Stealth liposomes and tumor targeting: One step further in the quest for the magic bullet. *Clin Cancer Res*. 2001;7(2):223-225.
15. Gabizon AA. Liposome circulation time and tumor targeting: Implications for cancer chemotherapy. *Adv Drug Deliv Rev*. 1995;16(2&3):285-294.
16. Reubi JC, Lang W, Maurer R, Koper JW, Lamberts SW. Distribution and biochemical characterization of somatostatin receptors in tumors of the human central nervous system. *Cancer Res*. 1987;47(21):5758-5764.
17. Reubi JC, Krenning E, Lamberts SW, Kvolis L. In vitro detection of somatostatin receptors in human tumors. *Metabolism*. 1992;41(9 Suppl 2):104-110.
18. Patel YC. Somatostatin and its receptor family. *Front Neuroendocrinol*. 1999;20(3):157-198.
19. Rens-Domiano S, Reisine T. Biochemical and functional properties of somatostatin receptors. *J Neurochem*. 1992;58(6):1987-1996.
20. Leitha T, Meghdadi S, Studnicka M, et al. The role of iodine-123-tyr-3-octreotide scintigraphy in the staging of small-cell lung cancer. *J Nucl Med*. 1993;34(9):1397-1402.
21. Kvolis LK, Brown ML, O'Connor MK, et al. Evaluation of a radiolabeled somatostatin analog (I-123 octreotide) in the detection and localization of carcinoid and islet cell tumors. *Radiology*. 1993;187(1):129-133.
22. Teunissen JJ, Kwekkeboom DJ, Valkema R, Krenning EP. Nuclear medicine techniques for the imaging and treatment of neuroendocrine tumours. *Endocr Relat Cancer*. 2011;18 Suppl 1:S27-51.
23. Esser JP, Krenning EP, Teunissen JJ, et al. Comparison of [(177)lu-DOTA(0),tyr(3)]octreotate and [(177)lu-DOTA(0),tyr(3)]octreotide: Which peptide is preferable for PRRT? *Eur J Nucl Med Mol Imaging*. 2006;33(11):1346-1351.
24. Kwekkeboom DJ, Bakker WH, Kam BL, et al. Treatment of patients with gastro-entero-pancreatic (GEP) tumours with the novel radiolabelled somatostatin analogue [177Lu-DOTA(0),Tyr3]octreotate. *Eur J Nucl Med Mol Imaging*. 2003;30(3):417-422.
25. Kwekkeboom DJ, Teunissen JJ, Bakker WH, et al. Radiolabeled somatostatin analog [177Lu-DOTA0,Tyr3]octreotate in patients with endocrine gastroenteropancreatic tumors. *J Clin Oncol*. 2005;23(12):2754-2762.
26. Kwekkeboom DJ, de Herder WW, Kam BL, et al. Treatment with the radiolabeled somatostatin analog [177lu-DOTA 0,Tyr3]octreotate: Toxicity, efficacy, and survival. *J Clin Oncol*. 2008;26(13):2124-2130.
27. Norenberg JP, Krenning BJ, Konings IR, et al. 213Bi-[DOTA0, Tyr3]octreotide peptide receptor radionuclide therapy of pancreatic tumors in a preclinical animal model. *Clin Cancer Res*. 2006;12(3 Pt 1):897-903.
28. Otte A, Herrmann R, Heppeler A, et al. Yttrium-90 DOTATOC: First clinical results. *Eur J Nucl Med*. 1999;26(11):1439-1447.
29. Goldstein J, Jerian S, Schechter G, Neeman T, Green M. FDA clinical review of BLA 98-0369; herceptin trastuzumab (rhuMab HER2). www.fda.gov/downloads/Drugs/.../ucm091364. Accessed Jan 18, 2013.
30. Green M. Clinical pharmacology review of herceptin, 98-0369. www.fda.gov/downloads/Drugs/.../ucm091373. Accessed Jan 18, 2013.
31. Breeman WA, Froberg AC, de Blois E, et al. Optimised labeling, preclinical and initial clinical aspects of CCK-2 receptor-targeting with 3 radiolabeled peptides. *Nucl Med Biol*. 2008;35(8):839-849.
32. Melis M, Breeman W, de Blois E, Berndsen S, Konijnenberg M, de Jong M. Increased specific activity of 177Lu-DOTA,Tyr3-octreotate (lu-tate) for peptide receptor radionuclide therapy (PRRT) to improve tumor radiation dose: First data from rat studies. *J Nucl Med* 2012;53(Meeting Abstracts):171.
33. Breeman WA, de Jong M, de Blois E, Bernard BF, Konijnenberg M, Krenning EP. Radiolabelling DOTA-peptides with 68Ga. *Eur J Nucl Med Mol Imaging*. 2005;32(4):478-485.
34. Luxton RW. Radiation nephritis. *Q J Med*. 1953;22(86):215-242.
35. Emami B, Lyman J, Brown A, et al. Tolerance of normal tissue to therapeutic irradiation. *Int J Radiat Oncol Biol Phys*. 1991;21(1):109-122.
36. Bodei L, Ferone D, Grana CM, et al. Peptide receptor therapies in neuroendocrine tumors. *J Endocrinol Invest*. 2009;32(4):360-369.
37. Rolleman EJ, Valkema R, de Jong M, Kooij PP, Krenning EP. Safe and effective inhibition of renal uptake of radiolabelled octreotide by a combination of lysine and arginine. *Eur J Nucl Med Mol Imaging*. 2003;30(1):9-15.
38. Prasad V, Fetscher S, Baum RP. Changing role of somatostatin receptor targeted drugs in NET: Nuclear medicine's view. *J Pharm Pharm Sci*. 2007;10(2):321s-337s.
39. Forrer F, Riedweg I, Maecke HR, Mueller-Brand J. Radiolabeled DOTATOC in patients with advanced paraganglioma and pheochromocytoma. *Q J Nucl Med Mol Imaging*. 2008;52(4):334-340.
40. Vegt E, Wetzels JF, Russel FG, et al. Renal uptake of radiolabeled octreotide in human subjects is efficiently inhibited by succinylated gelatin. *J Nucl Med*. 2006;47(3):432-436.
41. Gotthardt M, van Eerd-Vismale J, Oyen WJ, et al. Indication for different mechanisms of kidney uptake of radiolabeled peptides. *J Nucl Med*. 2007;48(4):596-601.
42. ten Dam MA, Branten AJ, Klasen IS, Wetzels JF. The gelatin-derived plasma substitute gelofusine causes low-molecular-weight proteinuria by decreasing tubular protein reabsorption. *J Crit Care*. 2001;16(3):115-120.
43. Veldman BA, Schepkens HL, Vervoort G, Klasen I, Wetzels JF. Low concentrations of intravenous polygelins promote low-molecular weight proteinuria. *Eur J Clin Invest*. 2003;33(11):962-968.
44. Vegt E, van Eerd JE, Eek A, et al. Reducing renal uptake of radiolabeled peptides using albumin fragments. *J Nucl Med*. 2008;49(9):1506-1511.
45. Vegt E, Eek A, Oyen WJ, de Jong M, Gotthardt M, Boerman OC. Albumin-derived peptides efficiently reduce renal uptake of radiolabelled peptides. *Eur J Nucl Med Mol Imaging*. 2010;37(2):226-234.
46. Bukowski RM. Amifostine (ethyol): Dosing, administration and patient management guidelines. *Eur J Cancer*. 1996;32A Suppl 4:S46-9.
47. Kouvaris JR, Kouloulas VE, Vlahos LJ. Amifostine: The first selective-target and broad-spectrum radioprotector. *Oncologist*. 2007;12(6):738-747.
48. Winczura P, Jassem J. Combined treatment with cytoprotective agents and radiotherapy. *Cancer Treat Rev*. 2010;36(3):268-275.

49. De Souza CA, Santini G, Marino G, et al. Amifostine (WR-2721), a cytoprotective agent during high-dose cyclophosphamide treatment of non-hodgkin's lymphomas: A phase II study. *Braz J Med Biol Res.* 2000;33(7):791-798.
50. Rolleman EJ, Forrer F, Bernard B, et al. Amifostine protects rat kidneys during peptide receptor radionuclide therapy with [177Lu-DOTA0,Tyr3]octreotate. *Eur J Nucl Med Mol Imaging.* 2007;34(5):763-771.
51. Perico N, Codreanu I, Schieppati A, Remuzzi G. Pathophysiology of disease progression in proteinuric nephropathies. *Kidney Int Suppl.* 2005;(94)(94):S79-82.
52. Cohen EP, Fish BL, Moulder JE. The renin-angiotensin system in experimental radiation nephropathy. *J Lab Clin Med.* 2002;139(4):251-257.
53. Cohen EP, Fish BL, Sharma M, Li XA, Moulder JE. Role of the angiotensin II type-2 receptor in radiation nephropathy. *Transl Res.* 2007;150(2):106-115.
54. Brenner BM. AMGEN international prize: The history and future of renoprotection. *Kidney Int.* 2003;64(4):1163-1168.
55. Wenzel UO, Abboud HE. Chemokines and renal disease. *Am J Kidney Dis.* 1995;26(6):982-994.
56. Taal MW, Brenner BM. Renoprotective benefits of RAS inhibition: From ACEI to angiotensin II antagonists. *Kidney Int.* 2000;57(5):1803-1817.
57. Cohen EP, Irving AA, Drobyski WR, et al. Captopril to mitigate chronic renal failure after hematopoietic stem cell transplantation: A randomized controlled trial. *Int J Radiat Oncol Biol Phys.* 2008;70(5):1546-1551.
58. Cohen EP, Fish BL, Moulder JE. Successful brief captopril treatment in experimental radiation nephropathy. *J Lab Clin Med.* 1997;129(5):536-547.
59. Rolleman EJ, Valkema R, Bernard B, Bijster M, Melis M, Krenning EP. Additive effect of an angiotensin II blocker to kidney protection by lysine in a rat model of radiation nephropathy. *EJNMMI.* 2007;34 Suppl.2(2):S240.
60. Behr TM, Behe M, Stabin MG, et al. High-linear energy transfer (LET) alpha versus low-LET beta emitters in radioimmunotherapy of solid tumors: Therapeutic efficacy and dose-limiting toxicity of 213Bi- versus 90Y-labeled CO17-1A fab' fragments in a human colonic cancer model. *Cancer Res.* 1999;59(11):2635-2643.
61. Breeman WA, Bakker WH, De Jong M, et al. Studies on radiolabeled somatostatin analogues in rats and in patients. *Q J Nucl Med.* 1996;40(3):209-220.
62. Arnberg H, Westlin JE, Husin S, Nilsson S. Distribution and elimination of the somatostatin analogue (111In-DTPA-D-Phe1)-octreotide (OctreoScan111). *Acta Oncol.* 1993;32(2):177-182.
63. Nayak TK, Atcher RW, Prossnitz ER, Norenberg JP. Enhancement of somatostatin-receptor-targeted (177)lu-[DOTA(0)-tyr(3)]-octreotide therapy by gemcitabine pretreatment-mediated receptor uptake, up-regulation and cell cycle modulation. *Nucl Med Biol.* 2008;35(6):673-678.
64. Poria RB, Norenberg JP, Anderson TL, et al. Characterization of a radiolabeled small molecule targeting leukocyte function-associated antigen-1 expression in lymphoma and leukemia. *Cancer Biother Radiopharm.* 2006;21(5):418-426.
65. Nayak TK, Hathaway HJ, Ramesh C, et al. Preclinical development of a neutral, estrogen receptor-targeted, tridentate 99mTc(I)-estradiol-pyridin-2-yl hydrazine derivative for imaging of breast and endometrial cancers. *J Nucl Med.* 2008;49(6):978-986.
66. Yu H, Hoppin J, Harlin K, McDonald J, Kuehl P, Anderson TL, Lackas C, Gershman B, Candelaria G, Hesterman JY, Norenberg JP. Implementation Of A 3D Topographic Thinning Model For Assessing Aerosol Deposition Of Radioactive Assays In Small-Animal CT/SPECT Imaging. *IEEE Nuclear Science Symposium Conference Record (NSS/MIC)* 2009;3705-3709.
67. Kuehl PJ, Anderson TL, Candelaria G, et al. Regional particle size dependent deposition of inhaled aerosols in rats and mice. *Inhal Toxicol.* 2012;24(1):27-35.
68. Leach C, Kuehl PJ, Chand R, Ketai L, Norenberg JP, McDonald J. Characterization of respiratory deposition of fluticasone-salmeterol hydrofluoroalkane-13a and hydrofluoroalkane-134a beclomethasone in asthmatic patients. *Annals of Allergy, Asthma & Immunology : Official Publication of the American College of Allergy, Asthma, & Immunology.* 2012;108(3):195-200.
69. Schultz MK, Cessna JT, Anderson TL, et al. A performance evaluation of 90Y dose-calibrator measurements in nuclear pharmacies and clinics in the united states. *Appl Radiat Isot.* 2008;66(2):252-260.

PRRT Using High-LET Radionuclides



A Comparison of High- Versus Low- Linear Energy Transfer Somatostatin Receptor Targeted Radionuclide Therapy In Vitro

Tapan Nayak, Jeffrey Norenberg, Tamara Anderson, and Robert Atcher



Abstract

Introduction: The somatostatin analog [DOTA⁰-Tyr³]-octreotide (DOTATOC) has been widely used to target somatostatin receptor expressing tumors for therapy using radionuclides such as ⁹⁰Y or ¹⁷⁷Lu. Aim: This aim of this study was to compare the effects of DOTATOC labeled to high linear energy transfer (LET) α -emitter ²¹³Bi and low-LET β -emitter ¹⁷⁷Lu in vitro.

Materials and Methods: Somatostatin receptor (sstr)-positive cell line Capan-2 and sstr-negative control cell line A549 were used for the experiments. The effects of two exposure times using different radiation doses of high-LET α -emitter ²¹³Bi and low-LET β -emitter ¹⁷⁷Lu were investigated using cell survival assay. The apoptotic effects were investigated using Cell Death Detection ELISA^{PLUS}10X. The cumulated activity and the mean absorbed dose per unit cumulated activity were calculated using MIRD cellular S- values.

Results: ²¹³Bi-DOTATOC had an approximately four times greater induction of apoptosis than ¹⁷⁷Lu- DOTATOC and a 100 times greater induction of apoptosis than non-radiolabeled DOTATOC. Nonspecific radiolabeled tetra-azacyclododecanetetra-acetic acid (DOTA) had a less pronounced effect on the cell survival and apoptosis, as compared to the sstr-specific radiolabeled DOTATOC.

Conclusion: ²¹³Bi-DOTATOC is significantly more potent than ¹⁷⁷Lu-DOTATOC in vitro because of its high-LET α -emission. ²¹³Bi-DOTATOC shows enhanced effects on mitotic and apoptotic cell deaths.

Introduction

Over the last decade, considerable progress has been made in the investigation of radiolabeled peptides for scintigraphy and therapy. A variety of radiolabeled somatostatin analogs have been used for peptide receptor radionuclide therapy (PRRT) for somatostatin receptor (sstr) positive tumors.^{1,2} One such somatostatin analog being used, [DOTA⁰, Tyr³]octreotide or DOTATOC, is specific to sstr subtypes 2 and 5. After the administration of radiolabeled DOTATOC, a receptor-radioligand compound is formed, which is internalized by the cell. These chelated compounds are transported to the lysosomal compartment in cytoplasm where they stay intracellularly for a long period of time and deliver the radiation dose inside the cell.^{3,4}

Many studies of radiolabeled DOTATOC for targeted therapy of somatostatin receptor expressing tumors have been presented with regard to efficacy and possible toxicity with the low linear energy transfer (LET) β -emitters, ⁹⁰Y and ¹⁷⁷Lu.⁴ This new receptor-mediated radiolabeled DOTATOC therapy has led to tumor responses in a majority of patients evaluated in these clinical studies, but has also posed problems caused by both renal and hematological toxicities. Kidney failures have even been reported after treatment with ⁹⁰Y-DOTATOC in two studies.^{5,6} In a completed clinical therapy study, it was observed that ⁹⁰Y-DOTATOC showed an overall response rate of 20%–30%.⁷ This indicates that only partial response and incomplete treatments have been achieved with this agent and that, possibly, higher relapse rates may occur in the future.

Solutions to these problems may lie in two factors: (1) choice of radionuclide and (2) absorbed dose of the radiolabeled DOTATOC. Over the past decade, there has been a progressively stronger interest in the use of high-LET α -particle emitters for radionuclide therapy.⁸

High-LET forms of radiation pose a higher relative biological effectiveness (RBE) for cell killing, have good localization characteristics resulting in energy deposition within 90 μ m of the decay site, greatly reduce oxygen sensitizing effects, and reduce cell-cycle stage dependence. High-LET radiation is, therefore, superior to low-LET radiation for cancer treatment in many ways.⁸

In this study, we compared the effects of DOTATOC labeled with different doses of the high-LET α -emitter ²¹³Bi and the low-LET β -emitter ¹⁷⁷Lu *in vitro* using cell-survival and apoptosis assays.

Methods and materials

Cell and Tissue Culture

Somatostatin receptors are expressed in high density in a variety of neoplastic tissues, particularly in gastric neuroendocrine tumors. For the purpose of this study, a human pancreatic adenocarcinoma cell line, Capan-2 (American Type Culture Collection; Manassas, VA), was selected as the somatostatin receptor-positive cell line. A human lung carcinoma cell line, A549 (American Type Culture Collection; Manassas, VA), was used as the control somatostatin receptor-negative cell line.

Radionuclides

^{225}Ac (Actinium-225) is an α -particle-emitting radionuclide with a 10.0-day half-life. A $^{225}\text{Ac}/^{213}\text{Bi}$ generator (National Institute of Health; Bethesda, MD) was eluted with 1–2 mL of double-distilled, de-ionized water and flushed with air to remove excess water. ^{213}Bi was slowly eluted with 1 mL of freshly prepared 0.1–0.15 M of hydroiodic acid over 2 minutes. ^{213}Bi chloride solution was buffered to a pH of 5.5 using 3 M of ammonium acetate solution.

The purity of ^{213}Bi was determined by γ -spectroscopy using a hyperpure Germanium detector (Canberra Industries, Meriden, CT).

^{177}Lu (International Isotopes Inc.; Idaho Falls, ID) was in the form of ^{177}Lu -chloride in 0.05 N of optima-grade hydrochloric acid.

Radiolabeling

SMT-487 (DOTATOC formulation kit) was labeled to ^{213}Bi and ^{177}Lu , as previously described.^{9,10} Incorporation yield was assessed using silica gel Instantaneous Thin Layer Chromatography (ITLC, Pall Corporation; Ann Arbor, MI) and 0.9% sodium chloride. The incorporation yield was measured using an automatic gamma counter (Wallace Wizard 1480, Perkin Elmer; Gaithersburg, MD). Radiochemical purity was assessed by high-pressure liquid chromatography (HPLC) using a C-18 column (JT Baker; Phillipsburg, NJ) with a radiometric detector (gamma-ram, INUS Systems Inc.; Tampa, FL). The tray temperature was 4°C, the column temperature was 30°C, and the injectate volume was 100 μL . A solvent system of 0.05 M of sodium acetate, at a pH of 5.5, as buffer A, and 100% methanol as buffer B, were used.

Radioligand Receptor Studies

To evaluate the ligand binding to the somatostatin receptor expressed on Capan-2 cells, direct-binding experiments were performed. The cell lines were incubated at room temperature for 90 minutes, with a known amount of radioligand and increasing concentrations of unlabeled DOTATOC in a HEPES buffer (pH, 7.4), with a total volume of 100 μL . After incubation, 1 mL of ice-cold HEPES buffer was added to each

assay mixture, and then the membrane-bound radioactivity was separated from unbound radioactivity by centrifugation for 5 minutes at 1200 rpm. The cell pellets were washed twice with ice-cold HEPES buffer and then counted in an automatic gamma counter. Specific binding was taken to be the total binding minus the binding in the presence of 10 μM of unlabeled DOTATOC.

Apoptosis Assay

Cell Death Detection ELISA^{PLUS}10X (Roche Applied Sciences; Indianapolis, IN) was used for the apoptosis assay. The Cell Death Detection ELISA^{PLUS} 10X is based on a quantitative sandwich-enzyme-immunoassay principle, using mouse monoclonal antibodies directed against DNA and histones, respectively. This allows for the specific detection and quantification of mono- and oligonucleosomes that are released into the cytoplasm of cells that die from apoptosis. Four treatments with a radiation dose of 37 kBq were prepared (^{213}Bi -DOTATOC, ^{213}Bi -DOTA, ^{177}Lu -DOTATOC, ^{177}Lu -DOTA), as well as an equimolar solution of nonradiolabeled DOTA-TOC. Cells were incubated at 37°C with the treatments in 96-well plates for 3 different time periods (24 hours, 48 hours, and 96 hours). After incubation, the plates were centrifuged for 10 minutes at 200 g. After removing the supernatant and resuspending the cell pellets in 200 μL of 1X lysis buffer solution, plates were incubated for 30 minutes at room temperature. After centrifuging as described above, 20 μL of supernatant (from each sample) was pipetted into a streptavidin-coated plate, and 80 μL of antihistone biotin and anti-DNA-POD antibodies was added to each sample. The samples were incubated in the streptavidin-coated plate at room temperature and shaken at 300 rpm for 2 hours. During this incubation period, the biotin-labeled antihistone antibody binds to the histone component of the nucleosomes and the streptavidin-coated microplate, whereas the POD-labeled, DNA-specific antibody binds to the DNA component of the nucleosomes. After the removal of unbound antibodies, by rinsing well (3 times) with 250 μL of incubation buffer, nucleosomes were photometrically detected at 405 nm (Molecular Devices SpectraMax 340, Global Medical Instrumentation, Inc.; Ramsey, MN) by measuring peroxidase (POD) activity with 100 μL of 2, 2'-Azino-di [3-ethyl-benz-thiazolin-sulfonate] (ABTS) as the substrate.

Cell Survival Studies

Cell survival studies were performed in order to establish the relationship between the radiation dose and the proportion of the cells that survived. The effects of exposures resulting from incubation times of 1 hour and 3 hours with 3 different doses of ^{213}Bi - and ^{177}Lu -labeled to DOTA or DOTATOC were determined by a colony-forming assay.

After a 15-day incubation at 37°C, colonies from each treatment were counted by 2 independent, blinded observers after washing twice with phosphate buffered saline (PBS) solution, fixing with formalin solution, and staining with 0.2% crystal violet.

Cellular Dosimetry

The cell nucleus is the critical target for either cell death or transformation.¹³ Therefore, the mean absorbed dose to the nucleus is of significance, particularly for PRRT, in which the peptide is internalized at the receptor target site and delivers a radiation dose inside the cell closer to the nucleus. The mean absorbed dose to the nucleus and the cumulated activity were calculated using the equations (see Equations 1 and 2) and the experimental data obtained from radioligand receptor studies and the geometric analysis of the cells.

$$D_N = \tilde{A}_{\text{cell}} \left[\sum_j f_{\text{cs}} b_j S_j (N \leftarrow \text{Cs}) + \sum_j f_{\text{cy}} b_j S_j (N \leftarrow \text{Cy}) \right] \quad (\text{Eq. 1; ref. 14})$$

$$\tilde{A}_{\text{cell}} = \frac{\mu A_i}{\lambda_p N} (e^{-\lambda_p T_i} - e^{-\lambda_p T}) \quad (\text{Eq. 2; ref. 1})$$

Where

D_N = Mean absorbed dose.

\tilde{A}_{cell} = Cumulative activity in the cell.

f_{cs} = fraction of activity that is on cell surface.

f_{cy} = fraction of activity that is in the cytoplasm.

$S(N \leftarrow \text{Cs})$ = S-value (cell surface to the nucleus)

$S(N \leftarrow \text{Cy})$ = S-value (cytoplasm to the nucleus)

j = daughter of the parent radionuclide

b_j = branching ratio of j th radionuclide

A_i = initial activity to the treatment group

λ_p = decay constant

T_i = incubation time with activity

T = total therapy time of the colony-forming assay

N = Total number of cells in the treatment group

μ = fraction of activity bound to the cell

In the cellular dosimetry model used (see Equations 1 and 2), the cellular radioactivity is assumed to be uniformly distributed in one of the following regions of the cells: throughout the cell (C), cytoplasm (Cy), cell surface (Cs), and cell nucleus (N). However this model does not take into account nonspherically symmetric cell shapes, nonuniform distribution of activity within the subcellular compartments, and acen-

tric cell nuclei. The changing volume (mass) of the cell during cell-cycle progression is also not taken into account in this cellular dosimetry model.^{1,14} The doses to the culture, self-dose, and cross-dose were taken into account for the calculations.

Statistical Analysis

All numerical data were expressed as the average of the values \pm the standard error of mean (SEM). A Student's t test was performed to compare data and results were considered statistically significant when a p value less than 0.05 was found. Graphpad Prism 4.01 (San Diego, CA) and Microsoft Office Excel version 2003 (Redmond, WA) were used for statistical analysis.

Results

Radionuclide and Radiochemical Purity

The obtained ^{213}Bi solution was tested for possible contaminations of ^{225}Ac . No γ emission from ^{225}Ac was observed in the ^{225}Ac window and γ emission particular to ^{213}Bi was observed in the ^{213}Bi window. Apart from the above observations, the decay characteristics studied over a period of time after each elution suggested that at

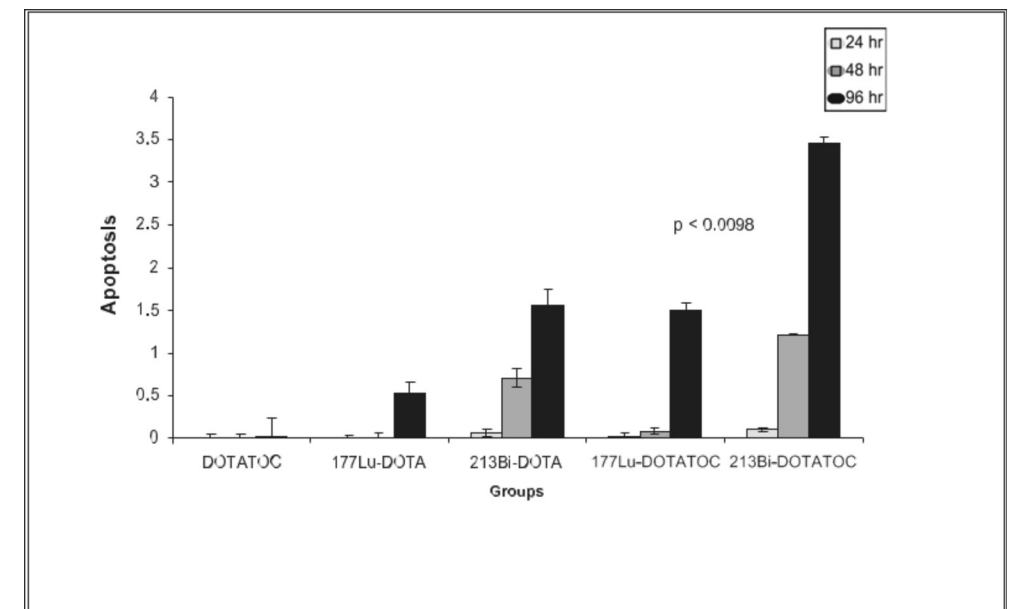


Figure 1. Effects of 37kBq of ^{177}Lu and ^{213}Bi labeled to DOTA and DOTATOC on somatostatin receptor expressing Cell Line Capan-2. The data are expressed as mean apoptosis \pm standard error of the mean. Apoptosis measured as corrected absorbance. Corrected absorbance = background corrected absorbance from treatment groups — background corrected absorbance from the control untreated group.

least 99% of radioactivity present in the samples was ²¹³Bi. All the experiments were performed using the eluted ²¹³Bi with no detectable impurities. ²¹³Bi and ¹⁷⁷Lu were successfully labeled to DOTATOC with high specific activity, an incorporation yield of over 99%, and a radiochemical purity of not less than 95%.

Apoptosis Studies

As shown in Figure 1, the high-LET α -emitter ²¹³Bi had a much greater induction of apoptosis, as compared to the low-LET beta emitter ¹⁷⁷Lu ($p<0.0098$). Target-specific ¹⁷⁷Lu- DOTATOC and nontarget-specific ²¹³Bi- DOTA had similar apoptotic effects. At 48 hours, ²¹³Bi-DOTATOC had an approximately 4 times greater induction of apoptosis than ¹⁷⁷Lu-DOTATOC and a 100 times greater induction of apoptosis than nonradioactive DOTATOC.

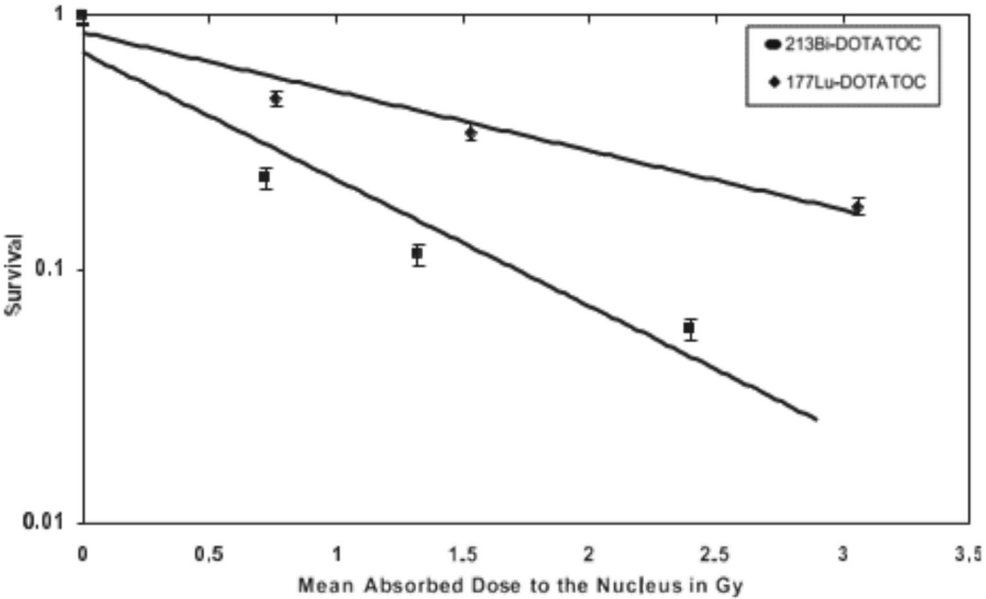


Figure 2. Cell Survival Curves of high-LET versus low-LET target-specific mean absorbed radiation doses to the nucleus for the somatostatin receptor expressing Capan-2 cell line.

Cell Survival

At the same calculated mean absorbed dose to the nucleus, ²¹³Bi-DOTATOC had significantly decreased cell survival, as compared to ¹⁷⁷Lu- DOTATOC (see Fig. 2). A similar concentration of radiolabeled DOTA had a less pronounced effect on cell survival than the sstr-specific radio-labeled DOTATOC, as shown in Table 1.

Table 1. Calculated Mean Absorbed Doses to the Nucleus and the Corresponding Percent Survival of Various Groups for the Somatostatin Receptor Expressing Capan-2 Cell Line

Group	D N	% Survival
¹⁷⁷ Lu-DOTA	0.62 Gy	58.82
¹⁷⁷ Lu-DOTA	1.25 Gy	47.05
¹⁷⁷ Lu-DOTA	2.50 Gy	29.41
²¹³ Bi-DOTA	0.35 Gy	41.17
²¹³ Bi-DOTA	0.64 Gy	29.41
²¹³ Bi-DOTA	1.19 Gy	17.64
¹⁷⁷ Lu-DOTATOC	0.76 Gy	47.05
¹⁷⁷ Lu-DOTATOC	1.53 Gy	35.29
¹⁷⁷ Lu-DOTATOC	3.06 Gy	17.64
²¹³ Bi-DOTATOC	0.72 Gy	23.52
²¹³ Bi-DOTATOC	1.32 Gy	11.62
²¹³ Bi-DOTATOC	2.40 Gy	5.82

Discussion

Currently, somatostatin receptor-targeted cancer beta-particle-emitting radionuclide therapy offers the potential for the systemic control of neoplasms and metastatic cancer, though the success rates are often very poor. From a radiobiological perspective, radionuclides that emit alpha particles offer advantages for certain radiotherapeutic applications. They emit much higher energy particles than most of the betas, yet their ranges are two orders of magnitude lower. Alpha particles have a LET that is about 100 times greater than the beta particles and this is manifested by a higher RBE and a much shorter range. Consequently, a much greater fraction of total energy is imparted to the targeted cancer cell and, thus, very few nuclear hits are required to kill the cell.^{15,16} Figure 2 and Table 1 show that a lower mean absorbed dose to the nucleus of the high- LET α -particle emitter ²¹³Bi is required to produce a greater loss of reproductive integrity than the low-LET β -emitter ¹⁷⁷Lu.

Radiation-induced apoptosis in cancer cells has been a topic of intense research during the last decade and is of great significance and a major strategy in cancer therapy. The apoptotic response correlates well with the antitumor efficacy of radiation, which makes it a candidate predictor of tumor-treatment response.¹⁷ Alpha emitters, such as ²¹³Bi, are known to cause G2M arrest and induce apoptosis in cancer cell lines.^{11,12} This study was performed to evaluate radiation- induced apoptosis and highlight the radiobiological and radiotherapeutical relevance of this mode of cell death in the selection of the best suitable type of radionuclide for therapy.

The results obtained (see Fig. 1) confirm and emphasize the superiority of α -particles with their greater induction of apoptosis.

Hence, high-LET radionuclide therapy clearly offers two advantages over low-LET radionuclide therapy: (1) loss of reproductive integrity and (2) greater induction of apoptosis. Which, in turn, are of great importance in cancer therapy.

Conclusion

The high-LET α -particle emitter ^{213}Bi -DOTA-TOC is significantly more potent than the low-LET β -particle emitter ^{177}Lu -DOTATOC *in vitro* because of its high-LET alpha emission and its enhanced effects on mitotic and apoptotic deaths.

Acknowledgments

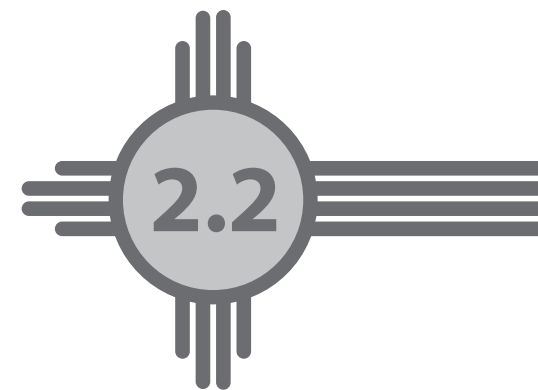
We are thankful to Dr. Michael G. Stabin (Vanderbilt University, Nashville, TN) and Dr. Roger Howell (University of Medicine and Dentistry of New Jersey, Newark, NJ) and for their valuable inputs and guidance related to cellular dosimetry. Technical support and laboratory assistance provided by Rahul B. Poria (University of New Mexico Health Sciences Center, Albuquerque, NM) is greatly appreciated. Gratitude is extended to Dr. Martin W. Brechbiel and Dr. Kayhan Garmestani, of the Radiation Oncology Branch, National Cancer Institute, National Institute of Health (Bethesda, MD), for providing the $^{225}\text{Ac}/^{213}\text{Bi}$ generator and technical assistance in its operation. This project was supported by the grant, DE-FG01-001NE23554, from the United States Department of Energy.

References

1. Capello A, Krenning EP, Breeman WA, et al. Tyr3-octreotide and Tyr3-octreotate radiolabeled with ^{177}Lu or ^{90}Y : Peptide receptor radionuclide therapy results *in vitro*. *Cancer Biother Radiopharm* 2003;18:761.
2. Krenning EP, Kwekkeboom DJ, Valkema R, et al. Peptide receptor radionuclide therapy. *Ann NY Acad Sci* 2004;1014:234.
3. Breeman WA, Bakker WH, de Jong M, et al. Studies on radiolabeled somatostatin analogs in rats and in patients. *Q J Nucl Med* 1996;40:209.
4. Reubi JC. Peptide receptors as molecular targets for cancer diagnosis and therapy. *Endocr Rev* 2003;24:389.
5. Otte A, Herrmann R, Heppeler A, et al. Yttrium-90 DOTATOC: First clinical results. *Eur J Nucl Med* 1999;26:1439.
6. Schumacher T, Waldherr C, Mueller-Brand J, et al. Kidney failure after treatment with ^{90}Y -DOTATOC. *Eur J Nucl Med Mol Imaging* 2002;29:435.
7. Lewington VJ. Targeted radionuclide therapy for neuroendocrine tumors. *Endocr Relat Cancer* 2003;10:497.
8. McDevitt MR, Sgouros G, Finn RD, et al. Radioimmunotherapy with alpha-emitting nuclides. *Eur J Nucl Med* 1998;25:1341.
9. Norenberg JP, Krenning BJ, Konings IR. ^{213}Bi -[DOTA⁰,TYR³] octreotide (bi-DOTATOC) in peptide receptor radionuclide therapy (PRRT): Radiolabeling, stability, and biodistribution. *Nucl Med Commun* 1999;20:383.
10. Breeman WA, de Jong M, Visser TJ, et al. Optimising conditions for radiolabeling of DOTA-peptides with ^{90}Y , ^{111}In , and ^{177}Lu at high specific activities. *Eur J Nucl Med Mol Imaging* 2003;30:917.
11. Palayoor ST, Humm JL, Atcher RW, et al. G2M arrest and apoptosis in murine T-lymphoma cells following exposure to ^{212}Bi alpha particle irradiation. *Nucl Med Biol* 1993;20:795.
12. Li Y, Rizvi SM, Ranson M, et al. ^{213}Bi -PAI2 conjugate selectively induces apoptosis in PC3 metastatic prostate cancer cell line and shows anti-cancer activity in a xenograft animal model. *Br J Cancer* 2002;86:1197.
13. Fisher DR, Harty R. The microdosimetry of lymphocytes irradiated by alpha-particles. *Int J Radiat Biol Relat Stud Phys Chem Med* 1982;41:315.
14. Murty Goddu S, Howell RW, Bouchet LG, et al. *MIRD Cellular S Values: Self-Absorbed Dose Per Unit Cumulated Activity for Selected Radionuclides and Monoenergetic Electron and Alpha Particle Emitters Incorporated into Different Cell Compartments*. Reston, Virginia: Society of Nuclear Medicine, 1997.
15. Allen BJ, Blagojevic N. Alpha- and beta-emitting radiolanthanides in targeted cancer therapy: The potential role of terbium-149. *Nucl Med Commun* 1996;17:40.
16. Lloyd EL, Gemmell MA, Henning CB, et al. Cell survival following multiple-track alpha particle irradiation. *Int J Radiat Biol Relat Stud Phys Chem Med* 1979;35:23.
17. Verheij M, Bartelink H. Radiation-induced apoptosis. *Cell Tissue Res* 2000;301:133.

Somatostatin-receptor targeted
 α -emitting ^{213}Bi is therapeutically
more effective than β --emitting
 ^{177}Lu in human pancreatic
adenocarcinoma cells

Tapan K Nayak, Jeffrey P Norenberg, Tamara L Anderson, Eric R Prossnitz,
Michael G Stabin, Robert W Atcher



Abstract

Advanced clinical cancer therapy studies of the patients treated with somatostatin-receptor (sstr) targeted [DOTA⁰-Tyr³]-octreotide (DOTATOC) labeled with low-Linear-Energy-Transfer (LET) β^- -emitters have shown overall response rates in the range of 15-33%. In order to improve outcomes, we sought to compare the therapeutic effectiveness of sstr-targeted high-LET α -emitting ^{213}Bi versus low-LET β^- -emitter ^{177}Lu by determining the relative biological effectiveness (RBE) using external γ -beam of ^{137}Cs as reference radiation.

The sstr-expressing human pancreatic adenocarcinoma Capan-2 cells and A549 control cells were used for this study. The effects of different radiation doses of ^{213}Bi and ^{177}Lu labeled to 1, 4, 7, 10-tetraazacyclododecane-1, 4, 7, 10-tetraacetic acid (DOTA) and sstr-targeted DOTATOC were investigated using a clonogenic cell survival assay. Apoptosis was measured using Cell Death Detection ELISA^{PLUS} 10X[®] kit.

Using equimolar DOTATOC treatment with concurrent irradiation with a ^{137}Cs source as reference radiation the calculated RBE of ^{213}Bi -DOTATOC was 3.4 as compared to 1.0 for ^{177}Lu -DOTATOC. As measured in terms of absorbance units ^{213}Bi -DOTATOC caused 2.3 fold greater release of apoptotic specific mono- and oligonucleosomes than ^{177}Lu -DOTATOC at the final treatment time at 96 hours ($p < 0.001$) in sstr-expressing Capan-2 cells.

In conclusion, at the same absorbed dose, ^{213}Bi -DOTATOC is therapeutically more effective in decreasing survival than ^{177}Lu -DOTATOC in human pancreatic adenocarcinoma cells due to its comparatively higher RBE.

Introduction

Pancreatic adenocarcinoma is the fourth leading cause of cancer death in the United States and has the lowest survival rate of non-hematological cancers (1). The lowest survival rate in pancreatic adenocarcinoma is explained by advanced and metastatic stage of disease at the time of diagnosis and resistance to all form of treatment (2, 3). In an attempt to improve the treatment options for pancreatic adenocarcinoma, researchers have explored a number of novel therapies such as endocrine therapy and immunotherapy. Unfortunately, most of these efforts have led at best to modest improvements in median survival, without any increase in cure rates (3).

The discovery that certain types of cancers and tumor types overexpress receptors for peptide hormones led to the field of peptide receptor scintigraphy and peptide receptor radionuclide therapy (PRRT) (4, 5). One such target for peptide receptor cancer therapy is the somatostatin receptor (sstr) (6). Five somatostatin receptors (sstr1-sstr5) have been identified and characterized in humans, all of which are members of the G protein-coupled receptor (7). Somatostatin receptor subtypes 2 and 5 are highly overexpressed in exocrine pancreatic adenocarcinomas of neuroendocrine origin. Somatostatins account for less than 2% of all pancreatic cancers (8, 9). Various somatostatin analogues were developed to specifically target sstr2 and 5 including [DOTA⁰, Tyr³] octreotide or DOTATOC for potential use as diagnostic and therapeutic radiopharmaceuticals in nuclear medicine and cancer therapy (4, 10, 11). Studies of radiolabeled DOTATOC for targeted therapy of sstr-expressing pancreatic tumor have demonstrated efficacy and possible toxicity with the β^- -emitter ^{90}Y (11, 12). The ^{90}Y -DOTATOC therapies led to overall pancreatic tumor responses in 15-33% of patients evaluated, but not without renal or hematological toxicities (4, 12, 13). Kidney failure has even been reported after treatment with ^{90}Y -DOTATOC in clinical studies (14, 15). In an attempt to overcome this problem, ^{177}Lu -DOTATOC was studied in rats bearing small tumors with an overall response rate ranging from 50-60% and minimal nephrotoxicity as result of lower absorbed radiation dose to the kidney due to lower energy and shorter mean path length (16).

A limiting factor associated with moderate success of previous studies may be the linear energy transfer (LET) of the β^- -emitting radioisotopes used. Over the past decade, there has been a growing interest in the use of high-LET α -emitting radionuclides for cancer therapy (17-19).

It is believed that the most important factor in radiation damage is DNA double strand breaks (20). When these double strand breaks are joined with wrong DNA ends during a subsequent nonhomologous end-joining event, the results may be deletion, chromosome aberrations and reproductive cell death (21, 22). It has been demonstrated that misjoining frequencies are higher with high-LET radiation than with low-LET radiation (23) and as a consequence the complex DNA damage produced by high-LET radiation is

not easily repaired even at low radiation doses of 2 Gy (24). Therefore, when compared to low-LET forms of radiation, high-LET forms of radiation pose a higher relative biological effectiveness (RBE) for cell killing and possess good localization characteristics resulting in energy deposition within 0.04 - 0.1 mm of the decay site (18, 19). It has also been shown that high-LET radiation can generate reactive oxygen species (25), induce apoptosis and cell cycle arrest (26-29). Therefore, it is hypothesized that high-LET forms of radiation could be used effectively in treating quiescent as well as hypoxic tumors which are usually resistant to conventional chemotherapy and radiotherapy.

In order to further improve the outcomes of sstr-targeted radionuclide therapy, we sought to compare the therapeutic effectiveness of sstr-targeted high-LET α -emitting ^{213}Bi versus low-LET β^- -emitter ^{177}Lu for treating human pancreatic adenocarcinoma cells by determining the effects on toxicity and calculating RBE using external γ -beam of ^{137}Cs as the reference radiation. In the past few years, the study of radiation-induced apoptosis has gained immense interest, therefore an apoptosis assay was performed to observe the differences in induction of apoptosis by radionuclides of varying LET. Conventionally, high-LET radioisotopes have been shown to be more successful in treating small-sized carcinomas than larger-sized carcinomas (18, 30-32) and therefore for this study we choose ^{177}Lu instead of ^{90}Y as ^{177}Lu was shown to be more successful than ^{90}Y for treatment of smaller-sized pancreatic carcinomas (33).

In the present study we report the comparison of high-LET radiation versus low-LET radiation for use in PRRT.

Materials and Methods

Cell Culture

Human pancreatic adenocarcinoma Capan-2 cells express high levels of sstr2 and sstr5 (34). Therefore for this study, Capan-2 was selected as the sstr-expressing test cell line. For control experiments A549 lung carcinoma cells were chosen as they do not express sstr2 and sstr5. Capan-2 cells were cultured in McCoy's 5a medium and supplemented with 1.5 mM L-glutamine, 10% (v/v) fetal bovine serum, 10%, 100 units/mL penicillin and 100 $\mu\text{g}/\text{mL}$ streptomycin. A549 cells were cultured in Ham's F12K medium and supplemented with 2 mM L-glutamine adjusted to contain 1.5 g/L sodium bicarbonate, 10% (v/v) fetal bovine serum, 100 units/ml penicillin and 100 $\mu\text{g}/\text{mL}$ streptomycin. All the cell lines, culture media and supplements were purchased from American Type Culture Collection (Manassas, VA, USA). Both the cell lines were grown at 37°C, in a humidified atmosphere of 5% CO_2 and 95% air.

Radionuclides and Preparation of Radiolabeled Peptide

The high-LET α -emitter ^{213}Bi (half-life: 45.6 minutes; E_{max} 5.87 MeV and E_{max} 8.38 MeV for daughter ^{213}Po) was obtained from an on-site $^{225}\text{Ac}/^{213}\text{Bi}$ generator provided by Dr. Martin W. Brechbiel and Dr. Kayhan Garmestani (Radioimmune and Inorganic Chemistry Section, Radiation Oncology Branch, NCI, Bethesda, MD, USA). The generator was eluted as previously described (35) and the purity of eluted ^{213}Bi was determined by γ -spectroscopy using Genie 2000 analysis software and a Canberra broad energy germanium detector (Meriden, CT, USA).

The low-LET β^- -emitter ^{177}Lu (half-life: 6.64 days; E_{max} 0.5 MeV) was obtained from International Isotopes Inc. (Idaho Falls, ID, USA) in the form of ^{177}Lu -chloride in 0.05 N optima grade HCl.

^{213}Bi solution was buffered to pH 5.5 using 3 M ammonium acetate and DOTATOC (Mallinckrodt medical, Petten, Netherlands) was added to the above-buffered solution. The reaction mixture was heated at 100°C for 15 minutes. Similarly, ^{177}Lu solution was buffered to pH 5 using 3 M ammonium acetate and DOTATOC was added. The reaction mixture was heated at 100°C for 15 minutes. To perform end-product quality control, 100 μL of the reaction mixture was added to 200 μL of 4 mM diethylenetriaminepentaacetic acid (DTPA) solution. Silica gel instantaneous thin layer chromatography (ITLC) and HPLC were performed on the above prepared quality control mixture.

Incorporation yield was assessed using ITLC in which acetone and 0.9% (w/v) sodium chloride solutions were used as organic and aqueous mobile phases, respectively. The strip was cut in half and the incorporation yield was measured by counting radioactivity on each half of the strip using Wallace Wizard 1480 automatic gamma counter (Perkin Elmer, Gaithersburg, MD, USA). Radiochemical purity was assessed via HPLC using a reverse-phase C-18 column (JT Baker, Phillipsburg, NJ, USA) with a Gamma-radiometric detector (INUS Systems Inc., Tampa, FL, USA). Injection volume was 100 μL and the detector wavelength was 254 nm. For the mobile phase, solvent system of 0.05 M sodium acetate buffer at pH 5.5 was used as solvent A and 100% methanol as solvent B with an isocratic gradient.

Radioligand Receptor Studies

To evaluate the ligand binding to the somatostatin receptor expressed on Capan-2 cells, direct binding and specific intracellular uptake experiments were performed with ^{177}Lu -DOTATOC as previously described (36). One day before the experiment 100,000 cells/well were transferred to 6 well plates. The cells were washed with 2 mL phosphate-buffered saline (PBS) and incubated in 1 mL HEPES buffer with 6 nM of radiotracer (^{177}Lu -DOTATOC) for 60 minutes at 37°C. To determine nonspecific internalization and binding, cells were incubated with 10 mM of unlabeled peptide. Cellular uptake was stopped by removing medium from the cells, followed by washing twice with 2 mL PBS. To discriminate

between internalized and not internalized (surface bound) radiopharmaceutical, same experiment was performed with a control group that was incubated on ice bath. The radioactivity associated with the final pellet was counted in Wallace Wizard 1480 automatic gamma counter.

Clonogenic Cell Survival Assay

Two thousand cells were treated with increasing doses of radiolabeled DOTATOC and DOTA and incubated for 1 hour before removing the radioactive cell culture medium and washing the cells with PBS. The effects of radiation exposures resulting from incubation times of 1 hour with different doses of ²¹³Bi and ¹⁷⁷Lu labeled to DOTATOC or DOTA were determined by a colony forming assay (37). Similarly, an experiment was performed with equimolar DOTATOC treatment in which the cells were exposed to different doses of external irradiation of ¹³⁷Cs source. After a 15-day incubation period at 37°C in a humidified atmosphere of 5% CO₂ and 95% air, colonies from each treatment groups were counted by two independent, blinded observers after washing twice with PBS solution, fixing with formalin solution, and staining with 0.2% (w/v) crystal violet solution. The peptide mass was constant in all the treatment groups.

Microscopy Studies for Cellular Geometry

Cells were plated on cover slips and fixed with 2 % (w/v) paraformaldehyde in phosphate-buffered saline. The nucleus and the whole cell were stained with TOPRO-3 and Alexa-546 carboxylic acid, succinimidyl ester (Invitrogen, Carlsbad, CA, USA), respectively. The confocal images were acquired using a Zeiss LSM 510 confocal system. TOPRO-3 and Alexa-546 carboxylic acid, succinimidyl ester was excited at 633 and 543 nm, respectively. The acquired images were analyzed using the orthogonal optical sectioning tool of Zeiss LSM 510 imaging software.

Cellular Dosimetry

The mean absorbed dose to the nucleus and the cumulated activity were calculated using equations 1 (38) and 2 (36). The experimental data obtained from radioligand receptor studies and the geometric analyses of the cells were used in these equations.

In the MIRD cellular dosimetry model used (see Equations 1 and 2), the cellular radioactivity was assumed to be uniformly distributed in one of the following regions of the cells: throughout the cell (C), cytoplasm (Cy), cell surface (Cs), and cell nucleus (N). However this model did not take into account non-spherically symmetric cell shapes, non-uniform distribution of activity within the subcellular compartments, and acentric cell nuclei. The changing volume (mass) of the cell during cell-cycle progression was also not taken into account in this cellular dosimetry model (23). The doses to the culture medium, self-dose and cross dose were taken into account for the final calculations.

Equation 1

$$\bar{D}_N = \tilde{A}_{\text{cell}} \left[f_{\text{cs}} \sum_j b_j S_j (N \leftarrow \text{Cs}) + f_{\text{cy}} \sum_j b_j S_j (N \leftarrow \text{Cy}) \right]$$

Equation 2

$$\tilde{A}_{\text{cell}} = \frac{\lambda_i A_i}{\lambda_p N} \left(e^{-\lambda_p T_i} - e^{-\lambda_p T} \right)$$

Where, \bar{D}_N = mean absorbed dose to the nucleus, \tilde{A}_{cell} = cumulative activity in the cell, f_{cs} = fraction of activity that is on cell surface, f_{cy} = fraction of activity that is in the cytoplasm, $S(N \leftarrow \text{Cs}) = S$ value (cell surface to the nucleus), $S(N \leftarrow \text{Cy}) = S$ value (cytoplasm to the nucleus), j = daughter of the parent radionuclide, b_j = branching ratio of j^{th} radionuclide, A_i = initial activity to the treatment group, λ_p = decay constant, T_i = incubation time with activity, T = total therapy time of the colony forming assay, N = total number of cells in the treatment group and

μ = fraction of activity bound to the cell.

Apoptosis Assay

The Cell Death Detection ELISA^{PLUS} 10X (Roche Applied Sciences, Indianapolis, IN, USA) was used to determine apoptosis using the protocol provided by the manufacturer. This kit is based on a quantitative sandwich-enzyme-immunoassay principle, using mouse monoclonal antibodies directed against DNA and histones, respectively which allows the apoptotic specific detection and quantification of mono- and oligonucleosomes that are released into the cytoplasm of cells that die from apoptosis.

The cells were treated with 37 kBq of radiolabeled DOTATOC, radiolabeled DOTA and equimolar non-radioactive peptide in a 96-well plate and incubated for 24, 48 and 96 hours. The nucleosomes were photometrically detected at 405 nm (SpectraMax 340, Molecular device, MN) by measuring POD activity with 100 μ L ABTS (2, 2'-azino-di [3-ethyl-benz-thiazolin-sulfonate]) as the substrate. The final absorbance was obtained by subtracting the observed absorbance of the negative control (untreated cells) and background. The peptide mass was constant in all the treatment groups.

Statistical Analysis

All numerical data ($n \geq 3$) were expressed as the mean of the values \pm the standard error of mean (S.E.M). Graphpad Prism version 4 (San Diego, CA, USA) was used for statistical analysis and a p value less than 0.05 was considered statistically significant.

Results

Radionuclide and Radiochemical Purity

The radionuclidic purity of ²¹³Bi obtained from the ²²⁵Ac/²¹³Bi generator was evaluated using gamma spectroscopy on a wide window, as well as on the ²¹³Bi window (404 keV ± 20%) over a period of 7 days. The ²¹³Bi eluted from the ²²⁵Ac/²¹³Bi generator was ≥ 99% pure, as no γ emission characteristic of ²²⁵Ac was detected over 7 days. The radionuclidic purity of ¹⁷⁷Lu was > 99% as described in certificate of analysis provided by the supplier.

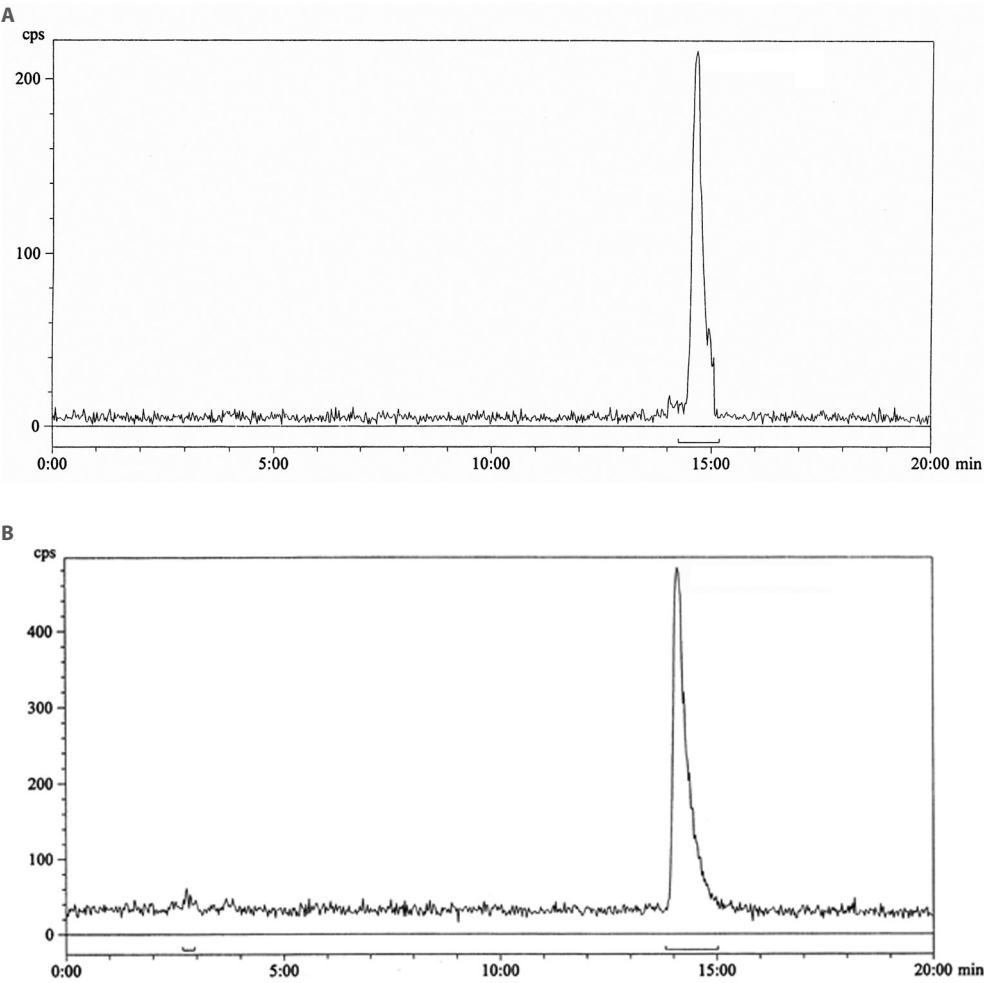


Figure 1: Representative HPLC radiochromatograms of (1A) ¹⁷⁷Lu-DOTATOC and (1B) ²¹³Bi-DOTATOC. Retention time for radiolabeled DOTATOC and radiolabeled DOTA were ~ 14.5 and 3 minutes respectively.

The radioisotopes ²¹³Bi and ¹⁷⁷Lu were successfully radiolabeled to DOTATOC with a high specific activity of 3.7 MBq/μg. A quality control sample was prepared by adding 200 μL of 4 mM DTPA to 200 μL of the reaction mixture. As estimated by ITLC, the incorporation yield was determined to be ≥ 98.5% and radiochemical purity was determined ≥ 95% by HPLC. The HPLC retention time for radiolabeled DOTATOC was approximately 14.5 minutes (Fig.1A) whereas the radiolabeled DTPA peak, corresponding to the free radiometal, was eluted at approximately 3 minutes (Fig. 1B).

Radioligand Receptor Studies

In order to perform cellular dosimetry and calculate \overline{D}_N , radioligand receptor studies were performed to determine specific binding and specific intracellular uptake. These studies were carried out with ~6 nM solution of ¹⁷⁷Lu-DOTATOC as a tracer. After 60 minutes at 37°C, the specific intracellular uptake was determined to be 5.36 ± 0.58 % of the total treatment.

Clonogenic Cell Survival Assay

Cell survival assays and cellular dosimetry calculations were performed to determine the RBE ofsstr-targeted ²¹³Bi and ¹⁷⁷Lu.

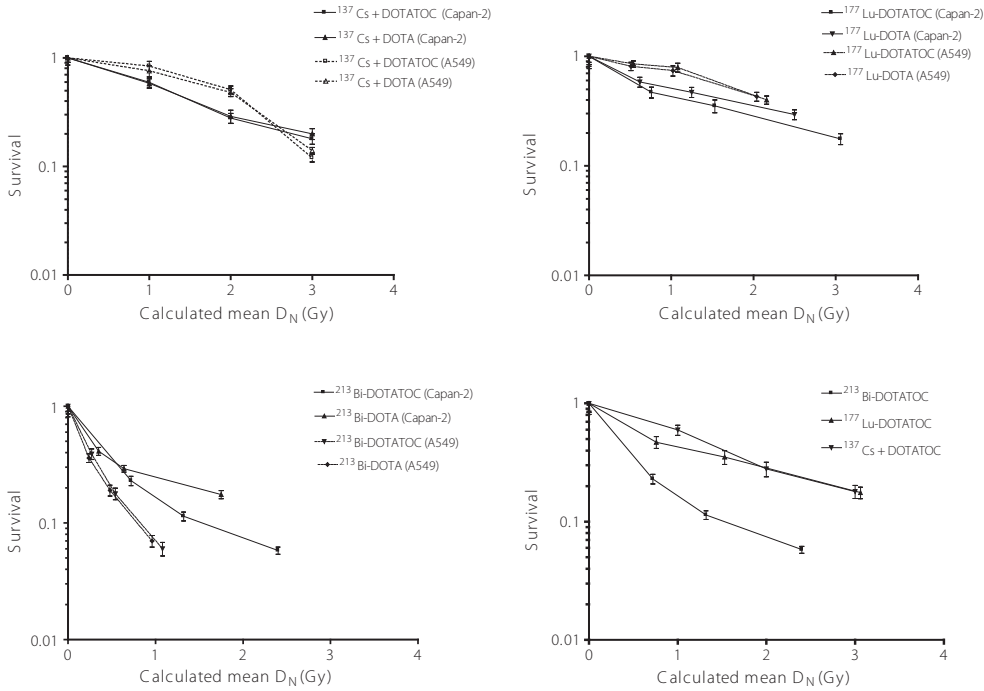


Figure 2: Survival curves of cells treated with (2A) ¹³⁷Cs, (2B) ¹⁷⁷Lu, (2C) ²¹³Bi and (2D) comparative Capan-2 survivals for DOTATOC with concurrent ¹³⁷Cs, ¹⁷⁷Lu-DOTATOC, ²¹³Bi-DOTATOC.

At the same calculated \overline{D}_N for Capan-2 cells, sstr-targeted ²¹³Bi-DOTATOC treatment significantly decreased cell survival as compared to target non-specific ²¹³Bi-DOTA (Fig. 2C) similar results were obtained with ¹⁷⁷Lu (Fig. 2B) whereas irradiation of ¹³⁷Cs with and without DOTATOC displayed no significant difference (Fig. 2A). ¹⁷⁷Lu-DOTATOC treatment displayed similar effects on cell survival when compared with cells treated with equimolar DOTATOC and concurrent irradiation with a ¹³⁷Cs source. ²¹³Bi-DOTATOC displayed greater decrease in cell survival when compared to both the ¹⁷⁷Lu and ¹³⁷Cs (Fig. 2D). For control A549 cells, no significant differences were observed between radiolabeled DOTATOC and radiolabeled DOTA alone (Fig 2 and Table 1A). Using equimolar DOTATOC treatment with concurrent irradiation with a ¹³⁷Cs source as the reference radiation, the RBE was calculated for high-LET α -particle emitter ²¹³Bi and the low-LET β^- emitter ¹⁷⁷Lu. Linear regression was performed to determine the \overline{D}_N required for a surviving fraction of 0.2 and the corresponding calculated \overline{D}_N was used to determine the RBE (Table 1A). Based on these calculations the RBE of ²¹³Bi-DOTATOC was determined to be 3.4 and RBE of ¹⁷⁷Lu-DOTATOC was determined to be 1.0 (Table 1B).

Table 1: Calculated mean absorbed doses to the nucleus (\overline{D}_N) and the corresponding surviving fractions (mean \pm S.E.M.) of various groups (1A). Physical characteristics and calculated RBEs of ²¹³Bi (E_{max} of 8.38 for daughter ²¹³Po) and ¹⁷⁷Lu labeled to DOTATOC in Capan-2 cells (1B).

1A				
Treatment groups	\overline{D}_N Capan-2	Surviving Fraction Capan-2	\overline{D}_N A549	Surviving Fraction A549
137Cs + DOTATOC	1.00 Gy	0.59 \pm 0.06	1.00 Gy	0.84 \pm 0.09
137Cs + DOTATOC	2.00 Gy	0.27 \pm 0.02	2.00 Gy	0.51 \pm 0.04
137Cs + DOTATOC	3.00 Gy	0.18 \pm 0.02	3.00 Gy	0.12 \pm 0.01
177Lu-DOTATOC	0.76 Gy	0.47 \pm 0.03	0.54 Gy	0.85 \pm 0.05
177Lu-DOTATOC	1.53 Gy	0.35 \pm 0.02	1.08 Gy	0.79 \pm 0.07
177Lu-DOTATOC	3.06 Gy	0.17 \pm 0.02	2.16 Gy	0.41 \pm 0.05
213Bi-DOTATOC	0.72 Gy	0.23 \pm 0.02	0.27 Gy	0.39 \pm 0.04
213Bi-DOTATOC	1.32 Gy	0.11 \pm 0.02	0.54 Gy	0.17 \pm 0.02
213Bi-DOTATOC	2.40 Gy	0.05 \pm 0.00	1.08 Gy	0.06 \pm 0.00

1B					
Radionuclide	Type	Half-life	E_{max} (MeV)	Mean particle range (mm)	Calculated RBE
¹⁷⁷ Lu	Low-LET β^-	6.7 d	0.50	0.28	1
²¹³ Bi	High-LET α	45.7 min	8.38	0.04 – 0.1	3.4

Apoptosis Assay

In sstr-expressing Capan-2 cells, 37 kBq of ²¹³Bi-DOTATOC was most effective in release of apoptotic specific mono- and oligonucleosomes in terms of absorbance units (Fig. 3A). When compared to 37 kBq of ¹⁷⁷Lu-DOTATOC at 96 hours, ²¹³Bi-DOTATOC caused 2.3 folds greater release of apoptotic specific mono- and oligonucleosomes and was statistically

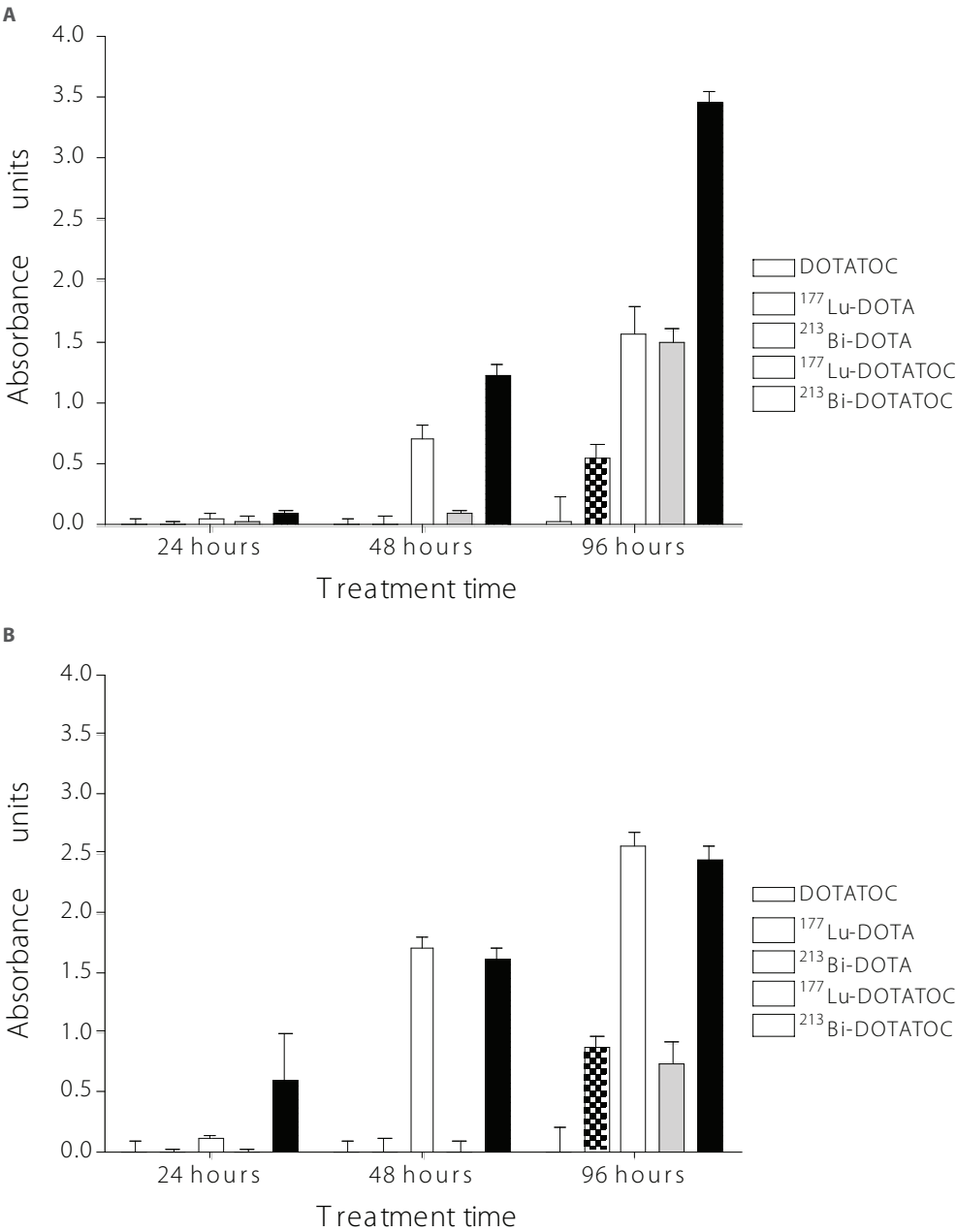


Figure 3: Radiation-induction apoptosis in (3A) sstr-expressing human pancreatic adenocarcinoma Capan-2 cells and (2B) control A549 cells. Apoptosis was expressed in terms of (mean \pm S.E.M.) absorbance units.

significant ($p < 0.001$). The onset of release of apoptotic specific mono- and oligonucleosomes by ^{213}Bi -DOTATOC was apparent from the incubation time of 48 hours whereas, similar effects were observed at 96 hours with ^{177}Lu -DOTATOC. At 96 hours, radiolabeled DOTATOC caused 3 fold more release of apoptotic specific mono- and oligonucleosomes for ^{177}Lu and 2.2 fold more for ^{213}Bi when compared to radiolabeled DOTA in sstr-expressing cells. For the control A549 cells, there was no significant difference between target-specific radiolabeled DOTATOC and non-specific radiolabeled DOTA (Fig. 3B).

Discussion

The primary objective of this study was to compare the therapeutic effectiveness of sstr-targeted high-LET α -emitting ^{213}Bi versus low-LET β -emitter ^{177}Lu in human pancreatic adenocarcinoma cells by determining their effects on toxicity and RBE using external γ -beam ^{137}Cs as the reference radiation. We found that the sstr-targeted high-LET α -emitting ^{213}Bi had a greater RBE and was more toxic than sstr-targeted low-LET β -emitting ^{177}Lu .

The critical feature of radiation damage is the stochastic clusterings of ionizations, directly in or very near to DNA, resulting in clustered initial molecular damage including various combinations of breaks, base damage, cross-links, etc. in the DNA. The final cellular effects from high-LET radiations are dominated by their more severe, and therefore less repairable, clustered damage, and that these are qualitatively different from the dominant low-LET damage (22, 39). Moreover, high-LET radiation depress enzymatic repair mechanisms, decrease variations of radiosensitivity during the cell division cycle, cause greater than expected delays in cell division, and decrease the protective effects of neighboring cells in organized systems by inducing apoptosis and therefore reinforcing the concept that high-LET damage is less easy to repair than low-LET damage (25, 27, 40).

The description of quality factors of high-LET α -emitting radionuclides has evolved in the last 2 decades and as has that for the RBEs (41). In the past few years, when compared with γ -emission, the in vitro as well as in vivo RBEs of α -particle emitting radionuclides have ranged from 2-7 depending upon experimental conditions and end-points (18, 42, 43). For targeted α -particle therapy of leukemia cells with a ^{213}Bi labeled CD-20 targeted mAb rituximab the RBE ranged from 2-5 (44). Our findings on RBE of α -emitting radionuclides are consistent with previous findings and support the fact that α -emitting radionuclides emit much higher energy particles than most of the β -emitting radionuclides and have a greater RBE (18, 39). A much greater fraction of the total energy is imparted to the targeted cancer cell and few nuclear hits are required to kill cells.

The high-LET α -emitting radionuclides have powerful cell killing properties and if targeted specifically to cancer cells can be a valuable tool in treatment of cancer. PRRT offers

a distinct and unique advantage by not only delivering the radionuclide to the cell receptor target site, but also by internalizing the receptor-ligand complex (45, 46), it delivers a higher radiation dose to the cell nucleus, arguably the most sensitive target in any cancer therapy.

We believe one of the advantages of using ^{213}Bi in PRRT is the target-specific intracellular localization of ^{213}Bi in which the nuclear recoil of the daughter nuclide and alpha decay to occurs intracellularly. The intracellular decay ensures greater proximity to nucleus particularly of the recoil daughter ^{213}Po with an α -emission of 8.38 MeV and half-life of 4.3 μs for which the distance from nucleus has shown to be vital for cell killing effects (47).

In this study, we also sought to compare the biological effects of different radioisotopes according to the conventional MIRD cellular dosimetry model (38). The MIRD cellular S values used assumes a spherical model; this may not give accurate absorbed doses for adherent Capan-2 cells. Another limitation lies in the fact that this model doesn't take into account the change of cell shape and size as a result of cell division and extracellular matrix (ECM) remodeling. The argument exists to have mechanical control of cell shape and size or use single cell suspensions but it has been shown that, this may have detrimental effects on ECM remodeling and tumor cell growth, division and survival (48, 49). The MIRD cellular S values are based on a model of the cell in which the nucleus and the cell membrane are concentric spheres. In reality, the nucleus is usually on one side of the cell, this may again result in errors in calculations. However, there is no foolproof or flawless model available that can be used for ^{213}Bi and ^{177}Lu and therefore the MIRD cellular S values were used to determine self-dose, cross-dose and the dose from the medium.

The conventional β -emitting radionuclides such as ^{131}I , ^{90}Y and ^{177}Lu used for cancer therapy have particle ranges much larger than the diameter of a cancer cell. The maximum β -energy varies from 0.5 to 2.0 MeV with 1-10 mm being the corresponding range, so the dose limiting normal cells will be irradiated even if the cancer cells are successfully targeted. The long range might possibly lead to radiotoxicity at higher doses (18, 19, 31, 50). Cancer therapy with β -emitting radionuclides has demonstrated success in treatment of thyroid cancer, bone palliation and hematological malignancies but often large amounts of radioactivity is required to compensate for cell killing inefficiency due its low-LET and therefore low RBE as demonstrated (31).

We have demonstrated the sstr-targeted high-LET α -emitting ^{213}Bi is therapeutically more effective than sstr-targeted low-LET β -emitting ^{177}Lu in human pancreatic adenocarcinoma cells in vitro. In the future, the use of α -emitting radionuclides such as ^{213}Bi , ^{212}Bi , ^{211}At and ^{225}Ac may provide a viable solution to the above described problems posed by β -emitting radionuclides and may be successfully used in treatment of metastatic, chemoresistant and hypoxic carcinomas which have been previously known to be resistant to treatment with β -emitting radionuclides. Recently, ^{213}Bi -DOTATOC was success-

fully used to decrease proliferation of sstr-expressing pancreatic carcinoma in an animal model without causing any major toxicity (30). It has been demonstrated that combining two different types of radioisotopes simultaneously can be beneficial in the treatment of cancer (33). Further studies should focus on radionuclide therapy combining α -emitting radionuclides such as ^{213}Bi with β -emitting radionuclides such as ^{90}Y or ^{177}Lu for treatment of carcinomas of varying sizes and volumes.

In conclusion, at the same absorbed dose, the sstr-targeted high-LET α -emitter ^{213}Bi -DOT-ATOC was therapeutically 3.4 fold more effective than the low-LET β -emitter ^{177}Lu -DOT-ATOC in decreasing survival of human pancreatic adenocarcinoma cells due to its greater RBE. Therefore, ^{213}Bi -DOTATOC is a promising targeted therapeutic radiopharmaceutical for further pre-clinical and clinical evaluation for treatment of sstr-expressing carcinomas.

Acknowledgements

We are thankful to Rahul Poria (University of New Mexico Health Sciences Center, Albuquerque, NM) for technical support and laboratory assistance. Critical manuscript-writing inputs from Dr. Robert Glew and Dr. Dorothy VanderJagt are highly appreciated. Gratitude is extended to Dr. Martin W. Brechbiel and Dr. Kayhan Garmestani (Radioimmune and Inorganic Chemistry Section, Radiation Oncology Branch, NCI, Bethesda, MD, USA) for providing the $^{225}\text{Ac}/^{213}\text{Bi}$ generator and technical assistance in its operation.

This study was performed under the auspices of the U.S. Dept. of Energy, Office of Science, Office of Biological and Environmental Research under contract 7405-ENG-36 (RWA), Grant DE-FG01-001NE23554 from the U.S Department of Energy (JPN), and the Society of Nuclear Medicine's Bradley-Alavi Student Fellowship Award funded by the Education and Research Foundation for the Society of Nuclear Medicine (TKN).

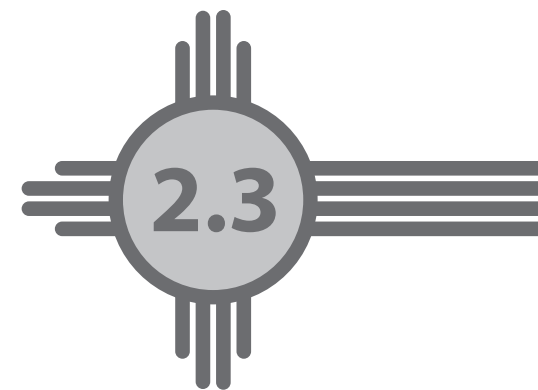
References

1. Jemal A, Siegel R, Ward E, Murray T, Xu J, Smigal C, et al. Cancer statistics, 2006. *CA Cancer J Clin* 2006;56(2):106-30.
2. Ko AH, Tempero MA. Treatment of metastatic pancreatic cancer. *J Natl Compr Canc Netw* 2005;3(5):627-36.
3. Blackstock AW, Cox AD, Tepper JE. Treatment of pancreatic cancer: Current limitations, future possibilities. *Oncology (Huntingt)* 1996;10(3):301,7; discussion: 308-23.
4. Krenning EP, Kwekkeboom DJ, Valkema R, Pauwels S, Kvols LK, De Jong M. Peptide receptor radionuclide therapy. *Ann N Y Acad Sci* 2004;1014:234-45.
5. Reubi JC. Peptide receptors as molecular targets for cancer diagnosis and therapy. *Endocr Rev* 2003;24(4):389-427.
6. Lamberts SW, Krenning EP, Reubi JC. The role of somatostatin and its analogs in the diagnosis and treatment of tumors. *Endocr Rev* 1991;12(4):450-82.
7. Patel YC. Somatostatin and its receptor family. *Front Neuroendocrinol* 1999;20(3):157-98.
8. Reubi JC, Krenning E, Lamberts SW, Kvols L. In vitro detection of somatostatin receptors in human tumors. *Metabolism* 1992;41(9 Suppl 2):104-10.
9. Tang C, Biemond I, Verspaget HW, Offerhaus GJ, Lamers CB. Expression of somatostatin receptors in human pancreatic tumor. *Pancreas* 1998;17(1):80-4.
10. Henze M, Schuhmacher J, Dimitrakopoulou-Strauss A, Strauss LG, Macke HR, Eisenhut M, et al. Exceptional increase in somatostatin receptor expression in pancreatic neuroendocrine tumour, visualised with (68) ga-DOTATOC PET. *Eur J Nucl Med Mol Imaging* 2004;31(3):466.
11. Otte A, Herrmann R, Heppeler A, Behe M, Jermann E, Powell P, et al. Yttrium-90 DOTATOC: First clinical results. *Eur J Nucl Med* 1999;26(11):1439-47.
12. Paganelli G, Zoboli S, Cremonesi M, Bodei L, Ferrari M, Grana C, et al. Receptor-mediated radiotherapy with 90Y-DOTA-D-Phe1-Tyr3-octreotide. *Eur J Nucl Med* 2001;28(4):426-34.
13. Waldherr C, Pless M, Maecke HR, Haldemann A, Mueller-Brand J. The clinical value of [90Y-DOTA]-D-Phe1-Tyr3-octreotide (90Y-DOTATOC) in the treatment of neuroendocrine tumours: A clinical phase II study. *Ann Oncol* 2001;12(7):941-5.
14. Schumacher T, Waldherr C, Mueller-Brand J, Maecke H. Kidney failure after treatment with 90Y-DOTATOC. *Eur J Nucl Med Mol Imaging* 2002;29(3):435.
15. Lambert B, Cybulla M, Weiner SM, Van De Wiele C, Ham H, Dierckx RA, et al. Renal toxicity after radionuclide therapy. *Radiat Res* 2004;161(5):607-11.
16. de Jong M, Breeman WA, Bernard BF, Bakker WH, Schaar M, van Gameren A, et al. ^{177}Lu -DOTA(0),Tyr3] octreotate for somatostatin receptor-targeted radionuclide therapy. *Int J Cancer* 2001;92(5):628-33.
17. McDevitt MR, Ma D, Lai LT, Simon J, Borchardt P, Frank RK, et al. Tumor therapy with targeted atomic nano-generators. *Science* 2001;294(5546):1537-40.
18. Mulford DA, Scheinberg DA, Jurcic JG. The promise of targeted $\{\alpha\}$ -particle therapy. *J Nucl Med* 2005;46 Suppl 1:199S-204S.
19. Milenic DE, Brady ED, Brechbiel MW. Antibody-targeted radiation cancer therapy. *Nat Rev Drug Discov* 2004;3(6):488-99.
20. ALPER T. Cellular radiobiology. *Annu Rev Nucl Sci* 1960;10:489-530.
21. Ritter MA, Cleaver JE, Tobias CA. High-LET radiations induce a large proportion of non-rejoining DNA breaks. *Nature* 1977;266(5603):653-5.
22. Goodhead DTN, Thacker JN, Cox RN. Effects of radiations of different qualities on cells: Molecular mechanisms of damage and repair. *Int J Radiat Biol* 1993;63(5):543-56.
23. Rydberg B, Cooper B, Cooper PK, Holley WR, Chatterjee A. Dose-dependent misrejoining of radiation-induced DNA double-strand breaks in human fibroblasts: Experimental and theoretical study for high- and low-LET radiation. *Radiat Res* 2005;163(5):526-34.

24. Okayasu R, Okada M, Okabe A, Noguchi M, Takakura K, Takahashi S. Repair of DNA damage induced by accelerated heavy ions in mammalian cells proficient and deficient in the non-homologous end-joining pathway. *Radiat Res* 2006;165(1):59-67.
25. Narayanan PK, Goodwin EH, Lehnert BE. Alpha particles initiate biological production of superoxide anions and hydrogen peroxide in human cells. *Cancer Res* 1997;57(18):3963-71.
26. Takahashi A, Matsumoto H, Yuki K, Yasumoto J, Kajiura A, Aoki M, et al. High-LET radiation enhanced apoptosis but not necrosis regardless of p53 status. *Int J Radiat Oncol Biol Phys* 2004;60(2):591-7.
27. Hendry JH, Potten CS, Merritt A. Apoptosis induced by high- and low-LET radiations. *Radiat Environ Biophys* 1995;34(1):59-62.
28. Palayoor ST, Humm JL, Atcher RW, Hines JJ, Macklis RM. G2M arrest and apoptosis in murine T lymphoma cells following exposure to ^{212}Bi alpha particle irradiation. *Nucl Med Biol* 1993;20(6):795-805.
29. Li Y, Rizvi SM, Ranson M, Allen BJ. ^{213}Bi -PAI2 conjugate selectively induces apoptosis in PC3 metastatic prostate cancer cell line and shows anti-cancer activity in a xenograft animal model. *Br J Cancer* 2002;86(7):1197-203.
30. Norenberg JP, Krenning BJ, Konings IR, Kusewitt DF, Nayak TK, Anderson TL, et al. ^{213}Bi -[DOTA0, Tyr3] octreotide peptide receptor radionuclide therapy of pancreatic tumors in a preclinical animal model. *Clin Cancer Res* 2006;12(3 Pt 1):897-903.
31. Behr TM, Behe M, Stabin MG, Wehrmann E, Apostolidis C, Molinet R, et al. High-linear energy transfer (LET) alpha versus low-LET beta emitters in radioimmunotherapy of solid tumors: Therapeutic efficacy and dose-limiting toxicity of ^{213}Bi - versus ^{90}Y -labeled CO17-1A fab' fragments in a human colonic cancer model. *Cancer Res* 1999;59(11):2635-43.
32. Ballangrud AM, Yang WH, Charlton DE, McDevitt MR, Hamacher KA, Panageas KS, et al. Response of LNCaP spheroids after treatment with an alpha-particle emitter (^{213}Bi)-labeled anti-prostate-specific membrane antigen antibody (J591). *Cancer Res* 2001;61(5):2008-14.
33. de Jong M, Breeman WA, Valkema R, Bernard BF, Krenning EP. Combination radionuclide therapy using ^{177}Lu - and ^{90}Y -labeled somatostatin analogs. *J Nucl Med* 2005;46 Suppl 1:13S-7S.
34. Kikutsuji T, Harada M, Tashiro S, Li S, Moritani M, Yamaoka T, et al. Expression of somatostatin receptor subtypes and growth inhibition in human exocrine pancreatic cancers. *J Hepatobiliary Pancreat Surg* 2000;7(5):496-503.
35. Ma D, McDevitt MR, Finn RD, Scheinberg DA. Breakthrough of ^{225}Ac and its radionuclide daughters from an $^{225}\text{Ac}/^{213}\text{Bi}$ generator: Development of new methods, quantitative characterization, and implications for clinical use. *Appl Radiat Isot* 2001;55(5):667-78.
36. Capello A, Krenning EP, Breeman WA, Bernard BF, Konijnenberg MW, de Jong M. Tyr3-octreotide and Tyr3-octreotate radiolabeled with ^{177}Lu or ^{90}Y : Peptide receptor radionuclide therapy results in vitro. *Cancer Biother Radiopharm* 2003;18(5):761-8.
37. Hall EJ. Cell survival curves. In: *Radiobiology for Radiobiologist*. fifth ed. Philadelphia, PA: Lippincott Williams and Wilkins; 2000. p. 32-50.
38. Murty Goddu S, Howell RW, Bouchet LG, Bolch WE, Rao DV. MIRD cellular S values: Self-absorbed dose per unit cumulated activity for selected radionuclides and monoenergetic electron and alpha particle emitters incorporated into different cell compartments. 0th ed. Reston, VA: Society of Nuclear Medicine; 1997.
39. Goodhead DT. Mechanisms for the biological effectiveness of high-LET radiations. *J Radiat Res (Tokyo)* 1999;40 Suppl:1-13.
40. Tobias CA, Blakely EA, Alpen EL, Castro JR, Ainsworth EJ, Curtis SB, et al. Molecular and cellular radiobiology of heavy ions. *Int J Radiat Oncol Biol Phys* 1982;8(12):2109-20.
41. Borak TB. Quality factors for alpha particles emitted in tissue. *Health Phys* 2002;82(1):102-4.
42. Azure MT, Archer RD, Sastry KS, Rao DV, Howell RW. Biological effect of lead-212 localized in the nucleus of mammalian cells: Role of recoil energy in the radiotoxicity of internal alpha-particle emitters. *Radiat Res* 1994;140(2):276-83.
43. Howell RW, Goddu SM, Narra VR, Fisher DR, Schenter RE, Rao DV. Radiotoxicity of gadolinium-148 and radium-223 in mouse testes: Relative biological effectiveness of alpha-particle emitters in vivo. *Radiat Res* 1997;147(3):342-8.
44. Vandenbulcke K, De Vos F, Offner F, Philippe J, Apostolidis C, Molinet R, et al. In vitro evaluation of ^{213}Bi -rituximab versus external gamma irradiation for the treatment of B-CLL patients: Relative biological efficacy with respect to apoptosis induction and chromosomal damage. *Eur J Nucl Med Mol Imaging* 2003;30(10):1357-64.
45. De Jong M, Bernard BF, De Bruin E, Van Gameren A, Bakker WH, Visser TJ, et al. Internalization of radiolabelled [DTPA0]octreotide and [DOTA0,Tyr3]octreotide: Peptides for somatostatin receptor-targeted scintigraphy and radionuclide therapy. *Nucl Med Commun* 1998;19(3):283-8.
46. Cescato R, Schulz S, Waser B, Eltschinger V, Rivier JE, Wester HJ, et al. Internalization of sst2, sst3, and sst5 receptors: Effects of somatostatin agonists and antagonists. *J Nucl Med* 2006;47(3):502-11.
47. Munro TR. The relative radiosensitivity of the nucleus and cytoplasm of chinese hamster fibroblasts. *Radiat Res* 1970;42(3):451-70.
48. Radisky D, Muschler J, Bissell MJ. Order and disorder: The role of extracellular matrix in epithelial cancer. *Cancer Invest* 2002;20(1):139-53.
49. Radisky DC, Bissell MJ. Cancer. respect thy neighbor! *Science* 2004;303(5659):775-7.
50. Rizvi SM, Allen BJ, Tian Z, Goozee G, Sarkar S. In vitro and preclinical studies of targeted alpha therapy (TAT) for colorectal cancer. *Colorectal Dis* 2001;3(5):345-53.

^{213}Bi -DOTATOC Peptide Receptor Radionuclide Therapy of Pancreatic Tumors in a Pre-Clinical Animal Model

Jeffrey P. Norenberg, Boudewijn J. Krenning, Inge R. H. M. Konings, Donna F. Kusewitt, Tapan K. Nayak, Tamara L. Anderson, Marion de Jong, Kayhan Garmestani, Martin W. Brechbiel, Larry K. Kvols



Abstract

Purpose: The somatostatin analog [DOTA⁰ Tyr³] octreotide (DOTATOC) previously has been labeled with low-Linear-Energy-Transfer beta-emitters such as ¹⁷⁷Lu or ⁹⁰Y for tumor therapy. In this study, DOTATOC labeled with the high Linear-Energy-Transfer (LET) α-emitter, ²¹³Bi, was evaluated.

Experimental Design: The radiolabeling, stability, biodistribution, toxicity, safety and therapeutic efficacy of ²¹³Bi-DOTATOC (specific activity 1 MBq/0.135 μg) were studied. Biodistribution studies to determine somatostatin receptor (sst) specificity were performed in Lewis rats 1 and 3 hours post-injection (PI). Histopathology on various organs was performed to evaluate toxicity and safety. Therapeutic efficacy of 4-22 MBq ²¹³Bi-DOTATOC was determined.

Results: Radiolabeling of the ²¹³Bi-DOTATOC was successfully achieved with radiochemical purity >95% and an incorporation yield >99.5%. Biodistribution data demonstrated specific binding to sst expressing tissues. Administration of free ²¹³Bi, compared to ²¹³Bi-DOTATOC, resulted in higher radioactivity accumulation at 3 hours PI in the kidneys (34.47 ± 1.40 percent injected dose/gram tissue versus 11.15 ± 0.46%, p < 0.0001) and bone marrow (0.31 ± 0.01% versus 0.06 ± 0.02%, p < 0.0324). A significant decrease in tumor growth rate was observed in rats treated with > 11 MBq of ²¹³Bi-DOTATOC 10 days PI compared to control groups (p < 0.025). In rats receiving doses > 20 MBq of ²¹³Bi-DOTATOC compared to < 11 MBq (p < 0.02), significant tumor reduction was seen.

Conclusions: ²¹³Bi-DOTATOC demonstrated notable anti-tumor effects with minimal treatment related organ toxicity. No acute or chronic hematologic toxicities were observed. Mild, acute nephrotoxicity was observed without evidence of chronic toxicity. ²¹³Bi-DOTATOC is a promising therapeutic radiopharmaceutical for further pre-clinical evaluation.

Introduction

Somatostatin is a 14-amino acid peptide hormone found on many cells of neuroendocrine origin that acts as a neurotransmitter in the central nervous system (1). Somatostatin receptors have been demonstrated on the surface of human tumor cells which includes the cells with amine precursor uptake and decarboxylation (APUD) properties such as pituitary tumors, endocrine pancreatic tumors, carcinoids, paragangliomas, small cell lung cancers, medullary thyroid carcinomas and pheochromocytomas (2, 3). Analogs of somatostatin were developed because human somatostatin has a very short half-life in circulation (2-3 minutes) and is easily broken down by endogenous peptidases (4). These analogs preserved two important molecular features of somatostatin, i.e., its cyclic form and the 4 amino acids involved in the binding to the receptor. One somatostatin analog that has been studied *in vitro* and *in vivo* extensively is octreotide which has been used as a hormonal treatment in patients with carcinoid syndrome (5). The presence of somatostatin receptors (sst) has been used to detect and localize carcinoid, islet cell tumors (6) and small-cell lung cancer (5).

Despite good imaging and diagnostic results with ¹¹¹In labeled [DTPA⁰] octreotide (Octreoscan®) in the last few years, there have been several reports describing new somatostatin radioligands for studying sst expression. Some like [DOTA⁰, Tyr³] octreotide (DOTATOC) labeled with ¹³¹I, ⁹⁰Y and ¹⁷⁷Lu are also being evaluated for use in the radionuclide therapy of tumors (7). The new Peptide Receptor Radionuclide Therapy (PRRT) using radiolabeled DOTATOC has led to tumor responses in the majority of patients, but has also posed problems with renal and hematological toxicities (7). In previous studies, kidney failures have been reported after treatment with DOTATOC labeled to β-particle emitter ⁹⁰Y (8-10). In previously completed clinical studies, it was observed that 10% to 34% patients had complete remission following ⁹⁰Y-DOTATOC treatment (11). The results of these studies illustrate the partial treatment potentials of this agent and the possible higher relapse rates that may occur in the future (12). The primary challenges that ⁹⁰Y or ¹⁷⁷Lu labeled DOTATOC faces are renal toxicities and incomplete treatments, especially in radio-resistant tumors. One solution is to use a high linear energy transfer α-emitter. Several α-emitters were considered and proposed for this purpose including ²¹¹At (13). ²¹¹At is attractive due its short half-life (7.2 hours), but has a daughter, ²⁰⁷Pb, which has long half-life (38 years) and a β-emitting decay product, ²⁰⁷Pb, as well as it requires on-site cyclotron production and target processing facilities. Some years ago, ²¹³Bi was proposed for α-immunotherapy (14, 15). It can be readily obtained from an "in-house" ²²⁵Ac/²¹³Bi radionuclide generator system (13). ²¹³Bi decays mainly (98%) by β-emission, with a 440-keV γ-emission and a half life (t_{1/2}) of 45.6 minutes to the ultra-short-lived high-energy (8.375-MeV) α-emitter ²¹³Po (t_{1/2} = 4.2 microseconds). ²¹³Bi also has a direct decay pathway (2%) by α-emission to the (3.980 MeV) β-particle emitter ²⁰⁹Tl (16). More detailed information of the decay scheme is shown in Figure 1.

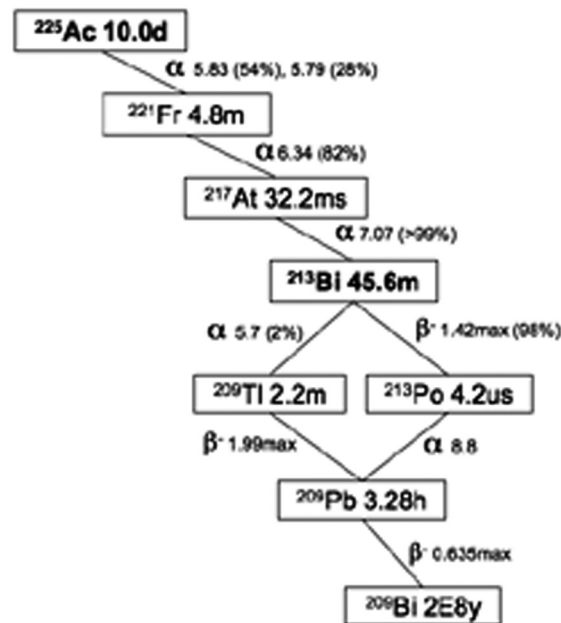


Figure 1: Decay scheme of ²²⁵Ac and ²¹³Bi showing the complexity of the isotopes, their half lives, decay modes, branching fractions and maximum energies.

cancer Institute, Bethesda, MD) (19). Prior to each elution, the ²²⁵Ac generator column was first rinsed with distilled water and then flushed with air to remove the water. In order to selectively elute the ²¹³Bi daughter, the column was eluted with 10 milliliter of 0.1 M hydrochloric acid. The eluate was diluted with water at 5.6 times the eluate volume of water (56 milliliter). This dilution was loaded onto a MP-50 cation-exchange column. This column was then reverse eluted with an additional 0.4 milliliter of freshly prepared 0.1 M hydroiodic acid that contained the desired ²¹³Bi (19).

Radiolabeling and serum stability

Freshly eluted ²¹³Bismuth (4 MBq) was added to 0.5 µg of DOTATOC solution and incubated for 5 minutes at 100°C in a hot block. Prior to heating, the pH of the final solution was adjusted to 6 to 7 using 3 M NH₄OAc solution.

Incorporation yield (IC) was assessed using Silica Gel instantaneous thin layer chromatography (ITLC) with 0.9% sodium chloride as the mobile phase. The radiolabeled samples were diluted with 4 mM diethylenetriamine pentaacetic acid (DTPA) at pH= 4.1. Five microliter of the diluted sample was spotted on an ITLC silica gel strip and allowed to develop in a chromatographic chamber. Upon completion of the migration to the solvent front, the ITLC sample strips were allowed to dry, cut in half and counted on a Wallac Wizard gamma counter (Perkin Elmer, Boston, MA) to determine the IC. Radiochemical

Several studies have been published on the beneficial use of α-emitters suggesting their therapeutic superiority (17, 18). In this study, we aim to evaluate the quantitative radiolabeling methods, stability, biodistribution safety and therapeutic efficacy of ²¹³Bi labeled to DOTATOC in the treatment of sst expressing pancreatic tumors.

Materials and Methods

Radionuclide

The ²¹³Bi used in these procedures was obtained from the “in house” ²²⁵Ac/²¹³Bi radionuclide generator system, (National Institutes of Health, National Cancer

purity (RCP) was assessed via high performance liquid chromatography (HPLC) analysis. The liquid chromatography system (Thermo Separation Products, San Jose, CA) consisted of a multisolvent-delivery pump, an auto sampler, a radiometric detector (γ-RAM, IN/US Systems, Inc., Tampa, Florida), and a C₁₈, 5µm, 4.6 x 250 mm, reverse-phase HPLC column. The mobile phase consisted of Buffer A: 0.5 M Ammonium Acetate in HPLC grade water, pH 5.5 and Buffer B: 100% HPLC grade methanol. The HPLC samples were analyzed with a 1:10 dilution in 4 mM DTPA. The flow rate was 1.0 milliliter per minute and the retention time for the radiolabeled product was 14.0 to 14.5 minutes.

The radiolabeled product, ²¹³Bi-DOTATOC, was incubated at 37°C in a CO₂ incubator for 1 hour in rat serum obtained from a male Lewis rat to study *in vitro* stability. After incubation the product was analyzed by the ITLC and HPLC methods previously described.

Animal Model

Lewis rats with and without CA-20948 tumor were used for the biodistribution and therapeutic efficacy studies. The tumor model was developed by first injecting CA-20948 cells (somatostatin receptor positive pancreatic cell line) received from the Netherlands (Department of Nuclear Medicine, Erasmus Medical Center, Rotterdam, the Netherlands) into the portal vein of a male Lewis rat and the tumor was allowed to grow in the liver for 14 days. At the 14th day, the animal was sacrificed and the liver was surgically removed. It was then pressed through a sterile screen where it was made into a homogenous solution with sterile phosphate buffered saline (PBS) by carefully mixing the solution in a sterile pipette to obtain a uniform suspension. This solution was then injected into the right flank of several male rats. Tumor cells were then passaged from rat to rat by injecting 10⁵ tumor cells into the right flank. After 5-12 days the tumor developed in the right flank. Tumor volume estimates were made following caliper measurement of the maximum tumor dimension (length, width, or height) using the formula for the volume of an ellipsoid as follows: (maximum tumor dimension)³ x π/6.

Biodistribution studies

Fifteen rats, twelve of them non-tumor bearing, were injected intravenously (penile vein) with either unlabelled free ²¹³Bi radionuclide or ²¹³Bi-DOTATOC. The animals were sacrificed 1 hour and 3 hours post injection at which time the pancreas, adrenals, pituitary, stomach, spleen, liver, testes, bone marrow, blood, muscle, bladder and kidneys were harvested to determine the biodistribution characteristics of the drug. Due to the extremely short half life of this isotope the 3 hour rats were given a larger dose of the radiolabeled peptide. The non-tumor bearing rats were given 174.3 ± 9.0 µCi for the 1 hour time point and 345 ± 69.5 µCi for the 3 hour time point, while the tumor bearing rats were given 251.7 ± 53.0 µCi for the 1 hour time point. All ²¹³Bi-DOTATOC injections had a specific activity of 7.4MBq ²¹³Bi/1 µg DOTATOC. The obtained organ samples were weighed and the corresponding localized radioactivity was measured using a gamma counter. Gamma counter sensitivity and efficiency was determined by counting 5 standards prepared by

geometric dilutions of the injectate on each day of use. The percent injected dose per gram of tissue was calculated by comparison with the injected dose per animal.

Cancer Treatment studies and toxicology

Toxicology was assessed at 25 days in 4 groups of tumor bearing male Lewis rats (average volume $0.75 \pm 0.3 \text{ mm}^3$). Rats in the first group, Cohort 1, were injected on day 1 only. Rats in second cohort were injected on days 1 and 2, while rats in the third cohort were injected on days 1, 2, and 3. Rats were injected with 2.56 μg , 0.5 μg , 0.5 μg DOTATOC, on day 1, day 2 and day 3, respectively, with a nominal activity of 3.7 MBq. Each dose was divided into 2 injections at 1 hour intervals. The rats received the following cumulative average activities per group: Cohort 1 (N=3) received $4.3 \pm 0.7 \text{ MBq}$, Cohort 2 (N=3) received $9.0 \pm 0.4 \text{ MBq}$, and Cohort 3 (N=4) received $12.6 \pm 0.3 \text{ MBq}$ of ²¹³Bi-DOTATOC. Cohort 4 (N=4) was added as control group and injected twice daily with unlabelled DOTATOC on three consecutive days.

After 24 days, the animals were put into a metabolic cage to collect urine samples for creatinine clearance analysis. Creatine clearance was determined as previously described (20). After 24 hour urine collection, the animals were euthanized with halothane. For blood collection, a cardiac puncture was performed. Blood analysis consisted of hemoglobin (Hgb), hematocrit (Hct), red blood cells (RBC's), and white blood cells (WBC's) with differential, and platelets (Pt's). Additionally T4 and FSH values were assessed using the serum.

Additional groups were then designed to study the effects of the treatment on a somatostatin receptor positive tumor. The first group was designed to study the effects of treatment on large volume tumors (average volume $1720 \pm 608 \text{ mm}^3$). This group, Cohort 5 (N=5), received three fractionated doses of ²¹³Bi-DOTATOC (specific activity 7.4 MBq ²¹³Bi /1 μg DOTATOC) with a total average cumulative dose of $13.0 \pm 0.5 \text{ MBq}$ of ²¹³Bi-DOTATOC. The last cohort, the sixth cohort (N=4), was injected with two fractionated doses, ²¹³Bi-DOTATOC (specific activity 7.4 MBq ²¹³Bi /1 μg DOTATOC) with a total average cumulative dose of $22.2 \pm 0.7 \text{ MBq}$ of ²¹³Bi-DOTATOC. As described earlier, each dose was divided into 2 injections separated by a 1 hour interval. Tumor response to the treatment was assessed in all cohorts by daily tumor measurements.

A 26 week toxicology study was performed in 3 groups of rats. The first group, Cohort 7 (N=3), received three fractionated doses ²¹³Bi-DOTATOC (specific activity 7.4 MBq ²¹³Bi /1 μg DOTATOC with a total average cumulative dose of $12.75 \pm 1.1 \text{ MBq}$. The second group, Cohort 8 (N=3), received D-lysine (concentration 400mg/mL) immediately before receiving three fractionated doses ²¹³Bi-DOTATOC with a specific activity 7.4 MBq ²¹³Bi /1 μg DOTATOC with a total average cumulative dose of $11.39 \pm 0.14 \text{ MBq}$. The third group, cohort 9 (N=3) received 3 fractionated doses of DOTATOC. Rats were injected with 2.56 μg , 0.5 μg , 0.5 μg DOTATOC, on day 1, day 2 and day 3, respectively. As described earlier, each dose was divided into 2 injections separated by a 1 hour interval.

Pathology

Organs were harvested and immediately placed in 10% formalin for a minimum of 48 hours. Following fixation in formalin, bone samples were placed in decalcifying solution for 36 hours. Trimmed organs were sent to the TriCore Laboratories (Albuquerque, NM) where they were embedded in paraffin, sectioned, and stained with Hematoxylin and Eosin (H and E). Histopathologic evaluation was performed by a board certified veterinary pathologist (DFK) who examined the following organs of each animal: heart, lung, kidneys, testicles, spleen, pancreas, pituitary bone marrow, urinary bladder, adrenals, and two different sections of the liver.

Sections of both the right and left kidneys were examined to determine nephrotoxicity in all cohorts. Bone marrow was examined to evaluate hypoplasia and other lesions in Cohorts 3 and 4. Interstitial nephritis and bone marrow were scored as follows: 0 no lesions, 1 minimal lesions, 2 mild lesions, 3 moderate lesions, and 4 severe lesions.

Statistics

For the pathology scoring, to evaluate nephrotoxicity on the 6 treatment groups, a frequency analysis was performed in StatXact-5 using the Jonckheere-Terpstra Test. For all other data, graphs and calculations were performed in SigmaStat®-3 and SigmaPlot®-9 as well as Graph Pad Prism®-4 using the t-test. For all statistical tests results were considered significant when $p < 0.05$. Animal biodistribution and tumor volume data are expressed as the average, plus or minus the SEM.

Results

The radiolabeling incorporation yields and radiochemical purity by ITLC and HPLC were greater than 99.9% and greater than 95%, respectively. ²¹³Bi-DOTATOC demonstrated acceptable stability and was unchanged after 1 hour of *in vitro* incubation in rat serum. The biodistribution data demonstrated specific binding to sst expressing tissues. Administration of free ²¹³Bi, compared to ²¹³Bi-DOTATOC, resulted in higher accumulation of radioactivity in non-tumor bearing rats at 3 hours post injection in the kidneys ($34.47 \pm 1.40\%$ injected dose/gram vs. $11.15 \pm 0.46\%$, $p < 0.0001$), the bone marrow ($0.31 \pm 0.01\%$ injected dose/gram vs. $0.06 \pm 0.02\%$, $p < 0.00023$), the spleen ($0.36 \pm 0.02\%$ injected dose/gram vs. $0.08 \pm 0.01\%$, $p < 0.00053$), the liver ($0.50 \pm 0.05\%$ injected dose/gram vs. $0.14 \pm 0.02\%$, $p < 0.002$), the blood ($0.07 \pm 0.01\%$ injected dose/gram vs. $0.02 \pm 0.00\%$, $p < 0.022$), the testis ($0.03 \pm 0.01\%$ injected dose/gram vs. $0.02 \pm 0.00\%$, $p < 0.016$) and the stomach ($0.25 \pm 0.00\%$ injected dose/gram vs. $0.08 \pm 0.01\%$, $p < 0.000015$). Administration of ²¹³Bi-DOTATOC in tumor bearing rats versus non-tumor bearing rats showed a decreased uptake at 1 hour in the pancreas ($3.15 \pm 0.4\%$ injected dose/gram vs. $1.44 \pm 0.05\%$, $p < 0.014$) and the adrenals ($3.55 \pm 0.57\%$ injected dose/gram vs. $0.50 \pm 0.05\%$, $p < 0.0061$) as shown in Figure 2.

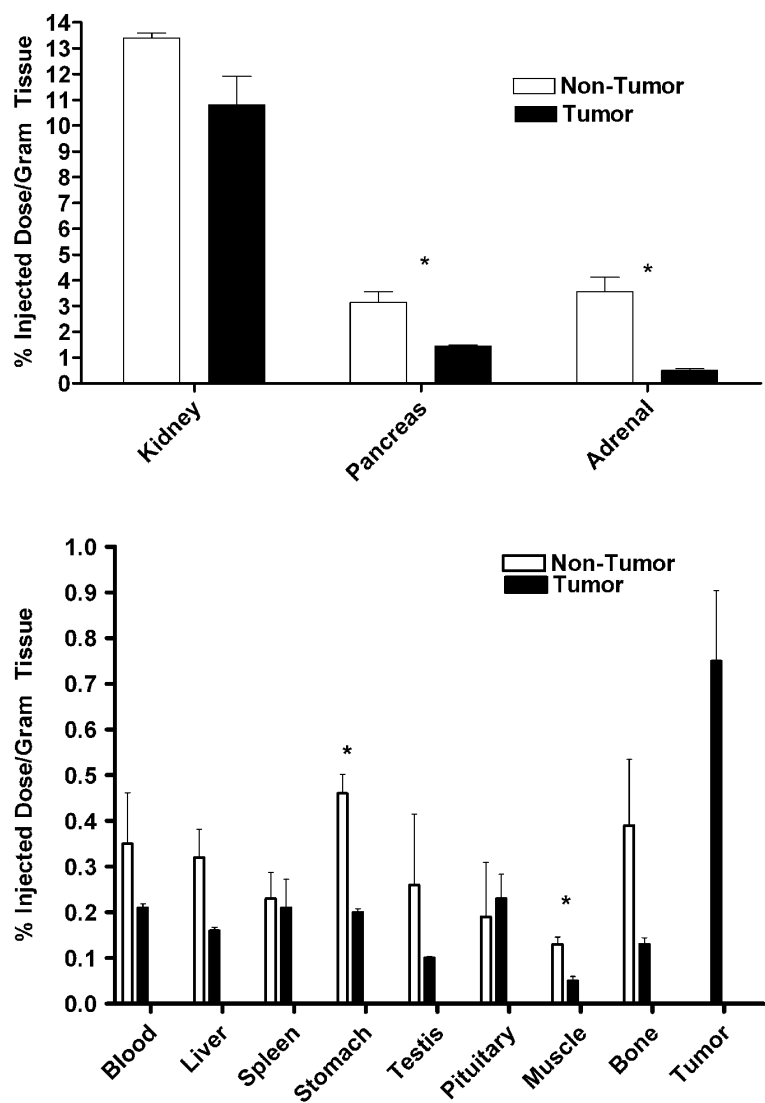


Figure 2: A, B Graphical comparisons of Tumor and Non-Tumor Bearing Rats at 1 hour post injection of ²¹³Bi-DOTATOC. Columns, means, Bars, SEM, white columns represent non-tumor bearing rats and black columns represent tumor bearing rats. Significance of p<0.05 is represented by a (*). A. Graph represents the high uptake organs, showing localization in the pancreas and adrenals was significantly higher in the non-tumor. B. Graph represents the low uptake organs, showing localizations were significantly higher in both the stomach and muscle.

No difference in creatinine clearance was seen between the control group (DOTATOC only) and the bismuth treated animals for the 25 day study. Hematology results also did not show any significant differences between the control group and the bismuth treated animals. No significant changes were found in the FSH values between treated and control animals. However, significance was seen with T4 values between the two highest

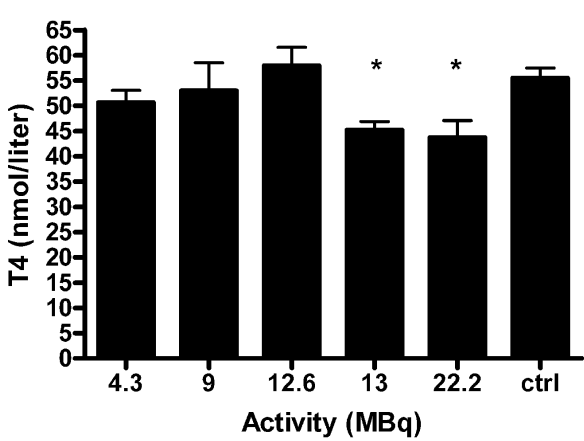


Figure 3: A graphical comparison of T4 values in serum taken from different treatment groups of ²¹³Bi-DOTATOC at 25 days. Columns, means, Bars, SEM. Significance of p<0.05 is represented by a (*). Graph represents the decreased T4 value in (nmol/liter) with the increase of injected activity.

treatment groups 22.2 MBq (p<0.024) and 13.0 MBq (p<0.006) as compared to control. (Figure 3)

The results of the bone marrow analysis for the DOTATOC control group versus the low dose (12.6 MBq) ²¹³Bi-DOTA-TOC treatment group showed no lesions at 25 days; neither hypoplasia nor hyperplasia was observed. The average histopathologic score for nephritis for each treatment group was < 1. Representative kidney sections of the treated animals are shown in Figure 4. Statistical analysis of the data showed that the likelihood of interstitial nephritis increased with increasing dose when all treatment groups were analyzed (p<0.04 with the Jonckheere-Terpstra Test). This significance was lost when the high-dose treatment group (22.2 MBq) was eliminated. Minimal toxicity was seen in the high-dose treatment cohort, except for one kidney in this group, which showed mild interstitial nephritis (Table 1).

Histopathological examination revealed no evidence of treatment induced toxicity at 25 days in the heart, lungs, liver, spleen, and urinary bladder. No histopathologic abnormalities were seen in any of the animals in the testes, adrenals, or pancreas. Pituitary cysts were seen in 2 out of 4 animals in the high-dose (22.2 MBq) treatment group. However, such cysts are generally considered to be incidental findings in Lewis rats (21).

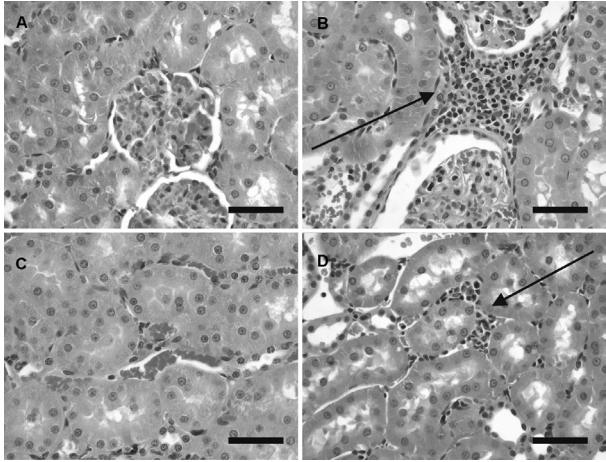


Figure 4: Unaffected animals had normal-appearing glomeruli (A, upper left) and convoluted tubules (C, lower left), and no inflammatory cells were seen in the interstitium (A upper left, C lower left). Animals with interstitial nephritis had normal-appearing glomeruli (B, upper right) and tubules (D, lower right), but there were small aggregates of mononuclear inflammatory cells in the interstitium (arrows, upper and lower right). Kidney sections were stained with hematoxylin and eosin. Bar = 50μm.

Table 1: Dose-related frequency of interstitial nephritis. Interstitial nephritis was scored as follows: 0 = no lesions, 1 = minimal lesions, 2 =mild lesions, 3 = moderate lesions, and 4 = severe lesions.

	Kidney Scores	0	1	2	3	4
cohort 1	4.3 Mbq ²¹³ Bi-DOTATOC	5	1	0	0	0
cohort 2	9 MBq ²¹³ Bi-DOTATOC	4	2	0	0	0
cohort 3	12.6 MBq ²¹³ Bi-DOTATOC	6	2	0	0	0
cohort 5	13 MBq ²¹³ Bi-DOTATOC	6	2	0	0	0
cohort 6	22.2 MBq ²¹³ Bi-DOTATOC	4	3	1	0	0
cohort 4	Control (DOTATOC only)	8	0	0	0	0

No difference in creatinine clearance was seen between the control group (DOTATOC only) and the bismuth treated animals for the 26 week study. Hematology results also did not show any significant differences between the control group and the bismuth treated animals. No significant changes were found in the FSH or T4 serum values between treated and control animals.

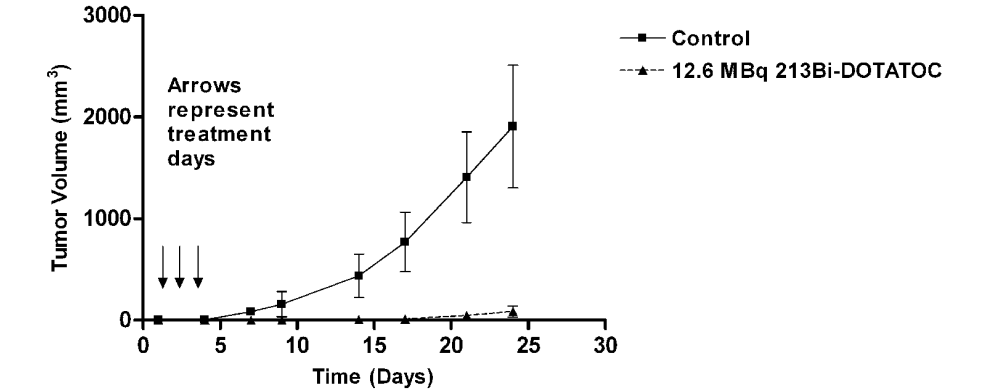


Figure 5: Graph of small volume tumor bearing Lewis rats given DOTATOC alone or a total 12.6 MBq of ²¹³Bi-DOTATOC. Symbols, means, Bars, SEM, Solid line with the square symbol represents the control, dashed line with the triangle symbol represents 12.6 MBq ²¹³Bi-DOTATOC. Rats were treated for 3 consecutive days with DOTATOC or ²¹³Bi-DOTATOC.

Histopathological examination at 26 weeks found minimal nodular cortical hyperplasia in both adrenals in all ²¹³Bi-DOTATOC treated rats, while only 2 rats in the D-lysine cohort had one adrenal each with nodular cortical hyperplasia; no adrenal hyperplasia was seen in the control cohort. Microcystic pancreatic degeneration, ranging from mild to moderate was seen in all of the cohorts. Cardiomyopathy was seen in one rat in the ²¹³Bi-DOTATOC group, 2 rats in the D-lysine group, and no rats in the control group. All groups contained some rats with mild to moderate microcystic degeneration in the pituitary. In the Bi-DOTATOC cohort, 83% of the kidneys had minimal to mild interstitial nephritis, while the Lysine and the controls cohorts had 67%. All groups showed some mild or moderate cholangiohepatitis and perivascultitis in the liver. Animals in most groups, including the control groups had minimal to mild interstitial pneumonia.

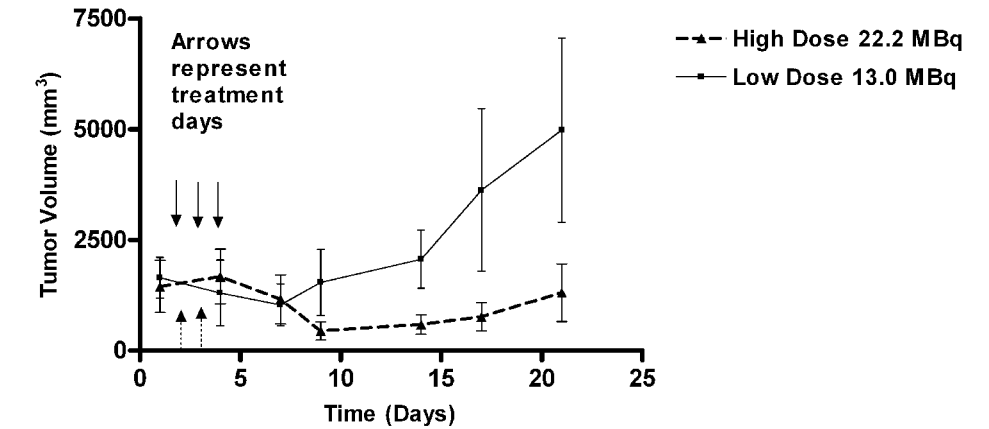


Figure 6: Graph of large tumor volume bearing Lewis rats given high 22.2 MBq and low 13.0 MBq doses of ²¹³Bi-DOTATOC. Symbols, means, Bars, SEM, Solid line with square symbol represents 13 MBq ²¹³Bi-DOTATOC, Dashed line with the triangle symbol represents 22.2 MBq ²¹³Bi-DOTATOC. Rats were treated for 3 consecutive days with ²¹³Bi-DOTATOC.

A significant decrease in the rate of tumor growth was observed at 9 days PI in small volume tumor bearing rats (0.75 mm³) treated with low-dose ²¹³Bi-DOTATOC (12.6 MBq) as compared to controls (p< 0.037) treated with only non-radioactive DOTATOC (Figure 5). In the large-volume tumor bearing cohorts (1720 mm³), rats receiving high-dose (22.2 MBq) ²¹³Bi-DOTATOC showed significant tumor reduction (approximately 3X) at 9 days PI as compared to the rats receiving low-dose treatments (13 MBq) (p< 0.025) (Figure 6).

Discussion

Radionuclide therapy is predominantly based on β - particle emitters such as ¹³¹I, ⁹⁰Y or ¹⁷⁷Lu. However, a few high-LET α -particle emitters have been evaluated in clinical studies and have demonstrated therapeutic advantages over low-LET radiation emitters in radionuclide therapy (22). It has been previously shown that the short-lived α -particle ²¹³Bi emits 20% of the total α -emission within 15 minutes after injection and only 6% of the total emission remains 3 hours post-injection (17). This property of ²¹³Bi makes this cytotoxic radionuclide an attractive candidate for sst targeted radionuclide therapy as the somatostatin analogue used in this study, DOTATOC, is known to localize in tumor within a few minutes after injection (23). The objective of this study was to evaluate the use of high-LET alpha particle ²¹³Bi labeled to a somatostatin receptor-targeted peptide DOTATOC as a targeted radiopharmaceutical for PRRT. As described above, the therapeutic efficacy of ²¹³Bi-DOTATOC was studied in male Lewis rats using biodistribution, tumor growth reduction and toxicology.

Tumor growth inhibition was observed in both small- and large-volume tumors when fractionated low- (12.6MBq) and high-dose (22.2MBq) ²¹³Bi-DOTATOC were given, respectively. Previous reports indicate that the dose-limiting factor in PRRT is often nephrotoxicity caused by the radiation absorbed dose to the kidneys. Our results show only minimal nephrotoxicity observed with the low-dose ²¹³Bi-DOTATOC (Table 1) and mild nephrotoxicity was observed with high-dose ²¹³Bi-DOTATOC in only one animal. No significant changes in creatine clearance levels were observed in any of the treatment groups. The only evidence of other treatment induced toxicities observed was a slightly lower T4 value in the 13 MBq and the 22.2 MBq treatment groups at 25 days.

Radionuclides such as ²¹³Bi that emit alpha particles offer radiotherapeutic advantages as they emit much higher energy particles than most of the betas, and yet their ranges are typically two orders of magnitude lower. Alpha particles have a high LET that is about 100 times greater than the beta particles, manifested by a higher RBE and a much shorter range. Consequently, a much greater fraction of total energy is imparted to the targeted cancer cell and thus very few nuclear hits are required to kill the cell (24, 25, 26). The small path-length cross-kill achievable with ²¹³Bi results in targeted cell killing with only minimal treatment related toxicities. This further illustrates a strong advantage over ⁹⁰Y, which conversely has a large path-length cross-kill, thus significantly increasing toxicity.

Conclusion

Quantitative radiolabeling of ²¹³Bi to DOTATOC was successfully achieved demonstrating serum stability for ≥ 24 hours. ²¹³Bi-DOTATOC showed sst targeted dose-related tumor anti-proliferative effects with minimal nephrotoxicity and no other acute or chronic toxicity. ²¹³Bi-DOTATOC is therefore a promising targeted therapeutic radiopharmaceutical agent for further pre-clinical evaluation.

Acknowledgements

The authors would like to thank Dr. Daniel P. Theele for his assistance with animal monitoring throughout the treatment and observation period. The authors would also like to thank Bert F. Bernard for his assistance with tumor biology and animal modeling. This research was supported through an unrestricted research grant from SPIRIT, funded by Mallinckrodt Medical, B.V., Petten, the Netherlands, the United States Department of Energy grant DE-FG01-001NE23554, and the University of New Mexico General Clinical Research Centers Grant supported by: DHHS/PHS/NIH/NCRR/GCRC, MO1 RRO0997.

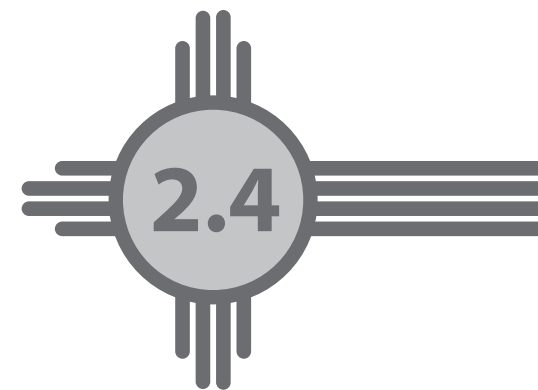
References

1. Reubi JC, Lang W, Maurer R, Koper JW, Lamberts SW. Distribution and biochemical characterization of somatostatin receptors in tumors of the human central nervous system. *Cancer Res* 1987;47:5758-64.
2. Reubi JC, Krenning E, Lamberts SW, Kvols L. In vitro detection of somatostatin receptors in human tumors. *Metabolism* 1992;41:104-10.
3. Patel YC. Somatostatin and its receptor family. *Front Neuroendocrinol* 1999;20:157-98.
4. Rens-Domiano S, Reisine T. Biochemical and functional properties of somatostatin receptors. *J Neurochem* 1992;58:1987-96.
5. Leitha T, Meghdadi S, Studnicka M, et al. The role of iodine-123-tyr-3-octreotide scintigraphy in the staging of small-cell lung cancer. *J Nucl Med* 1993;34:1397-402.
6. Kvols LK, Brown ML, O'Connor MK, et al. Evaluation of a radiolabeled somatostatin analog (I-123 octreotide) in the detection and localization of carcinoid and islet cell tumors. *Radiology* 1993;187:129-33.
7. Reubi JC. Peptide receptors as molecular targets for cancer diagnosis and therapy. *Endocr Rev* 2003;24:389-427.
8. Otte A, Herrmann R, Heppeler A, et al. Yttrium-90 DOTATOC: First clinical results. *Eur J Nucl Med* 1999;26:1439-47.
9. Lambert B, Cybulla M, Weiner SM, et al. Renal toxicity after radionuclide therapy. *Radiat Res* 2004;161:607-11.
10. Schumacher T, Waldherr C, Mueller-Brand J, Maecke H. Kidney failure after treatment with 90Y-DOTATOC. *Eur J Nucl Med Mol Imaging* 2002;29:435.
11. Krenning EP, Kwekkeboom DJ, Valkema R, Pauwels S, Kvols LK and De Jong M. Peptide receptor radionuclide therapy. *Ann N Y Acad Sci* 2004;1014:234-45.
12. Lewington VJ. Targeted radionuclide therapy for neuroendocrine tumours. *Endocr Relat Cancer* 2003;10:497-501.
13. McDevitt MR, Sgouros G, Finn RD, et al. Radioimmunotherapy with alpha-emitting nuclides. *Eur J Nucl Med* 1998;25:1341-51.
14. Geerlings MW, Kaspersen FM, Apostolidis C, van der Hout R. The feasibility of 225Ac as a source of alpha-particles in radioimmunotherapy. *Nucl Med Commun* 1993;14:121-5.
15. McDevitt MR, Scheinberg DA. Ac-225 and her daughters: The many faces of shiva. *Cell Death Differ* 2002;9:593-4.
16. Nuclear Decay Data in the MIRD Format [database on the internet]. Upton, (NY) : National Nuclear Data Center at Brookhaven National Laboratory (US). c1986 [updated 2005 January 26; cited February 7, 2005]. Available from: <http://www.nndc.bnl.gov/mird/index.html>
17. Behr TM, Behe M, Stabin MG, et al. High-linear energy transfer (LET) alpha versus low-LET beta emitters in radioimmunotherapy of solid tumors: Therapeutic efficacy and dose-limiting toxicity of 213Bi- versus 90Y-labeled CO17-1A fab' fragments in a human colonic cancer model. *Cancer Res* 1999;59:2635-43.
18. Li Y, Rizvi SM, Ranson M, Allen BJ. 213Bi-PAI2 conjugate selectively induces apoptosis in PC3 metastatic prostate cancer cell line and shows anti-cancer activity in a xenograft animal model. *Br J Cancer* 2002;86:1197-203.
19. Wu C, Brechbiel MW, Gansow OA. An improved generator for the production of 213Bi from 225Ac. *Radiochim Acta* 1997;79:141-4.
20. Comstock TJ. Assessment of renal function. In: DiPiro JT, Talbert RL, Yee GC, Matzke GR, Wells BG, Posey LM, editors. *Pharmacotherapy: A Pathophysiologic Approach*. Fourth ed. New York: McGraw-Hill Medical Publishing Division; 1999. p.686-705.
21. Quintanar-Stephano A, Munoz Fernandez L, Quintanar JL, Kovacs K. Cysts in the rat adenohypophysis: incidence and histology. *Endocr Pathol* 2001;12:63-71.
22. Milenic DE, Brady ED and Brechbiel MW. Antibody-targeted radiation cancer therapy. *Nat Rev Drug Discov* 2004;3(6):488-99.
23. Breeman WA, Bakker WH, De Jong M, et al. Studies on radiolabeled somatostatin analogues in rats and in patients. *Q J Nucl Med* 1996 Sep;40:209-20.

24. Rizvi SM, Allen BJ, Tian Z, Goozee G, Sarkar S. In vitro and preclinical studies of targeted alpha therapy (TAT) for colorectal cancer. *Colorectal Dis* 2001;3:345-53.
25. Zalutsky MR, Bigner DD. Radioimmunotherapy with alpha-particle emitting radioimmunoconjugates. *Acta Oncol* 1996;35:373-9.
26. Mulford DA, Scheinberg DA, Jurcic JG. The promise of targeted {alpha}-particle therapy. *J Nucl Med*. 2005 Jan;46 Suppl 1:199S-204S.

Radiation Absorbed Dose Estimates For Intravenously Injected ^{213}Bi -[DOTA₀]Tyr₃,Octreotide In Peptide Receptor Radionuclide Therapy

Jeffrey P. Norenberg, Boudewijn J. Krenning, Inge R. Konings, Robert W. Atcher, Kayhan Garmestani, Martin W. Brechbeil, Larry K. Kvols, Wouter A Breeman, Mark Konijnenberg, Marion de Jong



Abstract

Peptide receptor radionuclide therapy (PRRT) using high linear energy transfer (LET) radionuclides such as ^{213}Bi has therapeutic advantages over lower-LET emitters such as ^{90}Y , and ^{131}I . ^{213}Bi Bismuth decay (45.6 min half-life) yields α -, β -, and γ -emissions. Previously, ^{213}Bi -[DOTA⁰,Tyr³]octreotide (DOTATOC) demonstrated somatostatin receptor (SSTr) specific binding to tissues expressing SSTr and dose-related antiproliferative effects without inducing hematologic toxicity, indicating promise as PRRT for neuroendocrine tumors. The aim of this study is to estimate radiation absorbed dose for ^{213}Bi -DOTATOC in tumor-bearing rats to support translation to evaluation in humans.

Methods: ^{213}Bi Bismuth was obtained from a $^{225}\text{Ac}/^{213}\text{Bi}$ generator, labeled to DOTATOC at a specific activity of 12.4 MBq/nmole, and administered by intravenous injection via tail vein. Biodistribution studies using 9.6 ± 3 MBq ^{213}Bi -DOTATOC (45 MBq/kg) were performed in CA20948 tumor-bearing Lewis rats, 1 and 3 hours post-injection to determine the percent injected dose (%ID) per gram organ weight, and residence time in each of 12 organs and tumors. Radiation absorbed dose estimates were calculated using the spherical node model for ^{213}Bi and its daughters.

Results: The estimated radiation absorbed dose to 12 organs of interest is reported. The estimated radiation absorbed dose to a SSTr-expressing neuroendocrine tumor in male Lewis rats was 688 mGy/MBq. The organs receiving the highest radiation absorbed dose are the pituitary, adrenal, and bladder, respectively.

Conclusions: Previous work has demonstrated that ^{213}Bi -DOTATOC is effective in treating SSTr expressing tumors at doses of $8\text{E}-2$ MBq/g in rats without any evidence of significant toxicities. While the estimated radiation absorbed dose to the kidney is significant (749 mGy/MBq), if scaled to a 70 kg human, a cumulative clinical dose of 10-20 GBq of ^{213}Bi -DOTATOC is anticipated to deliver 7.5-15 Gy radiation absorbed dose to the kidney, a much lower amount than is associated with nephropathy following external beam radiation. Alpha therapy using ^{213}Bi -DOTATOC to target SSTr expressing tumors remains a compelling option for PRRT of SSTr-expressing tumors.

Introduction

Somatostatin is a naturally occurring, 14 amino acid peptide that plays an important role in the regulation of endocrine organs, including the pituitary and hypothalamus. Somatostatin (SST) is unsuitable for direct *in vivo* use due to its rapid enzymatic degradation. Octreotide, an eight amino acid peptide, is a more stable synthetic analog that binds to SST receptor (SSTr) subtypes 2 and 5. Octreotide analogs have been modified through the addition of a bifunctional chelate, and radiolabeled to form ^{111}In -[DTPA⁰]octreotide (^{111}In -OctreoScan[®]) for diagnostic imaging of SSTr-positive neuroendocrine tumors. Octreotide has established a prominent position in the treatment of symptoms caused by the overproduction of neurotransmitters such as serotonin and gastrin by neuroendocrine tumors. Octreotide has been further modified and radiolabeled with radionuclides such as ^{90}Y and ^{177}Lu to effect peptide-receptor radionuclide therapy (PRRT) of SSTr-positive neuroendocrine tumors. The rapid internalization of the SSTr receptor radioligand complex transports these compounds to lysosomal elements where the radiolabeled octreotide derivative is metabolized, and portions of the radioligand complex are localized intracellularly. The radioactive portion of the complex remains bound intracellularly for a long period of time. This intimate association of radiation with intracellular elements of tumor cells causes cytotoxicity and induces apoptosis. In this study, the use of a short-lived

α -emitting radionuclide, ^{213}Bi ($t_{1/2} = 45.6$ min), complexed to DOTATOC is investigated as a potential therapy for SSTr expressing neuroendocrine tumors. ^{213}Bi Bismuth was obtained from a previously described $^{225}\text{Ac}/^{213}\text{Bi}$ generator system¹. The radioactive decay of ^{225}Ac , ^{213}Bi , ^{209}Tl , ^{213}Po , and ^{209}Pb are shown in Figures 1 and 2. The objective of this study was to estimate the radiation absorbed dose of ^{213}Bi -DOTATOC to vital organs and SSTr positive neuroendocrine tumors in a pre-clinical model.

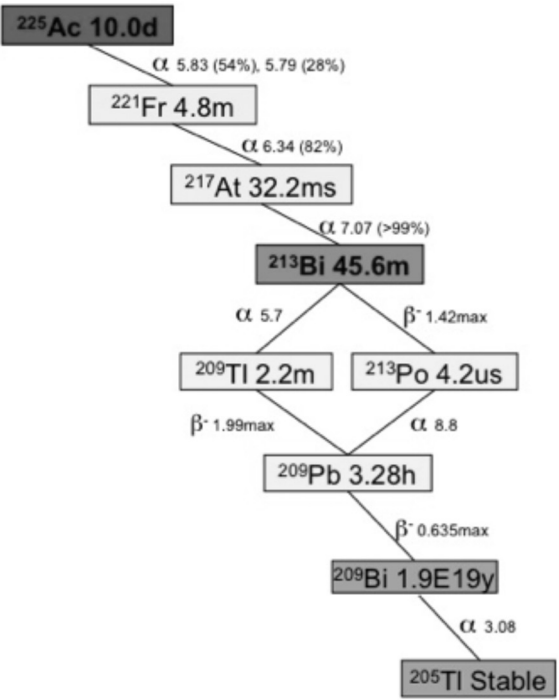


Figure 1: Radioactive decay scheme of ^{225}Ac , ^{213}Bi , ^{209}Tl , ^{213}Po , and ^{209}Pb

Methods

Radiolabeled ^{213}Bi -DOTATOC was prepared using a $^{225}\text{Ac}/^{213}\text{Bi}$ generator and radiolabeling methods

as previously described¹. All animal procedures were conducted according to a protocol approved by the Institutional Animal Care and Use Committee. Male Lewis rats were obtained from a commercial vendor (Charles River) at approximately 200 g body weight. Rats were maintained in AAALAC[®]¹-approved facilities with food and water available to them *ad libitum*.

SSTr activity was confirmed by analyzing biodistribution patterns using ²¹³Bi-DOTATOC (12.4 MBq/nmole) in 250g non-tumor bearing Lewis rats, 1 and 3 h post-intravenous injection. The organ biodistribution of un-reacted ²¹³Bi ("free Bi") was compared to the radio-labeled ²¹³Bi-DOTATOC to predict organ toxicity. The control group of rats received 250mg of DOTATOC prior to ²¹³Bi-DOTATOC in order to inhibit SSTr localization of Bi-DOTATOC. Comparisons of radioactive counts in each organ with and without prior SSTr blockade were performed to assess SSTr specificity.

Radiation absorbed dose was estimated by first assuming a single-exponential physiological clearance from each organ. The organ residence times were determined for ²¹³Bi-DOTATOC and its daughters, all assumed to remain conjugated with the peptide, according to the equations shown in the appendix. Twelve organs of interest were evaluated from the biodistribution data at 2 time-points in non-tumor bearing Lewis rats. Tumor uptake and residence times were estimated, in parallel with this study, in CA20948 tumor-bearing Lewis rats and have previously been published².

The percent injected activity per gram of tissue (%IA/g) was determined by harvesting organs (or samples of organs) at necropsy, weighing the organ/sample, and counting radioactivity via a NaI(Tl) well counter (Wallac Wizard 1480). Organs collected included blood (cardiac collection), kidneys, testicles, spleen, pancreas, pituitary, bone marrow (femur collection), urinary bladder, adrenals, muscle, stomach and liver. Blood samples were collected at the time of euthanasia, 1 and 3 h post injection. Radiation absorbed dose estimates for each organ were calculated using the residence time per gram of tissue and the spherical node S-values for ²¹³Bi and its daughters ²¹³Po, ²⁰⁹Tl and ²⁰⁹Pb³. Not all radiation exposure from ²¹³Bi is by a-particles (See Table 1). However, the energy resulting from the a-particles is completely absorbed in the organ in which it is localized. The b⁻-particles in the emission spectrum of ²¹³Bi, ²⁰⁹Tl and ²⁰⁹Pb, however, have a longer range and therefore, absorbed fractions of the emitted energy were derived for spherically sized organs. The cross-doses by the b⁻-particles and the g-radiation from one organ to the other have not been taken into account.

The absorbed dose to the urinary bladder was calculated by using specific S-values for ²¹³Bi and its daughters ²¹³Po, ²⁰⁹Tl and ²⁰⁹Pb. These S-values were determined for the 103 mg bladder wall inside the rat phantom model⁴. The radiation transport from radioactivity

Table 1: Principle emissions from ²¹³Bi radioactive decay

Radionuclide t1/2	Emission	Energy (keV)	End-point Energy (max keV)	Intensity (% Abundance)	Dose (MeV/ Bq-s)
²¹³ Bi 45.59 m	α	5869		1.94	1.14E-01
	β	492	1423	12.41	3.24E-01
	γ	440		25.94	1.14E-01
²¹³ Po 4.2 us	α	8376		100.00	8.38E+00
²⁰⁹ Tl 2.20 m	β	660	1827	98.80	6.52E-01
	γ	117		84.30	9.88E-02
	γ	465		96.90	4.51E-01
²⁰⁹ Pb 3.253 h	β	198	644	100.00	1.98E-01

in the 163 ml bladder contents was calculated with the Monte Carlo N-Particle Transport (MCNP) X Code (version 2.5.0, Los Alamos National Laboratory, Los Alamos, NM) for the a-particles of ²¹³Bi and ²¹³Po. All other radiation transport calculations were performed with MCNP (version 5, Los Alamos National Laboratory, Los Alamos, NM).

Results

The ²¹³Bi-DOTATOC used in these experiments showed quantitative incorporation of ²¹³Bi in DOTATOC; was unchanged following incubation for 24 hours at 37°C in rat serum; and demonstrated specific targeting of SSTr.

The organ residence times for ²¹³Bi-DOTATOC are shown in Table 2. The radiation absorbed dose to 12 organs of interest in 250g non-tumor bearing Lewis rats is given in Table 3. The largest dose was to the pituitary, adrenal, and bladder. The whole kidney, including the intact and un-washed renal pelvis thought to contain urine, received 749 mGy/MBq ²¹³Bi-DOTATOC (Table 3). The estimated radiation absorbed dose to tumors was 688 mGy/MBq ²¹³Bi-DOTATOC.

¹ Association for Assessment and Accreditation of Laboratory Animal Care International

Table 2: Organ residence times for ²¹³Bi-DOTATOC and its daughters in Lewis rats

Organ	% ID/g 1hr	SD (%IA/g)	% ID/g 3hr	SD (%IA/g)	Residence Time per gram of tissue (s/g)			
					²¹³ Bi	²¹³ Po	²⁰⁹ Tl	²⁰⁹ Pb
Blood	0.35	...	0.02	...	22.5	22.0	0.4	2.9
Liver	0.32	...	0.14	...	13.1	12.9	0.3	4.5
Kidney	13.40	...	11.96	...	527	516	11.0	416
Pancreas	3.15	...	1.16	...	132	130	2.7	39.6
Spleen	0.23	...	0.06	...	10.2	10.0	0.2	2.5
Adrenals	3.55	...	0.47	...	183	179	3.6	31.8
Stomach	0.46	...	0.09	...	21.7	21.2	0.4	4.5
Testes	0.26	...	0.02	...	15.4	15.1	0.3	2.2
Pituitary	0.19	...	0.21	...	7.5	7.4	0.2	9.9
Muscle	0.13	...	0.01	...	7.7	7.5	0.2	1.1
Bladder	34.07	...	0.13	...	5372	5259	98.1	381
Bone Marrow	0.39	...	0.03	...	23.1	22.6	0.5	3.3

Table 3: Radiation absorbed dose estimate per injected radioactivity

Organ	Radiation dose per injected activity (mGy/MBq ²¹³ Bi)				
	²¹³ Bi	²¹³ Po	²⁰⁹ Tl	²⁰⁹ Pb	Total
Blood	1.93	29.6	0.04	0.09	31.6
Liver	1.12	17.3	0.03	0.14	18.5
Kidney	44.2	691	1.04	12.8	749
Pancreas	11.0	174	0.25	1.21	186
Spleen	0.84	13.4	0.02	0.07	14.4
Adrenals	12.7	240	0.22	0.91	253
Stomach	1.83	28.4	0.04	0.14	30.4
Testes	1.30	20.2	0.03	0.07	21.6
Pituitary	0.47	9.9	0.01	0.27	10.6
Muscle	0.65	10.1	0.01	0.03	10.8
Bladder	57.5	88.3	1.62	1.29	149
Bone Marrow	1.90	30.3	0.04	0.10	32.3

Discussion

The organs receiving the highest radiation absorbed dose were the pituitary, adrenals, and bladder respectively. The radiation dose to the kidney was high, possibly the result of urine retained in the renal pelvis. However, it is much less than the amount associated with acute renal toxicity observed following external beam radiation⁵.

Our previous work showed that ²¹³Bi-DOTATOC produced SSTr-targeted dose-dependent tumor anti-proliferative effects with minimal nephrotoxicity and no other acute or chronic toxicity. Furthermore, that quantitative radiolabeling of ²¹³Bi-DOTATOC was achieved with demonstrated serum stability for ≥ 24 hours¹.

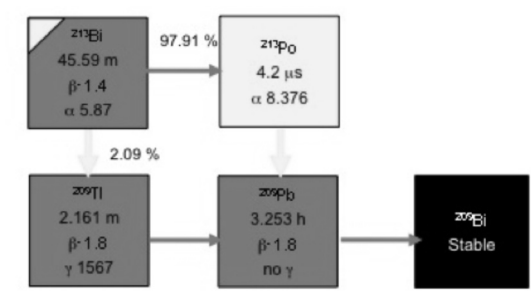


Figure 2. Decay scheme of ²¹³Bi and its daughters ²¹³Po, ²⁰⁹Tl and ²⁰⁹Pb. Decays by β-particle emission are indicated with the horizontal blue arrows and decays by α-particle emission are depicted by the vertical yellow arrows.

In a recently reported clinical study, ²¹³Bi-DOTATOC was administered by intra-arterial infusion to seventeen patients with gastroenteropancreatic neuroendocrine tumors (GEP-NET) refractory to previous treatment with chemotherapy and PRRT using ⁹⁰Y- or ¹⁷⁷Lu-DOTATOC⁶. No acute kidney, endocrine or hematologic toxicity higher than grade 0/I were observed after administration of ≤6 GBq per cycle. Moderate hair loss occurred in 3 of 6 patients receiving single doses of 6 to 10 GBq; 1 case of suspected radiation pneumonitis was observed

in the patient receiving 10 GBq. While morphologic long term response is still pending, shrinkage of primary tumors as well as liver and bone metastases has been observed. A complete response was achieved in two patients with durations of >11 and >12 months. Response was assessed with contrast enhanced sonography, MRI, ⁶⁸Ga-DOTATOC-PET/CT, and tumor markers. Markers for hematologic, kidney and endocrine toxicity were monitored initially, during, and after treatment.

The estimated radiation absorbed dose to the rat kidney is 749 mGy/MBq ²¹³Bi-DOTATOC. If scaled to a 70 kg human, a cumulative clinical dose of 10-20 GBq of ²¹³Bi-DOTA-TOC is anticipated to deliver 7.5-15 Gy to the kidney. A time activity curve of ²¹³Bi radioactivity and its decay daughters in the kidney for an administered dose of 10GBq is shown in Figure 3.

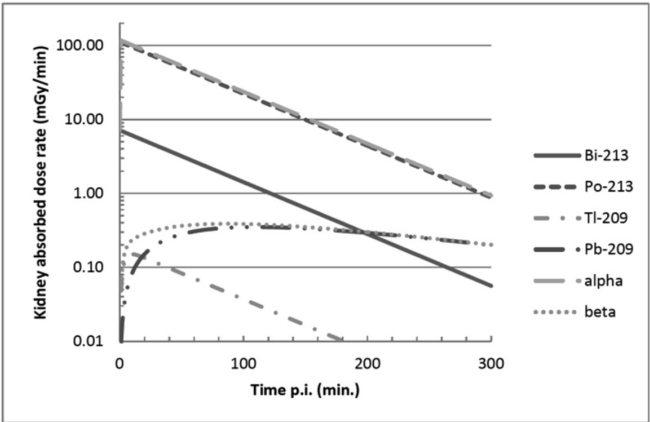


Figure 3. Time-activity curve of ²¹³Bi radioactivity concentration and its daughters in the kidneys for an administered dose of 10 MBq ²¹³Bi-DOTATOC.

The radiation dose estimate for blood was obtained using residence time/activity data from 1- and 3-hour post-injection only. Thus, the radiation dose to the bone marrow may be overestimated due to the lack of data ≤ 1 -hour post injection. The use of a macroscopic model for the kidneys with a-particle dosimetry is debatable, as the dose delivered by the a-particles will be restricted to the specific regions of uptake within the nephron and microdosimetry models should be applied to determine the absorbed dose in the most sensitive parts of the nephron⁷.

This study has shown that the dose threshold for renal damage is much higher in rats than in humans, as 60MBq ^{213}Bi -DOTATOC can be used in rats without expecting renal toxicity. Previous reports of cumulative doses of 10 GBq of ^{111}In -[DTPA⁰]octreotide, 5.7 GBq of ^{90}Y -DOTATOC, and 7.4 GBq of ^{177}Lu -DOTATOC have resulted in radiation absorbed doses to the kidney as high as 45 Gy. However, they did not show proteinuria, hypertension, significant changes in creatinine clearance, or other signs of deteriorating renal function.

Conclusions

The radiation dose estimates predict that ^{213}Bi -DOTATOC is capable of delivering anti-proliferative and tumoricidal doses of radiation to SSTR-expressing tumors without causing dose-limiting radiation-induced toxicity to non-target organs commonly associated with PRRT when using other radionuclides such as ^{90}Y -, ^{111}In -, and ^{177}Lu -DOTATOC. Thus, ^{213}Bi -DOTATOC remains the most promising targeted therapeutic radiopharmaceutical agent for PRRT of SSTR-expressing tumors and warrants further evaluation for the treatment of patients with SSTR-positive neuroendocrine tumors.

Acknowledgement

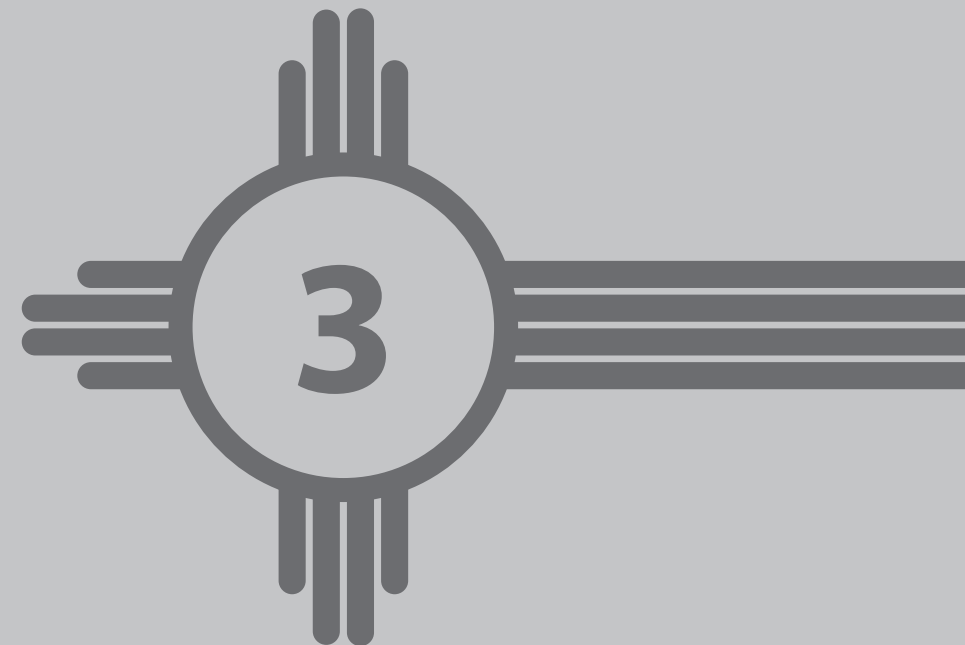
This research was supported in part by the Intramural Research Program of the NIH, National Cancer Institute, Center for Cancer Research, and research grant DOE DE-FG01-001NE23554.

References

1. Norenberg JP, Krenning BJ, Konings IR, et al. ^{213}Bi -[DOTA⁰, Tyr³]octreotide peptide receptor radionuclide therapy of pancreatic tumors in a preclinical animal model. *Clin Cancer Res.* 2006;12:897-903.
2. de Jong M, Breeman WA, Bernard BF, et al. Tumour uptake of the radiolabelled somatostatin analogue [DOTA⁰, Tyr³]octreotide is dependent on the peptide amount. *Eur J Nucl Med.* 1999;29(7):693-698.
3. Stabin MG, Konijnenberg M. Re-evaluation of absorbed fractions for photons and electrons in spheres of various sizes. *J Nucl Med.* 2000;41:149-60.
4. Konijnenberg MW, Bijster M, Krenning EP, de Jong M. A stylized computational model of the rat for organ dosimetry in support of preclinical evaluations of peptide receptor radionuclide therapy with (90)Y, (111)In, or (177)Lu. *J Nucl Med.* 2004;45:1260-1269.
5. Emami B, Lyman J, Brown A, Coia L, Goitein M, Munzenrider JE, Shank B, Solin LJ, Wesson M. Tolerance of normal tissue to therapeutic irradiation. *Int J Radiat Oncol Biol Phys.* 1991;21(1):109-122.
6. Morgenstern A, Bruchertseifer F, Apostolidis C, et al. Synthesis of ^{213}Bi -DOTATOC for peptide receptor alpha-therapy of GEP-NET patients refractory to beta therapy. *J Nucl Med.* 2012;53(S1):138P.
7. Hobbs RF, Song H, Huso DL, Sundel MH, Sgouros G. A nephron-based model of the kidneys for macro-to-micro α -particle dosimetry. *Phys Med Biol.* 2012;57:4403-4424.

Enhancement of somatostatin
receptor-targeted ^{177}Lu -[DOTA₀-Tyr₃]-
octreotide therapy by gemcitabine
pre-treatment-mediated receptor
uptake, up-regulation and cell cycle
modulation

Tapan K Nayak, Robert W Atcher, Eric R Prossnitz, Jeffrey P Norenberg



Abstract

Introduction: Clinical studies of patients treated with somatostatin-receptor (sstr) -targeted [DOTA⁰-Tyr³]-octreotide (DOTATOC) labeled with ^{177}Lu and ^{90}Y have shown overall response rates in the range of 9-33%. This study evaluates the potential for combination therapy with gemcitabine in an effort to improve clinical outcomes.

Methods: Human pancreatic adenocarcinoma Capan-2, rat pancreatic cancer AR42J, and human small cell lung cancer NCI-H69 cells were each treated with 1 $\mu\text{g}/\text{mL}$ gemcitabine for 4 days of treatment followed by replacement of the medium alone for 4 additional days. Cell cycle and direct receptor uptake studies were performed with ^{177}Lu -DOTATOC after the total 8-day treatment as described. Cell viability and apoptosis experiments were performed to study the effects of gemcitabine pre-treatment and ^{177}Lu -DOTATOC radionuclide therapy. Parallel control studies were performed with receptor non-targeted ^{177}Lu -DOTA and DOTATOC.

Results: Cells treated with gemcitabine for 4 days showed a down-regulation of sstr expression as determined by ^{177}Lu -DOTATOC uptake. However, after 4 days of additional growth in absence of gemcitabine the uptake of ^{177}Lu -DOTATOC was 1.5-3 times greater than the untreated control cells. In gemcitabine-pretreated capan-2 cells, 84% of the cell population was in the G₂M phase of the cell cycle. Due to sstr up-regulation and cell cycle modulations, synergistic effects of gemcitabine pre-treatment were observed in cell viability and apoptosis assays. ^{177}Lu -DOTATOC resulted in 2-3 times greater apoptosis in gemcitabine pre-treated Capan-2 cells compared to the untreated cells.

Conclusion: Gemcitabine pre-treatment up-regulates sstr expression and acts as a radiosensitizer through cell cycle modulation. The rational combination of gemcitabine and sstr-targeted radiopharmaceuticals represents a promising chemo-radiation therapeutic tool with great potential to improve clinical outcomes and thus merits further study.

Introduction

Radiolabeled somatostatin analogues such as ^{90}Y -DOTATOC have been used clinically for over 15 years for the treatment of neuroendocrine tumors. Studies indicate that $\geq 50\%$ tumor regression in 9 to 33% of patients in contrast; ^{177}Lu -DOTATATE treatment resulted in tumor regression of $\geq 50\%$ in 28% of patients and tumor regression of 25-50% in 19% of patients, stable disease in 35% of patients and progressive disease in 18% of patients [1-4]. When renal protective agents such as D-lysine were administered to the patients, nephrotoxic effects of radiolabeled DOTATOC treatments were decreased. However the incomplete response in many patients as well as the likelihood of relapse following initial regression suggests that improved therapeutic regimes are required.

The challenges that beta-emitting radionuclide DOTATOC therapy faces are renal toxicity in the absences of a renal protective agent and partial or limited response especially in radioresistant tumors.

In order to overcome the challenges posed by somatostatin-targeted beta-emitting radionuclide therapy, somatostatin-targeted alpha-emitting radionuclide therapies have been evaluated. Such studies have demonstrated the advantages of alpha-particle peptide therapy [5-7]. At the same absorbed dose, alpha-emitting ^{213}Bi -DOTATOC was 3.4 times more effective than beta-emitting ^{177}Lu -DOTATOC therapy in human pancreatic adenocarcinoma cells and demonstrated a relative biological effectiveness of 3.4 when compared with external source gamma-therapy using ^{137}Cs in combination with DOTATOC [5]. In an animal model, ^{213}Bi -DOTATOC demonstrated dose-dependent reduction of tumor growth with minimal toxicity demonstrating safety and efficacy *in vivo* [7]. However, alpha-particle therapy poses its own set of problems with respect to commercial availability of the radionuclide, the lack of long-term clinical toxicity data, and potential regulatory barriers. In a previous report, gemcitabine pre-treatment resulted in overexpression of the somatostatin receptor and suggested it could be used in combination therapy with sstr-targeted radionuclide therapy [8]. Nucleoside analogues, such as gemcitabine, are potent inhibitors of DNA synthesis, and as such, also inhibit various processes involved in the repair of genomic damages induced by radiation [9-12]. Gemcitabine is a pyrimidine analogue of deoxycytidine and has been used clinically as a chemotherapeutic agent both as a radiosensitizer in chemo-radiation combination therapy, and as first-line drug therapy in patients with pancreatic cancer [13, 14].

Concomitant chemo-radiotherapy is widely used in the treatment of various cancers. Numerous addictive and synergistic interactions are known between ionizing radiation and cytotoxic agents, which may modify the dose-response relationships *in vitro* and have demonstrated synergistic effects in clinical studies. The main interactions are spatial cooperation involving localized radiation therapy and systemic chemotherapy, independent cell killing, cell synchronization, inhibition of radiation damage repair, re-

oxygenation, reduction of the hypoxic fraction of the tumor and increased apoptosis. The combination of chemotherapeutic agent and radiation leads to increases in the number of unrepaired double-strand breaks [9]. Through these mechanisms and DNA damage by both the chemotherapeutic and radiation therapeutic modalities therapeutic efficiency is enhanced. The main outcomes of chemo-radiotherapeutic combination range from inhibition or antagonism, sub-additive, additive to synergistic effects [15-17]. The most important for clinical practice are synergistic effects, when the cytotoxic effect of the combination is greater than the sum of the effects of radiotherapy alone and that of chemotherapy alone [9].

Therefore in an effort to improve clinical outcomes, we sought to investigate the in vitro effects of combination therapy using gemcitabine and ^{177}Lu -DOTATOC on cell viability, apoptosis, cell cycle and receptor expression.

Materials and Methods

Cell culture

Human pancreatic adenocarcinoma Capan-2, rat pancreatic cancer AR42J, and human small cell lung cancer NCI-H69 cells were cultured in McCoy's 5a medium, F-12 medium and RPMI-1640 respectively and supplemented with 1.5 mM L-glutamine, 10% (v/v) fetal bovine serum, 10% of 100 units/mL penicillin and 100 µg/mL streptomycin. All the cell lines, culture media and supplements were purchased from American Type Culture Collection (Manassas, VA, USA). Cells were grown at 37°C, in a humidified atmosphere of 5% CO₂ and 95% air.

Radionuclide and preparation of radiolabeled peptide.

^{177}Lu (half-life: 6.64 days; E_{max} 0.5 MeV) was obtained from Perkin Elmer (Waltham, MA, USA) in the form of ^{177}Lu -chloride in 0.05 N optima grade HCl with the reported specific activity of 185 GBq/mg at the time of expiration. ^{177}Lu -DOTATOC and ^{177}Lu -DOTA were prepared as previously described [13].

Gemcitabine treatments

Gemcitabine was obtained as Gemzar® (Eli Lilly, Indianapolis, IN, USA).

Cohort 1

Depending upon the cell type a total of 2-4 million cells were plated overnight in T-75 flasks. On the day of the experiment, cells were washed with PBS and the tissue culture medium replaced. Gemcitabine was added to the cells at a concentration of 1 µg/mL and the cells were incubated for four days. The cells were washed twice with PBS, removed

from the flasks by trypsinization, resuspended as a single-cell suspension and counted for further experimentation.

Cohort 2

Cells in cohort 2 were treated as to those in Cohort 1, except that after the four day treatment, cells in cohort 2 were washed twice with PBS and medium (without gemcitabine) was added.

Since one of the objectives of our study was to determine if the increase in binding sites enhances combination therapy with radiolabeled somatostatin analogues, the incubation times and doses of gemcitabine were based on a previously published study [8]

Radioligand receptor-uptake studies

To evaluate ligand uptake to the somatostatin-receptor expressed on the cells from cohort 1, cohort 2 and untreated control cells, direct uptake experiments were performed with ^{177}Lu -DOTATOC as previously described [5]. Briefly, 100,000 cells/well were transferred to 6 well plates overnight. The cells were washed with 2 mL phosphate-buffered saline (PBS) and incubated in 1 mL HEPES buffer with 6 nM of radiotracer (^{177}Lu -DOTATOC) for 60 minutes at 37°C. To determine nonspecific, specific uptake, cells were incubated with excess of unlabeled peptide. Cellular uptake was stopped by removing medium from the cells, followed by washing twice with 2 mL PBS. The radioactivity associated with the final pellet was counted using a Wallace Wizard 1480 automatic gamma counter.

Cell cycle studies

Cells from cohort 2 and control cells were re-suspended with 5 mL PBS, centrifuged, re-suspended as single cell suspension in 0.5 mL PBS, fixed in tubes containing 4.5 mL cold 70% ethanol and stored at -20°C. On the day of cell cycle experiments the cells were centrifuged and washed once with 5 mL PBS, re-suspended in 1mL propidium iodide solution containing Triton-X 100 and RNAase and incubated at 37°C for 20 minutes. Cell cycle was analyzed using a FACSCalibur™ flow cytometer (10,000 events/sample) and Cell Quest™ Pro software (BD Biosciences, CA, USA).

Cell viability studies

Cells from cohort 2 and control cells were incubated with 37 kBq of ^{177}Lu -DOTATOC, ^{177}Lu -DOTA and equimolar DOTATOC. After appropriate incubation times, cell viability was evaluated using the CellTiter-Glo® Luminescent Cell Viability Assay (Promega, Madison, WI), a homogeneous method for determining the number of viable cells in culture based on ATP quantification, which reflects the presence of metabolically active cells. For the experiment, 5,000 cells (100 µL) were cultured in opaque-walled 96 well plates. After 24 and 48 hours of incubation, the plate was equilibrated at room temperature for approximately 30 minutes. CellTiter-Glo® reagent equal to the volume of the cell culture medium was added and the contents of the plate were mixed on a shaker for 2 minutes to induce cell lysis. The plate was then incubated

for 10 minutes at room temperature to stabilize the luminescence signal. The luminescence was recorded using Tecan-Genios Magellan plate reader (Durham, NC, USA).

Apoptosis studies

Cells from cohort 2 and control cells were incubated with 37 kBq of ¹⁷⁷Lu-DOTATOC, ¹⁷⁷Lu-DOTA and equimolar DOTATOC and after appropriate incubation times, apoptosis was measured using The Cell Death Detection ELISA^{PLUS} 10X (Roche Applied Sciences, Indianapolis, IN, USA) as previously described [13].

Statistical Analysis

Experiments were performed in triplicates. All numerical data were expressed as the mean of the values ± the standard error of mean (S.E.M). Graphpad Prism version 4 (San Diego, CA, USA) was used for statistical analysis and a *p* value < 0.05 was considered statistically significant.

Results

Preparation of radiolabeled peptide

¹⁷⁷Lu-DOTATOC and ¹⁷⁷Lu-DOTA were prepared with radiochemical purities ≥ 95% and incorporation yields ≥ 99 % as determined by HPLC and ITLC, respectively as previously reported [5].

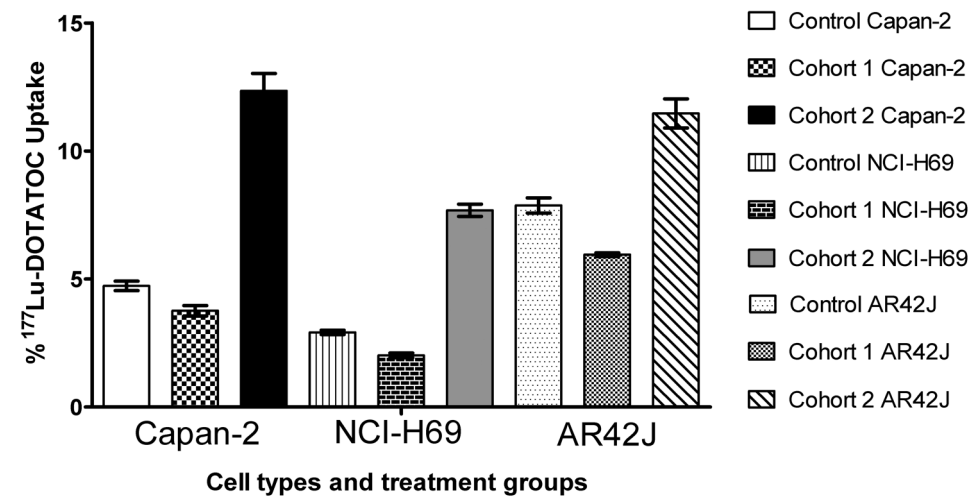


Figure 1- Somatostatin-receptor targeted radioligand-uptake studies: Effects of gemcitabine treatment from cohort 1 and 2 on human pancreatic adenocarcinoma Capan-2, human small cell lung carcinoma NCI-H69 and rat pancreatic carcinoma AR42J cells resulting in either decreased or increased uptake of ¹⁷⁷Lu-DOTATOC when compared to untreated control cells.

Radioligand receptor-uptake studies

To evaluate the effects of gemcitabine on ¹⁷⁷Lu-DOTATOC uptake tosstr direct cell-uptake studies were performed. As observed in Fig. 1 the percent ¹⁷⁷Lu-DOTATOC uptake ranged from 2.9 to 7.9% for gemcitabine untreated Capan-2, untreated NCI-H69 and untreated AR42J controls. ¹⁷⁷Lu-DOTATOC uptake, and presumably the available receptor binding sites, decreased in cohort 1 and increased in cohort 2. For cohort 1, ¹⁷⁷Lu-DOTATOC uptake for Capan-2 was decreased from 4.7 ± 0.2 (n=10) to 3.8 ± 0.2 (n=4) [*p* < 0.05], for NCI-H69 from 2.9 ± 0.1 (n=8) to 2.0 ± 0.1 (n=4) [*p* < 0.001] and for AR42J from 7.9 ± 0.2 (n=8) to 6.0 ± 0.1 (n=4) [*p* < 0.05]. Whereas, for cohort 2, ¹⁷⁷Lu-DOTATOC uptake increased to 12.3 ± 0.7 (n=6) [*p* < 0.001] for Capan-2 cells, to 7.7± 0.3 (n=4) [*p* < 0.001] for NCI-H69 cells and to 11.5 ± 0.6 (n=4) [*p* < 0.001] for AR42J cells.

Cell cycle studies were performed to evaluate the role of gemcitabine as a radiosensitizer through modulation of the cell cycle. For control Capan-2 cells (Fig. 2A), approximately 8% of the total cell population (taken as the sum of G₁/G₀, S and G₂/M) was in the G₂/M phase as compared to approximately 84% of the cell population for the gemcitabine pretreated Capan-2 cells from cohort 2 (Fig. 2B). Similarly for untreated NCI-H69 cells, approximately 20% of the cell population was in G₂/M as compared to approximately 54% for gemcitabine pretreated cells from cohort 2.

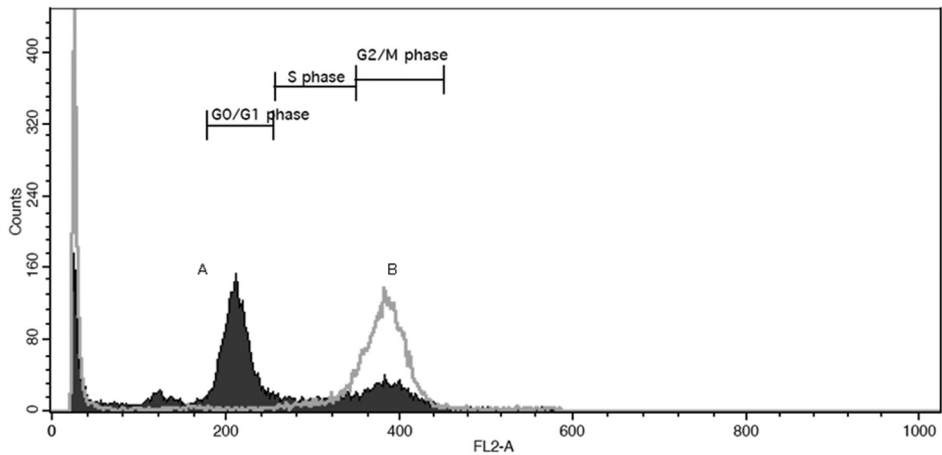


Figure 2- Cell cycle analysis: Representative cytogram of gemcitabine-induced effect on human pancreatic adenocarcinoma Capan-2 cells (gray border with no fill, labeled as B) resulting in an increased fraction of cells in G₂/M phase as compared to the untreated control cells (black border with fill, labeled as A).

Cell viability and apoptosis

Cell viability and apoptosis experiments were performed on untreated control cells and the cells from cohort 2 due to increased uptake of ¹⁷⁷Lu-DOTATOC and presumably increased absorbed radiation dose from the same amount of added radioactivity. As shown

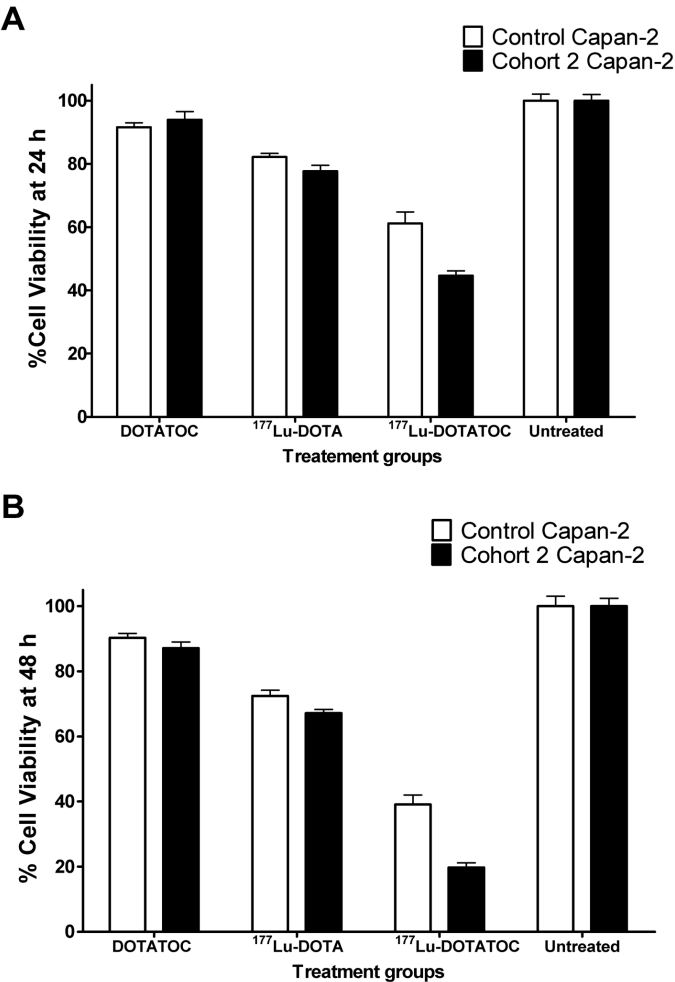


Figure 3- Cell viability studies: Decreased cell viability of human pancreatic adenocarcinoma Capan-2 cells from cohort 2 when treated with sstr-targeted ^{177}Lu -DOTATOC after 24 hour (A) and 48 hour (B) incubation. The data is expressed as mean \pm S.E.M., $n \geq 3$.

in Fig. 3A, following 24 hour incubation with ^{177}Lu -DOTATOC there were 1.5 times more viable cells in Capan-2 cells compared to gemcitabine treated cells from cohort 2. After 48 hour incubation with ^{177}Lu -DOTATOC, there was approximately twice as many viable cells in untreated control Capan-2 cells than gemcitabine pre-treated cells from cohort 2 (Fig. 3B). For untargeted ^{177}Lu -DOTA, the effects of gemcitabine were less pronounced and equimolar non-radioactive DOTATOC did not have significant effects on cell viability when compared to control cells (Fig. 3).

In the apoptosis study, after a 72 hour incubation with ^{177}Lu -DOTATOC, the release of apoptosis specific mono- and oligonucleosomes was 2.5 times higher in gemcitabine

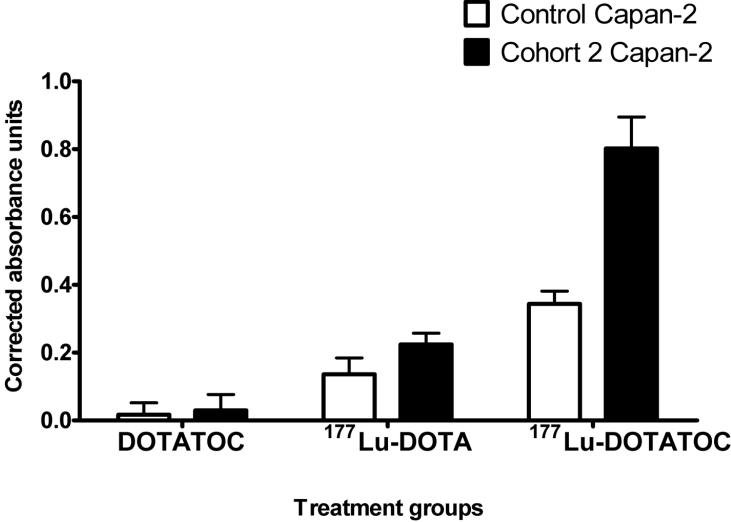


Figure 4- Apoptosis studies: Increased apoptosis of human pancreatic adenocarcinoma Capan-2 cells from cohort 2 when treated with sstr-targeted ^{177}Lu -DOTATOC after 72 hour incubation. The data is expressed as mean \pm S.E.M., $n \geq 3$.

treated Capan-2 cells from cohort 2 than in gemcitabine untreated cells (Fig. 4). In contrast, after a 72 hour incubation with ^{177}Lu -DOTA, the release of apoptotic specific mono- and oligonucleosomes was 1.5 times greater in gemcitabine treated Capan-2 cells from cohort 2 than in untreated cells.

Discussion

Cancer represents a major challenge to oncologists because of its chemoresistant and metastatic nature and dismal outcomes. In the past decade tremendous progress has been made in the field of sstr-targeted radionuclide therapy. However, the success of this therapy in routine clinical use in the United States has been limited due to the concerns of toxicity and relatively high relapse rates with radiolabeled DOTATOC [1, 18-20]. In addition, the standard treatment option of single-drug chemotherapy has yielded limited success due to low rates of complete remission and chemoresistance [21]. There is a growing consensus that the future of cancer treatment for solid tumors lies in a multi-modality approach [14, 21-23].

In this project we have evaluated the combination of gemcitabine and ^{177}Lu -DOTATOC for potential treatment of sstr-expressing carcinomas. It was previously reported that gemcitabine pre-treatment increased the high-affinity and low-affinity binding sites for ^{111}In -DOTA-Lanreotide binding to human pancreatic carcinoma cells [8]. In our study, we found

that gemcitabine treatment alone (cohort 1) decreased ^{177}Lu -DOTATOC uptake whereas gemcitabine followed by recovery period (cohort 2) increased ^{177}Lu -DOTATOC uptake by a factor of 1.5-3 in Capan-2, NCI-H69 and AR42J cells (Fig. 1). Cell cycle studies performed on gemcitabine-treated cells from cohort 2 demonstrated the cell cycle modulation in which most of the viable cells were in G₂M phase (Fig. 2). This cell cycle modulation can be critical for radiation therapy as the G₂M has been shown to be the most radiosensitive phase of the cell cycle and therefore, will produce greater radiation-induced cell damage and death [9]. As observed in the cell viability and apoptosis studies, the gemcitabine-treated cells from cohort 2 exhibited decreased cell viability and increased apoptosis upon treatment with ^{177}Lu -DOTATOC (Fig. 3 and 4). In a previously published report [24], measuring ATP levels, as a cell viability assay, was compared to the clonogenic survival assay. This study revealed no significant difference between the two methods for determining survival fractions upon exposure to radiation using five different cervical carcinoma cell lines. However, considering the observed two-fold increase in ^{177}Lu -DOTATOC uptake and the accumulations of cells in G₂M, the most radiosensitive cell phase, one might expect a more pronounced effect of ^{177}Lu -DOTATOC than the one observed in this study. In our studies, the cell number was kept constant for untreated control cells and gemcitabine-treated cells. Gemcitabine by itself decreased the cell number by 15-30% depending upon cell type by decreasing proliferation and increasing cell death. Therefore, if the therapeutic effect is determined on initial population of cells plated (at day zero) is considered then the synergistic effects of the combination are potentially far greater than those presented in this study. Similar observations of sstr-up-regulation following irradiation have been reported *in vitro* and *in vivo* [25-27]. In CA20948 tumor-bearing rats, injected with 185 MBq of ^{111}In -DOTATATE, a nearly two-fold increase in the sstr density was observed in escaped tumor cells upon re-growth [26]. Similarly, upon 185 MBq of ^{177}Lu -DOTATATE injection to CA20948 tumor-bearing rats, there were significant decreases in sstr expression after therapy although tumors escaping from therapy showed 2-5 times higher expression of sstr as compared to controls [25]. These observations highlight the complex cellular and molecular role of somatostatin of in cell survival, response to DNA damage and repair.

In this study, we used a chemotherapeutic agent that essentially mimics DNA damage and may induce the same repair signaling pathways as that resulting from radiation-induced DNA damage. Hypothetically the repair mechanism may play a role in the up-regulation of sstr in response to DNA damage induced by radiation and gemcitabine. The increased accumulation of ^{177}Lu -DOTATOC may result from increased endocytosis of agonist-bound somatostatin receptors, an ATP dependent process. The precise mechanisms of somatostatin receptor regulation are an interesting question and worthy of future investigation at the cellular and molecular level as well as in animal models. Although we have investigated a specific treatment regime, many permutations and combinations of dosing and scheduling would be required to optimize increased *in vivo* accumulation of radiolabeled octreotide in tumors. The ultimate goal of any therapy is to have maxi-

mum therapeutic efficacy with minimal or acceptable toxicity. The dose-limiting factor for ^{177}Lu -DOTATOC or ^{90}Y -DOTATOC used in clinical treatment is renal and hematological toxicity and as a result, lower doses are given resulting in incomplete tumor response. The rational combination of gemcitabine, a first-line treatment option for pancreatic cancer, and sstr-targeted radionuclide therapy may not only improve clinical outcomes but may also decrease renal toxicity as less radioactivity may be required due to higher receptor-mediated accumulation of the radionuclide in the tumor resulting in greater absorbed radiation dose.

In conclusion, gemcitabine pre-treatment up-regulates sstr expression and acts as a radiosensitizer. The combination of gemcitabine and sstr-targeted radiotherapy has a great potential to improve clinical outcomes and merits further study in animal models.

Acknowledgments

This study was performed under the auspices of the U.S. Dept. of Energy, Office of Science, Office of Biological and Environmental Research under contract 7405-ENG-36 (RWA), and Grant DE-FG01-001NE23554 from the U.S Department of Energy (JPN). The cell cycle data was generated in the Flow Cytometry Shared Resource Center supported by the University of New Mexico Health Sciences Center and the University of New Mexico Cancer Center. Technical assistance by Kamalika Nag (University of New Mexico, Albuquerque, NM) in the operation of flow cytometer is appreciated.

References

1 Van Essen M, Krenning EP, De Jong M, Valkema R, and Kwekkeboom DJ. Peptide Receptor Radionuclide Therapy with radiolabelled somatostatin analogues in patients with somatostatin receptor positive tumours. *Acta Oncol*, 2007. 46(6): p. 723-34.

2 Krenning EP, Kwekkeboom DJ, Valkema R, Pauwels S, Kvols LK, and De Jong M. Peptide receptor radionuclide therapy. *Annals N Y Academy of Sciences*, 2004. 1014: p. 234-245.

3 Kwekkeboom DJ, Teunissen JJ, Bakker WH, Kooij PP, et al., Radiolabeled Somatostatin Analog [177Lu-DOTA0,Tyr3]Octreotate in Patients With Endocrine Gastroenteropancreatic Tumors. *J Clin Oncology*, 2005. 23(12): p. 2754-2762.

4 Otte A, Herrmann R, Heppeler A, Behe M, Jermann E, Powell P, et al. Yttrium-90 DOTATOC: first clinical results. *E J Nucl Med*, 1999. 26(11): p. 1439-1447.

5 Nayak TK, Norenberg JP, Anderson TL, Prossnitz ER, Stabin MG, and Atcher RW. Somatostatin-receptor-targeted alpha-emitting (213)Bi is therapeutically more effective than beta(-)-emitting (177)Lu in human pancreatic adenocarcinoma cells. *Nucl Med and Biol*, 2007. 34(2): p. 185-193.

6 Nayak T, Norenberg J, Anderson T, and Atcher R. A comparison of high- versus low-linear energy transfer somatostatin receptor targeted radionuclide therapy in vitro. *Canc Biotherapy & Radiopharmaceuticals*, 2005. 20(1): p. 52-57.

7 Norenberg JP, Krenning BJ, Konings IR, Kusewitt DF, Nayak TK, Anderson TL, et al. 213Bi-[DOTA0, Tyr3] octreotide peptide receptor radionuclide therapy of pancreatic tumors in a preclinical animal model. *Clin Canc Research*, 2006. 12(3 Pt 1): p. 897-903.

8 Fueger BJ, Hamilton G, Raderer M, Pangerl T, Traub T, Angelberger P, et al. Effects of chemotherapeutic agents on expression of somatostatin receptors in pancreatic tumor cells. *J Nucl Med*, 2001. 42(12): p. 1856-1862.

9 Wardman P. Chemical radiosensitizers for use in radiotherapy. *Clin Oncol*, 2007. 19(6): p. 397-417.

10 Latz D, Fleckenstein K, Eble M, Blatter J, Wannenmacher M, and Weber KJ. Radiosensitizing potential of gemcitabine (2',2'-difluoro-2'-deoxycytidine) within the cell cycle in vitro. *Int J Rad Oncol, Biol, Phys*, 1998. 41(4): p. 875-882.

11 Lawrence TS, Chang EY, Hahn TM, Hertel LW, and Shewach DS. Radiosensitization of pancreatic cancer cells by 2',2'-difluoro-2'-deoxycytidine. *Int J Rad Oncol, Biol, Phys*, 1996. 34(4): p. 867-872.

12 Feng L, Achanta G, Pelicano H, Zhang W, Plunkett W, and Huang P. Role of p53 in cellular response to anti-cancer nucleoside analog-induced DNA damage. *Int J of Mol Med*, 2000. 5(6): p. 597-604.

13 Burris HA, 3rd, Moore MJ, Andersen J, Green MR, Rothenberg ML, Modiano MR, et al. Improvements in survival and clinical benefit with gemcitabine as first-line therapy for patients with advanced pancreas cancer: a randomized trial. *J Clin Oncol*, 1997. 15(6): p. 2403-13.

14 Orditura M, Martinelli E, Galizia G, Vitiello F, Fasano M, et al., Chemoradiotherapy as adjuvant treatment of gastric cancer. *Ann Oncol*, 2007. 18 Suppl 6: p. vi133-5.

15 Fields MT, Eisbruch A, Normolle D, Orfali A, et al., Radiosensitization produced in vivo by once- vs. twice-weekly 2',2'-difluoro-2'-deoxycytidine (gemcitabine). *Int J Rad Oncol, Biol, Phys*, 2000. 47(3): p. 785-791.

16 Shewach DS, Hahn TM, Chang E, Hertel LW, and Lawrence TS. Metabolism of 2',2'-difluoro-2'-deoxycytidine and radiation sensitization of human colon carcinoma cells. *Canc Research*, 1994. 54(12): p. 3218-3223.

17 Shewach, D.S. and T.S. Lawrence, Gemcitabine and radiosensitization in human tumor cells. *Investigational New Drugs*, 1996. 14(3): p. 257-263.

18 Forrer F, Uusijarvi H, Storch D, Maecke HR, and Mueller-Brand J. Treatment with 177Lu-DOTATOC of patients with relapse of neuroendocrine tumors after treatment with 90Y-DOTATOC. *J Nucl Med*, 2005. 46(8): p. 1310-6.

19 Lewington VJ. Targeted radionuclide therapy for neuroendocrine tumours. *Endocrine-Related Cancer*, 2003. 10(4): p. 497-501.

20 Lambert B, Cybulla M, Weiner SM, Van De Wiele C, Ham H, Dierckx RA, et al. Renal toxicity after radionuclide therapy. *Rad Research*, 2004. 161(5): p. 607-611.

21 Blackstock AW, Cox AD, and Tepper JE. Treatment of pancreatic cancer: current limitations, future possibilities. *Oncology (Williston Park, N.Y.)*, 1996. 10(3): p. 301-7; discussion: 308-23.

22 Crane CH, Varadhachary G, Pisters PW, Evans DB, and Wolff RA. Future chemoradiation strategies in pancreatic cancer. *Semin Oncol*, 2007; 34:335-46.

23 Blackstock AW and Govindan R. Definitive chemoradiation for the treatment of locally advanced non small-cell lung cancer. *J Clin Oncol*, 2007. 25(26): p. 4146-52.

24 Tam KF, Ng TY, Liu SS, Tsang PC, Kwong PW, and Ngan HY. Potential application of the ATP cell viability assay in the measurement of intrinsic radiosensitivity in cervical cancer. *Gynecol Oncol* 2005;96:765-70.

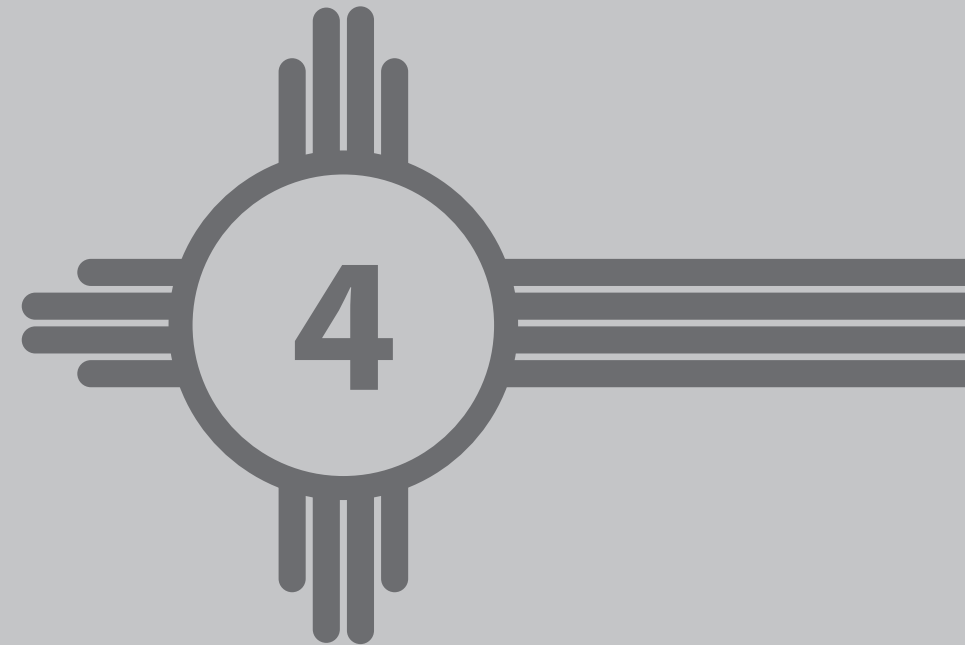
25 Melis M, Forrer F, Capello A, Bijster M, Bernard BF, Reubi JC, et al. Up-regulation of somatostatin receptor density on rat CA20948 tumors escaped from low dose [(177)Lu-DOTA(0),Tyr(3)]octreotate therapy. *Q J Nucl Med Mol Imaging*, 2007. 51(4): p. 324-33.

26 Capello A, Krenning E, Bernard B, Reubi JC, Breeman W, and de Jong M. 111In-labelled somatostatin analogues in a rat tumour model: somatostatin receptor status and effects of peptide receptor radionuclide therapy. *Eur J Nucl Med Mol Imaging*, 2005. 32(11): p. 1288-95.

27 Oddstig J, Bernhardt P, Nilsson O, Ahlman H, and Forssell-Aronsson E. Radiation-induced up-regulation of somatostatin receptor expression in small cell lung cancer in vitro. *Nucl Med Biol*, 2006. 33(7): p. 841-6.

Characterization of a radiolabeled small molecule targeting LFA-1 expression in lymphoma and leukemia

Rahul B. Poria, MS, Jeffrey P. Norenberg, MS, Pharm.D, Tamara L. Anderson, BS, Carston R. Wagner, PhD, Jeffrey B. Arterburn, PhD, Richard S. Larson, MD, PhD



Abstract

Leukocyte function-associated antigen-1 (LFA-1) is constitutively expressed on leukocytes, including over expression on lymphomas and leukemias. We have developed a derivative of BIRT 377, an allosteric inhibitor of LFA-1 which may be chemically tagged without affecting binding. In this study, we modified this derivative (butylamino-NorBIRT) and demonstrated its potential as a non-invasive imaging agent.

Methods: Specific binding of fluorescein-labeled butylamino-NorBIRT to both human and murine cells was demonstrated using equilibrium binding and dissociation techniques. A radiometal, Lutetium-177 (Lu-177), was incorporated into the butylamino-NorBIRT through 1,4,7,10-Tetraazacyclododecane-N,N',N'',N'''-tetraacetic acid (DOTA) as a chelator.

Results: Equilibrium binding experiments demonstrated that fluorescein-labeled butylamino-NorBIRT specifically binds human and murine LFA-1 with affinity constants of 135 nM and 186 nM, respectively. Dissociation kinetic experiments demonstrated an off-rate of 0.168 sec^{-1} on murine cells, consistent with the observed affinity constant. Lutetium-177 was used for labeling, with $\geq 99.99\%$ radiochemical purity and incorporation yield. This radiolabeled derivative exhibited high stability in fetal bovine serum at 37°C over 72 hours. ^{177}Lu -DOTA-butylamino-NorBIRT showed a binding affinity of 235 nM to human LFA-1 for equilibrium binding and competitive binding experiments.

Conclusion: The radiolabeled DOTA-butylamino-NorBIRT may have potential as a non-invasive imaging or therapeutic agent in both human and mouse models.

Introduction

Non-invasive molecular imaging of cancer is a promising area of research with potential for significant clinical impact. The current methods for non-invasive detection of cancer are based on non-specific cellular characteristics such as metabolic activity or growth of mass lesions. Thus, a critical need exists to develop tumor-specific non-invasive imaging agents. This study reports a recently developed small molecule that binds to LFA-1 (CD18, CD11a)¹, a integrin cell surface receptor specifically expressed on leukocytes, lymphoma and leukemia cells.²⁻⁴ The limited expression of LFA-1 on normal white blood cells versus significant overexpression on lymphomatous cells coupled with the observation that lymphomas grow as mass lesions, while reactive processes tend to be diffusely infiltrating, makes LFA-1 an attractive target for non-invasive imaging. Therefore, a radiolabeled small molecule that binds LFA-1 could be employed as a non-invasive imaging agent in several clinical scenarios, particularly to determine if extranodal masses are lymphomatous.

BIRT 377 is a small molecule that interacts specifically with LFA-1 through non-covalent binding to the CD11a chain thereby preventing LFA-1 from binding to its ligand, intercellular adhesion molecule-1 (ICAM-1).⁵ Through a variety of structure-function and molecular derivatization studies, we have developed a derivative of BIRT 377 that binds LFA-1 solely through nonionic interactions.^{5,6} The derivative of BIRT 377, butylamino-NorBIRT, has an alkyl chain with a terminal amine group. In this study, we took advantage of this terminal group by linking fluorescein or DOTA chelating groups. As a first step in exploring the potential of butylamino-NorBIRT as a lymphocyte-specific imaging agent, we studied the affinity of fluoresceinated and Lutetium-177 (^{177}Lu) labeled complexes to both human and mouse cells. Fluorescein-labeled butylamino-NorBIRT has been previously shown to bind to the I domain (located in each leukocyte integrin responsible for ligand binding) of LFA-1 where it inhibits the binding of the ICAM-1 ligand to LFA-1.¹ The radioisotope ^{177}Lu was selected for radiolabeling butylamino-NorBIRT as it is a lanthanide that binds with extremely high stability using the 1,4,7,10-Tetraazacyclododecane-N,N',N'',N'''-tetraacetic acid (DOTA) chelator⁷; it has a long half-life (6.7 days) for radioconjugate development, radiolabeling studies, and serum stability studies; and it can potentially be used for both imaging with its 208 keV gamma emission and therapy with a medium energy 500 keV beta emission. The findings presented here indicate that radiolabeled DOTA-butylamino-NorBIRT may be used as a potential non-invasive imaging and/or therapeutic agent for future *in vivo* studies in mice and humans.

Material and methods

Cell Lines and Reagents

Two cell lines, HL-60 human promyelocytic leukemia cell line and EL-4 mouse lymphoma cell line (American Tissue Culture Corporation) were grown in RPMI-1640 media supplemented with 2 mM L-glutamine, 100 units/mL penicillin, 100 µg/mL streptomycin, 10 mM 4-(2-hydroxyethyl)-1-piperazineethanesulfonic acid (HEPES) pH 7.4, and 10% heat-inactivated fetal bovine serum (FBS). Both cell lines were cultured at 37°C in a humidified atmosphere of 5% CO₂ and 95% air. The FITC anti-human CD11a and anti-mouse CD11a were purchased from Immunogen, Inc. and Caltag laboratories, respectively. The 1,4,7,10-tetraazacyclododecane-1,4,7,10-tetraacetic acid mono(*N*-hydroxysuccinimide ester) (DOTA-NHS) was purchased from Macrocyclics. ¹⁷⁷Lu was purchased from the University of Missouri Research Reactor Center.

Synthesis of DOTA-butylamino-NorBIRT

1-(*N*-Fluoresceinylthioureidobutyl)-[5R]-(4-bromobenzyl) - 3-(3, 5-dichlorophenyl)-5-methyl-imidazolidine-2, 4-dione, Triethylammonium salt (FBA-NorBIRT) was produced as previously described.¹ Synthesis of the DOTA-butylamino-NorBIRT conjugate was carried out as follows - A solution of (R)-1-(4-aminobutyl)-5-(4-bromobenzyl)-3-(3,5-dichlorophenyl)-5-methylimidazolidine-2,4-dione (butylamino-NorBIRT) (3.5 mg, 7 mmol) in dry dimethylformamide (20 mL) was placed in a conical glass closed vial equipped with a magnetic stirrer and was cooled to 0°C. The DOTA-NHS (3.5 mg, 7 mmol) was added, followed by triethylamine (6 mL, 42 mmol). The reaction mixture was allowed to warm to room temperature and was stirred for 12 hours. The reaction mixture was concentrated *in vacuo*, and the residue was washed with 0.5 mL of water, twice. The product was recovered by filtration, washed with water and dried under high vacuum to provide a white powder (5.7 mg, 6.4 mmol, 92% yield). Quality control was achieved by mass spectrometry-electrospray ionization (MS-ESI) and nuclear magnetic resonance (NMR).

Radiolabeling of DOTA – butylamino-NorBIRT with ¹⁷⁷Lu

DOTA-butylamino-NorBIRT (10 µL; 0.565 mM in ultrapure water) was mixed with ¹⁷⁷LuCl₃ solution buffered to pH 5-6 using 3 M ammonium acetate. The reaction mixture was heated at 100°C for 20 minutes. Fifty microliters of the reaction mixture was added to 200 µL of 4.0 mM diethylenetriaminepentaacetic acid (DTPA) solution for quality control. Incorporation yield was assessed by Instant Thin Layer Chromatography (ITLC) on Silica Gel strips (Gelman Sciences, Inc.) with 0.9% NaCl solution as the mobile phase. The strips were scanned using a thin-layer chromatography imaging scanner (AR-2000, BioScan®) to obtain the labeling yield. The radiochemical purity of ¹⁷⁷Lu-DOTA-butylamino-NorBIRT was assessed by Reverse Phase-High Performance Liquid Chromatography (HPLC) (Thermo Separations Products) and a radiometric detector (gamma-ram, INUS Systems Inc.). The radiolabeled compound was injected on a C-18 column (Waters®), and was eluted using an isocratic system starting at 85% Buffer A (0.1% trifluoroacetic acid in HPLC water)

and 15% Buffer B (100% Acetonitrile) for 5 minutes, and then a step gradient 85%A and 15%B initially and ending at 10% Buffer A and 90% Buffer B for 30 minutes. All HPLC was performed at the flow rate of 1 mL per minute for a total of 35 minutes.

In Vitro stability of ¹⁷⁷Lu-DOTA-butylamino-NorBIRT

To test the stability of the compound *in vitro*, ¹⁷⁷Lu-DOTA-butylamino-NorBIRT was incubated in fetal bovine serum (FBS) at 37°C at 1, 6, 24, 48, and 72 hours. The radiochemical stability (in terms of radiochemical purity) of the compound was determined by HPLC at multiple time points as described above. The HPLC conditions are described above.

Equilibrium binding of Butylamino-NorBIRT

For equilibrium binding studies of fluorescent butylamino-NorBIRT (FBA-NorBIRT), human HL-60 cells and murine EL-4 cells were incubated with a range of concentrations (1-500 nM) of the FBA-NorBIRT in the presence or absence of 1 mM MnCl₂ (Mn²⁺ ions stimulate LFA-1 receptors to their high affinity state) as previously described.¹ Non-specific binding was determined with a 500-fold excess of NorBIRT. Incubations were performed for 60 minutes on ice (4°C). Analysis was performed with a FACScan (Becton-Dickinson), and 7500 events were acquired. The data were analyzed to determine the affinity constant (K_d) from the binding curve generated by Graphpad Prism® 4 software. The experiments were repeated thrice in duplicate. For the saturation binding of ¹⁷⁷Lu-DOTA-butylamino-NorBIRT, human HL-60 cells were treated with a range of concentrations (1-400 nM) of the radiolabeled butylamino-NorBIRT and non-specific binding was determined with a 500-fold excess of NorBIRT. Incubations were performed for 60 minutes on ice (4°C). Cells were centrifuged and then separated from the supernatant. The cells were rinsed with phosphate-buffered saline before the cellular radioactivity was measured with a gamma counter (Wallac Wizard 1480) to remove any unbound radioactivity, and the counts per minute (CPM) were recorded for each sample. The CPM data was analyzed to determine the K_d from the binding curve generated with GraphPad Prism® 4.

Kinetic Analysis of FBA-NorBIRT binding and dissociation on Murine cells

EL-4 cells (1 x 10⁶/mL) were incubated with 400 nM FBA-NorBIRT for 60 minutes on ice (4°C) with 500 rpm stirring. The samples were analyzed using a FACS acquisition. A baseline was established prior to treatment with a 500-fold excess of block (FBA-NorBIRT). Addition of the block initiated dissociation of the FBA-NorBIRT. Dissociation (off-rate) kinetics were obtained by converting the resultant data to mean channel fluorescence (MCF) over time using FACSQuery software developed by Dr. B. Edwards (University of New Mexico). Curve fits were performed using GraphPad Prism® 4. The experiments were carried out in duplicates and replicated twice.

Competition binding of ^{175}Lu -DOTA- butylamino-NorBIRT on HL-60 cells

Non-radioactive lutetium (^{175}Lu) was incorporated into DOTA- butylamino-NorBIRT in the same manner as the ^{177}Lu . For competition binding experiments, HL-60 cells were incubated with a range of ^{175}Lu -DOTA- butylamino-NorBIRT concentrations (0-10000 nM) for 60 minutes on ice (4°C). The cells were then incubated with FBA-NorBIRT (50 nM) for 30 minutes on ice (4°C). Analysis was performed on a FACScan and 7500 events were acquired. The data was plotted and the inhibitory constant (EC_{50}) was determined from the binding curve generated with GraphPad Prism® 4.

Results

Product

Product analysis was determined using MS-ESI where the calculated mass to charge ratio (M/Z) for molecular ion (M) for $\text{C}_{37}\text{H}_{47}\text{BrCl}_2\text{N}_7\text{O}_9$ was 884.20 and the obtained value was 884.08. Proton nuclear magnetic resonance showed the following results: (CD_3OD , 400 MHz) δ 1.52-1.9

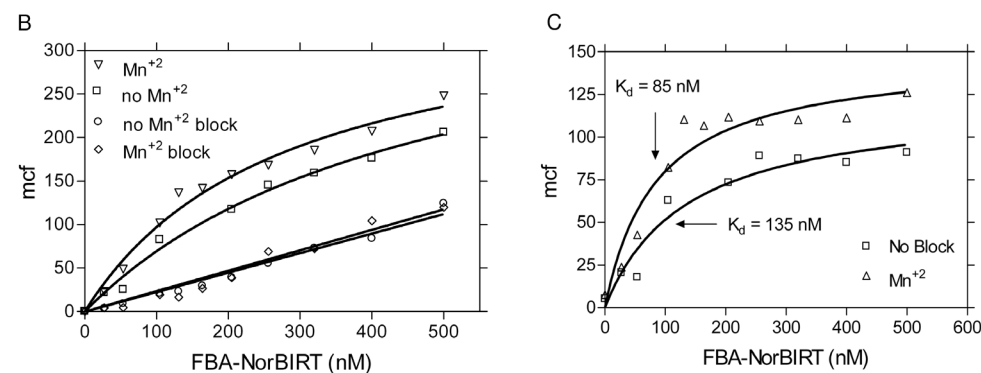
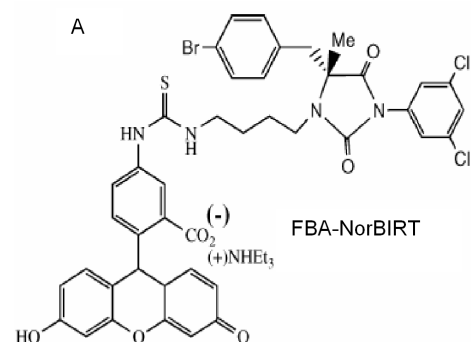


Figure 1 – Equilibrium binding of FBA-NorBIRT to human cells. (A) Chemical structure of fluorescein-labeled butylamino-NorBIRT (FBA-NorBIRT). (B) Equilibrium binding experiments using HL-60 cells treated with a range of concentrations (1-500 nM) of FBA-NorBIRT in the presence and absence of 1 mM MnCl_2 and over one hour of incubation on ice. Non-specific binding was determined using a 500-fold excess of unlabeled NorBIRT. The total binding in the presence and absence of 1 mM Mn^{2+} and non-specific binding were obtained by graphing the mean channel fluorescence (MCF), obtained from FACScan (Becton-Dickinson) using GraphPad Prism® 4 software. (C) Specific binding curves in the presence and absence of Mn^{2+} (1 mM) were generated by subtracting the MCF of the blocked samples from the total fluorescence at each respective concentration of FBA-NorBIRT. All the samples were run in parallel. Representative data of two experiments is shown.

(m, 4H); 1.67 (s, 3H); 2.67 (s, 2H); 2.95-3.75 (m, 28H); 6.84-6.87 (m, 2H); 7.00-7.05 (m, 2H); 7.40-7.46 (m, 3H).

Equilibrium binding to live cells using Fluorescein-butylamino-NorBIRT

The FBA-NorBIRT (Fig. 1A) binding on the human leukemic cell line HL-60 was selected to confirm the K_d on human cells. The total and non-specific binding data were similar to those observed by Larson et. al.¹ (Fig. 1A & 1B). The K_d obtained for FBA-NorBIRT was 135 nM ($R^2=0.95$, Fig. 1C). FBA-NorBIRT had a slightly higher K_d of 85 nM ($R^2=0.93$, Fig. 1C) after stimulation with 1mM Mn^{2+} .

We next examined whether FBA-NorBIRT could bind with relatively high affinity to murine LFA-1 (Fig. 2). To evaluate FBA-NorBIRT as a potential imaging agent in murine models, we performed equilibrium binding studies with increasing concentrations of FBA-NorBIRT (Fig 2). The K_d

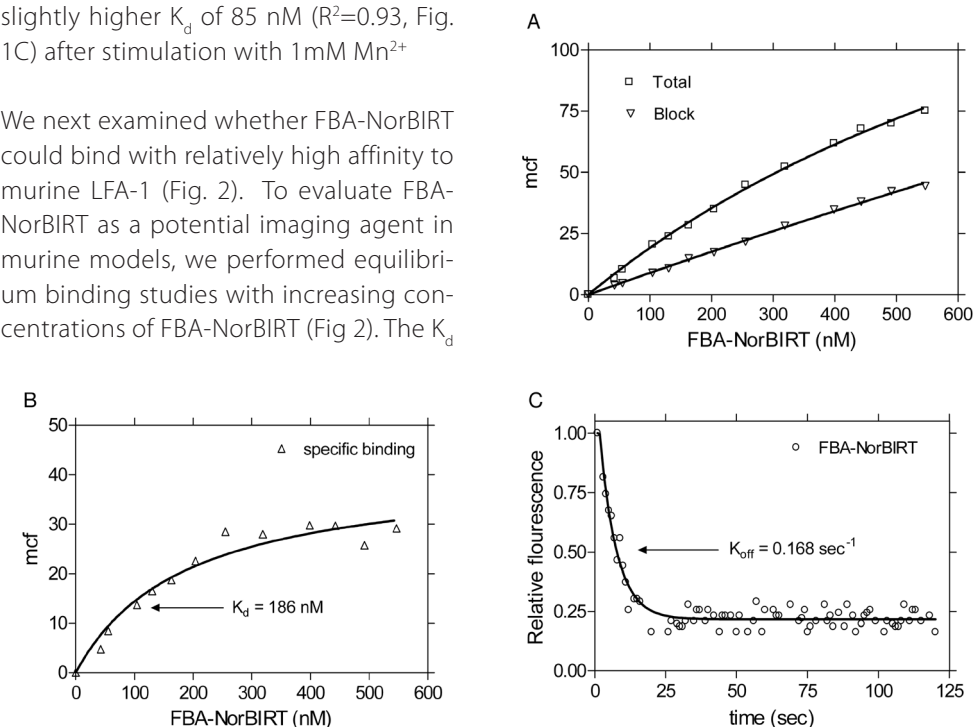


Figure 2 – Equilibrium binding and off-rate kinetics of FBA-NorBIRT to murine cells. (A) Equilibrium binding experiments using EL-4 cells treated with a range of concentrations (1-550 nM) of FBA-NorBIRT with an hour of incubation on ice. Non-specific binding was determined using a 500-fold excess of unlabeled NorBIRT and the same incubation conditions. The total binding and non-specific binding were obtained by graphing the mean channel fluorescence (MCF), obtained from FACScan (Becton-Dickinson) on GraphPad Prism® 4. (B) Specific binding curves were generated by subtracting the MCF of the blocked samples from the total fluorescence at each respective concentration of FBA-NorBIRT. All the samples were run in parallel. The data is expressed as the mean of three experiments. (C) Kinetic off-rate of FBA-NorBIRT experiments using EL-4 cells ($1 \times 10^6 \text{ mL}^{-1}$) incubated with 400 nM FBA-NorBIRT over ice for an hour with 500 rpm stirring. Flow cytometric analysis was performed continuously for up-to 1000 seconds. The samples were analyzed for 50-240 seconds to establish a smooth baseline, and then treated with 500-fold excess of block (NorBIRT) and FACS acquisition was immediately re-established, losing 5-10 seconds of the total time course. On addition of the block, dissociation of the FBA-NorBIRT followed. Dissociation (off-rate) kinetics was obtained by converting the resultant data to mean channel fluorescence over time using FACSQuery software developed by Dr. B. Edwards (University of New Mexico). Curve fits were performed using GraphPad Prism® 4. Representative data of three experiments is shown.

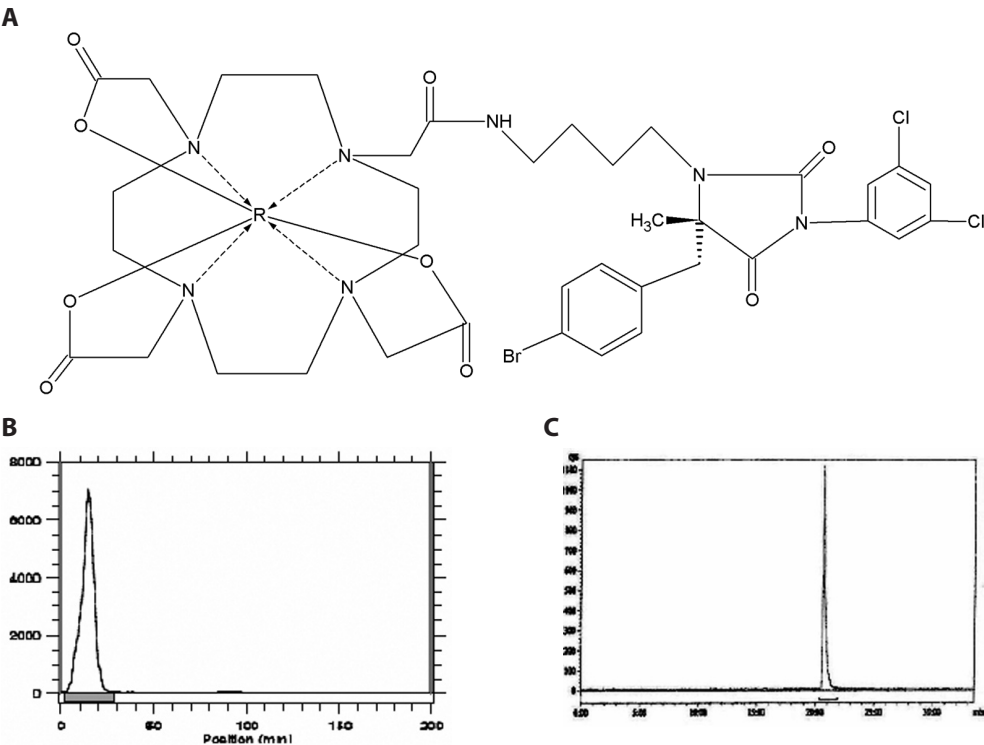


Figure 3 – Radiolabeling of DOTA–butylamino-NorBIRT. (A) Chemical Structure of ¹⁷⁷Lu-DOTA-butylamino-NorBIRT. {4-[5-(4-Bromo-benzyl)-3-(3,5-dichloro-phenyl)-5-methyl-2,4-dioxo imidazolidin-1-yl]-butyl-ammonium–DOTA–¹⁷⁷Radiometal}. (B) ITLC chromatogram showing > 99% incorporation yield of ¹⁷⁷Lu-DOTA-butylamino-NorBIRT. (C) HPLC chromatogram with a single radiometric peak, indicating ≥ 99.99% radiochemical purity of the ¹⁷⁷Lu-DOTA-butylamino-NorBIRT. For ITLC, the activity at the origin and the solvent front was determined with the AR-2000 (Bioscan) yielding peaks for the conjugated radiometal (origin) and free radiometal (solvent front).

for FBA-NorBIRT on the murine cell line EL-4 was 186 nM ($R^2=0.95$, Fig. 2A, B). Interestingly, there was no effect of the activator Mn^{2+} on the binding affinity of FBA-NorBIRT to murine LFA-1 (data not shown). The equilibrium binding results were further confirmed by studying the dissociation characteristics of FBA-NorBIRT (Fig. 2C). A rate constant of dissociation (K_{off}) of 0.168 sec^{-1} was observed for FBA-NorBIRT. Assuming a rate constant of association (K_{on}) value ($1\times10^{-6}\text{ M}^{-1}\text{ sec}^{-1}$) which appears to be relatively constant for small molecules¹, and the observed K_{off} of 0.168 sec^{-1} a K_d of 168 nM is predicted. This predicted K_d is in agreement with the observed K_d (186 nM) measured by equilibrium binding. (see Table 2 for equations).

Populations of receptors are typically associated with heterogeneity in their affinity state. To verify the receptor affinity state for LFA-1 on murine lymphoma cells (EL-4), the kinetic analysis of the dissociation of the fluorescent probe was used. The dissociation kinetics of FBA-NorBIRT fit a single exponential curve (Fig. 2C). The above observation together with

Table 2 – Kinetic data equation

Kinetic data Equation
$K_d=K_{off}/K_{on}$

Where K_d = affinity constant, K_{off} = rate constant of dissociation, K_{on} = rate constant of association and observed K_d = observed association rate constant.

the results from the equilibrium binding of FBA-NorBIRT on EL-4 and HL-60 cells, confirm the homogeneity of the affinity state of LFA-1 receptors on the cell surface and a uniform association rate for the FBA-NorBIRT towards LFA-1.

Radiolabeling of DOTA – butylamino-NorBIRT with ¹⁷⁷Lu

¹⁷⁷Lu into DOTA-butylamino-NorBIRT (Fig. 3A) demonstrated an incorporation yield ≥ 99.99% (n=3) as determined using ITLC (Fig. 3B) with a specific activity of 15 MBq/μg. The radiochemical purity of the labeled compound was assessed by HPLC where a single radiometric peak was observed with a retention time of 20.8 minutes (Fig. 3C), indicating radiochemical purity ≥ 99.99%.

In Vitro stability studies for ¹⁷⁷Lu-DOTA-butylamino-NorBIRT

The radiolabeled butylamino-NorBIRT showed less than 2% degradation after 72 hours of incubation at 37°C (see Table 1).

Table 1 –In Vitro Stability study for ¹⁷⁷Lu-DOTA-butylamino-NorBIRT

Time	37°C in FBS -%RCP
1 hour	98.89
6 hour	98.69
24 hour	98.58
48 hour	98.06
72 hour	98.00

Where %RCP= Percent radiochemical Purity

Equilibrium binding and competition binding of ¹⁷⁷Lu-DOTA-butylamino-NorBIRT on live cells

The K_d obtained for ¹⁷⁷Lu-DOTA-butylamino-NorBIRT was 235 nM ($R^2=0.81$, Fig. 4A, B). Competition binding of DOTA-butylamino-NorBIRT and FBA-NorBIRT on LFA-1 expressed on EL-4 were performed in order to confirm specific binding (Fig. 4C). These competitive binding assays were performed by adding a fixed amount of FBA-NorBIRT to each cell sample and an increasing amount of DOTA-butylamino-NorBIRT. An EC_{50} value of 143 nM was observed for DOTA-butylamino-NorBIRT ($R^2=0.97$, Fig. 4C).

Discussion

In this study, we synthesized and characterized ^{177}Lu -butylamino-NorBIRT that binds to leukocyte function-associated antigen-1 (LFA-1) on human and murine leukocytes. Over-expression of LFA-1 on lymphomas and lack of expression on non-hematopoietic cells make it an

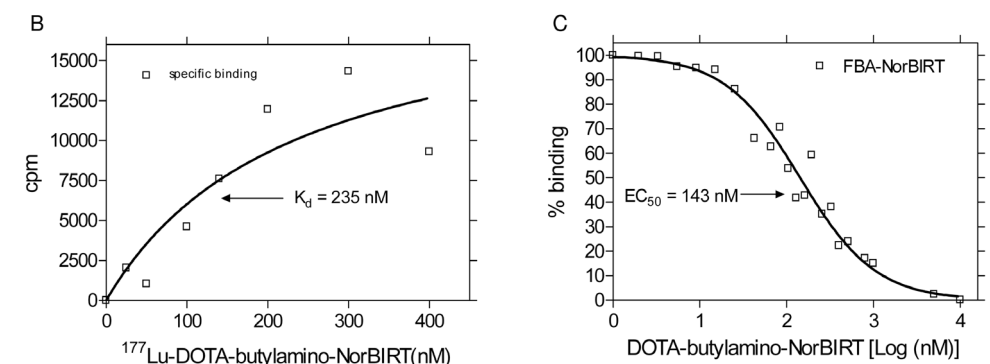


Figure 4 – Equilibrium binding and competition analysis of Lutetium labeled DOTA-butylamino-NorBIRT on HL-60 cells. (A) Equilibrium binding experiments using HL-60 cells treated with a range of concentrations (1–400 nM) of ^{177}Lu -DOTA-butylamino-NorBIRT with an hour of incubation on ice. Non-specific binding was determined using 500-fold excess of unlabeled NorBIRT and same incubation conditions. The total binding (Δ) and non-specific binding (\circ) were obtained by graphing the counts per minute (CPM), obtained from a Wallac Wizard 1480 gamma counter (Wallac) using GraphPad Prism[®] 4. (B) Specific binding curves (\square) were generated by subtracting the CPM of the blocked samples from the total CPM at each respective concentrations of ^{177}Lu -DOTA-butylamino-NorBIRT. All the samples were run in parallel. (C) Representative curve of competition analysis between FBABIRT and DOTA-butylamino-NorBIRT. Aliquots of HL-60 cells were incubated for 1 h on ice with 50 nM FBABIRT and increasing concentrations of DOTA-butylamino-NorBIRT as described in the experimental procedures. The MCF was measured by flow cytometry. The percent binding was calculated according to the following formula: percent binding = (MCF derivative - MCF total block)/(MCF 0 block - MCF total block). The log of the concentration of the DOTA-butylamino-NorBIRT was plotted against the percent binding, and the EC_{50} was calculated using GraphPad Prism[®] 4. Representative data of three experiments is shown.

amenable target for imaging and therapy. Lymphoma, a clonal malignant expansion of leukocytes, typically grows as a tumor. Therefore, the development of a LFA-1 specific radioligand could have significant utility in the non-invasive assessment of an extranodal mass as lymphomatous, a common oncologic scenario.

In previous studies, cross species variation in the interaction of LFA-1 and its ligand ICAM-1 has been shown.⁸ Murine ICAM-1 binds to the human LFA-1, yet murine LFA-1 displayed sub-optimal binding to the human ICAM-1. Thus, it was important to demonstrate that the butylamino-NorBIRT binds mouse as well as human cells. Using fluorescein labeled

ButylaminoNorBIRT, the observed binding affinity was slightly lower for murine LFA-1 (186 nM) in comparison to human LFA-1 (135 nM), but of suitable affinity for imaging agents *in vivo*. Since a comparison of the murine and human sequence homology show an overall 72% identity⁹, the small difference in binding affinity may result from minor structural differences.

We replaced the fluorescein group linked to butylamino-NorBIRT with a chelating group, which allowed introduction of a radiometal. The chelator DOTA was used to incorporate ^{177}Lu , an effective bi-functional chelator with exceptionally high thermodynamic stability and kinetic inertness. The rationale for using Lutetium was its long half life of 6.7 days allowing multiple *in vitro* experiments to characterize LFA-1 targeting and it's ideal for therapeutic applications. Lutetium-177 was successfully incorporated into DOTA-butylamino-NorBIRT with $\geq 99.99\%$ incorporation yield and radiochemical purity. To assess the potential stability of the radiolabel ligand under physiological conditions, ^{177}Lu -DOTA-butylamino-NorBIRT was incubated at 37°C in FBS. Greater than 98% of the radiolabel was retained, even after incubations for 72 hr, implying that the compound is likely to be stable under physiological conditions. In addition, the observed K_d values ranged from 235 to 286 nM when determined by two different approaches, indicating that that the compound should have sufficient affinity for *in vivo* imaging studies. For actual imaging applications, ^{67}Ga , ^{68}Ga , or ^{111}In could be substituted for the ^{177}Lu in order to improve *in vivo* dosimetry.

Lymphoma is a hematologic disease, often disseminated to extranodal sites. Current imaging modalities to stage or determine relapse of lymphoma include CT and MRI scanning coupled with ^{67}Ga -citrate scintigraphy and PET using Fluorine-18 Deoxyglucose (^{18}F -FDG). Not surprisingly, these techniques are prone to give false positive and occasionally false negative results, since they are based on non-specific markers of metabolic activity. Further, gallium scintigraphy is only valid for thoracic or bone examination, since not all active sites/tissues demonstrate ^{67}Ga uptake.^{8, 10} The cellular uptake of ^{18}F -FDG may be significantly lower for some types of lymphomas. In addition, high uptake of FDG can be observed in tissues where the rate of glycolysis is increased due to inflammation, infection or in benign tumor growth¹¹. Further, asymmetric and/or focal uptakes in high metabolically active tissues or lower detection limit to the amount of radioactivity by PET camera, could lead to false negative results. For example, uptake in the neck and upper chest within muscle or adipose tissue may mimic uptake in cervical lymph nodes.¹¹ A tissue specific agent such as butylamino-NorBIRT not only compliments ^{67}Ga and PET imaging, but can also overcome some of their limitations. The development of an accurate imaging agent based on binding to tissue-specific cell types is needed. Radiolabeled- DOTA-butylamino-NorBIRT is a promising targeted radiopharmaceutical for molecular imaging of lymphoma or leukemia.

Currently, monoclonal antibody based radionuclide targeted therapy is available for relapsed or refractory low-grade or follicular, CD20+, B-cell non-Hodgkin's lymphoma (NHL).¹²⁻¹⁴ Non-antibody based targeted therapy could also be applied using molecules such as butylamino-NorBIRT when chelated with alpha or beta emitting radionuclides. The major advantage of small molecules over macromolecules is faster blood clearance. Small molecules may also potentially avoid the infusion reactions and side effects associated with antibody therapy. In addition, radiolabeled-DOTA-butylamino-NorBIRT could be an effective therapeutic agent for a variety of lymphomas, since it specifically targets LFA-1 expressed on both B- and T-cells.³

Conclusion

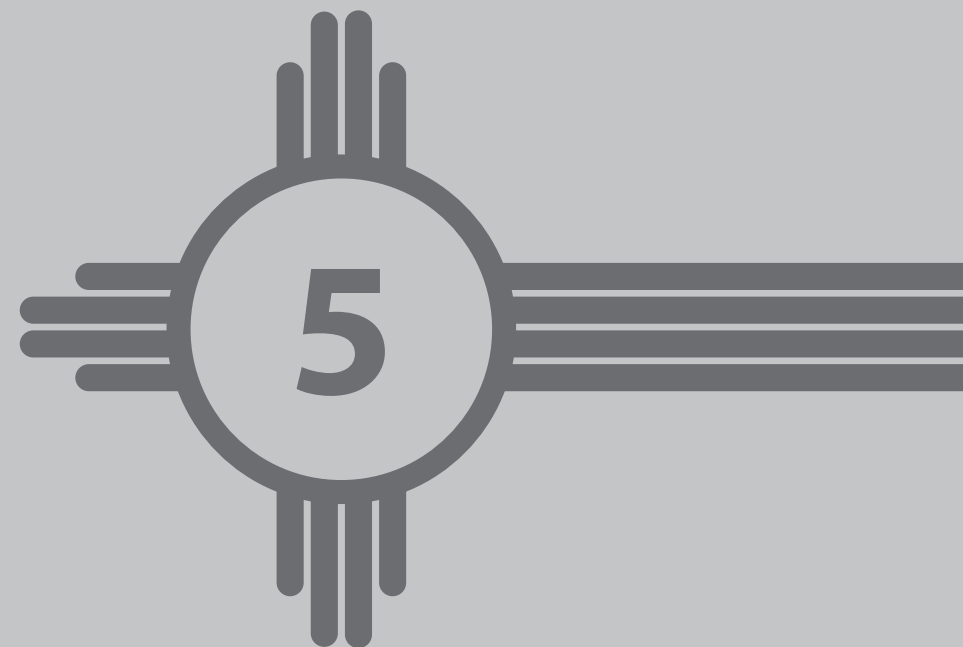
The results presented here indicate that butylamino-NorBIRT and both fluoresceninated and radiolabeled analogs bind to LFA-1 expressed by human and murine cells. Future *in vivo* studies with radiolabeled DOTA-butylamino-NorBIRT in animal models will establish the potential utility of this novel agent for imaging and therapy of lymphoma.

References

1. Larson RS, Davis T, Bologna C, Semenuk G, Vijayan S, Li Y, Oprea T, Chigaev A, Buranda T, Wagner CR, Sklar LA.; Dissociation of I domain and global conformational changes in LFA-1: Refinement of small molecule-I domain structure-activity relationships; *Biochemistry*; 44; 4322 (2005).
2. Inghirami G, Wiecek R, Zhu BY, Silber R, Dalla-Favera R, Knowles DM; Differential expression of LFA-1 molecules in non-hodgkin's lymphoma and lymphoid leukemia; *Blood*; 72;1431; (1988).
3. Horst E, Radaszkiewicz T, Hooftman-den Otter A, Pieters R, van Dongen JJ, Meijer CJ, Pals ST; Expression of the leucocyte integrin LFA-1 (CD11a/CD18) and its ligand ICAM-1 (CD54) in lymphoid malignancies is related to lineage derivation and stage of differentiation but not to tumor grade; *Leukemia*; 5;848 (1991).
4. Bechter OE, Eisterer W, Dirnhofer S, Pall G, Kuhr T, Stauder R, Thaler J; Expression of LFA-1 identifies different prognostic subgroups in patients with advanced follicle center lymphoma (FCL). *Leuk Res*;23; 483; (1999).
5. Kelly TA, Jeanfavre DD, McNeil DW, Woska JR Jr, Reilly PL, Mainolfi EA, Kishimoto KM, Nabozny GH, Zinter R, Bormann BJ, Rothlein R; Cutting edge: A small molecule antagonist of LFA-1-mediated cell adhesion; *J Immunol*;163;5173 (1999).
6. Last-Barney K, Davidson W, Cardozo M, Frye LL, Grygon CA, Hopkins JL, Jeanfavre DD, Pav S, Qian C, Stevenson JM, Tong L, Zindell R, Kelly TA; Binding site elucidation of hydantoin-based antagonists of LFA-1 using multidisciplinary technologies: Evidence for the allosteric inhibition of a protein--protein interaction; *J Am Chem Soc*; 123; 5643; (2001).
7. Schmitt A, Bernhardt P, Nilsson O, Ahlman H, Kolby L, Maecke HR, Forsell-Aronsson E; Radiation therapy of small cell lung cancer with 177Lu-DOTA-Tyr3-octreotate in an animal model; *J Nucl Med*; 45; 1542; (2004).
8. Johnston SC, Dustin ML, Hibbs ML, Springer TA; On the species specificity of the interaction of LFA-1 with intercellular adhesion molecules; *J Immunol*; 145;1181;(1990).
9. Kaufmann Y, Tseng E, Springer TA; Cloning of the murine lymphocyte function-associated molecule-1 alpha-subunit and its expression in COS cells. *J Immunol*; 147;369; (1991).
10. Morton KA, Jarboe J, Burke EM; Gallium-67 imaging in lymphoma: Tricks of the trade; *J Nucl Med Technol*; 28; 221; (2000).
11. Barrington SF, O'Doherty MJ; Limitations of PET for imaging lymphoma; *Eur J Nucl Med Mol Imaging*; 30 Suppl 1; S117; (2003).
12. Panayi GS, Hainsworth JD, Looney RJ, Keystone EC; Panel discussion on B cells and rituximab: Mechanistic aspects, efficacy and safety in rheumatoid arthritis and non-hodgkin's lymphoma; *Rheumatology (Oxford)*; 44 Suppl 2; ii18; (2005).
13. Emmanouilides C; Radioimmunotherapy for non-hodgkin's lymphoma; *Semin Oncol*; 30; 531; (2003).
14. Hainsworth JD, Burris HA 3rd, Morrissey LH, Litchy S, Scullin DC Jr, Bearden JD 3rd, Richards P, Greco FA; Rituximab monoclonal antibody as initial systemic therapy for patients with low-grade non-hodgkin lymphoma; *Blood*; 95; 3052; (2000).

Preclinical Development of a
Neutral, Estrogen Receptor–
Targeted, Tridentate $^{99\text{m}}\text{Tc}(\text{I})$ -
Estradiol- Pyridin-2-yl Hydrazine
Derivative for Imaging of Breast and
Endometrial Cancers

Tapan K. Nayak, Helen J. Hathaway, Chinnasamy Ramesh, Jeffrey B. Arterburn, Donghai Dai,
Larry A. Sklar, Jeffrey P. Norenberg, and Eric R. Prossnitz



Abstract

Breast and endometrial cancers are the most common invasive malignancies in women, with more than 217,000 new diagnoses per year in the United States. These cancers are often classified into 2 subtypes based on the expression of the classical estrogen receptor. In this study, we describe a new structural class of neutral tridentate $^{99m}\text{Tc}(\text{I})$ -estradiol-pyridin-2-yl hydrazine derivatives for potential use in breast and endometrial cancer imaging.

Methods: The $^{99m}\text{Tc}(\text{I})$ -estradiol-pyridin-2-yl hydrazine derivative was synthesized via the Sonogashira cross-coupling reaction and radiolabeled via the tricarbonyl approach. Radiochemical purity was assessed by high-performance liquid chromatography. Cell-binding studies were performed with human breast adenocarcinoma MCF-7 cells. The in vivo biodistribution of the $^{99m}\text{Tc}(\text{I})$ derivative was evaluated in virgin female C57BL/6 mice in defined phases of the estrous cycle. Biodistribution and SPECT/CT studies were performed with mice bearing MCF-7 and primary human endometrial tumors.

Results: Radiochemical analysis demonstrated that the postpurification purity of the $^{99m}\text{Tc}(\text{I})$ -estradiol-pyridin-2-yl hydrazine derivative was 95%, with a specific activity of ^{99m}Tc of 47.5 TBq/mmol. Cell-binding studies yielded a dissociation constant (mean \pm SEM) of 11 ± 1.5 nM. In vivo studies revealed that receptor-mediated uptake was present in all phases of the estrous cycle in reproductive organs and mammary glands but was highest during the diestrous phase of the estrous cycle. Despite high nonspecific uptake in the liver, significant receptor-mediated uptake was observed in target tissues and estrogen receptor–expressing tumors (0.67% for MCF-7 tumors and 0.77% for endometrial tumors.) Tumor uptake was reduced by approximately 50% on coinjection with 17β -estradiol.

Conclusion: We have characterized a novel neutral tridentate $^{99m}\text{Tc}(\text{I})$ -estradiol- pyridin-2-yl hydrazine derivative for potential use in breast and endometrial cancer imaging. This study represents the first step on a path toward the design of estrogen-based Tc-labeled tracers with improved targeting and SPECT imaging characteristics.

Introduction

Over 250,000 new cases of breast, ovarian, and endo-metrial cancers were diagnosed in the United States in 2006 (1). Such cancers are often hormonally regulated and can be divided into 2 subtypes on the basis of whether or not tumor cells express the classical estrogen receptor (ER), ER α . Estrogen promotes cell proliferation and inhibits apoptosis through a complex signaling cascade resulting in transcriptional changes that may include the modulation of tumor suppressor function. The presence of ER α in approximately two thirds of breast cancers correlates with whether the tumors are estrogen dependent or independent (2) and represents one of the best prognostic factors in breast cancer because of the availability of antiestrogens such as tamoxifen and fulvestrant and, more recently, the aromatase inhibitors. With the recent characterization of a novel transmembrane ER, GPR30, in multiple cancer types, the exact causes and mechanisms underlying estrogen dependence and resistance in cancers may be more complex than previously appreciated (3–5). Nevertheless, it is clear that if a cancer can be detected at an early stage and characterized for ER status and metastatic state, then patients can display improved outcome with appropriate treatment (6,7). As a result, in the past decade, greater emphasis has been placed on the development of radio-imaging approaches for breast and other cancers that are based on either SPECT or PET (8). Whole-body imaging is possible with PET and SPECT and therefore offers a non-invasive approach for assessing regional and disseminated cancers.

In 1986, a study involving 547 patients demonstrated the predictive value of determining estrogen-binding activity for the clinical behavior of breast cancer in women (9). Throughout the 1980s, a variety of ^{18}F -labeled estrogen derivatives were tested in animals and shown to demonstrate ER selectivity (10,11). The most successful ^{18}F -labeled estrogen derivative, 16α - ^{18}F - 17β -estradiol (^{18}F -FES), has been evaluated clinically, with promising results for the imaging of estrogen-binding tumors and for predicting the responsiveness of breast tumors to antiestrogen drugs such as tamoxifen (12,13). The role of estrogen in endometrial carcinogenesis has been well documented (14,15), and successful applications of ^{18}F -FES have been reported for endometrial and other gynecologic cancers (16). Subsequent efforts have been directed to developing methods for labeling estrogen imaging agents with the widely available and longer-lived radio-nuclide ^{99m}Tc for SPECT, through both pendant and integrated-chelate approaches (17). Reports have described the generation and use of both steroidal and nonsteroidal estrogen derivatives labeled with ^{99m}Tc (SPECT) and ^{94m}Tc (PET) for ER imaging. However, the agents described to date have demonstrated suboptimal target tissue selectivity in vivo, possibly as a result of the high lipophilicity or rapid metabolism of these agents. The complex chemistry involved in the radiosynthesis of these compounds to obtain high yields and purities has further hampered their development for clinical use (18,19).

We recently described a new class of neutral tridentate rhenium-estradiol-pyridin-2-yl hydrazine derivatives (see Table 1 in the article by Ramesh et al. (20)). These compounds were biologically evaluated by competitive radiometric binding assays with 3H-estradiol to determine their relative binding affinities for ER α and ER β . The relative binding affinities compared favorably with those of the best examples of previously reported estradiol tricarbonyl-Re(I) complexes (8,17,18). Binding to the alternate ER, GPR30, was also shown to be of high affinity. A functional assay based on the rapid receptor-mediated mobilization of intracellular calcium elicited by binding to ER α , ER β , or GPR30 revealed that the alkyne-linked complex yielded the highest levels of receptor activation. It was also previously reported that the substitution of a 17 α -ethynyl group reduced the affinity of estrogen derivatives for α -fetoprotein and sex steroid-binding protein, resulting in more favorable in vivo pharmacokinetics (21,22). In this report, we describe the detailed chemical and biologic evaluation of a $^{99m}\text{Tc}(\text{I})$ -estradiol-pyridin-2-yl hydrazine derivative with an alkyne linkage for the diagnostic imaging of breast and endometrial cancers.

Materials and methods

Radiosynthesis of $^{99m}\text{Tc}(\text{I})$ -Estradiol-Pyridin-2-yl Hydrazine Derivative

The ^{99m}Tc -tricarbonyl complex [$^{99m}\text{Tc}(\text{CO})_3(\text{H}_2\text{O})_3$] $^{+}$ was pre-pared by adding 3.7 GBq of freshly eluted Na- $^{99m}\text{TcO}_4$ to the Isolink kit reagent (Tyco Healthcare, Mallinckrodt) and heating the reaction mixture for 40 min at 100°C. The [$^{99m}\text{Tc}(\text{CO})_3(\text{H}_2\text{O})_3$] $^{+}$ complex was allowed to cool for 20 min on ice. Because of the acid sensitivity of the tertiary propargylic 17 β -alcohol of the estradiol chelate, the alkaline mixture was neutralized to pH 7 with acetic acid. The estradiol-pyridin-2-yl hydrazine derivative was prepared as previously described (20). To generate the radiolabeled complex, the estradiol-pyridin-2-yl hydrazine derivative (10 μg , 21.7 nmol) was added to the neutralized [$^{99m}\text{Tc}(\text{CO})_3(\text{H}_2\text{O})_3$] $^{+}$ complex, and the mixture was stirred for 2 h at room temperature. Heating was avoided to prevent β -elimination of the 17 β -alcohol.

Inorganic impurities from the Isolink kit, aqua ions of ^{99m}Tc (if any) and excess ligand were separated by solid-phase extraction with C-18 SepPak Plus cartridges (Waters). Impurities and excess ligand were eluted with four 0.5-mL aliquots of 40% ethanol in water. Elution of the ^{99m}Tc -labeled estradiol-pyridin-2-yl hydrazine derivative was accomplished with 4x0.5 mL aliquots of 100% ethanol. Reverse-phase high-performance liquid chromatography (HPLC) was performed before and after purification to assess radiochemical purity with a reverse-phase C-18 column (JT Baker) with a g-ram radiometric detector (INUS Systems Inc.). The injection volume was 100 μL , and the ultraviolet (UV) detector wavelength was 254 nm. The mobile phase (solvent A) consisted of 100% HPLC-grade ethanol whereas the stationary phase (solvent B) consisted of 100% HPLC-grade water.

The elution gradient was 60%–70% solvent A over 10 min followed by 70%–100% over 15 min with a flow rate of 1 mL/min. Specific activity was determined from the integrated peak radioactivity (compensating for the elution profile of the ^{99m}Tc generator and the transient equilibrium between the parent and the daughter radionuclides) and the UV absorption with a calibration curve of known quantities of unlabeled compound.

Stability and Transchelation Studies

In separate tubes, the ^{99m}Tc derivative (final ligand concentration, 1 mM) was added to 900 μL of phosphate-buffered saline solution (PBS), mouse serum, 1 mM cysteine solution, 1 mM histidine solution, or 1 mM diethylenetriaminepentaacetic acid (DTPA) solution. The samples were incubated at 37°C and analyzed by HPLC and instant thin-layer chromatography after 1, 3, and 24 h.

Partition Coefficient Studies

Determination of log octanol/water partition coefficient ($P_{(o/w)}$) values was performed by the shake flask method. To a solution containing 200 μL of octanol and 200 μL of water (obtained from a saturated octanol-water solution), 10 mL of 50 nM $^{99m}\text{Tc}(\text{I})$ -estradiol-pyridin-2-yl hydrazine derivative was added. The resulting solution was vortexed at room temperature for 10 min and incubated at 37°C for 1 h. Aliquots (50 μL) were removed from the octanol and from the water phases, and the radioactivity measured in a Wallace Wizard 1480 automatic γ -counter.

Cell Culture

ER α / β - and GPR30-expressing human breast adeno-carcinoma MCF-7 cells (HTB 22; American Type Culture Collection) were cultured in Dulbecco's minimal essential medium containing 10% fetal bovine serum, penicillin at 100 U/mL, and streptomycin at 100 μg /mL. Cells were grown as a monolayer at 37°C in a humidified atmosphere of 5% CO_2 and 95% air.

Receptor-Binding Studies

To evaluate ligand binding to the estrogen receptors expressed in MCF-7 cells, direct binding was performed with the ^{99m}Tc -labeled estradiol derivative. For saturation binding studies, 500,000 cells per tube in tissue culture medium were treated with increasing concentrations of the ^{99m}Tc -labeled estradiol derivative and incubated for 1 h at 37°C. The cells were pelleted and washed 3 times with 1 mL of PBS. The radioactivity associated with the final pellet was counted using a Wallace Wizard 1480 automatic γ -counter. To determine nonspecific binding, the cells were incubated with 10 μM 17 β -estradiol. To establish the affinity of the corresponding Re-labeled derivative (20), which serves as an isosteric nonradioactive surrogate for the ^{99m}Tc -labeled derivative (19,23), cells were treated with a trace amount of the radioligand and competition was performed with increasing amounts of the Re-estradiol derivative. Binding data were analyzed with GraphPad Prism, Version 4 (GraphPad Software, Inc.).

Animal and Tumor Models

Animal use protocols were approved by the University of New Mexico Health Sciences Center Institutional Animal Care and Use Committee. To determine uptake during various stages of the estrous cycle, wild-type mature (8–10 wk old) female C57BL/6 mice (Harlan Inc.) were used. Estrous cycle was determined by cytologic examination of vaginal flushings (24). The mice used in this study were determined to be cycling by examination over 3–5 consecutive days before the day of the experiment.

Estrogen-dependent human breast adenocarcinoma MCF-7 tumors were generated by injecting 2–4 million MCF-7 cells subcutaneously in 8-wk-old female athymic NCr-*nu/nu* mice (NCI- Frederick). One day before injection of the cells, a 60-d release 17β -estradiol pellet (1.7 mg, Innovative Research of America) was implanted subcutaneously. After 6 wk, tumors ranging from 0.6 to 0.9 cm in diameter were observed; at this stage, ovariectomy was performed and the pellet was removed. After a 1-wk recovery period, biodistribution and imaging studies were performed.

The collection and use of human tumor specimens was approved by the Human Research Review Committees at the University of New Mexico Health Sciences Center. Fresh patient endometrial tumor specimens were rinsed with cold sterile PBS and grossly necrotic tissue was trimmed away. The tumor was minced and rinsed with PBS again. Approximately 100 mg of tumor suspended in 100 μL of Dulbecco's minimal essential medium was injected subcutaneously into 8-wk-old female athymic NCr-*nu/nu* mice (25). Xenograft tumors were harvested before any dimension reached 20 mm. The tumor used in this study was shown to be ER-positive by immunohistochemical staining (data not shown).

Biodistribution and SPECT/CT Studies

All mice were injected intravenously (tail vein) with the ^{99m}Tc -labeled estradiol derivative. To determine receptor specificity, 17β -estradiol (5 μg) was coinjected with the radiotracer. At the desired time point, the animals were sacrificed by CO_2 euthanasia. After sacrificing the animals, organs were carefully removed and isolated to determine the biodistribution characteristics of the tracer. The organ samples were weighed and the corresponding localized radioactivity was measured using an automated g-counter after verifying the counting efficiency with standards. The percentage injected dose per gram of tissue (%ID/g) was calculated by comparison with standards representing the injected dose per animal.

SPECT/CT studies were performed using a multi-pinhole SPECT/CT small-animal imager (Bioscan Inc.). Whole-body imaging studies were performed on anesthetized animals using 1.5%–2.0% isoflurane on a temperature-controlled bed. The images were reconstructed, fused and analyzed using the InVivoScope software program (Bioscan Inc.). All animal experiments were conducted in compliance with the guidelines and approved protocols established by the Institutional Animal Care and Use Committee.

Statistical Analysis

All numeric data were expressed as the mean of the values \pm the SEM. Graphpad Prism, Version 4, was used for statistical analysis, and a P value of less than 0.05 was considered statistically significant.

Results

Radiochemical Purity

Preparation of the $[\text{}^{99m}\text{Tc}(\text{CO})_3(\text{H}_2\text{O})_3]^+$ “semiaqua” intermediate was performed yielding a radiochemical purity of $>95\%$ ($n>30$). The starting aqua ion $[\text{}^{99m}\text{TcO}_4]^-$ had a retention time of 0.9 min and the intermediate semiaqua ion precursor had a retention time of 1.4 min. Over 85% of the $[\text{}^{99m}\text{Tc}(\text{CO})_3(\text{H}_2\text{O})_3]^+$ precursor was subsequently incorporated into the estradiol-pyridin-2-yl hydrazine derivative (Fig. 1). The pre-purification radiochemical purity assessed by HPLC was greater than 85% ($n>25$) (Supplemental Fig. 1A) (supplemental materials are available online only at <http://jnm.snmjournals.org>). The two resolved radiometric peaks (4.1 and 5.2 min) likely represent the two diastereoisomeric chelates of the final product based on similar chromatographic profiles of the corresponding Re-labeled derivatives (20). Based on the HPLC analyses (and taking into account the elution profile of the ^{99m}Tc generator and the transient equilibrium between the parent and the daughter radionuclides), the calculated specific activity of the final product was approximately 47.5 TBq of ^{99m}Tc /mmol. The radiochemical purity was further improved to $>95\%$ by solid-phase purification to remove excess ligand and unincorporated $[\text{}^{99m}\text{Tc}(\text{CO})_3(\text{H}_2\text{O})_3]^+$. Typical radiochemical yields after purification ranged from 60% to 80%.

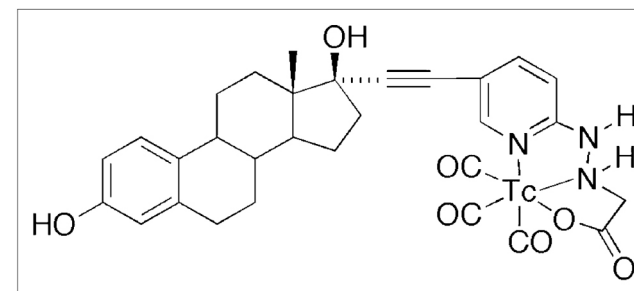


Figure 1. Chemical structure of the $^{99m}\text{Tc}(\text{I})$ -estradiol-pyridin-2-yl hydrazine derivative possessing an alkyne linkage and prepared by the tricarbonyl approach

Stability, Transchelation, and Partition Coefficient Studies

The final $^{99m}\text{Tc}(\text{I})$ -estradiol-pyridin-2-yl hydrazine derivative demonstrated high stability in buffer and mouse serum after 24 h of incubation at 37°C (Table 1). Up to 30% transchelation was observed in the presence of a 1,000-fold molar excess of histidine or cysteine after 24 h of incubation at 37°C . The complex exhibited a $\log P_{(o/w)}$ value of 3.9 ± 0.5 ($n=4$) determined by shake flask method, compared with values of estradiol in the range of 3.3–5 (23).

Receptor-Binding Studies

Direct intact cell-binding studies were performed on ERα/β- and GPR30-expressing human breast adenocarcinoma MCF-7 cells. The ^{99m}Tc(I)-estradiol-pyridin-2-yl hydrazine derivative exhibited a dissociation constant (K_d) of 11 ± 1.5 nM with a calculated maximal number of binding sites (B_{max}) of 1.3x10⁴ ± 0.1x10⁴ sites per cell (Fig. 2A), similar to previous estimates of the number of estrogen-binding sites in these cells (21). The inhibitory concentration of 50% (IC₅₀) of the nonradioactive rhenium conjugate (15 ± 1.4 nM, dissociation constant of an inhibitor [K_i] = 10.3 nM) was similar to the K_d of the ^{99m}Tc-conjugate (Fig. 2B). These values also compare well with our previous determinations with the rhenium conjugate using competition of tritiated estrogen for purified ERα and a fluorescent estrogen for GPR30 in permeabilized cells where the relative binding affinities were 20% and 42%, respectively (20). The diastereoisomeric ^{99m}Tc(I)-estradiol-pyridin-2-yl hydrazine derivatives were separated by HPLC fractionation. Diastereoisomer A (retention time, 4.1 min) exhibited a K_d of 12 ± 2.9 nM, whereas diastereoisomer B (retention time, 5.2 min) exhibited a K_d of 7.7 ± 2.6 nM.

Role of Estrous Cycle

Receptor-mediated uptake was observed in reproductive organs and the mammary gland in all stages of the estrous cycle (Table 2). The highest uptake of the tracer in reproductive organs and the mammary gland was observed in diestrus and the lowest uptake during estrus (Table 2). At 3 h after injection, the uptake in the mammary glands was 0.22 ± 0.02 %ID/g in estrus and increased to 1.31 ± 0.13 %ID/g in metestrus and 3.11 ± 0.24 %ID/g in diestrus. A similar trend of increasing uptake levels from estrus to metestrus and diestrus was found in uterus and ovaries. However, the uptake of the radiotracer by the ovaries was not significantly different between estrus (0.60 ± 0.06 %ID/g) and metestrus (0.76 ± 0.04 %ID/g). As shown in Table 2, in bone, blood, and muscle, the uptake was not receptor mediated because there was no statistically significant difference in the values between unblocked and blocked treatments.

Biodistribution in Non-Tumor-Bearing C57BL/6 Animals in Diestrus

The ^{99m}Tc-estradiol derivative demonstrated significant uptake in ER-expressing organs of interest with robust target tissue-to-muscle ratios in the range of 10:1 and moderate target tissue-to-blood ratios in the range of 1:1. In biodistribution studies, high liver uptake levels of 9.48, 8.34, and 7.84 %ID/g at 1, 3, and 24 h after injection, respectively, probably resulted from high compound hydrophobicity (Table 3). Low uptake in the kidney and bladder at 1 and 3 h after injection suggested excretion occurred slowly via urine. At 3 h after injection, approximately 5–10 %ID was excreted in the feces and less than 2 %ID was excreted in the urine. Urine and blood plasma was collected 3 h after injection and HPLC analysis were performed. No detectable radioactive metabolites were observed in the urine (Supplemental Fig. 1B) or plasma radiochromatograms (Supplemental Fig. 1C).

Biodistribution in Tumor-Bearing Animals

In tumor-bearing animals, in addition to receptor-mediated uptake in the estrogen-binding target organs, the ^{99m}Tc-estradiol derivative also displayed uptake in MCF-7 tumors and human primary endometrial tumors (Fig. 3). As in C57BL/6 mice, high liver uptake values were obtained in animals bearing MCF-7 tumors (Fig. 4) and human primary endometrial tumors. High levels of radioactivity were again found in the feces. The uptake in the blood for MCF-7 tumor bearing animals was 1.25, 2.03, and 0.81 %ID/g at 1, 3, and 24 h after injection, respectively. Similarly, uptake in the blood was 1.27, 1.59, and 1.00 %ID/g at 1, 3, and 24 h after injection, respectively. The target-to-muscle ratios were reasonably high to moderate, ranging from 3.5 to 7.05 over the period of time; however, the target-to-blood ratios were poor and ranged from 0.3 to 1.0 (Table 4). At 3 h after injection, the tumor-to-muscle ratio was 5.67 and the tumor-to-blood ratio was 0.35. The tumor-to-muscle and tumor-to-blood ratios were significantly reduced to 2.64 and 0.19, respectively, when blocking was performed with coinjection of 5 µg of 17β-estradiol.

Table 1 Stability of ^{99m}Tc(I)-Estradiol-Pyridin-2-yl Hydrazine Derivative

Time (h)	% Stability in presence of:				
	1 mM histidine	1 mM cysteine	1 mM DTPA	PBS	C57BL/6 serum
1	88.8 ± 0.7 ^a	89.2 ± 0.4	97.6 ± 0.2	97.4 ± 0.5	97.4 ± 0.6
3	86.9 ± 0.4	84.7 ± 2.2	95.2 ± 0.9	96.1 ± 1.2	95.5 ± 1.1
24	76.3 ± 2.8	68.2 ± 2.7	92.0 ± 4.0	97.3 ± 1.4	93.9 ± 2.3

Samples were incubated at 37°C in 1 mM histidine, 1 mM cysteine, 1 mM DTPA, PBS, and C57BL/6 serum. Stability was assessed by HPLC and instant thin-layer chromatography. Data represent mean ± SEM from 3 determinations.

Imaging Studies

Imaging studies were performed after injecting 18.5 MBq of the ^{99m}Tc(I)-estradiol-pyridin-2-yl hydrazine derivative via the tail vein. Whole-body imaging studies at 60 s per projection were performed under anesthesia with a temperature-controlled bed (36°C–38°C). In this study, very low counts were obtained in tumors and they were only visualized once the image threshold was reduced to 2% maximum intensity. Whole-body imaging studies also revealed high uptake in the liver and intestines (i.e., feces) (82.8% ± 1.9 %ID combined). Uptake in the MCF-7 tumor (3 h after injection) was relatively low (0.078% ± 0.010 %ID) when compared with the background. A focused study at 600 s per projection was performed postmortem for better visualization of the tumor to obtain higher counts. In this study, tumor visualization was better without significantly reducing the %ID scale (Fig. 5). In the reconstructed coregistered SPECT/CT maximum-intensity-projection image (Fig. 5A) and the reconstructed coregistered SPECT/CT sagittal slice (Fig. 5B), the radioactivity in the tumor and the liver can be visualized, whereas in the reconstructed

coregistered SPECT/CT transverse slice (Fig. 5C) the localization of radioactivity can be visualized without any significant background.

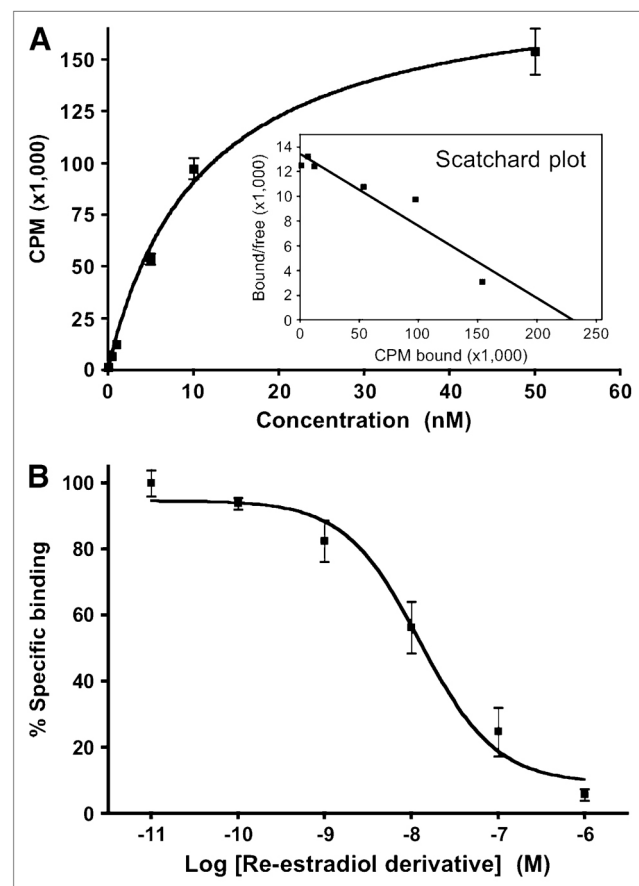


Figure 2. (A) Saturation binding curve with inset Scatchard plot of radioligand receptor-binding studies performed with $^{99m}\text{Tc}(\text{I})$ -estradiol-pyridin-2-yl hydrazine derivative and MCF-7 human breast adenocarcinoma cells. $^{99m}\text{Tc}(\text{I})$ -estradiol-pyridin-2-yl hydrazine derivative had K_d of 11.0 ± 1.5 nM and B_{max} of $1.3 \times 10^4 \pm 0.1 \times 10^4$ sites per cell. (B) Competition binding curve from radioligand receptor-binding studies performed with $^{99m}\text{Tc}(\text{I})$ -estradiol-pyridin-2-yl hydrazine derivative as radio-tracer, corresponding nonradioactive Re-labeled derivative as competitor, and MCF-7 cells. Nonradioactive Re-labeled estradiol-pyridin-2-yl hydrazine derivative had IC_{50} of 15.0 ± 1.5 nM and calculated K_i of 10.3 nM. Values were determined from 3 independent experiments.

labeled estradiol derivatives were modified at the 7 α - and 17 α -positions for incorporation of ^{99m}Tc (18,19). None of these reported steroidal analogs was successful as ideal imaging agents, because of either low binding affinity or the difficulty in preparing ^{99m}Tc -labeled derivatives with high specific activity and yields. However, it was observed that the ana-

Discussion

Advances in molecular and cellular biology are transforming our understanding of basic physiology and pathology; similar advances in molecular imaging technologies now permit dynamic and quantitative studies in vivo with minimal invasiveness. In this study, we have developed a novel γ -emitting estradiol derivative and used it to investigate the interaction with estrogen receptors in defined stages of the estrous cycle in normal animals and also to evaluate its effectiveness in imaging mouse xenograft breast and endometrial tumors with SPECT.

Because of the desirable imaging characteristics of ^{99m}Tc , several groups have prepared ^{99m}Tc -labeled estradiol derivatives as breast cancer imaging agents. Most of the previously described ^{99m}Tc -la-

logs with the best characteristics were those substituted at the 17 α -position. Based on our previous characterization of 17 α -substituted estradiol derivatives with respect to receptor binding and cell activation (20), we surmised that the use of an ethynyl group for linkage at the 17 α -position would enhance receptor binding as well as cell permeability. Incorporation of a pyridyl moiety would allow for the incorporation of a $[\text{}^{99m}\text{Tc}(\text{CO})_3(\text{H}_2\text{O})_3]^+$ group for production of an imaging agent. As a result, we prepared a neutral tridentate $^{99m}\text{Tc}(\text{I})$ estradiol pyridin-2-yl hydrazine derivative using the tricarbonyl approach.

Because of the acid sensitivity of the tertiary propargylic 17 β -alcohol of estradiol, the alkaline mixture was neutralized with acetic acid rather than HCl and heating was avoided to prevent elimination. Direct saturation binding studies were performed with the radioactive ^{99m}Tc -labeled derivative, and competition binding studies were performed with the nonradioactive Re-labeled derivative on human breast adenocarcinoma MCF-7 cells. Performing receptor-binding studies on whole cells with steroidal analogs poses challenges related to ligand equilibrium, the lipophilic nature of the ligand, estimation of free ligand, the processes of receptor activation and degradation, and the presence of multiple estrogen receptor types, including GPR30 (26). As a result, careful consideration is required for data interpretation as one can easily over- or underestimate the K_d . The $^{99m}\text{Tc}(\text{I})$ estradiol pyridin-2-yl hydrazine derivative demonstrated a K_d of 11 ± 1.5 nM on MCF-7 cells, much higher than typically reported values of estradiol itself (~ 0.1 – 1 nM (27)) but comparable to the affinity of estrogen for GPR30 (~ 6 nM (26,28)). Furthermore, this K_d value is consistent with the affinities previously determined for the Re-labeled derivative (20). Because chelate diastereoisomers demonstrated similar binding affinities in vitro, in vivo studies with separated diastereoisomers were not performed. For in vivo evaluation, a mixture of diastereoisomers was injected in mature (8–10 wk old) female C57BL/6 mice in defined stages of estrous cycle. In studies with radiolabeled estrogen derivatives, it has been observed that the maximum uptake in the uterus is achieved during the diestrus phase (29,30); our finding that the highest uptake of ^{99m}Tc -labeled estrogen derivative in uterus, ovaries, and mammary gland occurs during diestrus is consistent with these observations. Circulating estrogens are low during estrus, metestrus, and early diestrus. Then, toward late diestrus and into proestrus, just before ovulation, levels rise significantly. Available estrogen receptor concentration is determined by circulating estrogens, being reduced by ligand binding, but also being upregulated by estrogen-mediated receptor synthesis (31). Thus, at diestrus the combined conditions of minimal estrogen levels and maximum estrogen receptor levels favor radiotracer uptake.

Another factor that may influence radiotracer uptake is hormonal regulation of the vasculature during the reproductive cycle. Blood flow to the ovaries but not to the uterus is increased during estrus (32). However, uptake in the ovaries during estrus and metestrus was not significantly different (33). In addition, blood flow is not uniform in the left and right ovaries and therefore may affect experimental outcomes. In a recently published clinical study, endometrial standardized uptake values determined by ^{18}F -FES PET were

significantly higher in the proliferative phase than in the secretory phase (34), highlighting the influence of menstrual cycle and endogenous estrogen levels in radiotracer uptake in humans.

Table 2 Uptake of ^{99m}Tc(I)-Estradiol-Pyridin-2-yl Hydrazine Derivative Throughout Estrous Cycle

Organ	%ID/g					
	Estrus	Estrus (block)*	Metestrus	Metestrus (block)*	Diestrus	Diestrus (block)*
Blood	2.30 ± 1.02	1.92 ± 0.95	2.50 ± 0.88	2.54 ± 1.63	2.70 ± 0.12	2.42 ± 0.24
Bone	0.22 ± 0.06	0.17 ± 0.02	0.15 ± 0.04	0.24 ± 0.10	0.14 ± 0.01	0.17 ± 0.02
Muscle	0.09 ± 0.01	0.09 ± 0.02	0.11 ± 0.01	0.08 ± 0.04	0.15 ± 0.02	0.13 ± 0.02
Mammary glands ^{y,z}	0.22 ± 0.02	0.08 ± 0.01	1.31 ± 0.13	0.19 ± 0.02	3.11 ± 0.24	0.78 ± 0.06
Uterus ^{y,z}	0.55 ± 0.02	0.36 ± 0.02	0.79 ± 0.09	0.48 ± 0.04	1.44 ± 0.07	0.63 ± 0.04
Ovaries ^{y,s}	0.60 ± 0.06	0.24 ± 0.03	0.76 ± 0.04	0.39 ± 0.05	1.24 ± 0.22	0.60 ± 0.05

*Receptor blocking studies were performed by coinjecting 5 mg of 17β-estradiol with radiotracer.
yUptake values (n ≥4) in each phase of estrous cycle were significantly different (P <0.05) from uptake values in same phase of estrous cycle in presence of 5 mg of coinjected 17β-estradiol.
zUptake values (n ≥4) in each phase of estrous cycle were significantly different (P < 0.05) from one another.
sUptake values (n ≥4) in each phase of estrous cycle were not significantly different (P<0.05) from one another in comparisons of estrus and metestrus and in comparisons of metestrus and diestrus. However, values were significantly different in comparison of estrus and diestrus.
Reproductive organs, mammary glands, bone, blood, and muscle of 8- to 10-wk-old female C57BL/6 mice in defined stages of estrous cycle were evaluated. Uptake was determined from biodistribution studies. Data represent mean ± SEM from 4 determinations.

Less is known about changes in the normal vasculature of the mammary gland; however, it has been observed that vascular permeability (but not blood flow or vascular density) is highest at diestrus (35). Importantly, the increase in vascular permeability at diestrus correlates with increased breast cancer growth rate and postresection metastasis (35). Thus it is possible that the 14-fold increase in radiotracer uptake at diestrus is related to changes in vascular permeability. It would be worth investigating the possibility that elevated ligand availability during the luteal phase in women is linked to reduced 5-y disease-free survival in women with breast cancer who undergo mastectomy (along with tamoxifen and oophorectomy) in the follicular phase as compared with the luteal phase (36). It should also be noted that not all human studies have found a difference in disease-free survival linked to the menstrual cycle (12).

The major goal for cancer imaging is accurate disease characterization through the application of functional and molecular imaging studies. ¹⁸F-FES PET cancer imaging has been

Table 3 Time-Dependent Uptake of Tc(I)-Estradiol-Pyridin-2-yl Hydrazine Derivative

Organ	%ID/g at the following time (h) after injection:		
	1	3	24
Kidneys	1.70 ± 0.33	1.31 ± 0.06	1.19 ± 0.12
Adrenal glands	1.87 ± 0.75	3.10 ± 0.46	0.58 ± 0.15
Heart	1.17 ± 0.23	1.61 ± 0.51	0.86 ± 0.12
Small intestine	0.44 ± 0.20	1.87 ± 0.54	0.68 ± 0.05
Large intestine	0.28 ± 0.06	3.24 ± 0.95	0.89 ± 0.19
Liver	9.48 ± 0.99	8.34 ± 0.18	7.84 ± 0.24
Urinary bladder	0.19 ± 0.05	0.96 ± 0.27	5.99 ± 4.34
Blood	2.47 ± 0.07	2.79 ± 0.21	1.02 ± 0.39
Bone	0.28 ± 0.16	0.14 ± 0.01	0.85 ± 0.53
Lungs	1.49 ± 0.39	1.12 ± 0.19	0.83 ± 0.17
Stomach	0.85 ± 0.14	1.08 ± 0.37	0.34 ± 0.04
Muscle	0.10 ± 0.01	0.18 ± 0.03	0.35 ± 0.10
Mammary glands	1.21 ± 0.26	3.07 ± 0.40	1.59 ± 0.59
Uterus	1.32 ± 0.37	1.48 ± 0.10	1.60 ± 0.17
Ovaries	1.40 ± 0.32	1.19 ± 0.26	0.97 ± 0.25
Brain	0.06 ± 0.01	0.10 ± 0.01	0.02 ± 0.01

Uptake was determined from biodistribution studies of ^{99m}Tc(I)- estradiol-pyridin-2-yl hydrazine derivative in selected organs of 8- to 10-wk-old female C57BL/6 mice in diestrus. Data represent mean ± SEM from at least 6 determinations.

immensely valuable to clinical oncologists for staging and visualizing primary and meta-static carcinomas (16,37). The supplemental molecular characterization and receptor- ex- pression assessment of the tumor has often assisted in determining endocrine therapy options (12,13,38). As an alternative to PET, we wanted to evaluate the utility of a ^{99m}Tc(I)- estradiol-pyridin-2-yl hydrazine derivative in SPECT of breast and endometrial cancers. In previously published studies, problems encountered in developing a neutral Tc-estradiol derivative suitable for imaging of tumors were associated with excessive lipophilicity (i.e., logP values of >5 (23)) resulting in high liver and intestine uptake, low tumor-to-blood ratios, and relatively low uptake in the tumor compared with that in the background (17–19). In the present study, we encountered similar problems despite the fact that the logP value of our tracer was not significantly different from that previously reported for estradiol itself (3.9 vs. approximately 3.7 (23), respectively). From biodistribution studies,

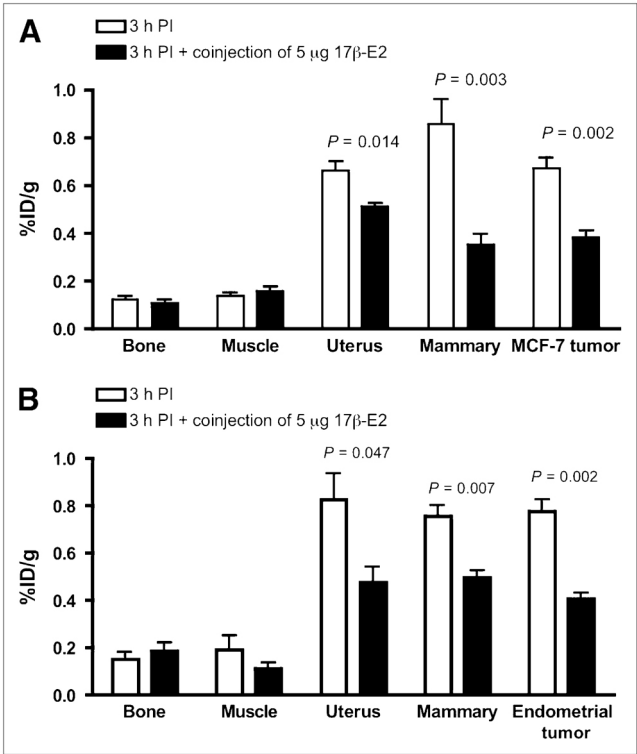


Figure 3. Receptor-mediated uptake of ^{99m}Tc(l)-estradiol- pyridin-2-yl hydrazine derivative in ovariectomized female athymic NCr-nu/nu mice bearing MCF-7 human breast adeno- carcinoma tumors (A) or human primary endometrial tumors (B). Uptake values are expressed as %ID/g and were determined from biodistribution studies. Data represent mean ± SEM from at least 3 determinations. PI = postinjection.

additional technical challenges involving ovariectomy and estrogen supplementation with pellets. For example, when we performed radiotracer studies 3 d after removing the estrogen pellet and the ovaries, the uptake in target organs was not blocked by excess ligand, likely attributable to high endogenous levels of estrogen. It is also known that estrogen supplementation and pregnancy can elevate the levels of sex steroid-binding protein and α-fetoprotein, which result in lower target-to-blood ratios (30). Our studies revealed that a period of at least 8 d after pellet and ovary removal was required to obtain significant results, although oophorectomy is not typically an option in the clinical setting. The low level of tracer uptake in tumor compounded with a high background resulted in poor whole-body SPECT/CT images at 60 s per projection. The image quality was greatly improved when a focused study was performed at 600 s per projection (Fig. 5). As a proof of principle, we have demonstrated that the tracer localizes in the tumor; however, such long acquisition time studies may not be feasible in clinical settings.

uptake of the radiotracer in the tumor was receptor-mediated based on the significantly lower uptake on coinjection with excess 17β-estradiol. Care must be taken while performing receptor blocking experiments with high doses of 17β-estradiol as estrogen alters vascular physiology, blood flow and receptor expression levels (39). Consequently, when the blocking dose was injected 1 h before the injection of the radiotracer, we observed higher uptake in organs such as liver and lungs.

In this study, we chose the MCF-7 tumor model as representative of estrogen-dependent carcinomas; however, this model requires estrogen supplementation, which creates

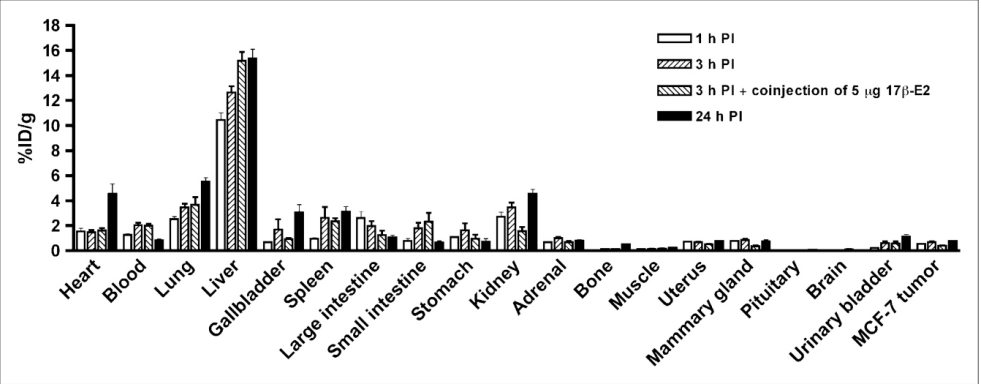


Figure 4. Uptake of ^{99m}Tc(l)-estradiol- pyridin-2-yl hydrazine derivative in selected organs of ovariectomized female athymic NCr-nu/nu mice bearing MCF-7 human breast adenocarcinoma tumors. Biodistribution data were obtained at 1, 3, and 24 h after injection. All uptake values are expressed as %ID/g. Data represent mean ± SEM from at least 4 determinations. PI = postinjection.

Currently, there are no readily available and easily synthesized SPECT agents for assessing reproductive cancers expressing estrogen-binding activity. Despite the challenges and drawbacks, newer ^{99m}Tc-based estradiol derivatives have been reported, including the one in this study. However, to date, all of them have failed to provide an alternative to 18F- FES PET, mainly attributable to low tumor uptake compounded with high background levels. To overcome the problems posed by such steroidal analogs, we propose the development of neutral nonsteroidal analogs that would specifically bind to each estrogen receptor subtype (ERα, ERβ, and GPR30) with high affinity (28,40).

Table 5. Target-to-Muscle and Target-to-Blood Ratios of ^{99m}Tc(l)-Estradiol-Pyridin-2-yl Hydrazine Derivative

Target-to-background	Ratio at the following time (h) after injection:			
	1	3	3 (block)*	24
Uterus-to-muscle	6.44 ± 0.81	5.21 ± 1.12	3.32 ± 0.46	3.58 ± 0.47
Mammary gland-to-muscle	7.05 ± 0.87	6.74 ± 1.21	2.45 ± 0.51	3.50 ± 0.82
MCF-7 tumor-to-muscle	4.75 ± 0.43	5.67 ± 1.06	2.64 ± 0.53	3.54 ± 0.26
Uterus-to-blood	0.57 ± 0.02	0.34 ± 0.04	0.24 ± 0.02	1.02 ± 0.16
Mammary gland-to-blood	0.62 ± 0.05	0.43 ± 0.05	0.18 ± 0.02	0.91 ± 0.11
MCF-7 tumor-to-blood	0.43 ± 0.07	0.35 ± 0.05	0.19 ± 0.02	1.03 ± 0.19

*Receptor blocking studies were performed by coinjecting 5 µg of 17β-estradiol with radiotracer. All ratios at 3 h after injection were significantly different (P<0.05) from ratios at 3 h after injection when radiotracer was coinjected with 5 µg of 17β-estradiol to block receptor.

^{99m}Tc(l)-estradiol-pyridin-2-yl hydrazine uptake was determined in ovariectomized female athymic NCr-nu/nu mice bearing MCF-7 human breast adenocarcinoma tumors. Data represent mean ± SEM from at least 4 determinations.

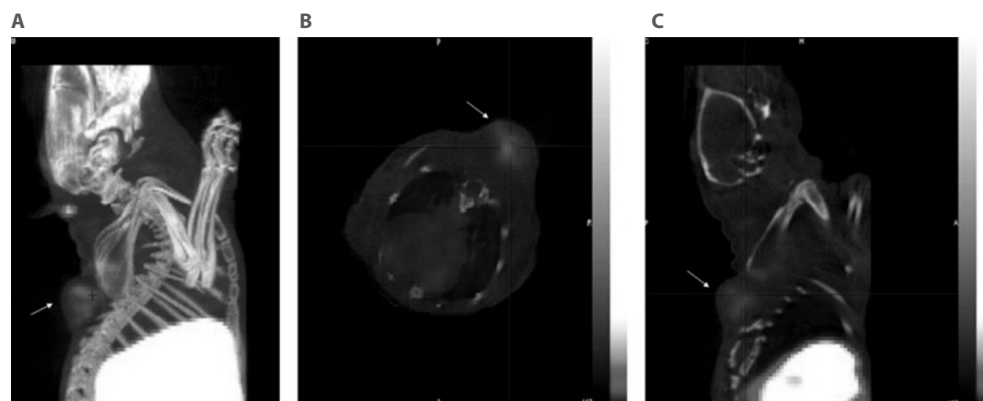


Figure 5. (A) Reconstructed coregistered maximum-intensity-projection SPECT/CT image. (B) Reconstructed coregistered transverse SPECT/CT slice image. (C) Reconstructed coregistered sagittal SPECT/CT slice image. In all images, the tumor is indicated by an arrow. Images were acquired from ovariectomized female athymic NCr-nu/nu mice bearing MCF-7 human breast adenocarcinoma tumors and injected with approximately 18.5 MBq of $^{99m}\text{Tc}(\text{I})$ -estradiol-pyridin-2-yl hydrazine derivative via tail vein. Images were acquired post-mortem at 3 h after injection. For SPECT image, focused scan at 600 s per projection was used; CT image was acquired with 180 projections (pitch of 1.5 and energy of 45 kVp). Energy window for SPECT acquisition of ^{99m}Tc was set at 140 ± 14 keV. Images were reconstructed, fused, and analyzed with InVivoScope software program. In these representative SPECT images, maximum intensity of color scale was set to 25%.

Conclusion

In conclusion, in the present study, the highest levels of target uptake were observed during diestrus consistent with differential expression of ER and estrogen levels during the estrous cycle. Although the $^{99m}\text{Tc}(\text{I})$ -estradiol-pyridin-2-yl hydrazine derivative showed encouraging results in standard biodistribution studies, as it demonstrated receptor-mediated uptake in normal target organs as well as human breast adenocarcinoma MCF-7 tumors and primary human endometrial tumors, further structural modifications are needed to optimize these compounds for improved imaging characteristics.

Acknowledgments

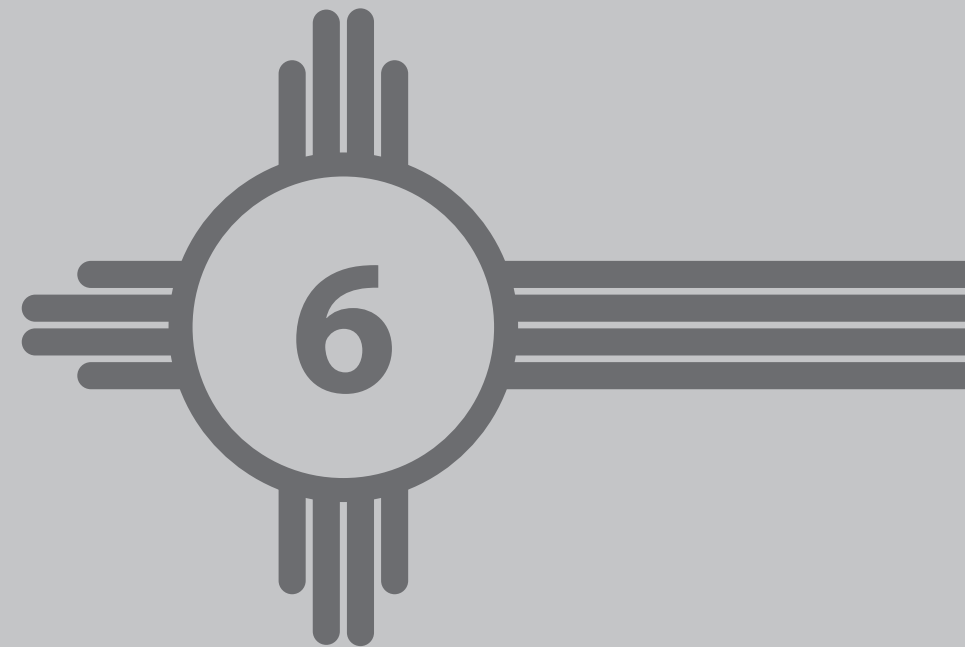
This study was supported by NIH grants CA116662 and CA127731, NIH grant SCORE GM08136, NIH grant MH074425, the University of New Mexico Cancer Research and Treatment Center (NIH P30 CA118100), the New Mexico Cowboys for Cancer Research Foundation, the Oxnard Foundation, and the Stranahan Foundation. Images in this article were generated at the Keck-UNM Small Animal Imaging Resource established with funding from the W.M. Keck Foundation. The technical assistance of Tamara Anderson and Kamalika Nag is greatly appreciated. We thank Dr. Robert Atcher (Biosciences Division, Los Alamos National Laboratory) for his valuable insights and Dr. Mary Dyszlewski (Tyco Healthcare, Mallinckrodt) for providing the Isolink kit.

References

- Jemal A, Siegel R, Ward E, et al. Cancer statistics, 2006. *CA Cancer J Clin.* 2006;56:106–130.
- Yager JD, Davidson NE. Estrogen carcinogenesis in breast cancer. *N Engl J Med.* 2006;354:270–282.
- Filardo EJ, Graeber CT, Quinn JA, et al. Distribution of GPR30, a seven membrane-spanning estrogen receptor, in primary breast cancer and its association with clinicopathologic determinants of tumor progression. *Clin Cancer Res.* 2006;12:6359–6366.
- Smith HO, Leslie KK, Singh M, et al. GPR30: a novel indicator of poor survival for endometrial carcinoma. *Am J Obstet Gynecol.* 2007;196:386.e1–9.
- Jordan CV, Lewis-Wambi J, Kim H, et al. Exploiting the apoptotic actions of oestrogen to reverse anti-hormonal drug resistance in oestrogen receptor positive breast cancer patients. *Breast.* 2007;16(suppl 2):S105–S113.
- Bafaloukos D. Neo-adjuvant therapy in breast cancer. *Ann Oncol.* 2005;16(suppl 2):ii174–ii181.
- Veronesi U, Boyle P, Goldhirsch A, Orecchia R, Viale G. Breast cancer. *Lancet.* 2005;365:1727–1741.
- Katzenellenbogen JA, Welch MJ, Dehdashti F. The development of estrogen and progestin radiopharmaceuticals for imaging breast cancer. *Anticancer Res.* 1997;17:1573–1576.
- Vollenweider-Zerargui L, Barrelet L, Wong Y, Lemarchand-Béraud T, Go'mez F. The predictive value of estrogen and progesterone receptors' concentrations on the clinical behavior of breast cancer in women: clinical correlation on 547 patients. *Cancer.* 1986;57:1171–1180.
- Landvatter SW, Kiesewetter DO, Kilbourn MR, Katzenellenbogen JA, Welch MJ. (2R*, 3S*)-1-[^{18}F]fluoro-2,3-bis(4-hydroxyphenyl)pentane ([^{18}F]fluoronor-hexestrol), a positron-emitting estrogen that shows highly-selective, receptor-mediated uptake by target tissues in vivo. *Life Sci.* 1983;33:1933–1938.
- Mathias CJ, Welch MJ, Katzenellenbogen JA, et al. Characterization of the uptake of 16 α -[^{18}F]fluoro-17 β -estradiol in DMBA-induced mammary tumors. *Int J Rad Appl Instrum B.* 1987;14:15–25.
- Linden HM, Stekhova SA, Link JM, et al. Quantitative fluoroestradiol positron emission tomography imaging predicts response to endocrine treatment in breast cancer. *J Clin Oncol.* 2006;24:2793–2799.
- Mortimer JE, Dehdashti F, Siegel BA, Katzenellenbogen JA, Fracasso P, Welch MJ. Positron emission tomography with 2-[^{18}F]fluoro-2-deoxy-D-glucose and 16 α -[^{18}F]fluoro-17 β -estradiol in breast cancer: correlation with estrogen receptor status and response to systemic therapy. *Clin Cancer Res.* 1996;2:933–939.
- Hecht JL, Mutter GL. Molecular and pathologic aspects of endometrial carcinogenesis. *J Clin Oncol.* 2006;24:4783–4791.
- Shang Y. Molecular mechanisms of oestrogen and SERMs in endometrial carcinogenesis. *Nat Rev Cancer.* 2006;6:360–368.
- Yoshida Y, Kurokawa T, Sawamura Y, et al. The positron emission tomography with F18 17 β -estradiol has the potential to benefit diagnosis and treatment of endometrial cancer. *Gynecol Oncol.* 2007;104:764–766.
- Bigott HM, Parent E, Luyt LG, Katzenellenbogen JA, Welch MJ. Design and synthesis of functionalized cyclopentadienyl tricarbonylmetal complexes for technetium-94m PET imaging of estrogen receptors. *Bioconjug Chem.* 2005;16: 255–264.
- Luyt LG, Bigott HM, Welch MJ, Katzenellenbogen JA. 7 α - and 17 α -substituted estrogens containing tridentate tricarbonyl rhenium/technetium complexes: synthesis of estrogen receptor imaging agents and evaluation using microPET with technetium-94m. *Bioorg Med Chem.* 2003;11:4977–4989.
- Skaddan MB, Wust FR, Jonson S, et al. Radiochemical synthesis and tissue distribution of Tc- 99m -labeled 7 α -substituted estradiol complexes. *Nucl Med Biol.* 2000;27:269–278.
- Ramesh C, Bryant B, Nayak T, et al. Linkage effects on binding affinity and activation of GPR30 and estrogen receptors ER α /ER β with tridentate pyridin-2-yl hydrazine tricarbonyl-Re/(^{99m}Tc) chelates. *J Am Chem Soc.* 2006;128:14476–14477.

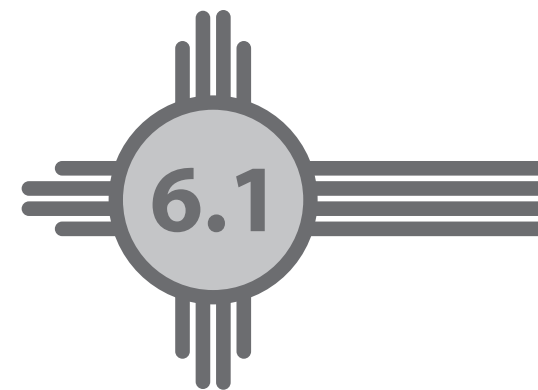
21. Hochberg RB, Rosner W. Interaction of 16 alpha-[125I]iodo-estradiol with estrogen receptor and other steroid-binding proteins. *Proc Natl Acad Sci USA*. 1980;77:328–332.
22. Murphy BE. Binding of testosterone and estradiol in plasma. *Can J Biochem*. 1968;46:299–302.
23. Skaddan MB, Wust FR, Katzenellenbogen JA. Synthesis and binding affinities of novel Re-containing 7a-substituted estradiol complexes: models for breast cancer imaging agents. *J Org Chem*. 1999;64:8108–8121.
24. Nelson JF, Felicio LS, Randall PK, Sims C, Finch CE. A longitudinal study of estrous cyclicity in aging C57BL/6J mice: I. Cycle frequency, length and vaginal cytology. *Biol Reprod*. 1982;27:327–339.
25. Dai D, Albitar L, Nguyen T, Laidler LL, Singh M, Leslie KK. A therapeutic model for advanced endometrial cancer: systemic progestin in combination with local adenoviral-mediated progesterone receptor expression. *Mol Cancer Ther*. 2005;4:169–175.
26. Revankar CM, Cimino DF, Sklar LA, Arterburn JB, Prossnitz ER. A trans- membrane intracellular estrogen receptor mediates rapid cell signaling. *Science*. 2005;307:1625–1630.
27. Kuiper GG, Carlsson B, Grandien K, et al. Comparison of the ligand binding specificity and transcript tissue distribution of estrogen receptors alpha and beta. *Endocrinology*. 1997;138:863–870.
28. Bologa CG, Revankar CM, Young SM, et al. Virtual and biomolecular screening converge on a selective agonist for GPR30. *Nat Chem Biol*. 2006;2:207–212.
29. De Hertogh R, Ekka E, Vanderheyden I, Hoet JJ. In vivo observation on cyclic variations of estradiol-17beta,6,7-3H uptake by the uterus of the adult rat. *Endocrinology*. 1971;88:175–179.
30. McElvany KD, Carlson KE, Katzenellenbogen JA, Welch MJ. Factors affecting the target site uptake selectivity of estrogen radiopharmaceuticals: serum binding and endogenous estrogens. *J Steroid Biochem*. 1983;18:635–641.
31. Brenner RM, West NB. Hormonal regulation of the reproductive tract in female mammals. *Annu Rev Physiol*. 1975;37:273–302.
32. Dowell RT, Gairola CG, Diana JN. Reproductive organ blood flow measured using radioactive microspheres in diestrous and estrous mice. *Am J Physiol*. 1992;262:R666–R670.
33. Silberstein GB, Van Horn K, Hrabeta-Robinson E, Compton J. Estrogen- triggered delays in mammary gland gene expression during the estrous cycle: evidence for a novel timing system. *J Endocrinol*. 2006;190:225–239.
34. Tsuchida T, Okazawa H, Mori T, et al. In vivo imaging of estrogen receptor concentration in the endometrium and myometrium using FES PET: influence of menstrual cycle and endogenous estrogen level. *Nucl Med Biol*. 2007;34:205–210.
35. Wood PA, Bove K, You S, Chambers A, Hrushesky WJ. Cancer growth and spread are saltatory and phase-locked to the reproductive cycle through mediators of angiogenesis. *Mol Cancer Ther*. 2005;4:1065–1075.
36. Love RR, Duc NB, Dinh NV, et al. Mastectomy and oophorectomy by menstrual cycle phase in women with operable breast cancer. *J Natl Cancer Inst*. 2002;94: 662–669.
37. McGuire AH, Dehdashti F, Siegel BA, et al. Positron tomographic assessment of 16 a-[18F] fluoro-17 beta-estradiol uptake in metastatic breast carcinoma. *J Nucl Med*. 1991;32:1526–1531.
38. Bennink RJ, van Tienhoven G, Rijks LJ, Noorduin AL, Janssen AG, Sloof GW. In vivo prediction of response to antiestrogen treatment in estrogen receptor- positive breast cancer. *J Nucl Med*. 2004;45:1–7.
39. Haas E, Meyer MR, Schurr U, et al. Differential effects of 17beta-estradiol on function and expression of estrogen receptor alpha, estrogen receptor beta, and GPR30 in arteries and veins of patients with atherosclerosis. *Hypertension*. 2007;49:1358–1363.
40. Revankar CM, Mitchell HD, Field AS, et al. Synthetic estrogen derivatives demonstrate the functionality of intracellular GPR30. *ACS Chem Biol*. 2007;2: 536–544.

Characterization of respiratory
deposition of fluticasone-
salmeterol hydrofluoroalkane-
134a and hydrofluoroalkane-134a
beclomethasone in asthmatic
patients



Implementation of a 3D Topographic Thinning Model for Assessing Aerosol Deposition of Radioactive Assays in Small-Animal CT/SPECT Imaging

Honggang Yu, Jack Hoppin, Ky Harlin, Jacob McDonald, Philip Kuehl, Tamara Anderson, Christian Lackas, Benjamin Gershman, Gabriel Candelaria, Jacob Y. Hesterman, Jeffrey P. Norenberg



Abstract

Nuclear imaging serves as an important tool for the visualization and analysis of nebulized radiolabeled particle deposition in the lung, enabling assessment of both nebulizer properties and lung function. To date, most research in this field has been focused on mathematical modeling from empirical data. This work examines the use of high-resolution 3D CT/SPECT imaging technology accompanied by automated lung segmentation to build a novel analysis model based on topographic thinning of the dual-modality tomograms.

Introduction

Nuclear imaging is an important tool for the visualization and analysis of nebulized radio-labeled particle deposition in the lung, enabling assessment of both nebulizer properties and lung function. A variety of lung models and segmentation approaches have been successfully implemented to quantify particle distributions in both planar and tomographic data with both human and animal subjects [1-4]. This manuscript presents a two-step analysis technique that was developed as part of a study to examine the relationship between particle size and deposition of particles in the lung for mice and rats [5]. In the first step, an automated segmentation was applied to micro-CT data (from SPECT/CT data sets) to extract regions-of-interest corresponding to the lungs. In the second step, topographic thinning analysis was applied to the SPECT data corresponding to these segmented regions-of-interest.

A reliable and accurate segmentation of the lungs and the precise measurement of their volume are integral to the topographic thinning analysis. However, manual tracing of organs for purposes of volume estimation and radioactivity quantification is tedious, time-consuming, and subject to inter- and intra-observer variability. Therefore, in addition to the novel lung modeling approaches outlined below, this work presents the development and evaluation of a new, robust, and fully-automated 3D lung segmentation method for high-resolution CT small-animal images.

Automated segmentation techniques enable accurate and systematically reproducible volume measurements. The design of the fully-automated segmentation method, developed in a commercial software package, was guided by study-specific needs. First, the algorithm was required to accommodate a large variability in lung appearance and shape arising from the desire to use a single routine on multiple mice and rats. The algorithm design also focused on handling the region near the branching of the lung into left and right lobes, as this region is critical to estimates of particle deposition and is often indistinct in standard, small-animal micro-CT. The resulting algorithm integrates multi-threshold segmentation, 3D region growing, mathematical morphology, and knowledge-based classification to meet these criteria.

Following segmentation, a model of the generations of the lung is employed to assess the deposition of the radiolabeled particles as a function of nebulizer settings. Researchers have proposed numerous approaches to modeling lung morphology in both planar and tomographic imaging studies [1-4]. In this work, a novel analysis model is presented analogous to an "onion" segmentation of the 3D tomograms. The layers of the so-called onion or topographic thinning approach are developed either through peeling or radical profiling as outlined below. The mean concentration of the radioisotope at each onion layer is in turn used as surrogates of uptake across lung generation.

The rest of the article is organized as follows. In Section 2, the data acquisition method, the algorithm for lung segmentation and the topographic thinning model are described. Section 3 presents the results of the segmentation evaluation, along with the radioactivity deposition quantification. Finally, in Section 4, conclusion and further discussion are presented.

Method

Data Sets and Image Acquisition

Sixteen mice and sixteen rats were exposed via nose-only inhalation to Technitium-99m radiolabeled sulfur colloid particles with specific particle sizes: 0.5, 1.0, 3.0 and 5.0 micron (total 32 data sets). Aerosols were generated with a series of compressed air jet nebulizers

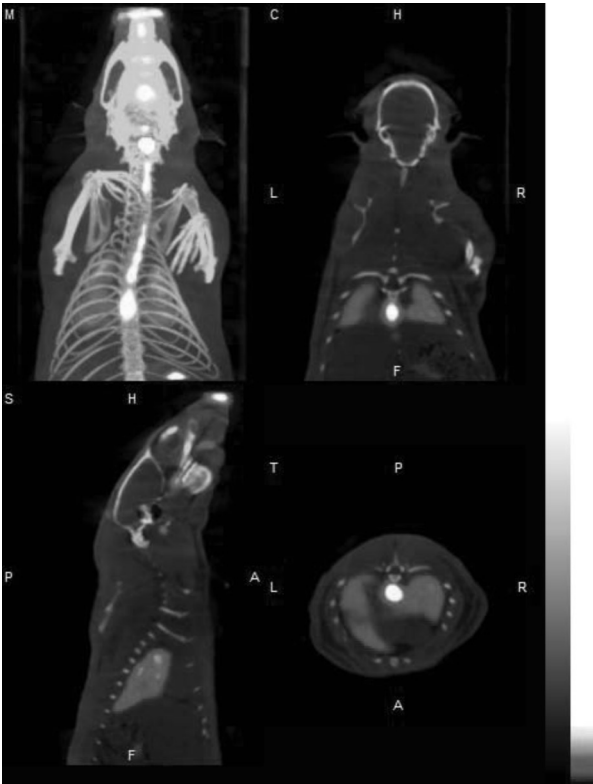


Fig 1 3D co-registered CT/SPECT rat image MIP reconstruction in InVivoScope

to achieve each specific particle size. Animals were sacrificed immediately following three minutes of inhalation exposures and imaged using a high-resolution small-animal SPECT/CT system (Nano-SPECT/CT™, Bioscan, Inc.) CT data were reconstructed using MIP algorithm in the InVivoScope™ post-processing package with a typical size: 170×170×280 voxels (Fig. 1) and spatial resolution of 0.2×0.2×0.2mm³ for mice and 0.4×0.4×0.4mm³ for rats. Each data set was cropped to the volume of interest (VOI) (~170×170×100 voxels) to include the lung region as a pre-processing step for the automated segmentation routine.

Segmentation Algorithms

Analysis of particle deposition via topographic thinning requires accurate segmentation of the lung region. Of particu-

lar importance in this study is the ability to precisely delineate the left and right lobes of the lungs at their branching point. A fully-automated 3D CT lung segmentation scheme for mice and rats was written in the Cognition Network Language (CNL) language under the Definiens Develop XD platform (Fig. 2) [6]. With this scripting language, a knowledgeable developer may incorporate anatomical information to guide conventional segmentation techniques in complex, context-dependent image analysis tasks. A segmentation routine consisting of six steps was developed using CT scans from three mice.

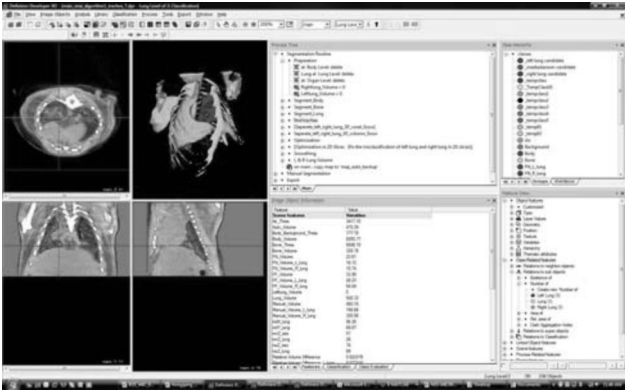


Fig 2 Screenshot of mice lung segmentation in Definiens Developer XD. Top images are transverse view and 3D surface reconstruction. Bottom images are coronal view and sagittal view.

A two-phase automatic threshold segmentation is applied to isolate high-contrast regions, specifically the animal body and skeleton. A 5x5x5 Gaussian smoothing kernel is used to reduce the impact of local inhomogeneities. The first automatic threshold separates the body from the background. A second automatic threshold is applied to segment the bones from the body.

Anatomical information, incorporated into the segmentation script, is used to identify the rib cage region of the skeleton. Another automatic segmentation threshold, influenced by local intensity and homogeneity measurements, separates airways from body tissue in this region. Anatomical features such as size, location, and relation to already identified neighbor regions (i.e., the rib cage) are used to further classify lung tissue.

In step three, the air is classified into regions of lung and trachea. The trachea is detected by searching for a darker circular airway region above (i.e., towards the head) the rib cage and near the center of the body in the transverse view. A region-growing procedure identifies the extent of the trachea, stopping when a rapid expansion in trachea dimension is detected as a function of axial position, which indicates the merging of the trachea and lung tissue.

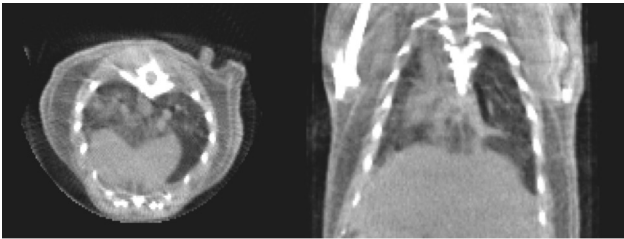


Fig 3 A example of mouse CT data set. (a) Transverse view (b) Coronal view

Motion artifacts, poor soft tissue contrast, and indistinct boundaries complicate delineation of the mediastinum from the left and right lung [e.g. see Fig 3 (a)]. One relevant image feature is that the large blood vessels near the mediastinum tend to indicate thin junctions between mediastinum and the lung lobes [e.g. see Fig 3 (b)]. A 3D region-growing method, incorporating this information and 3D spatial characteristics of surrounding organ tissue is applied. In this iterative algorithm, contiguous sets of lung voxels (primitive image objects) are merged with adjacent candidate regions, based upon the shared surface border of the candidate lung tissue and the reference lung tissue grown so far. The algorithm runs until no candidate regions remain that fulfill the merge condition.

The merged airway regions (image objects) are classified using anatomical knowledge and appearance features, including volume, location, shape, and compactness, to identify the left and right lung lobes and to remove the mediastinum.

3D morphological operators (i.e., erosion, dilation) are used to fill the small holes, include small vessels in the left and right lung region and to smooth the irregular boundary. Voxel maps for the regions-of-interest corresponding to the left and right lungs are exported for use in topographic thinning analysis.

Comparison of the lung segmentation algorithm to manual segmentation

Lung regions were manually segmented from sixteen mice CT scans using the same commercial software package. A knowledgeable analyst traced left and right lung boundaries on every fifth slice in each scan. A constrained region growing method was used to delineate the borders of intermediate slices.

Volumetric overlap (VO) and relative absolute volume difference (RVD) values between the manual and the automatic segmentations were computed [7]. These parameters are defined as:

$$VO = \frac{V_a \cap V_R}{V_a \cup V_R}$$

$$RVD = \left| \frac{V_a - V_R}{V_R} \right| \times 100\%$$

where \cap indicates the overlapping volume between the automatic segmentation and manual segmentation (reference), and \cup indicates the union of two segmentations. V_a and V_R indicate the volumes of the automatic segmentation and reference segmentation, respectively. VO has value 1 and RVD has value 0 when there is a perfect match between automatic segmentation and reference.

D. Topographic Thinning or Onion Model

Upon completion of the automated CT segmentation, three different approaches were used to bin the co-registered SPECT data into layers of deposition.

The first was a topographic thinning approach in which layers of voxels were stripped away from the 3D segmented lung and catalogued; this process was then repeated until there were no more layers available.

An additional method was derived by generating a line segment connecting a seeded center point within the onion to each outer surface voxel of the segmented lung. The profile of radioactive uptake along each of these line segments is in turn normalized to arbitrary length, and the mean across all segments is visualized. In this work two seeds for this approach were employed: the center-of-mass (COM) of each lung or a manual selection of the primary bronchus (Seed).

Results

A. Comparison of the lung segmentation algorithm to manual segmentation

A qualitative comparison of the manual and automatic segmentation results is shown in Fig 4. The automated segmentation could be completed in 15.1 seconds on a workstation computer with Intel Core 2 Duo CPU at 3.0 GHz with 3.0 G RAM. Fig 4 (b) shows the segmentation of body, rib cage and three segmented regions in lung tissue by region-growing. The mediastinum was identified and removed and the left and right lungs were smoothed in Fig. 4 (c). Fig 5 shows the volumetric overlap for the sixteen manually segmented mice data sets. The average volumetric overlaps for the left and right lungs are 0.73 and 0.76, respectively. The large variety of the lung appearance and shape in

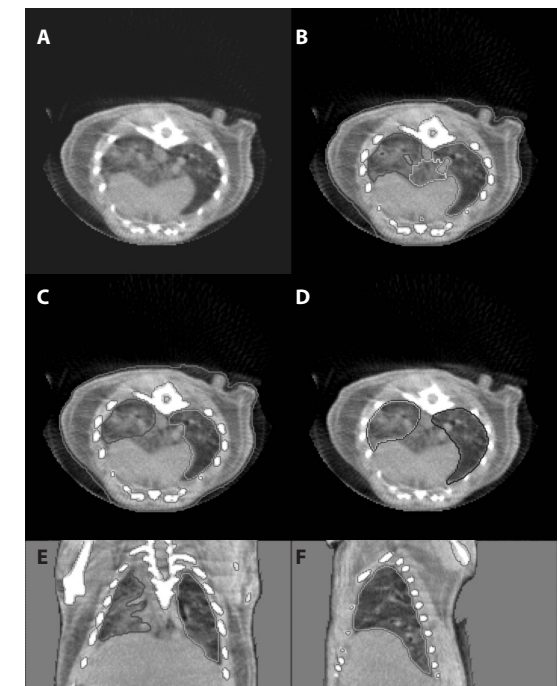


Fig 4 (a) Transverse CT slice of a mouse (b) Region-growing generated three image regions (c) Final classification and segmentation excludes mediastinum (d) Manual tracing (e) Final segmentation in coronal view (f) Final segmentation in sagittal view.

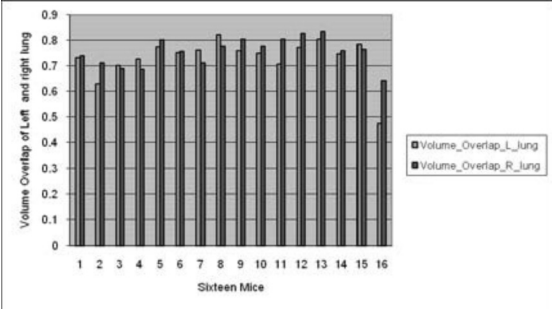


Fig 5 Volumetric overlap for the sixteen manually segmented mice data sets

respectively. Fig. 8 shows the positive false and negative false of left and right automated segmentation. In most cases, false positive values are bigger than false negative values. It indicates that automated methods classified parts of mediastinum tissue into left or right lung regions in those cases where the mediastinums have similar intensities as the lung tis-

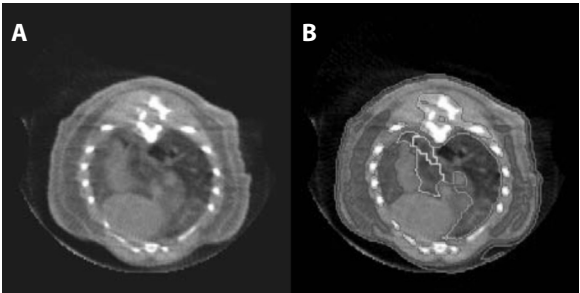


Fig 6 (a) A mouse CT example in transverse view **(b)** misclassification of left lung region

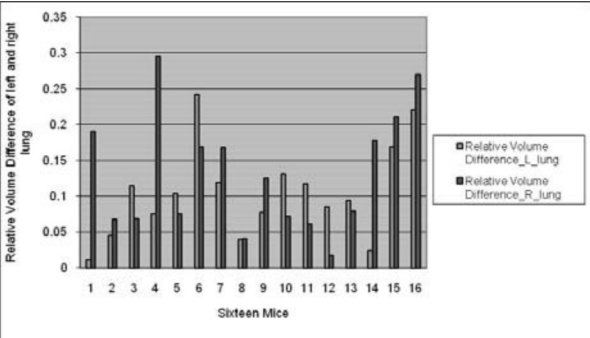


Fig 7 Relative absolute volume difference for sixteen mice CT data sets

B. Quantification results

Fig. 10 and 11 below demonstrate the functionality of the approach developed here for aerosol deposition analysis of radioactive assays in the lungs. Fig. 10 displays the 3D topographic thinning model on SPECT/CT data set of a mouse imaged using the 0.5 micron particle setting. In Fig. 11, the 3D topographic thinning model enables a plot of the profile across regions

Micro-CT images may result in inaccurate lung volume estimation. Fig 6 (a) shows an outline example in the mice data sets. The lung tissue is blurry and indistinct in appearance, and thus the automated method misclassified it as mediastinum in Fig 6 (b). Fig 7 shows the relative volume difference for the same sixteen data sets. The average values for the left and right lungs are 0.10 and 0.13,

sue. And that is common in standard, small-animal Micro-CT images. Linear regression was used to show the correlation between the manual segmented volumes and those obtained by automated method for sixteen mice data sets (Fig. 9). The correlation coefficients between the automated and manual method are 0.95 and 0.90 for left and right lung, respectively.

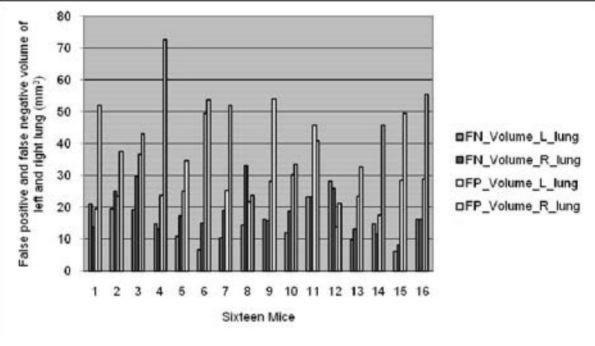


Fig 8 False positive and False negative for sixteen mice CT data sets

Conclusions

Novel methods for imaging and analyzing radiolabeled sulfur-colloid particle deposition in the lungs of small-animals have been developed. The “onion” model analysis presented here provides

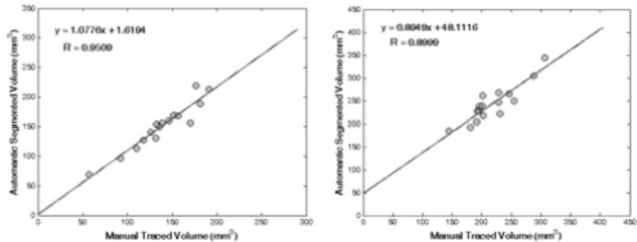


Fig 9 Linear regression plot of automated segmented volumes and manual traced volumes of sixteen mice CT data sets.

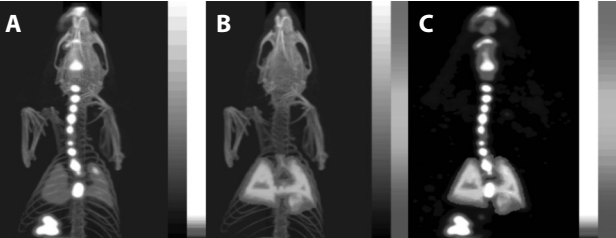
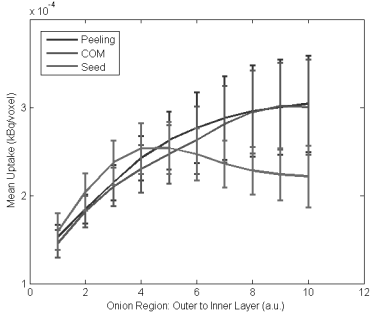


Fig 10 (a) the maximum-intensity projection of a SPECT/CT data set **(b)** the 3D topographic thinning model of the segmented lung. **(c)** The model superimposed on the SPECT data set.

results show that the fully-automated segmentation method described in this work is fast, efficient and accurate.

Fig 11 Three “onion” model profile plots in the segmented lung. The arbitrary units of the x-axis run from the outside to the inside of the lung “onion” model. Each profile is averaged over four mice imaged with 0.5 micron particle size.



of the lung. The profile plots correspond to the three aforementioned “onion” models: peeling, center-of-mass and manually seeded model. SPECT images were collected in units of kBq per voxel and mean concentrations across layers of the onion model were calculated for each of the models.

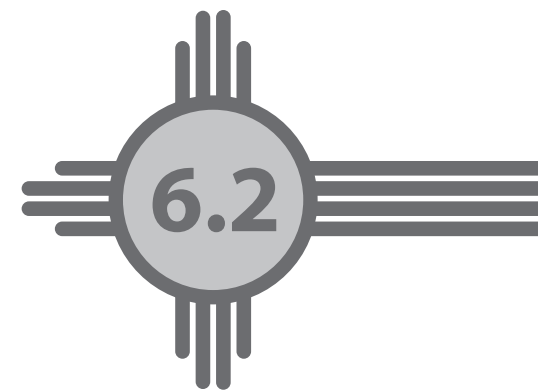
a reliable tool to quantify and visualize the deposition of radiolabeled particles in three dimensions. The model-based quantification analysis requires accurate segmentations of the lungs. Even though further evaluation is required, preliminary

References

- 1 Schroeter, J.D., Martonen, T.B., Pritchard, J.N. and D. Hwang: *Airway Identification Within Planar Gamma Camera Images*. Ann Occup Hyg 2002 46: 342; doi:10.1093/annhyg/46.suppl_1.342
- 2 Fleming, J.S., Quint, M., Bolt, L., Martonen, T.B. and Conway, J.H. (2006) *Comparison of SPECT aerosol deposition data with twenty- four-hour clearance measurements*. Jour. of Aero. Med., 19, (3), 261- 267.
- 3 Schroeter, J. D., Pritchard, J.N., Hwang, D., Martonen, T.B., *Airway Identification Within Planar Gamma Camera Images Using Computer Models of Lung Morphology*. Pharmaceutical Research, 22, (10), 1692-1699, 2005.
- 4 Fleming, J. S., Epps, B.P., Conway, J. H., and Martonen, T. B., *Comparison of SPECT Aerosol Deposition Data with a Human Respiratory Tract Model*. Jour. Of Aero. Med., 19, (3), 268-278.
- 5 Kuehl, P.J., Anderson, T., Gershman, B., Holmes, T., Irwin, D., Thompson, E., Norenberg, J., and J. D. McDonald: *Effect of Particle Size on the Regional Deposition of Technitium-99m Labeled Particles in Rodents*. 2009 Society of Toxicology Conference (abstract #2080), Baltimore, MD, March 2009.
- 6 <http://www.definiens.com>
- 7 Gerig, G., Jomier, M., Chakos, M., *Valmet: A new validation tool for assessing and improving 3D object segmentation*. MICCAI 2001, Springer, Berlin, 516-523. 2001.

Regional particle size dependent deposition of inhaled aerosols in rats and mice

Philip J. Kuehl, Tamara L. Anderson, Gabriel Candelaria, Benjamin Gershman, Ky Harlin, Jacob Y. Hesterman, Thomas Holmes, John Hoppin, Christian Lackas, Jeffrey P. Norenberg, Hongang Yu, and Jacob D. McDonald



Abstract

Context: The current data analysis tools in nuclear medicine have not been used to evaluate intra organ regional deposition patterns of pharmaceutical aerosols in preclinical species. *Objective:* This study evaluates aerosol deposition patterns as a function of particle size in rats and mice using novel image analysis techniques. *Materials and Method:* Mice and rats were exposed to radiolabeled polydisperse aerosols at 0.5, 1.0, 3.0, and 5.0 μm MMAD followed by SPECT/CT imaging for deposition analysis. Images were quantified for both macro deposition patterns and regional deposition analysis using the LRRI-developed Onion Model. *Results:* The deposition fraction in both rats and mice was shown to increase as the particle size decreased, with greater lung deposition in rats at all particle sizes. The Onion Model indicated that the smaller particle sizes resulted in increased peripheral deposition. *Discussion:* These data contrast the commonly used 10% deposition fraction for all aerosols between 1.0 and 5.0 μm and indicate that lung deposition fraction in this range does change with particle size. When compared to historical data, the 1.0, 3.0, and 5.0 μm particles result in similar lung deposition fractions; however, the 0.5 μm lung deposition fraction is markedly different. This is probably caused by the current aerosols that were polydisperse to reflect current pharmaceutical aerosols, while the historical data were generated with monodisperse aerosols. *Conclusion:* The deposition patterns of aerosols between 0.5 and 5.0 μm showed an increase in both overall and peripheral deposition as the particle size decreased. The Onion Model allows a more complex analysis of regional deposition in preclinical models.

Introduction

Inhalation drug delivery is currently the preferred route of administration for several respiratory diseases, including asthma and COPD, and is expanding as an optional delivery route for other diseases, lung cancer, and lung transplant. It is largely accepted that the particle size of an inhalation aerosol affects the regional deposition of the aerosol in both clinical and preclinical *in vivo* models. More recently, the effect that regional deposition has on the efficacy of an aerosol has started to take shape for a more targeted delivery of therapeutic aerosols (Leach et al., 2009). To this end, a need has arisen for a more complex analysis of regional deposition in both clinical and preclinical settings.

However, while there is extensive information detailing the deposition patterns of aerosols in the human respiratory tract (Leach et al., 2002; Backer, et al., 2010; Weers et al., 2009) and several manuscripts detailing deposition in preclinical species such as rodents (Raabe et al., 1988; Schlesinger, 1988; Miller, 2000; Asgharian et al., 2003; Martin et al., 2008) the majority of these data in rodents were generated prior to significant advancements in imaging capabilities (Raabe et al., 1988; Schlesinger, 1988). The advancements in nuclear imaging technologies now facilitate submillimeter resolution with simultaneous collection of single photon emission computer tomography (SPECT) and computer tomography (CT) images. Collection of these types of data have allowed nuclear imaging, in the form of 2D and 3D gamma imaging, to continue to develop into the primary tool for the visualization and analysis of deposition pattern throughout the lungs (Adams et al., 2010).

Using these new tools in the field of nuclear medicine to evaluate or quantify deposition patterns has become a mainstay in inhalation drug development and can accurately be applied to preclinical species, including a variety of lung models and segmentation approaches that have been successfully proposed and implemented to quantify particle distributions in both planar and SPECT human data sets (Schroeter et al., 2002; Fleming et al., 2006; Schroeter et al., 2005; Fleming et al., 2006). However, they must be refined and transferred to rodent species. This will allow similar regional analyses developed and used for traditional human regional analysis (central [C] to peripheral [P] ratio or penetration index) to be applied to preclinical species, thus facilitating the development of therapeutics that target desired regions of the respiratory tract.

Furthermore, the majority of the published deposition studies in preclinical species have been conducted with monodisperse aerosols (Raabe et al., 1988; Asgharian et al., 2003). This is in contrast to the majority of current pharmaceutical aerosols, which are primarily polydisperse. Therefore, there is the potential that the existing preclinical deposition models may not accurately or completely predict the deposition of today's pharmaceutical aerosols.

Based on these needs, the work detailed herein seeks to evaluate the deposition patterns of polydisperse aerosols, that more accurately mimic today's pharmaceutical aerosols, in mice and rats, to determine macro regional deposition patterns of these aerosols for comparison to historical data and to develop a regional analysis method that will facilitate a more complex deposition analysis in these preclinical models.

To address these needs, rats and mice were exposed to four different validated radiolabeled polydisperse aerosols having 0.5, 1.0, 3.0 and 5.0 μm mass median aerodynamic diameter (MMAD) and imaged via SPECT/CT immediately following exposures. This range of aerosol particle size was selected as it covers the primary range of most pharmaceutical aerosols.

Methods

Animal model

All procedures were conducted under protocols approved by the Institutional Animal Care and Use Committee at University of New Mexico Health Sciences Center (UNM HSC), which is accredited by the Association for Assessment and Accreditation of Laboratory Animal Care International. Animals were fed 2016C Harlan Global certified rodent chow *ad libitum*, with unlimited access to clean water. Animals were housed (four per cage) in an environmentally controlled room with 12-hour light cycles.

Aerosol development and label validation

Several commercially available compressed air jet nebulizers were used to develop aerosols at the four different median target aerosol sizes (0.5, 1.0, 3.0, and 5.0 μm MMAD). To optimize the particle size, a combination of nebulizer makes and models, inlet pressures, and aerosol treatments were used. Targeted aerosol particle size distributions were developed with unlabeled or decayed sulfur colloid kits (preparation detail follows). Particle size was determined with a Mercer-style cascade impactor (InTox Products, Moriarty, NM). The MMAD was determined by differential weight analysis of the substrates and the activity MMAD (AMAD) substrates. The impactor samples were collected at a rate of 2 L per minute.

All aerosols transitioned from the nebulizer through a stainless steel delivery line into a 6-port, flow past, nose-only inhalation exposure chamber (InTox Products, Moriarty, NM). An example schematic is shown in Figure 1.

Once the conditions to achieve the targeted particle sizes were determined, the radiolabeling of the aerosol was initiated. Technetium-99m ($^{99\text{m}}\text{Tc}$, as sodium pertechnetate in saline) was used to radiolabel sulfur colloid particles (Pharmalucence, Bedford, MA). The final vol-

ume of the prepared sulfur colloid suspension was modulated to 8 mL of total volume by addition of normal saline (0.9% NaCl in water). This radiolabeled suspension was transferred directly to the appropriate nebulizer and aerosolized into the exposure chambers.

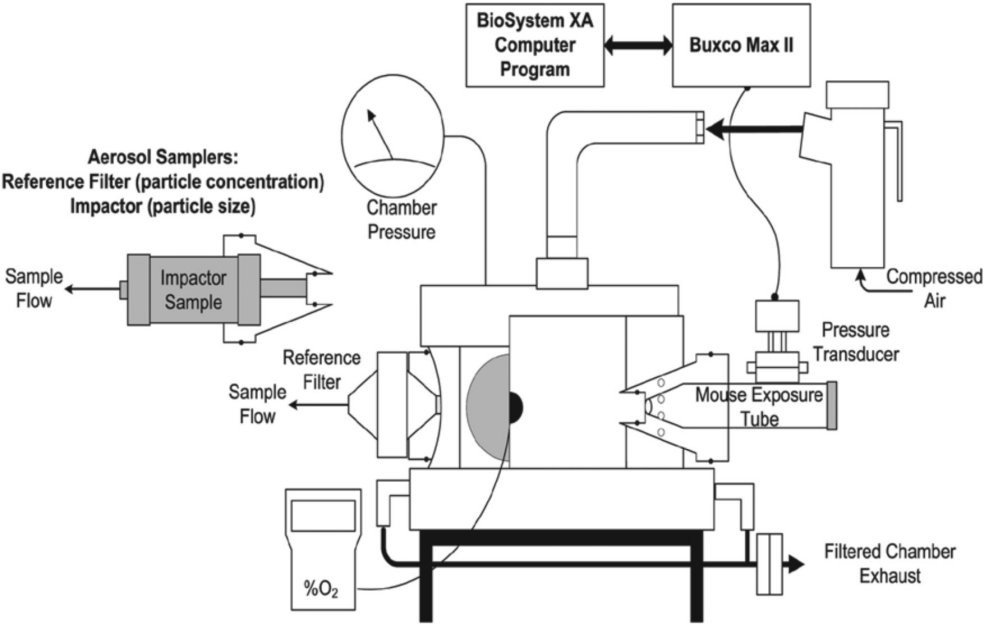


Figure 1. Example schematic of the nose-only inhalation exposure system.

In accordance with the International Society for Aerosols in Medicine workshop “Standards for *in vitro*/*in vivo* measurements for MDIs,” (Dolovich, 1996) each aerosol was tested and analyzed to validate the relationship between the MMAD and the activity particle size distribution AMAD. These validation studies were conducted to ensure that the $^{99\text{m}}\text{Tc}$ acted as a viable tracer for each aerosol. Specifically, they established the relationship between MMAD and AMAD in repeated studies to ensure that during the exposures the two particle size distributions agreed with one another and therefore the activity analysis of the images reflects the true deposition of the aerosol.

Inhalation exposure

Four mice (C57BL/6) and four rats (Fisher 344) were exposed via nose-only inhalation to $^{99\text{m}}\text{Tc}$ labeled sulfur colloid labeled particles at each of four different target aerosol sizes (0.5, 1.0, 3.0, and 5.0 μm MMAD). For each particle size and species, all animals were exposed at the same time. A total of eight exposures were conducted. Prior to exposure, each animal underwent at least two conditioning sessions for acclimation to the exposure restraint tubes. Prior to each exposure, animals were placed in the restraint tubes for approximately 5 minutes (to allow their breathing rates to stabilize) before initiating aerosol generation and exposure.

Exposures to the 0.5, 1.0, and 3.0 μm particles were conducted for 4 minutes and 5.0 μm particles for 3 minutes. Immediately after exposure, animals were euthanized via intra-peritoneal administration of pentobarbital. The immediate sacrifice was conducted to stop particle clearance mechanisms that may skew the initial particle deposition that occurred.

During each exposure, the aerosol concentration and particle size were determined. The aerosol concentration was determined via collection of a filter sample (Pall Life Sciences, Ann Arbor, MI) at the breathing zone of the nose-only exposure system using a controlled vacuum flow. The activity on the filter was quantified with a radio-isotope calibrator (Capintec, Model CRC7R, Ramsey, NJ). Aerosol activity concentration was determined by dividing the total activity by the total volume of air pulled through the filter. The particle size was determined, as above, with a Mercer-style cascade impactor.

Real time plethysmography

To provide the most accurate data analysis of an inhalation exposure, real time plethysmography was used. Each rat and mouse exposure tube was fitted with a double layer of latex dental dam around the neck of the animal to separate the chest from the head. The body portion was fitted to a calibrated pneumotachometer and monitored by plethysmography (Buxco Max II, Buxco Electronics, Sharon, CT). Prior to each exposure day, the pneumotachometer was calibrated with a traceable glass syringe between 0.1 and 2 mL pulses. Data were collected and analyzed with Biosystem XA (Buxco, version 2.9.4, Sharon, CT) to determine the respiratory minute volume (RMV) for each animal. Specifically, breaths per minute (BPM) and tidal volume were used to determine the RMV every second. The RMV over the time course of each exposure was then averaged for each animal to determine the RMV used for all calculations.

SPECT and CT and data acquisition

Images were collected using a high-resolution small-animal SPECT/CT system (Nano-SPECT/CTTM, Bioscan, Inc., Washington, DC). CT data were reconstructed using the In-VivoScopeTM post-processing package with a typical size: $170 \times 170 \times 280$ voxels, and spatial resolution of $0.2 \times 0.2 \times 0.2 \text{ mm}^3$ for mice and $0.4 \times 0.4 \times 0.4 \text{ mm}^3$ for rats. Each data set was cropped to the volume of interest (VOI) ($\sim 170 \times 170 \times 100$ voxels) to include the lung region as a preprocessing step for the subsequent automated segmentation routine.

SPECT and CT data analysis

Coregistration of the two image data sets allowed anatomical information from CT to be coregistered with radiolabeled aerosol deposition data from SPECT. A representative SPECT/CT overlay is shown in Figure 2a. Image analysis was first conducted to determine the radioactivity in the specific ROI throughout each rat and mouse. The ROIs included oral/nasal, trachea/bronchial, bifurcation, lung (split between right and left lung), stomach, and entire field of view (FOV). These ROIs were manually drawn in VivoQuantTM (In-

Vivo, LLC, software version 1.14) using the CT overlay to assist in manually defining each ROI to determine the activity in each ROI. To more completely characterize the regional deposition patterns of the different particle sizes, a lung segmentation model was developed and applied to the lungs of each animal. In this model, three different techniques were developed: peeling, SEED, and center-of-mass (COM), each defined and detailed below. In each model, 10 slices of lung (of arbitrary length) were defined and quantified.

The first approach to quantifying the lung ROI distribution was a topographic thinning model whereby layers were peeled from the outside inwards in all three dimensions. The process of peeling each layer was repeated until no more layers were available. This method was named the *peeling* method.

The second and third methods worked from a center point in the lung and moved outward. While both methods segmented the lung into slices moving from the inside to the outside, they used two different seed points as their origin. The COM method used the center of the lung mass (reflected the center of the lung from the CT) as the origin point and the SEED method seeded the origin from the CT as the primary bronchus. For each of these models, the profile of deposition in each region was determined (normalized for the volume in each region) and evaluated as a function of distance from the center point. The review, of all described data sets (peeling, SEED and COM) determined that the COM method was the most appropriate for the rodent species in these studies. In Figure 2b, the segmented lung appears to follow the segmentation pattern of an onion – the dark red region is the center-of-mass (origin) with segments represented by each color change moving outward. Therefore this model was named the “Onion Model” because the lung, when segmented in this manner, appears to follow the segmentation pattern of an onion.

Calculation of particle deposition fraction

To calculate the fraction of the aerosol that deposited in the rodent lungs (deposition fraction), the activity aerosol concentration (measured for each exposure) and measured RMV were used in the following equation:

$$\text{Total Inhaled Dose} = \text{Measured RMV} \\ \times \text{Measured Aerosol Conc.} \\ \times \text{Exposure Duration}$$

From this, the deposition fraction was calculated as follows:

$$\text{Deposition Fraction} = \left(\frac{\text{Deposition Dose}}{\text{Total Inhaled Dose}} \right) \times 100$$

Where the deposited dose is the activity measured from the ROI analysis of the images.

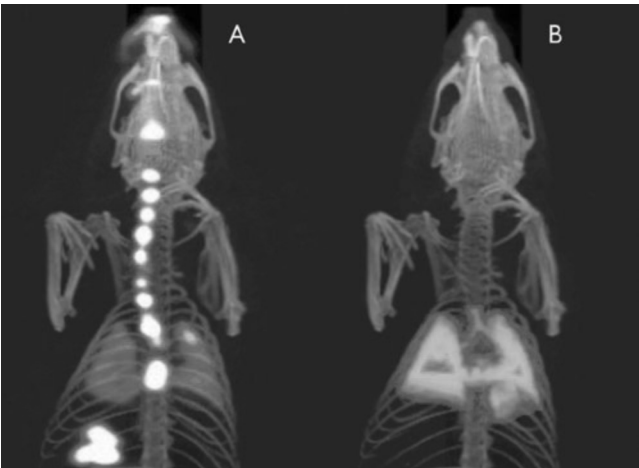


Figure 2. (a) Overlay of the SPECT and the CT data set for a mouse with a 0.5 μm particle size, and (b) the Onion Model of the lungs shown with the COM segmentation where the dark red color indicates the region of origin and each color shows the segments of the lung.

Multiple-path particle dosimetry model

Multiple-Path Particle Dosimetry Model (MPPD, version 2) simulations were performed in the rat airway model (with default assym. Multiple-path model), using our experimental parameters when possible. Specifically, MMAD, GSD and aerosol concentration from rat exposures, no inhalability correction, and tidal volume as the actual data from the real time plethysmography. Results were generated as a regional fraction in the whole lung. When modeling the monodisperse aerosols the exact same input data were used only the GSD was changed to 1.4.

Results

Validation of radiolabeled aerosols

The nebulizer and operating conditions for each particle size is shown in Table 1. The radiolabeling validation studies indicated that for each aerosol the $^{99\text{m}}\text{Tc}$ was uniformly associated with the aerosol, i.e. the MMAD and AMAD were in agreement. An example of a validation impactor analysis is shown in Figure 3.

Real time plethysmography

To highlight the importance of the real time plethys- mography data, the RMV calculated from Bide (based on the animal body weight prior to exposures), the measured RMV, and the percent difference are shown in Table 2. The Bide equation was selected over other models, as it has been shown that for rodents the Bide model is no different than the AIT model (Kuehl, 2009). RMV values were calculated for each individual animal and then averaged (Alexander et al., 2008; Bide et al., 2000). The measured RMV values, measured breath- ing frequency and tidal volume were averaged over the entire exposure duration for each animal and then av-

Table 1. Nebulizer used to achieve each target particle size along with the actual particle size (and geometric standard deviation [GSD]) from each exposure.

Target particle size (μm)	Nebulizer	Species	AMAD (μm)	GSD	Aerosol concentration (mCi/L)
0.5	Swirler	Mouse	0.5	1.6	0.613
0.5	Swirler	Rat			0.598
1.0	Collison	Mouse	1.0	2.1	0.217
1.0	Collison	Rat			0.142
3.0	Pari LC Plus	Mouse	2.8	2.6	0.923
3.0	Pari LC Plus	Rat			0.836
5.0	Retec	Mouse	5.0	2.2	0.976
5.0	Retec	Rat			1.025

eraged for each particle size and species. These data clearly show that even with two prior conditioning peri- ods and allowing the animals to acclimate to the tube for 5 minutes prior to exposures, the most accurate method to determine RMV is to measure RMV during the exposure. The actual data provide more accurate analyses and conclusions.

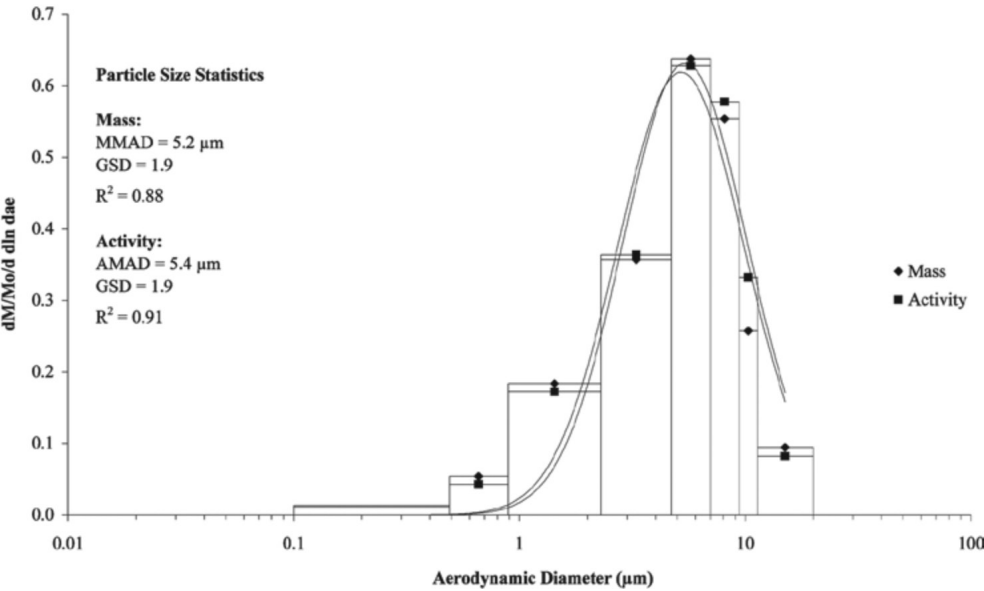


Figure 3. Example MMAD and AMAD relationship from validation conducted prior to exposures. The y-axis label $[(\text{dm}/\text{mo})/\text{d} \ln \text{dae}]$ refers to the differential mass, normalized to total mass within a specified particle size range.

Total particle deposition by region

The lung deposition fraction is shown graphically in Figure 4. Regional distribution, in the lungs and the extrathoracic regions, in terms of percent of total body burden are shown in Tables 3 and 4, and graphically in Figure 5.

Onion model

Throughout all analyses, the activity in each ROI or slice (Onion Model) had been normalized to the activity aerosol concentration measured for each exposure. This is due to the fact that each nebulizer had a different aerosol output despite loading each nebulizer with approximately 125 mCi of activity to achieve the targeted aerosol concentrations. The activity aerosol concentrations for all exposures are also shown in Table 1.

The Onion Model using the COM method data are presented as the mean lung voxel value normalized by aerosol concentration (previously detailed and justified) with error bars of plus or minus (±) standard error across four animals per species for each particle size cohort (0.5, 1.0, 3.0, and 5.0 μm). These data are shown graphically in Figures 6 and 7 for mice and rats, respectively.

Table 2. Comparison of average predicted RMV and average measured RMV.

Species	Group	Bide RMV (L/min)	Measured RMV (L/min)	Difference (%)	Breathing Frequency (bpm)	Tidal Volume (mL)
Mouse	0.5	0.028	0.046	59.5	280.6	0.164
Mouse	1.0	0.029	0.059	48.9	294.4	0.201
Mouse	3.0	0.032	0.054	58.6	245.5	0.221
Mouse	5.0	0.031	0.064	48.3	280.3	0.228
Rat	0.5	0.155	0.253	61.1	186.4	1.36
Rat	1.0	0.165	0.288	57.3	177.8	1.62
Rat	3.0	0.186	0.336	55.3	177.2	1.87
Rat	5.0	0.186	0.370	50.3	183.2	2.00

Discussion

The data indicate what would be scientifically expected, in that the deposition fraction decreases as a function of increasing particle size in both species. Further, the deposition fraction for the rat was higher than for the mouse across the entire particle size range. Over the range of all particle sizes tested, the lung deposition fraction was in contrast to the deposition fraction often used for preclinical toxicological studies, where it is assumed that the deposition fraction of particles between 1.0 and 5.0 μm MMAD is 10% (US FDA, 2007).

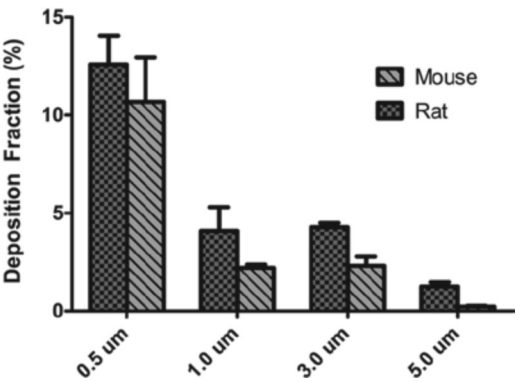


Figure 4. Deposition fraction for mice and rats at each particle size with error bars representing the standard error of the mean between the four animals in each group.

While the deposition fraction does decrease as the particle size increases, there appears to be a relative flattening of the changes between 1.0 and 3.0 μm. This is explained by the polydispersity of the aerosols in this region, as discussed by (Menache et al., 1996).

To evaluate and compare these data to existing data, the Multiple-Path Particle Dosimetry Model (MPPD version 2.0, CIIT) was used to model the predicted rat deposition fraction. The MPPD model does not have capabilities to model mouse deposition; therefore, the data shown in Figure 8 is only for the rat.

Table 3. Percent deposited dose (standard error) in each ROI for mice.

Particle (μm)	Oral/nasal	Trach/bronch	Bifurcation area	Stomach	Lungs
0.5	28.6 (2.7)	2.0 (0.7)	6.8 (1.8)	50.6 (3.9)	12.0 (0.9)
1.0	58.0 (3.7)	8.2 (1.5)	4.5 (2.0)	23.3 (4.2)	5.9 (0.6)
3.0	46.6 (4.4)	4.7 (0.9)	2.4 (1.2)	45.1 (5.0)	1.1 (0.3)
5.0	61.7 (7.8)	4.5 (1.1)	3.0 (0.8)	30.5 (7.8)	0.2 (0.0)

For the particle sizes 1.0, 3.0, and 5.0 μm, the experimental data and the MPPD modeled data are mostly in agreement. However, the MPPD modeling under-predicts the lung deposition fraction when compared to the experimental data for the 0.5 μm particle size.

Table 4. Percent deposited dose (standard error) in each ROI for rats.

Particle (μm)	Oral/nasal	Trach/bronch	Bifurcation area	Stomach	Lungs
0.5	30.6 (3.4)	18.2 (2.4)	10.5 (1.1)	8.3 (6.1)	32.4 (4.7)
1.0	34.2 (1.4)	19.8 (3.3)	6.0 (1.7)	18.7 (3.8)	21.3 (2.1)
3.0	44.8 (6.1)	18.6 (1.9)	6.0 (1.9)	10.5 (2.0)	20.1 (4.1)
5.0	56.2 (6.4)	14.1 (1.7)	12.0 (3.9)	10.4 (5.2)	7.2 (0.6)

As the MPPD models were developed using assumptions for monodisperse aerosols, our experimental data were modeled in the MPPD software using a GSD of 1.4, shown as MPPD – Monodisperse in Figure 8. Interestingly the change from the polydisperse actual aerosols to the monodisperse in the simulation didn't change the comparison between our data and the MPPD modeling.

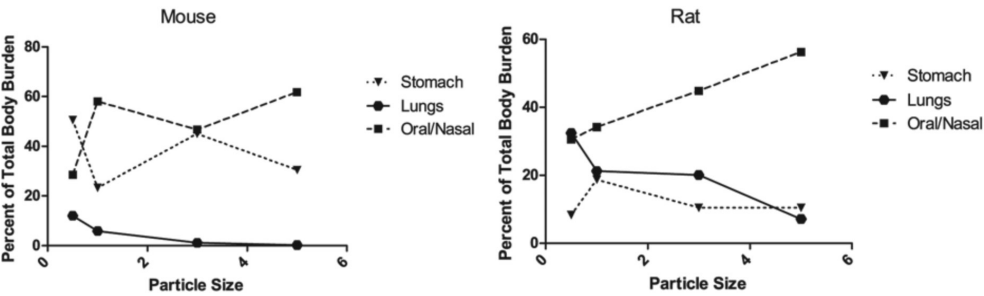


Figure 5. Mouse and rat percent of total body burden as a function of particle size.

The deposition fraction data were compared against historical data on the deposition patterns in rats and mice. A comparison to Otto Raabe’s 1988 ¹⁶⁹Y is shown in Tables 5 and 6 for mice and rats, respectively. For mice, our experimental data showed a lower deposition at the 1.0 μm particle size, greater deposition at the 3.0 μm particle size, and nearly the same deposition at the 5.0 μm particle size. For the rats, our data showed a lower deposition fraction at all particle sizes. The Raabe data were revisited by Menache et al. in 1995. Comparison of our experimental data to the Menache data suggests that our experimental data have a lower deposition fraction at the larger particle sizes (3.0 and 5.0 μm) and our experimental data have a higher deposition fraction at the lower particle sizes (0.5 and 1.0 μm). In a similar manner, the experimental data and Asgharian’s data (Asgharian et al., 2003), showed an overall increase in lung deposition as particle size decrease.

Table 5. Comparison of Raabe’s 1988 deposition fraction data to experimental data for mice.

Particle size (μm)	Raabe pulmonary deposition	Experimental deposition
0.5	NA	10.7
1.0	9.7	2.2
3.0	0.9	2.3
5.0	0.23	0.2

To address the potential causes for the differences between our experimental data and the published data, we considered the different methodologies among the studies. The primary difference for the current study when compared to results in literature is that the historical studies have all been conducted with monodisperse aerosols. The Raabe exposures were conducted for up to 45 minutes and the experimental exposures were

Table 6. Comparison of Raabe’s 1988 deposition fraction data to experimental data for rats.

Particle size (μm)	Raabe pulmonary deposition	Experimental deposition	Experimental Deposition (corrected for inhalability)
0.5	NA	12.6	13.0
1.0	8.75*	4.1	4.4
3.0	6.6	4.3	5.4
5.0	4.8	1.3	1.7

*Two data points of 6.5 and 11.0 averaged.

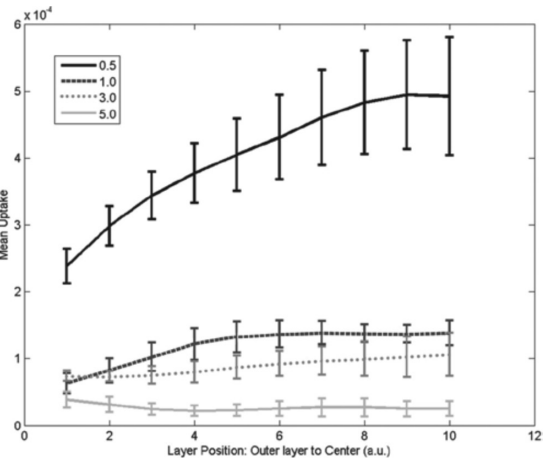


Figure 6. Mouse deposition in each slice of the Onion Model.

and this is more appropriate for application and extrapolation of today’s pharmaceutical aerosols, as they are primarily polydisperse. In the calculation of MMAD, the aerosol particles are normalized to a density of 1 g/cm³. There is insufficient data on the differences in deposition patterns of similarly sized aerosols with different densities to speculate its potential to cause the noted differences. However, it may have played a role. The potential for the calculated versus measured RMV has been highlighted above.

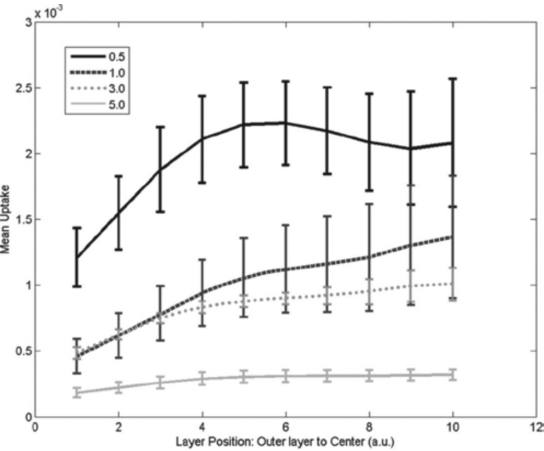


Figure 7. Rat deposition in each slice of the Onion Model.

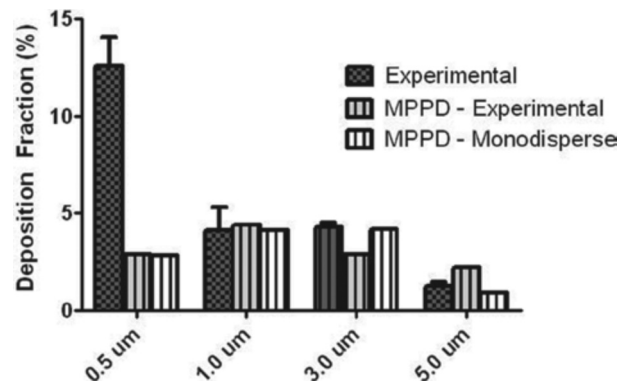


Figure 8. Rat deposition fraction from the MPPD modeling software and from the experimental data. Experimental data are shown with standard error of the mean while MPPD data are shown without error, as the model does not provide an error output.

Exposure duration differences between the studies may have also had an impact. There is a potential that the Raabe lung data may under estimate the

lung deposition because mucociliary clearance of particles was occurring throughout the 45 minute exposure duration that was used (Hofmann and Asgharian, 2003). The studies reported here used short exposure durations and sacrificed the animals immediately after exposure to minimize the impact of mucociliary clearance on the results. This does not explain the differences observed between the two studies, as the deposition reported by Raabe was generally higher than reported here.

Several previous reports have taken into account the inhalability of the material to normalize the deposited dose in rats (Menache, et al. 1995). With this correction, the deposition fraction for the aerosols is only calculated for the aerosols that are assumed to be inhaled into the respiratory tract. For small particles such as 0.5 μm, this correction is negligible. The correction for 5 and 3 micron aerosols are 65 % and 75% (Menache, et al. 1995). For our experimental data the deposition fraction for 5 and 3 μm aerosols were 1.3 and 4.3, which would change to 1.7 and 5.4 with the inclusion of the inhalability correction, Table 6. The smaller aerosols would have a smaller degree of correction, including only a 3 % correction for the 0.5 μm aerosol and a 7 % correction for the 1 μm aerosol. There are no published assumptions for the inhalability correction in mice.

The addition of the inhalability correction permits improved understanding of the deposition of material after it is inhaled. Data are often modeled with this assumption, because aerosol deposition models are linked to the particle physics and fluid dynamic assumptions once they are in the respiratory tract. While the data can be used for these comparisons once normalized for inhalability, the data emphasis of this work was to understand the dose of aerosols that are presented to the animal at different particle sizes that are considered to be respirable. These data are important for enabling species comparisons where the only known experimental data are particle size and concentration.

Overall, it is hypothesized that our experimental data are more applicable to current pharmaceutical aerosol deposition patterns than many historical data sets.

Of particular interest is the percentage of the body burden in the stomach for both species (between 23% and 50% for mice and between 8% and 19% for rats) even after a four- or five-minute exposure. The amount of material in the stomach for all mice exposures and the 3.0 and 5.0 μm rat exposures was greater than the amount in the lungs, even for these nose-only inhalation exposures. It is often believed that through the conduct of nose-only inhalation exposures, the stomach deposition is minimized or even eliminated. These data clearly confirm that even over the course of approximately 7 minutes (four- to five-minute exposures followed by immediate euthanasia) particles can be cleared from the ciliated airways of the upper and lower respiratory tract and swallowed. Moreover it is interesting that the percent of the total in the stomach is not a function of oral or nasal deposition. Specifically in the rat, as the oral or nasal deposition moves from approximately 30% to 56%, the stomach percentages remain fairly constant. It is believed that this is due to more control and uniformity of the time allowed for the particles to be cleared from their initial deposition location to the stomach. Then the amount in the stomach likely would have shown a trend where the larger particle sizes would have resulted in a higher amount

in the stomach had the animals been euthanized at a later time point.

A review of the Onion Model data indicates an increased particle deposition in the peripheral lung for the smaller particle sizes and an increased deposition in the proximal lung for the larger particle regardless of species. The regional deposition data mirror the deposition fraction data in that the difference between the deposition of the 0.5 and 1.0 μm particles is greater than the difference between the 1.0 and 3.0 μm particles despite the fact that the magnitude of the difference in size (0.5 μm versus 2.0 μm) is greater for the 1.0 and 3.0 μm particles. This is likely a function of the rodent anatomy in the efficiency that they filter materials in this range.

Conclusions

Radiolabeled aerosols of 0.5, 1.0, 3.0, and 5.0 μm MMAD were developed and validated for use in mouse and rat nose-only exposures. Analysis of the deposition patterns was conducted in two manners: macro deposition analysis, and more complex regional analysis via the developed Onion Model. Analysis of the lung deposition fraction in both species showed an increase in the lung deposition fraction as the particle size decreased. Over the size range studied, it was shown that the actual deposition fraction is different than the commonly used 10% deposition fraction.

The developed Onion Model allowed for regional deposition analysis in both species. The regional deposition analysis showed an increased lung peripheral deposition with

the smaller particles. This model of deposition analysis has been shown to facilitate a more complex regional deposition analysis that will benefit regional drug targeting in a preclinical setting.

Acknowledgments

Small-animal SPECT and CT images were generated by the Keck-UNM Small-animal imaging resource (KUSAIR) established with funding from the W.M. Keck Foundation, and supported by NCI Cancer Center Support Grant (P30CA118100-06).

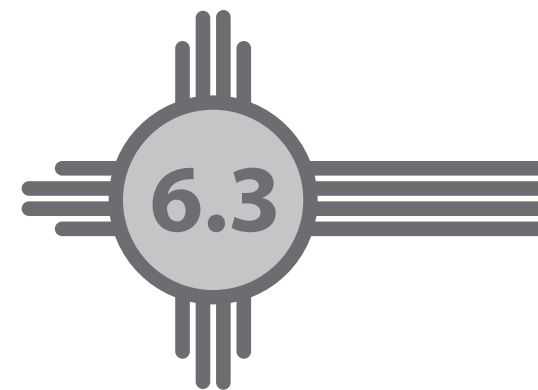
References

1. Adams WP, Ahrens RC, Chen ML, Christopher D, Chowdhury BA, Conner DP, Dalby R, Fitzgerald K, Hendeles L, Hickey AJ, Hochhaus G, Laube BL, Lucas P, Lee SL, Lyapustina S, Li B, O'Connor D, Parikh N, Parkins DA, Peri P, Pitcairn GR, Riebe M, Roy P, Shah T, Singh GJ, Sharp SS, Suman JD, Weda M, Woodcock J, Yu L. 2010. Demonstrating Bioequivalence of Locally Acting Orally Inhaled Drug Products (OIPs): Workshop Summary Report. *J Aerosol Med Pulm Drug Deliv* 23:1–29.
2. Alexander DJ, Collins CJ, Coombs DW, Gillison IS, Hardy CJ, Healey G, Karantabias G, Johnson N, Karlsson A, Kilgour JD, McDonald P. 2008. Association of Inhalation Toxicologists (AIT) working party recommendation for standard delivered dose calculation and expression in non-clinical aerosol inhalation toxicology studies with pharmaceuticals. *Inhal Toxicol* 20:1179–1189.
3. Asgharian B, Kelly JT, Tewksbury EW. 2003. Respiratory deposition and inhalability of monodisperse aerosols in Long-Evans rats. *Toxicol Sci* 71:104–111.
4. De Backer W, Devolder A, Poli G, Acerbi D, Monno R, Herpich C, Sommerer K, Meyer T, Mariotti F. 2010. Lung deposition of BDP/ formoterol HFA pMDI in healthy volunteers, asthmatic, and COPD patients. *J Aerosol Med Pulm Drug Deliv* 23:137–148.
5. Bide RW, Armour SJ, Yee E. 2000. Allometric respiration/body mass data for animals to be used for estimates of inhalation toxicity to young adult humans. *J Appl Toxicol* 20:273–290.
6. Dolovich M. 1996. *In vitro* measurements of delivery of medications from MDIs and spacer devices. *J Aerosol Med* 9 Suppl 1:S49–S58.
7. Fleming JS, Quint M, Bolt L, Martonen TB, Conway JH. 2006.
8. Comparison of SPECT aerosol deposition data with twenty-four- hour clearance measurements. *J Aerosol Med* 19:261–267.
9. Fleming JS, Epps BP, Conway JH, Martonen TB. 2006. Comparison of SPECT aerosol deposition data with a human respiratory tract model. *J Aerosol Med* 19:268–278.
10. Hofmann W, Asgharian B. 2003. The effect of lung structure on mucociliary clearance and particle retention in human and rat lungs. *Toxicol Sci* 73:448–456.
11. Kuehl P. 2009. RMV data analysis and conclusions by AIT Working Party. *Inhal Toxicol* 21:434.
12. Leach C, Colice GL, Luskin A. 2009. Particle size of inhaled corticosteroids: Does it matter? *J Allergy Clin Immunol* 124:S88–S93.
13. Leach CL, Davidson PJ, Hasselquist BE, Boudreau RJ. 2002. Lung deposition of hydrofluoroalkane-134a beclomethasone is greater than that of chlorofluorocarbon fluticasone and chlorofluorocarbon beclomethasone: A cross-over study in healthy volunteers. *Chest* 122:510–516.
14. Martin AR, Thompson RB, Finlay WH. 2008. MRI measurement of regional lung deposition in mice exposed nose-only to nebulized superparamagnetic iron oxide nanoparticles. *J Aerosol Med Pulm Drug Deliv* 21:335–342.
15. Menache MG, Raabe OG, and Miller FJ. 1996. An empirical dosimetry model of aerodynamic particle deposition in the rat respiratory tract. *Inhal Toxicol* 8:539–578.
16. Ménache MG, Miller FJ, Raabe OG. 1995. Particle inhalability curves for humans and small laboratory animals. *Ann Occup Hyg* 39:317–328.
17. Miller FJ. 2000. Dosimetry of particles in laboratory animals and humans in relationship to issues surrounding lung overload and human health risk assessment: A critical review. *Inhal Toxicol* 12:19–57.
18. Raabe OG, Al-Bayati MA, Teague SV, and Rasolt A. 1988. Regional Deposition of Inhaled Coarse and Fine Aerosol Particles in Small Laboratory Animals. *Ann Occup Hyg* 32:53–63.
19. Schlesinger RB. 1988. Biological disposition of airborne particles: Basic principles and application to vehicular emissions. In: A.Y. Watson,
20. R.R. Bates and D. Kennedy (eds.), *Air Pollution, the Automobile, and Public Health*. Washington, DC: National Academies Press, 239–298.

21. Schroeter JD, Martonen TB, Pritchard JN, and Hwang D. 2002. Airway identification within planar gamma camera images. *Ann Occup Hyg* 46:342; doi:10.1093/annhyg/46.suppl_1.342.
22. Schroeter JD, Pritchard JN, Hwang D, Martonen TB. 2005. Airway identification within planar gamma camera images using computer models of lung morphology. *Pharm Res* 22:1692–1699.
23. United States Food and Drug Administration presentation at Association of Inhalation Toxicologists, 2007. Timothy McGovern, Ph.D, Supervisory Pharmacologist, US FDA, Silver Spring, MD.
24. Weers J, Metzheiser B, Taylor G, Warren S, Meers P, Perkins WR. 2009.
25. A gamma scintigraphy study to investigate lung deposition and clearance of inhaled amikacin-loaded liposomes in healthy male volunteers. *J Aerosol Med Pulm Drug Deliv* 22:131–138.

Characterization of respiratory deposition of fluticasone/salmeterol HFA and HFA beclomethasone in asthmatics.

Chet L. Leach, PhD, Philip J. Kuehl, PhD, Ramesh Chand, MS, Loren Ketai, MD, Jeffrey P. Norenberg, PharmD, and Jacob D. McDonald, PhD



Abstract

Background: Fixed combination fluticasone/salmeterol is the most utilized anti-inflammatory asthma treatment in North America yet no studies report the actual respiratory tract dose or the distribution of drug within the lungs. Inflammation due to asthma affects all airways of the lungs, both large and small. Inhaled steroid delivery to airways results from a range of drug particle sizes with emphasis on smaller sized drug particles capable of reaching the peripheral airways. Previous studies suggested that smaller drug particles increase pulmonary deposition and decrease oropharyngeal deposition, thus potentially having both efficacy and safety implications.

Objective: This study characterized the dose of fluticasone/salmeterol HFA (Advair® HFA; particle size 2.7 µm) delivered to asthmatics and examined the drug distribution within the lungs. The results were compared to the inhalation delivery of HFA-beclomethasone (QVAR®; particle size 0.7 µm).

Methods: A cross-over study was conducted in asthmatics with commercial formulations of fluticasone/salmeterol and HFA beclomethasone radiolabeled with Technetium-99m. Deposition was measured using SPECT/CT gamma scintigraphy.

Results: 2-Dimensional planar image analysis indicated that 58% of the HFA beclomethasone and 16% of the fluticasone/salmeterol HFA deposited in the patient's lungs. Oropharyngeal cavity and the gut analyses indicated that 77% of the fluticasone/salmeterol HFA was deposited in the oropharynx compared with 35% of the HFA beclomethasone.

Conclusions: The decreased peripheral airway deposition and increased oropharyngeal deposition of fluticasone/salmeterol HFA was a result of its larger particle size.

The smaller particle size of HFA beclomethasone allowed a greater proportion of lung deposition with a concomitant decrease in oropharyngeal deposition.

Introduction

The NAEPP guidelines call for the use of monotherapy of an inhaled steroid along with a short acting beta agonist as needed for the initial treatment of mild to moderate persistent asthma.¹ However in the US, contrary to the guidelines nearly 70% of patients in this category are prescribed combination products as first line therapy.² Recently the US FDA has provided further guidance regarding treatment of persistent asthma and has placed emphasis on the use of single agent ICSs as first line therapy. The FDA has further recommended limiting the long-term use of LABAs with or without an ICS.³ The question arises as to whether there are differences between particle sizes of combination products versus monotherapies which may affect safety and efficacy.

Fluticasone/salmeterol is the most prescribed fixed combination anti-inflammatory inhaled product in North America yet there are no published studies characterizing the actual dose of drug delivered to the respiratory tract of the patients or the distribution of drug within the lungs. Fluticasone/salmeterol HFA is a metered dose inhaler combination product that is classified as a drug suspension product. Such products rely on physical micronizing the solid drug particle to as low a size as practical in order to reach the lungs and avoid oropharyngeal deposition. However there is a physical limit to the particle size to which it can be micronized Fluticasone/salmeterol HFA delivers an average particle size of approximately 2.7 microns MMAD. Previous studies have shown that similarly sized Flovent CFC™ (particle size 2.6 microns) delivered 13% of the drug to the lungs with comparatively little penetration to the peripheral lung regions.⁴ The remaining delivered dose was deposited in the oropharynx.

More recent technology has enabled some steroids to be formulated as a solution product wherein the steroid is dissolved in the propellant and by adjusting the droplet size of the spray, particles much smaller than traditional suspension technology can be generated. Thus more appropriate particle sizes optimum for total lung penetration could be produced. This optimal particle has the added benefit of reducing oropharyngeal deposition and also reduces the need for a spacer.⁵ One such solution based product is beclomethasone HFA (QVAR™). Previous studies have shown that HFA beclomethasone lung deposition ranged from 50-60% in adults, with penetration to all lung airways.^{6,7,8,9} A recent article described the importance of reaching all airways including the small airways in order to maximize treatment of inflammation sites due to asthma.¹⁰

The purpose of this open label cross-over design inhalation study in asthmatics was to characterize and compare the lung deposition of large particle fluticasone/salmeterol HFA with small particle HFA beclomethasone.

Methods

Radiolabeling

The radionuclide technetium-99m (^{99m}Tc) was used to radiolabel the formulations by the method for pressurized metered dose inhalers (pMDIs) previously described.⁴⁻⁹ Briefly, the radiolabel was extracted out of the aqueous phase in 3-pentanone, which was then added to and evaporated from an empty canister. The contents of a filled canister containing the respective formulation were added at -80°C and a valve was crimped in place. The vial was weighed, sonicated in water for 15 minutes and weighed again. When it was determined that the vial was not leaking aerosol, prestudy quality control (QC) analysis was performed to assure that the radiolabeled product matched the formulation and delivery characteristics of the original products.

Quality control analysis

To quantify the amount of radioactivity presented to each patient prior to dosing, the radiolabeled pMDI was actuated into a filter with a flow rate of 30 L/min drawn through the filter. Immediately following the actuation of one dose into the filter, the actuator, filter and stem wipe were individually placed in a dose calibrator for quantification of radioactivity.

To confirm particle size distribution, each radiolabeled pMDI was actuated into a Next Generation Impactor (NGI). The actuator, USP throat, each impactor stage and back up filter were quantified for radioactivity in a dose calibrator prior to conduct of each day's dosing. Thus the original drug dose and particle size from each canister was assured prior to patient use. The respective extracts were then held for at least 48 hours to decay prior to analysis via high pressure liquid chromatography with ultra violet detection (HPLC-UV) for drug particle size analysis.

Study design

The primary objective of this open-label, nonrandomized study was to compare lung deposition of a single dose of HFA beclomethasone versus fluticasone/salmeterol HFA pMDI. Males aged 18 to 55 classified as mild asthmatics (as per the National Asthma Education Program¹), with a forced expiratory volume in one second (FEV1) of more than 90% of predicted normal were eligible for inclusion. Patients were required to have abstained from smoking for at least one year and had to be 155-180 cm in height with a normal body weight for their height and frame size. Exclusion criteria included receiving a radiation dose within the last 12 months for clinical or diagnostic tests, unstable or clinically significant endocrine, hematological, hepatic, renal, gastrointestinal, neurological psychiatric or immunological disease known or likely hypersensitivity to fluticasone/salmeterol HFA or HFA beclomethasone or their excipients, respiratory tract infection within the 2 weeks prior to screening and/or history or current of substance or alcohol abuse. There were no restrictions on medications. This study was reviewed and approved by the University of New Mexico Medical Center Institutional Review Board.

Patients were administered one dose of the respective radiolabeled formulations. The patients inhaled using standard inhalation techniques described in the package inserts of the respective products. Breath pattern parameters (e.g. inspiration time and time to actuation) were collected each time a patient was dosed with the radiolabeled formulation in order to eliminate patient inhaler technique bias. These results showed that all patients conducted an approximate three second inhalation that initiated immediately prior to actuation of the radiolabeled pMDI. Breath holds were manually timed for each patient in order to achieve an approximate 10 second breath hold.

After the breath hold, patients were immediately subjected to a planar gamma camera scan, followed by single photon emission computed tomography (SPECT) scan, and then by a second planar scan. During one of the treatment days, patients received a computed tomography (CT) scan in order to locate the tissues in the oropharynx and thorax for future drug deposition overlays.

Analysis of planar distribution and deposition

Immediately following the dose administration, the patient was returned to the previously established position and a 45 second dynamic planar image was collected with a Siemens Symbia SPECT/CT. Acquisition was conducted with Syngo MI Applications (version 8.1.15.7). For analysis, the CT data were resampled and resized to match the voxel size and dimensions of the SPECT data. The dynamic planar data were loaded and a region mask was applied to a 2-dimensional (2D) plane. The lung regions were identified and split into left and right lobes. The lung locations were used to establish geometrical oropharyngeal and gut overlay masks. Therefore, the final mask consisted of four distinct regions - left lung, right lung, oropharyngeal region, and gut.

3D SPECT analysis

Analysis of the 3-dimensional (3D) data was conducted using an in-house Lung Onion Model analyzing topographic thinning. In this model a seeded automatic 3D segmentation routine was used to extract the lung and airway regions from the CT. The seed point of the onion, identified from the co-registered CT image overlay, was the primary bronchus for each right and left lung section. From this seed point, a topographic thinning model was applied to look at the deposition of radioactivity as a function of the distance from the seed point. Imaging data were then normalized for the inhaled dose so that all presented data represent dose fractions for direct correlation to dose.

C to P ratio analysis

An analysis of the central (C) to peripheral (P) deposition (C to P ratio) was conducted on the 3D data as has been previously described.¹¹ In this, the lung was segmented into two regions (C and P) with the C region making up 33% of the lung area and the P region comprising 67% of the lung area. The fraction of the lung dose in each region was then determined and used in the equation below to calculate the C to P ratio.

$$C \text{ to } P \text{ ratio} = \left(\frac{\text{Fraction in Central Region}}{\text{Fraction in Peripheral Region}} \right)$$

Statistical analysis

In order to compare the Region of Interest (ROI) analysis, a Wilcoxon matched-pairs signed rank test (paired, two-tailed T test with 95% confidence interval) was used to compare the average dose fraction for each product. Differences were determined to be statistical for $p < 0.05$.

Results

A seven patient cross-over study was conducted with commercial formulations of HFA beclomethasone (40 mcg beclomethasone dipropionate per actuation) and fluticasone/salmeterol HFA® (115 mcg fluticasone propionate and 21 mcg salmeterol per actuation), each radiolabeled with ^{99m}Tc. Prior to patient dosing, a validation of the radiolabeling procedure was conducted to ensure the fidelity of the radiolabel to the respective drug. These results of these procedures showed that the particle size distribution of the original product was not altered for either HFA beclomethasone or fluticasone/salmeterol HFA after labeling with ^{99m}Tc (Figures 1 and 2).

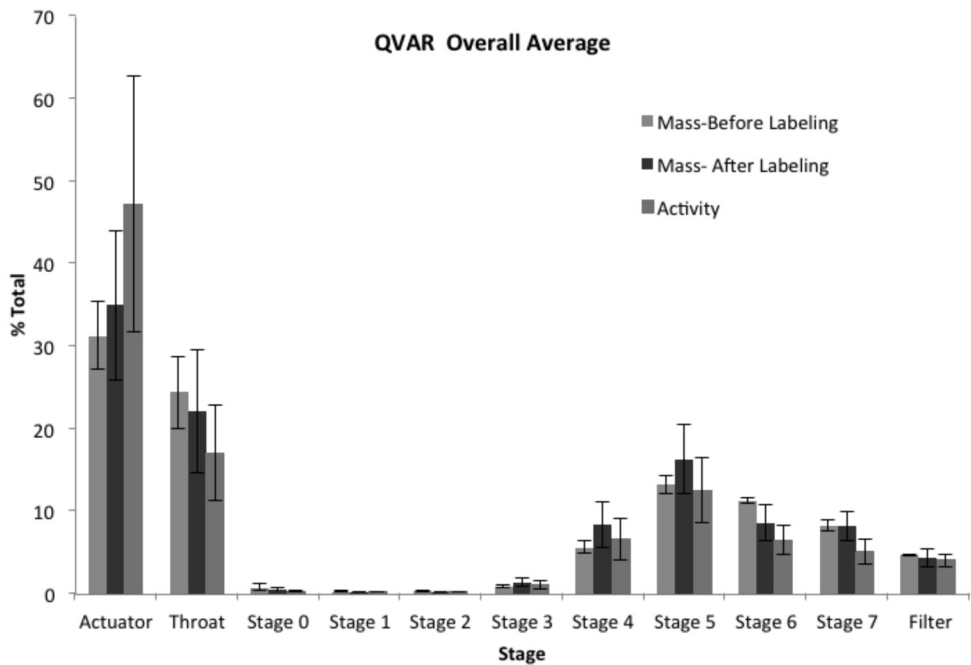


Figure 1. Overall average of pre and post dose particle size analysis for HFA beclomethasone on all study days.

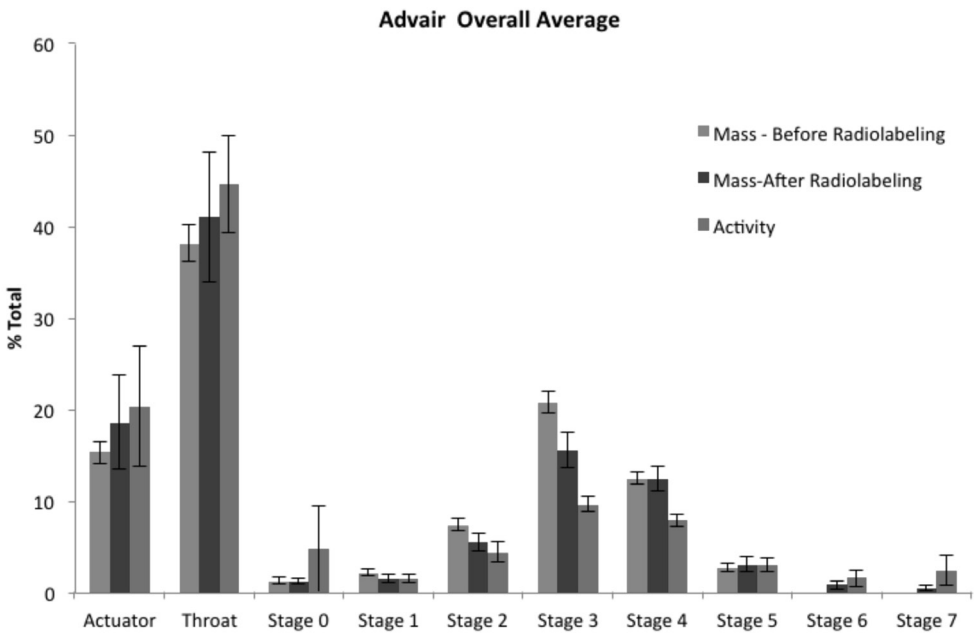
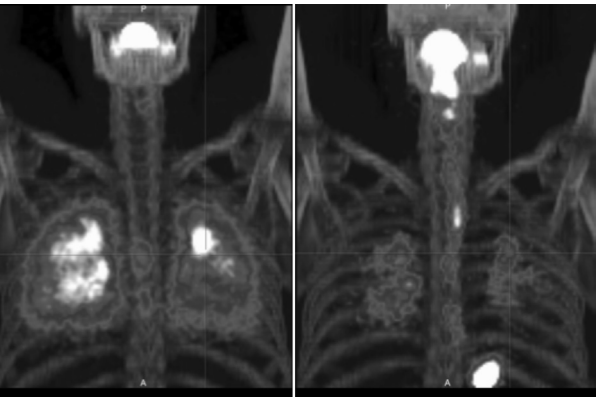


Figure 2. Overall average of pre and post dose particle size analysis for fluticasone/salmeterol HFA on all study days.

Planar analysis and deposition

Quantitative image analysis HFA beclomethasone and fluticasone/salmeterol HFA 2D images was conducted to determine the percentage of the dose in the lungs (right lung added with the left lung), the oropharynx and gut and the amount exhaled. Qualitative inspection of the images initially showed different deposition patterns. Examples of the HFA beclomethasone and fluticasone/salmeterol HFA planar deposition patterns for a representative patient are shown in Figure 3. These images showed a more complete central and peripheral coverage of the lungs with HFA beclomethasone when directly compared with fluticasone/salmeterol HFA.



The individual patient lung dose and oropharynx and gut dose fraction data are shown in Figure 4. Analysis of the 2D images showed that overall average of 58% of the HFA beclomethasone dose deposited

Figure 3. Example deposition patterns of HFA beclomethasone (left image) and fluticasone/salmeterol HFA (right image) for the same patient.

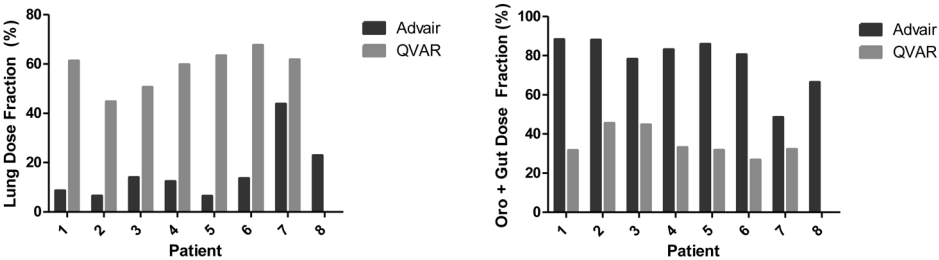


Figure 4. Direct comparison of dose fraction for the lung and oropharynx + gut for all patients with the 2D data. Note patient 8 only received fluticasone/salmeterol HFA and not HFA beclomethasone.

in the lungs of the patients compared with 16% for fluticasone/salmeterol HFA ($p < 0.05$). Similarly, analysis of the oropharyngeal cavity and the gut indicated that 77% of the Fluticasone/salmeterol HFA dose was deposited in the oropharynx, while only 35% of the HFA beclomethasone dose initially deposited in the oropharynx ($p < 0.05$).

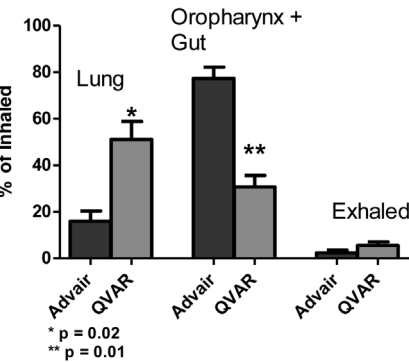


Figure 5. Summary data of all patients imaged following HFA beclomethasone and fluticasone/salmeterol HFA dose administration for the 2D data.

0.008) for fluticasone/salmeterol HFA when compared with HFA beclomethasone.

3D SPECT analysis

The 2D data was used to evaluate initial deposition for both the head and thorax regions and the 3D date was used to determine within lung deposition comparisons such as the C/P analyses. Quantitative image analysis of the 3D images was conducted to determine the percentage of the drug in the

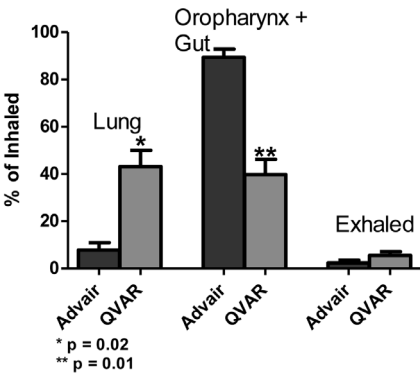


Figure 6. Summary data of all patients imaged following HFA beclomethasone and fluticasone/salmeterol HFA dose administration for the SPECT data.

Table 1. Patient Central (C) to Peripheral (P) lung fractions (x 100) and C to P ratios.

Patient ID	HFA-BDP C Fraction	HFA-BDP P Fraction	HFA-BDP C to P	Fluticasone/salmeterol HFA C Fraction	Fluticasone/salmeterol HFA P Fraction	Fluticasone/salmeterol HFA C to P
1	55	45	1.2	64	36	1.8
2	41	59	0.7	59	41	1.5
3	64	36	1.8	61	39	1.5
4	72	28	2.6	93	7	12.4
5	72	28	2.5	84	16	5.1
6	35	65	0.5	94	6	16.5
7	67	33	2.0	21	79	0.3
8	—*	—	—	21	79	0.3
Mean			1.6	Mean		4.9
SD			0.8	SD		6.2

*Not performed

lungs (right lung added with the left lung), the oropharynx, the gut and the amount exhaled. The individual patient lung and oropharynx plus gut dose fraction data consistently showed for all patients that the dose fraction deposited in the lung was greater for HFA beclomethasone, with a higher dose fraction of fluticasone/salmeterol HFA being deposited in the oropharynx and gut.

The individual 3D SPECT patient data were averaged and analyzed via a paired T test (Wilcoxon matched-pairs signed rank test) shown in Figure 6. These analyses indicated that there was a significantly greater amount of lung deposition from the HFA beclomethasone formulation when compared with the fluticasone/salmeterol HFA formulations ($p = 0.016$). Further the oropharynx plus gut deposition was significantly greater ($p = 0.008$) for fluticasone/salmeterol HFA when compared to HFA beclomethasone.

The fraction of the lung dose in each of the C and P regions for HFA beclomethasone and fluticasone/salmeterol HFA is shown in Table 1. These data demonstrated an increase in the C to P ratio for fluticasone/salmeterol HFA which is the result of decreased deposition in the peripheral regions of the lung. The time required for the initial 2D scan was less than 60 seconds. However the time required for the 3D scans was approximately 12 minutes. These 12 minutes were enough time for oropharyngeal clearance through oral and gut membranes to begin to affect the total mass balance of drug to be calculated. Thus the 2D analyses were considered most appropriate for initial deposition numbers when comparing lung with oropharyngeal dose deposition. The 3D analyses were considered most appropriate for within lung deposition determinations such as the C/P analyses.

Discussion

Asthma is a disease of the entire respiratory tract. Inflammation occurs in all airways, both large and small, even in the case of mild and moderate asthmatics. It is generally known that steroids work best when they are targeted directly to the sites of inflammation. Figure 7 represents a lung scan from a typical adult male. There is not the necessary resolution to display the small airways but the large and intermediate airways are grossly visible. It is clear that on a gross level anywhere where there is lung tissue, there are airways. Given the fact that inflammation from asthma is present in all airways, it is to be expected that inhaled steroids would be most effective if the entire lung was covered by the radiolabeled steroid. The results illustrated by Figure 3 show that the small particle HFA beclomethasone formulation covered all airways in the lungs as opposed to the large particle fluticasone/salmeterol HFA formulation which covered primarily the central airways, similar to the coverage obtained from Flovent radiolabeled studies previously reported.⁴ This central deposition of large particle inhaled steroids is reflected by the results illustrated in Table 1 where the ratio of central lung deposition to peripheral deposition



Figure 7. Lung scan of an adult male subject depicting large and intermediate size airways.

was much higher and more variable for fluticasone/salmeterol HFA compared with HFA beclomethasone.

It is hypothesized that greater overall lung deposition with a small particle ICS may have implications for both safety and efficacy. Many clinical studies have supported this benefit. Beclomethasone CFC (BecliventTM) is the same drug (i.e. beclomethasone dipropionate) contained in QVAR. They differ primarily in particle size with HFA beclomethasone being about 1 micron and Beclovent be-

ing about 3.5 microns. Several studies^{12,13,14} conducted in moderate to severe asthmatics showed that asthma control was effectively maintained at half the dose of the small particle HFA beclomethasone compared with Beclovent, despite using FEV_1 as the primary variable, a measure known to be insensitive to small airways function. When using FEF_{25-75} (presumed to be a better measure of small airways function) in one study¹⁴, it was calculated that for a given dose of HFA beclomethasone it would require 3.2-fold more dose of Beclovent to provide the same improvement. This hypothesis of requiring less dose of a small particle inhaled steroid was recently confirmed in a large retrospective study of asthmatics in the UK.¹⁵ The data showed that 82% of the patients were well controlled on a prescribed and assumed HFA beclomethasone dose of 339 ug/day without long acting beta agonists or combination products compared with 79% of patients being controlled on a prescribed and assumed Flovent dose of 574 ug/day. Thus based on prescribed doses, equivalent control required approximately twice the dose of Flovent compared with HFA beclomethasone, a result most likely due to the improved lung deposition with HFA beclomethasone. Additional supportive studies have also shown that markers of inflammation such as exhaled nitric oxide were improved in HFA beclomethasone treated patients who exhibited significantly less exhaled alveolar nitric oxide than patients using large particle beclomethasone.¹⁶ Finally a recent large retrospective clinical study comparing HFA beclomethasone with large particle beclomethasone CFC showed that patients were more likely to achieve asthma control with HFA beclomethasone and HFA beclomethasone was effective at controlling asthma at half of the dose of beclomethasone CFC.¹⁷

This study shows that smaller, more optimized inhaled steroid particles can deposit more drug to the lungs with better distribution within the airways and less deposition in the oropharynx than larger particle inhaled steroids. Based on drug deposition overlays on lung tissue, this optimized particle hypothesis appears to support the clinical benefit of small particle formulations observed in studies cited above.

Acknowledgments

The authors wish to thank the following persons for their invaluable technical assistance in conducting this study: Gabriel Candelaria, Rosemarie Wilson and Tamara Anderson.

References

1. National Asthma Education and Prevention Program Expert Panel Report 2: Guidelines for the Diagnosis and Management of Asthma. National Institutes of Health, National Heart, Lung and Blood Institute. NIH Publication 1997;97-4051.

2. Friedman HS, et al. Clin Ther. 2008;30:1908-1917.

3. Chowdhury BA, Dal Pan G. The FDA and safe use of long-acting beta-agonists in the treatment of asthma. N Engl J Med. 2010;362(13):1169-1171.

4. Leach CL, Davidson PJ, Hasselquist BE, Boudreau RJ. Lung deposition of HFA-Beclomethasone is greater than that of CFC-fluticasone and CFC-beclomethasone: A cross-over study in healthy volunteers. Chest 2002;122 (2): 510-516.

5. Leach CL, Davidson PJ, Boudreau RJ. Improved airway targeting with the CFC-free HFA-beclomethasone metered dose inhaler compared with CFC-beclomethasone. Eur Res J 1998;12:1346-1353.

6. Leach CL. Effect of formulation parameters on hydrofluoroalkane-beclomethasone dipropionate drug deposition in humans. J. Allergy Clin Immunol 1999;104:S250-252.

7. Leach CL, Davidson PJ, Hasselquist BE, Boudreau RJ. Influence of particle size and patient dosing technique on lung deposition of HFA-beclomethasone from a metered dose inhaler. J Aerosol Med 2005;18(4): 379-385

8. Leach CL, Colice GL, Luskin A. Particle size of inhaled steroids: Does it matter? J Allergy Clin Immunol 2009;124:S88-93.

9. Leach CL, Colice GL. A pilot study to assess lung deposition of HFA-beclomethasone and CFC-beclomethasone from a pressurized metered dose inhaler with and without add-on spacers and using varying breathhold times. J Aerosol Med 2010;23(6):355-361.

10. Gelfand EW, Kraft M. The importance and features of the distal airways in children and adults. J Allergy Clin Immunol 2009; 124:S84-7.

11. Smaldone GC, Walser L, Perry RJ, Ilowite JS, Bennett WB, Greco M. Generation and administration of aerosols for medical and physiological research studies. J Aerosol Med 1989; 2(2): 81-87.

12. Gross G, Thompson PJ, Chervinsky P, Vanden Burt J. Hydrofluoroalkane-134a beclomethasone dipropionate, 400 microg. is as effective as chlorofluorocarbon beclomethasone dipropionate, 800 microg for the treatment of moderate asthma, Chest 1999;115:342-51.

13. Davies RJ, Stampone P, O'Connor BJ. Hydrofluoroalkane-134a beclomethasone dipropionate extrafine aerosol provides equivalent asthma control to chlorofluorocarbon beclomethasone dipropionate at approximately half the total daily dose. Respir Med 1998;92(suppl A):22-31.

14. Busse WW, Brazinsky S, Jacobson K, Stricker W, Schmitt K, Vanden Burt J, et al. Efficacy response of inhaled beclomethasone dipropionate in asthma is proportional to dose and is improved by formulation with a new propellant, J Allergy Clin Immunol 1999;104:1215-22.

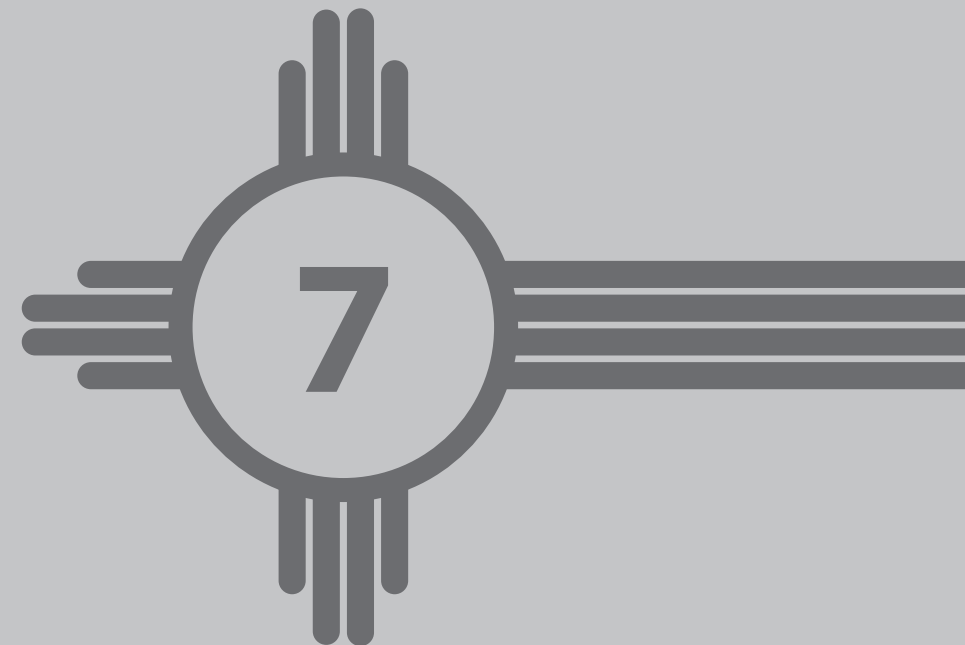
15. Price D, Martin RJ, Barnes N, Dorinsky P, Israel E, Roche N, et al. Prescribing practices and asthma control with hydrofluoroalkane-beclomethasone and fluticasone: a real world observational study. J Allergy Clin Immunol. 2010;126:511-8.

16. Nicolini G, Chetta A, Simonazzi A, Tzani P, Aiello M, Olivieri D. Both bronchial and alveolar exhaled nitric oxide are reduced with extrafine beclomethasone dipropionate in asthma. Allergy Asthma Proc 2010;31:e85-90.

17. Barnes N, Price D, Colice G, Chisolm A, Dorinsky P, et al. Asthma control with extrafine-particle hydrofluoroalkane-beclomethasone vs. large-particle chlorofluorocarbon-beclomethasone: a real-world observational study. Clin Exp Allergy 2011;Jul 14, doi:10.1111/j.1365-2222.2011.03820.x10:1-12.

A Performance Evaluation of 90Y Dose Calibrator Measurements in Nuclear Pharmacies and Clinics in the United States

Michael K. Schultz PhD, Jeffrey T. Cessna BS, Tamara L. Anderson BS, James A. Ponto MS,
Neil Petry MS, Richard J. Kowalsky PharmD, Matthew R. Palmer PhD, Uwe F. Beinlich PhD,
Chaitanya R. Divgi, MD, Jeffrey P. Norenberg PharmD



Abstract

A blind performance test was conducted to evaluate dose calibrator measurements at nuclear pharmacies in the United States (US). Two test-sample geometries were chosen to represent those used for measurements of ^{90}Y -ibritumomab tiuxetan (ZEVALIN®). The radioactivity concentration of test samples was verified by the US National Institute of Standards and Technology. Forty-five results were reported by 10 participants. Eighty percent of reported values were within the US Pharmacopoeia content standard ($\pm 10\%$) for ^{90}Y -ZEVALIN®. All results were within US Nuclear Regulatory Commission conformance limits ($\pm 20\%$) for defining therapeutic misadministrations.

Introduction

The application of targeted radiotherapy techniques for treatment of human cancer continues to increase. These techniques promise enhanced treatment options not only for malignancies refractory to traditional chemotherapy, but also as a primary therapeutic option (Maloney and Press, 1998; Allen et al., 2004; Connors, 2005; Kaminski, et al., 2005). To ensure that the radioactivity dose administered to the patient is within prescribed limits, a radioactivity measurement is performed prior to administration of the drug. In most cases, this measurement is performed in the radiopharmacy or nuclear medicine clinic. Thus, the safety and effectiveness of these radiopharmaceuticals for patients depend on, among other factors, the ability of these facilities to make accurate radioactivity measurements.

To promote good radioactivity measurement practice, ongoing “measurement assurance” programs (MAPs) are commonly administered by regulatory and standards organizations. A MAP can be defined as an ongoing series of measurement performance tests that are administered by a recognized standards organization. For nuclear medicine facilities, several such programs are administered outside of the United States (US; Oropesa et al., 2005). The purpose of these programs is to improve radioactivity measurement accuracy and precision and provide for a linkage between routine measurements and national standards (Oropesa et al., 2005). In the US, the National Institute of Standards and Technology (NIST), under an agreement with the Nuclear Energy Institute (NEI) has operated a MAP for radiopharmaceutical manufacturers since the mid-1970's (Golas, 1982; Golas and Calhoun, 1983; Golas, 1998). In the NEI/NIST Program, traceability of radioactivity measurements to national standards is demonstrated by radiopharmaceutical manufacturers through ongoing-blind proficiency testing using NIST Standard Reference Materials (SRM's; Cavallo et al., 1979; Golas et al., 1983; Golas, 1998). Test-samples are manufactured, calibrated, and distributed to participating laboratories, where radioactivity measurements are conducted. To demonstrate measurement proficiency, participants make required measurements and report the results for each test to NEI, which evaluates the reported values (relative to NIST certified values) and returns an official report to the participant. The program has operated successfully for approximately 30 years (Cavallo et al., 1979; Golas, 1982; Golas et al., 1983; Golas, 1998). On the other hand, recent efforts to monitor the proficiency of radioactivity measurements conducted in US radiopharmacies and nuclear medicine clinics have been minimal. Prior to the current study, the most recent evaluations of radioactivity measurements performed in these facilities were carried out by NIST (then known as the National Bureau of Standards, NBS) from 1970 through 1980 at the request of College of American Pathologists (CAP) and the US Atomic Energy Commission (AEC, now known as the US Department of Energy, DOE; Golas, 1982; NCRP, 1985). No such ongoing MAP exists for evaluating radioactivity measurement performance of nuclear medicine clinics and radiopharmacies in the United States today.

In this work, a performance test (referred to as the NRQMP0305 performance test) of ⁹⁰Y dose-calibrator measurements conducted in US radiopharmacies and nuclear medicine clinics is described. The test was administered by the NIST in collaboration with the National Association of Nuclear Pharmacists (NANP). Study design and an analysis of the reported results are highlighted. The feasibility of an ongoing measurement-assurance program for radioactivity measurements in US radiopharmacies and nuclear medicine clinics is examined.

Materials and Methods

Performance Test Description

The NRQMP0305 performance test was a blind test — an estimate of the activity level was provided for informational purposes to each participant, but the certified activities were unknown. A total of 11 facilities agreed to participate in this study. Ten participants reported results of measurements to NIST (Table 1). Measurements were conducted using dose calibrators located within the participating radiopharmacies and/or within the clinical facilities serviced by the radiopharmacies. The intention of the organizers was to select a group of nuclear medicine facilities that represents (to the extent possible) a reasonable cross-section of nuclear medicine facilities in the US.

A commercial radionuclide manufacturer (QSA Global, Inc., Burlington, MA US; formerly AEA Technologies, GmbH, Braunschweig, Germany) prepared and distributed all test-samples to participants for this study. Participants were instructed to perform measurements according to “routine” procedures for measurements of ⁹⁰Y-ZEVALIN®. In summary, participants received the materials through normal channels, unpacked the samples, made requested measurements, recorded the results, completed the enclosed reporting forms and returned the report forms, and test-samples to NIST for certification. No decay correction was required for reporting measurement results. There appeared to be some ambiguity in initial reporting forms, where the reporting field for analysis results for each measurement was identified by the heading “Readout (MBq)”. Consequently, in some cases results were reported without the required multiplication factors to convert the “readout” of the dose calibrator to actual “activity”. To remedy this apparent ambiguity in reporting fields, an updated reporting form was sent to all participants. In this updated reporting form, the field was identified more precisely as the “Prescribed Activity (MBq)”. Participants were instructed to update the values that were originally reported and to return the updated values to NIST (including a description of the conversion factors used to convert the instrument readout to the activity value).

Reference Time and Uncertainties

All radioactivity values presented in this paper are as of the reference time 17 March 2005 12:00 PM Eastern Standard Time (EST). All evaluations of uncertainties adhere to accepted conventions used by the NIST Radioactivity Group and are in concordance with those recommended by the principal metrology standards organizations (Taylor and Kuyatt, 1994; ISO, 1995). All individual uncertainty components are given as estimated experimental standard deviations (or standard deviations of the mean, if appropriate), or quantities assumed to correspond to standard deviations, regardless of the method used to evaluate their magnitude. Unless otherwise stated explicitly, all uncertainties cited in this paper are “standard uncertainties,” corresponding to a one uncertainty interval.

Table 1 List of participants that reported results for the NRQMP0305 performance test.

Participant	Organization/Location
William Baker, PhD	Pharmaceutical & Diagnostic Services West Valley City, Utah
George H. Hinkle, RPh, BCNP, FASHP, FAPhA	Ohio State University Medical Center Columbus, Ohio
Joseph C. Hung, PhD, BCNP	Mayo Clinic Rochester, Minnesota
Richard J. Kowalsky, PharmD, BCNP, FAPhA	University of North Carolina Chapel Hill, North Carolina
Jeffrey P. Norenberg, PharmD	University of New Mexico Albuquerque, New Mexico
Matthew R. Palmer, PhD	Beth Israel Deaconess Medical Center Boston, Massachusetts
Neil Petry, RPh, MS, BCNP, FAPhA	Duke University Medical Center Durham, North Carolina
James A. Ponto, MS, RPh, BCNP, FAPhA, FASHP	University of Iowa Hospitals and Clinics Iowa City, Iowa
Timothy Quinton, PharmD, MS	Radiopharmacy, Inc. Evansville, Indiana
Peter A. Rice, RPh, BCNP	Massachusetts General Hospital Boston, Massachusetts

For verification measurements conducted at NIST, all solution transfers were performed using disposable high-density polyethylene pycnometers (Canus Plastics, Ottawa, Ontario, Canada) to minimize effects of evaporation during transfers and mass measurements. Gravimetric measurements were performed by determining the difference in pycnometer

weights before and after transfers of activity solutions and diluents. A six-decimal-place microbalance (model M5, Mettler-Toledo, Toledo, OH, US) was employed for all gravimetric measurements made at NIST. Appropriate air-buoyancy and balance-tare corrections were made for each gravimetric measurement. The resulting uncertainty from balance measurements is estimated to be approximately 0.05%.

Test Samples

Test samples were prepared so as to represent the composition and geometries provided as part of the "kit" for preparing and dispensing the radiopharmaceutical ⁹⁰Y-ibritumomab tiuxetan (ZEVALIN[®]) at the time of this performance test. Half lives and nuclear data were adopted from current-published sources (Kossert and Schrader, 2004, Table 2). The test-sample geometries were 10 mL ⁹⁰Y solution in a 10-mL reaction vial (RV) and a ⁹⁰Sr/⁹⁰Y source designed to simulate 4 mL ⁹⁰Y solution in a 10-mL plastic syringe (TS). The RV is identical to reaction vials supplied as part of the ⁹⁰Y-ZEVALIN[®] kit (Witzig et al., 2003; ENSDF, 2005).

Table 2 Half lives and uncertainties (Unc) used for decay corrections and activity calculations (29-30).

Radionuclide	Half Life (Unc)
⁹⁰ Y	64.053 ± 0.020 hours
³ H	12.32 ± 0.02 years
⁹⁰ Sr	28.79 ± 0.06 years

Individual RV solutions were prepared by dispensing 1 mL (nominally) of ⁹⁰Y stock solution (⁹⁰Y chloride, ⁹⁰YCl₃) in 0.1 mol L⁻¹ hydrochloric acid (HCl) to each reaction vial and diluting to a nominal total volume of 10 mL with a solution of 25 mg mL⁻¹ stable Y³⁺ as YCl₃ in 0.1 mol L⁻¹ HCl. A precise determination of the mass of dispensed solution was made in each case. Previous comparisons of calibration factors for dose calibrators reveal no apparent dependence on solution composition for ⁹⁰Y (whether as chloride 1 mol L⁻¹ HCl or the ⁹⁰Y-ZEVALIN[®] drug product, Zimmerman et al., 2004). To minimize the variability in dose calibrator response arising from differences in the volume contained in each RV, dispensed-solution volumes were held constant to within 0.2% (calculated as the relative standard deviation of the grand average for all dispensed RV solutions). The precision of dispensed volume was controlled by automated volumetric dispensing using a model Microlab 500B auto-dispensing system (Hamilton, Inc., Bondaluz, Switzerland). Confirmatory mass measurements of dispensed volumes were conducted using a digital microbalance (Sartorius model LA230S) with a readability of 0.1 mg (Sartorius AG, Goettingen, Germany). The total activity dispensed to each reaction vial was approximately 1.5 GBq as of the reference time.

The TS is a long-lived ⁹⁰Sr/⁹⁰Y enclosed-sealed calibration source (model number SIM.SY2 ⁹⁰Sr/⁹⁰Y Transfer Standard, QSA Global), constructed in a 10-ml syringe geometry (in an aluminum casing, Thieme et al., 2004). The device is designed to simulate the dose calibrator response resulting from the use of a 10-ml plastic Becton Dickinson Luer-Lok[™] type syringe (BD syringe, model number 300192, Becton, Dickinson and Company, Franklin Lakes, NJ US) containing 4 mL ⁹⁰Y solution (approximately 1.2 GBq equivalent). The design utilizes the bremsstrahlung radiation produced as a result of the ⁹⁰Sr/⁹⁰Y beta-particle interactions with the syringe materials, source holder, and construction material of the dose-calibrator ionization chamber. Thus, the ⁹⁰Y-simulated-total activity is instrument

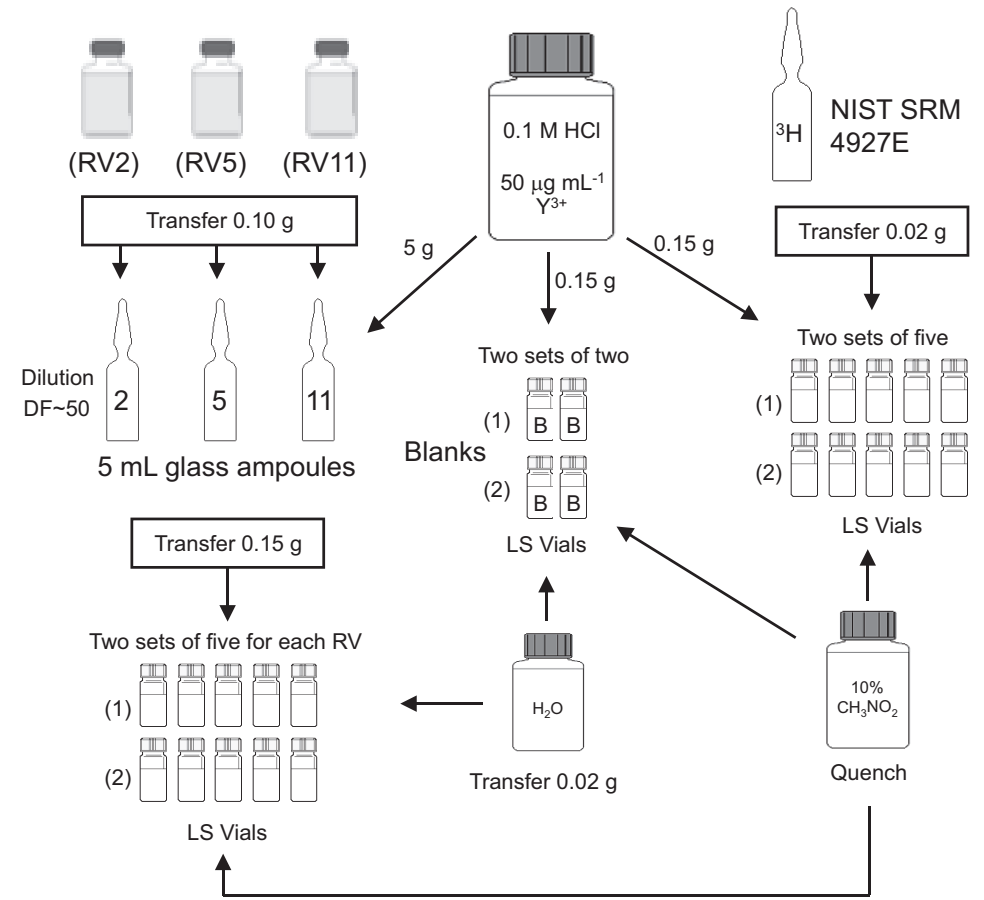


Figure 1 Flow diagram depicting preparation of ⁹⁰Y, ³H, and Blank (B) sources for liquid scintillation (LS) counting using NIST Standard Reference Material ³H in water (H₂O) SRM 4927E. Two sample sets were prepared for ⁹⁰Y, ³H, and Blank (signified by numbers 1, 2). Sample sets differed in LS cocktail employed (Set 1: ReadySafe[™]; Set 2: Opti-Fluor[™]). Arrows indicate transfer of solutions. Masses shown are approximate values. RV solutions were diluted by a factor (DF) of 50. Matrix matching of liquid scintillation sources was accomplished by matching H₂O, stable yttrium (Y³⁺) carrier, and hydrochloric acid (0.1 M HCl) fractions as shown. Effect of quench was monitored by addition of known amounts (1 to 8 drops per sample) of nitromethane (CH₃NO₂, diluted to 10% volume:volume concentration with ethanol) to all samples.

dependant. Although the device was designed specifically for use with the Capintec Model CRC-15R dose calibrator (Capintec, Inc., Ramsey, NJ US), the current study extends the use of the device to two other dose calibrators (Capintec model CRC-12; and Biodex model AtomLab 100, Biodex Medical Systems, Shirley, NY US; Table 3). The intended purpose of the device is for calibrations required for the ⁹⁰Y-ZEVALIN® procedure (Witzig et al., 2003; Thieme et al., 2004).

Table 3 Summary of dose calibrators employed, number of results submitted for Reaction Vial and Transfer Standard measurements and NIST determined dial settings for available dose calibrators for the NRQMP0305 comparison test.

Reaction Vial-RV (10-mL fill volume)		
Dose Calibrator	Number of Results [‡]	NIST Dial Setting [§]
CRC-4*	1	NA
CRC-5R*	2	NA
CRC-7*	1	NA
CRC-12*	2	(39±1) x 10
CRC-15R*	16	(39±1) x 10
CRC-15W*	1	NA
CRC-30BC*	1	NA
CRC-127R*	2	NA
Transfer Standard-TS (4-mL fill volume)		
Dose Calibrator	Number Results [‡]	NIST Dial Setting [§]
CRC-12*	2	(58±1) x 10
CRC-15R*	16	(52±1) x 10
Atomlab 100 [†]	1	382±2

*Manufactured by Capintec, Inc.
†Manufactured by Biodex Medical Systems.
‡Number of reported results submitted by participants for each model.
§Dial setting determined by NIST
||NA signifies that the model was not available at NIST.

Test-Sample Activity Certifications

All test samples were returned to NIST for radioactivity certification and verification following measurements at the participants' facilities. The CIEMAT (Centro de Investigaciones Energéticas, Medioambientales y Tecnológicas de España)/NIST method of tritium (³H) efficiency tracing of matrix-matched liquid-scintillation (LS) counting sources was employed for activity determination of the RV solution (Fig. 1; Zimmerman et al., 2004). LS sources were prepared from a secondary dilution of three randomly-selected RV's (RV2, RV5, RV11). Two separate LS-sample sets were prepared using ReadySafe™ (Beckman-Coulter, Inc., Fullerton, CA US) and Opti-Fluor™ (PerkinElmer Life Sciences, Inc., Shelton, CT, US) LS cocktails. Five LS-sources were prepared for each cocktail for RV's and ³H samples (Fig. 1). Two blanks were prepared for each cocktail. Sources (n=44 total) were counted for 10 cycles, in 10 minute count-time intervals, using a model number LS7800 liquid-

scintillation counter (Beckman Coulter) for a total count time of approximately 3 days. After allowing sufficient time (>60 days) for the decay of unsupported ⁹⁰Y, the level of ⁹⁰Sr impurity present in the RV solutions was determined in a separate experiment using the same LS measurement approach. The ⁹⁰Y-activity value (as determined by LS counting) was then used to determine dial settings for two dose calibrator models available at NIST (Capintec models CRC-12 and CRC-15R), according to previously published methods (Thieme et al., 2004; Zimmerman et al., 2004). Reagents were American Chemical Society (ACS) grade or equivalent. High-purity acids were used for preparation of carrier solution (Fisher Scientific International, Hampton, NJ, US). Stable Y³⁺ carrier solution was prepared by volumetric dilution of NIST SRM 3167a (NIST, Gaithersburg, MD, US).

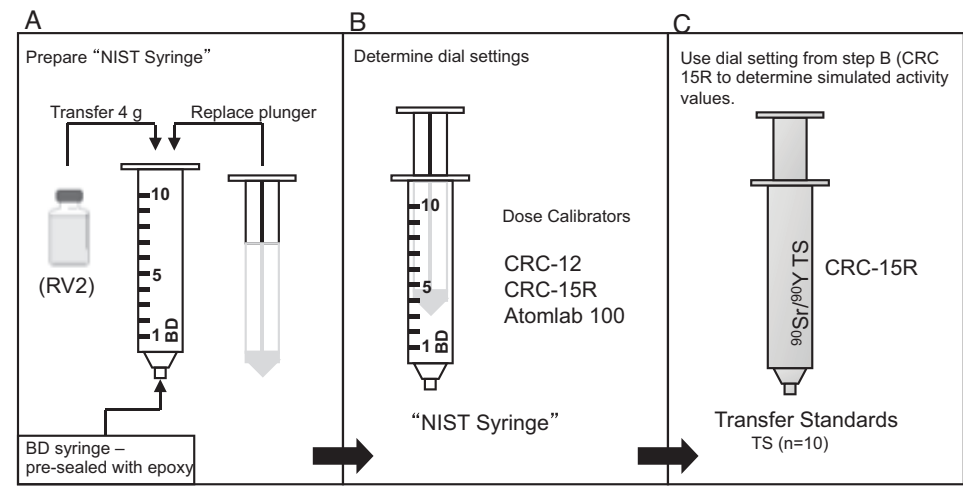


Figure 2 A. Depiction of the preparation of the "NIST Syringe". A four gram (g) aliquot (nominally) of Reaction Vial 2 (RV2) ⁹⁰Y solution was transferred (and weighed precisely) to a 10 mL BD syringe. The hypodermic needle had been removed and the Luer Lok™ fitting had been sealed previously with epoxy. Following transfer of solution the plunger was replaced for counting in dose calibrators B. Dial settings were then determined in each of three dose calibrator models. C. Finally, the total-simulated ⁹⁰Y activity of the Transfer Standards (TS, n=10) was obtained by use of the dial setting derived from step B using the model CRC-15R dose calibrator at NIST.

The total volume contained in each RV was approximately 10 mL. A verification of the activity concentration for individual RV's was carried out by direct measurements utilizing the NIST 4πγ Ionization Chamber ("Chamber A", Calhoun, 1987). For this purpose, two precisely-weighed aliquots of each returned RV (approximately 5 g each) were transferred to individual 5-mL glass ampoules. Exceptions were RV2 and RV6. In the case of RV2, a single 5-mL ampoule of RV2 solution was prepared for verification measurements. The remainder of RV2 solution was used to prepare the "NIST Syringe" — used to determine dial settings for TS-simulated-activity determinations (Fig. 2; preparation described below). Dose calibrator dial-setting determinations conducted at NIST were carried out using the

unopened RV2 prior to preparation of the verification source and the NIST syringe. The methodology employed has been described previously (Thieme et al., 2004; Zimmerman et al., 2004). RV6 was not returned in time for ampoule preparation. Each ampoule (n=21) was counted for 20 cycles of approximately 10 seconds each in Chamber A. The average decay-corrected value for total activity (corrected for blank and background) is then divided by the precisely-determined mass of the transferred solution for each ampoule to obtain the activity concentration for each RV. The activity concentration of the RV solution, as determined by LS counting, was confirmed by comparison to the average activity concentration as determined by Chamber A measurements of the 5-mL ampoules. Vial-to-vial variability (heterogeneity) of the RV solution was characterized by examining the standard deviation of the activity concentration as determined by Chamber A measurements of the prepared 5-mL glass ampoules.

TS simulated-total activities were determined for each TS by comparison to a 10-mL BD syringe, filled with a precisely-weighed aliquot (approximately 4 mL) of a solution transferred directly from test sample RV2 ("NIST Syringe", Fig. 2). To prepare the NIST Syringe, the piston was removed from a BD syringe and the Luer-Lok™ fitting was sealed with a carefully-placed drop of fast-sealing epoxy (Hardman™, Harcros Chemicals, Belleville, NJ; Thieme et al., 2004). Solution from RV2 was transferred to the syringe and the piston replaced for counting. When reinserting the piston, a thin-metal wire was positioned along the inner wall of the syringe to allow escape of the air-volume displaced as the piston is replaced. The derived-total-activity value of the transferred solution is based on the

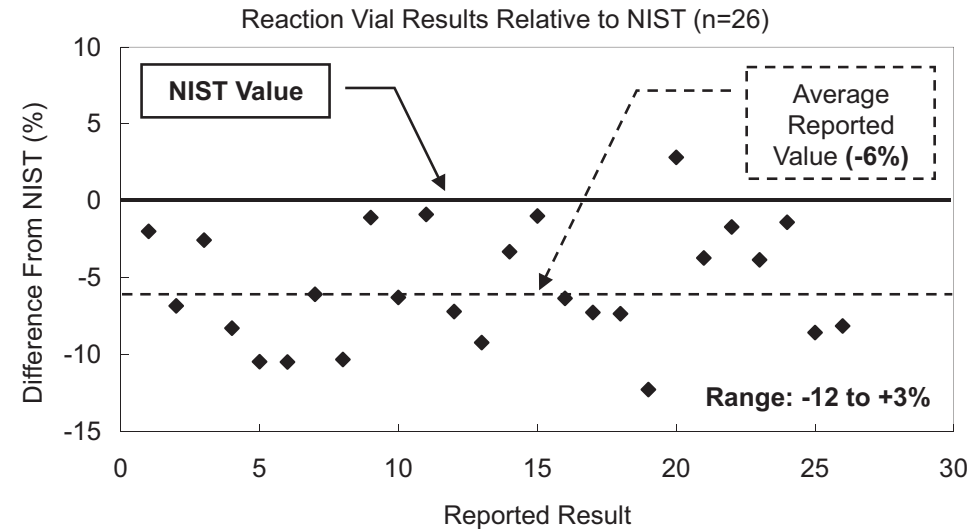


Figure 3 Comparison of reported results (n=26) of the Reaction Vials to the "NIST Certified Value" for the NRQMP0305 comparison test. An overall average bias of -6% was observed with a standard deviation of 4% and range of -12% to +3%.

activity concentration value determined by LS counting of RV solutions and the mass of solution transferred to the NIST Syringe (Fig. 1-3). The derived-total activity value was then used to determine dial settings for three dose calibrator models available at NIST (Capintec models CRC-12 and CRC-15R; and Biodex model Atomlab 100), according to previously published methods (Thieme et al., 2004; Zimmerman et al., 2004). These dial settings were then used to determine the NIST-certified value for each TS. The reported values were compared to the NIST-certified value to assess the accuracy of the reported result. The approach allowed the direct comparison of each TS to a NIST-certified radioactivity solution in the geometry the TS is designed to simulate.

Statistical Analyses

Reported results for this study were compared to a NIST-certified value as a measure of the accuracy of the measurements at the individual laboratories. Bias in a measurement result is defined by the percent difference from the NIST value (relative to the NIST value). The mean, standard deviation, and range of measurement results are reported separately for RV and TS results. A statistical test was employed to confirm that the use of mean-centered statistics was reasonable (i.e., that the data are normally distributed). The test employed was a normal probability regression technique, which uses the correlation coefficient (R) as a test statistic (Filliben, 1975). The approach entails ranking the submitted values (in the present study, normalized to the NIST value) in ascending order, plotting the data versus the normal order statistic medians (NORM), performing a least-squares regression, and comparing the resulting regression coefficient (R) to a numerically-determined "critical value" (V_c). The V_c represents a theoretical-threshold for testing the hypothesis of normality (within familiar confidence levels). For this study, all comparisons of V_c 's to calculated values for R were made at the 95% confidence level. Critical values were obtained from published tables (Filliben, 1975). Calculated values for R were obtained using the PEARSON function in the software program Microsoft® Excel™ (Version 2002 SP2, Microsoft Corporation, Redman, WA US) and confirmed by comparison to values obtained using NIST internally-developed software. Comparisons of R values obtained from these two sources agreed to within $\pm 0.1\%$. For a given confidence level, the V_c approaches unity as the population size increases. In the assessment of the "normality" of a given dataset, the value of R is compared to the numerically-determined V_c . For a given distribution of related numbers (such as normalized reported measurement results), a value of R that is greater than the numerically-determined V_c indicates that the distribution of reported results appears to be "normal" and mean-centric statistical analysis is reasonable (Filliben, 1975). On the other hand, a value of R that is less than the V_c is an indication that the dataset has "non-normal" characteristics (e.g., presence of outliers).

Results

NIST Certifications and Dial Settings

The NIST certified value of ^{90}Y activity concentration of the RV solution was determined (as of the reference time by LS measurements) to be $1.54\text{E}+8 \text{ Bq g}^{-1} \pm 1.10\text{E}+6 \text{ Bq g}^{-1}$, where the uncertainty is an expanded uncertainty, which represents an approximate 95% confidence interval (coverage factor of $k = 2$). Included component uncertainties are: LS counting (^{90}Y) source to source (0.10%); LS counting cycle to cycle (0.10%); half life propagation (^{90}Y , 0.28%); effect of the background standard deviation on ^{90}Y count rate (0.002%); live time (LS counting, 0.10%); possible impurities (0.01%); gravimetric measurements (LS sources, 0.05%, vial preparation, 0.05%); and dilutions (0.09%). The certified activity concentration is corrected for minimal ^{90}Sr impurity. The ratio of ^{90}Sr Bq g^{-1} : ^{90}Y Bq g^{-1} at the reference time was determined by a separate liquid-scintillation counting procedure to be approximately $3.4\text{E}-7$.

Based on these results, dial settings of $(39 \pm 1) \times 10$ and $(39 \pm 1) \times 10$ were determined for dose calibrator models CRC-12 and CRC-15R respectively (Table 3). The uncertainties are the combined standard uncertainties arising from instrument readout instability, curve fitting, and the results of replicate measurements.

Results of the Chamber A measurements of the prepared ampoules confirm the liquid scintillation results. The average activity concentration, based on Chamber A results is $1.52\text{E}+8 \text{ Bq g}^{-1} \pm 1.67\text{E}+6 \text{ Bq g}^{-1}$, representing an average difference of -1.3% from the value determined by LS measurements. The uncertainty is an expanded uncertainty ($k = 2$). Included component uncertainties are: gravimetric measurements (0.05%); radium reference source ratio (0.10%); source positioning uncertainty (0.10%); and the relative standard deviation of the average activity concentration obtained from counting 21 ampoules (0.53%). Based on the relative standard deviation of the average activity of ampoule counting results, solution heterogeneity can be characterized as negligible.

The NIST certified value of ^{90}Y -total activity of the NIST Syringe was determined to be $6.45\text{E}+8 \text{ Bq g}^{-1} \pm 4.68\text{E}+6 \text{ Bq g}^{-1}$, where the uncertainty is an expanded uncertainty ($k=2$). The value is based on the results of the RV-solution ^{90}Y activity-concentration determination by LS counting and the mass measurement of the solution transferred to the plastic syringe (4.197199 g, Fig. 2). The uncertainty comprises all uncertainties arising from the determination of the NIST-certified value for the RV solution activity concentration as well as uncertainty arising from gravimetric measurement (0.05%) of the solution transferred to the NIST Syringe.

Based on the NIST-certified value for the NIST Syringe, dial settings of $(58 \pm 1) \times 10$, $(52 \pm 1) \times 10$, and 382 ± 2 were determined for dose calibrator models CRC-12, CRC-15R, and Atomlab100 respectively, where the uncertainties are the combined standard uncertainties

arising from instrument readout instability, curve fitting, and the results of replicate measurements (Table 3).

Reported Results

Ten laboratories submitted a total of 45 individual measurement results for this exercise (26 RV, 19 TS). All reported results were within conformance limits of $\pm 20\%$ published by the US NRC for defining misadministration of therapeutic doses (25). The average bias for all reported RV results, when compared to the NIST-certified value at the reference time is -6% with a standard deviation of 4%, and a range of -12% to +3% (Fig. 3). An examination of the results (normalized to the NIST value) by normal probability regression analysis indicates that the distribution is not non-normal ($R = 0.983 > V_c = 0.956$). Of the 26 RV measurement results reported to NIST, four values (approximately 15%) fall outside of the content standard published by USP ($\pm 10\%$) for ^{90}Y -ZEVALIN® (26).

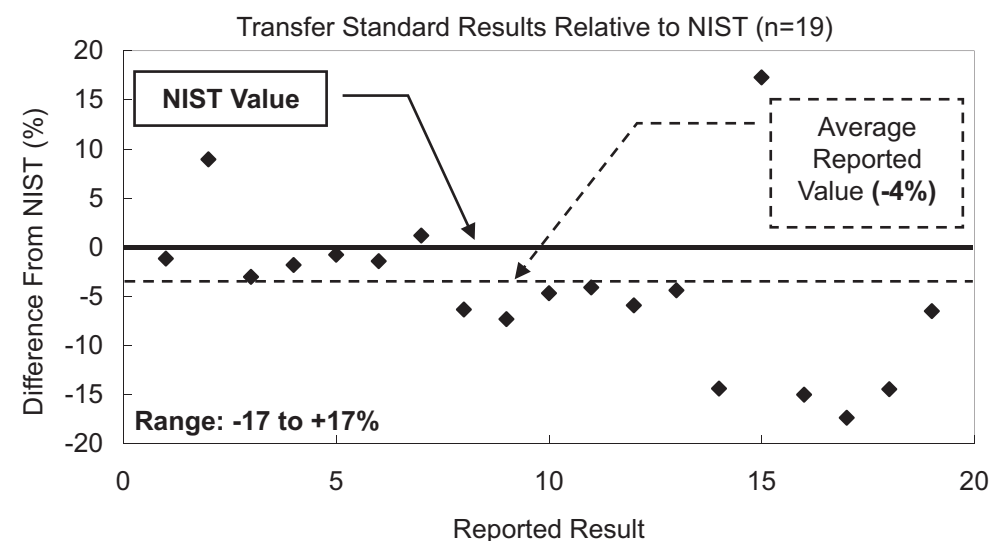


Figure 4 Comparison of reported results ($n=19$) of the Reaction Vials to the "NIST Certified Value" for the NRQMP0305 comparison test. An overall average bias of -4% was observed with a standard deviation of 8% and range of -17% to +17%.

A similar distribution of results was obtained through the analysis of the reported TS measurements compared to the NIST-certified values. The average bias for all reported TS results is -4%, with a standard deviation of 8%, and range of -17% to +17% (Fig. 4). The results appear to be normally distributed ($R = 0.954 > V_c = 0.948$). Five reported results (26% of submitted values), lie outside of the content standard published by USP ($\pm 10\%$) for ^{90}Y -ZEVALIN® (26).

Discussion

Laboratory Performance

The size and scope of this pilot performance test is small when compared to the size of the entire population of nuclear medicine clinics and radiopharmacies in the US. Further, the instructions provided with the performance testing samples (although intended to represent "routine" procedures) may not reflect precisely the standard operating procedures of individual laboratories. Nonetheless, the results of this test can be considered as guidelines, within which the value of an on-going measurement assurance program can be examined.

The calculated average of reported results (relative to the NIST values) for the RV and TS measurements are within the acceptable limits ($\pm 20\%$ of prescribed dose) codified in NRC Regulations (NRC, 2005). However, a substantial number ($n=9$) of the combined measurements ($N=45$) result in an activity determination that is beyond the content standard limits of $\pm 10\%$ outlined in USP for ^{90}Y ibritumomab tiuxetan (USP, 2005). The cause for errant reported values is unclear. Reporting forms distributed with the test-samples for this exercise included a field, in which a description of the instrument quality-control procedure employed by the participant was requested. The field requested a description of the quality assurance procedures, including check-source identification, radionuclide employed, and the procedure used for checking the instrument used. All participants reported the use of an instrument quality-control procedure (prior to measurements) using a ^{137}Cs check source. Two of the 10 participants reported the use also of a ^{57}Co source for monitoring the daily stability of the instrument. All participants reported that quality control limits were met prior to conducting measurements for this study. Although these quality control measurements may be appropriate as system checks or calibrations for certain radionuclides, no relationship can be established between the accuracy of ^{90}Y (in the measurement geometries of the test) and the results of these system performance checks conducted prior to measurements for this test.

The results showed no statistically-significant relationship to the dose-calibrator model employed for measurements in this performance test. All results submitted to NIST for RV measurements were conducted using instruments manufactured by the same company (Capintec, Inc.). Sixteen of 26 reported reaction-vial measurement results were obtained by use of a single dose calibrator model (Table 3). The number of results reported for remaining dose calibrator models employed was small. Similarly, of the 19 results submitted for TS measurements, 16 values were obtained by participants using the same model dose calibrator (Table 3).

Perhaps the most obvious characteristic of the reported results is the persistent negative bias when compared to the NIST value. Participants indicated that the manufacturer of the ZEVALIN® drug product (Biogen IDEC, Inc.) provided instructions for carrying out

calibrations of dose calibrators prior to distributing the radiopharmaceutical to pharmacies. Although it is possible that the persistent negative bias is the result of an error introduced by the manufacturer during the initial calibration of dose calibrators for the ZEVALIN product, quantification of the relationship is not possible based on the results of this test. All participants in this intercomparison test had also participated in a measurement training/certification program provided by the manufacturer of the ZEVALIN® drug product (Biogen IDEC, Inc.) prior to this test. Further, the average bias of results for each of the geometries is within acceptable limits found in USP and NRC regulations. On the other hand, a significant number of experimental results (20%) fell outside of content standards published by USP for preparing and dispensing ^{90}Y ibritumomab tiuxetan.

Pilot Test Evaluation

Measurement assurance programs are an effective tool for monitoring the radioanalytical-measurement performance of medical laboratories (Herrera and Paras, 1983; Debertin and Schrader, 1992; Woods et al., 1996; Szorenyi et al., 1998; Iwahara et al., 2002; dos Santos et al., 2004; Oropesa et al., 2005). The technique has been demonstrated to be effective in evaluating individual laboratory performance and identifying the presence of variances related to instrument performance and technical procedures. The test described in this paper represents a pilot exercise designed not only to assess the current state-of-the art in measurement capabilities of nuclear medicine facilities in the US, but also to evaluate the feasibility of implementing an ongoing program for these institutions. In evaluating the success of the present pilot test, certain drawbacks in the design and implementation (and possible solutions to the difficulties) must be pointed out.

Based on an analysis of the current test, definite improvements to the reporting format would be necessary for a successful ongoing program. For example, although an attempt was made to capture the procedures used to determine the reported values, the actual calibration procedure used for obtaining the dial settings used for activity estimation by the participants was not asked for explicitly. This hinders the ability of the organizers to assist participants in making necessary adjustments to calibration procedures on a timely basis. Successful measurement assurance programs demonstrate the need for continuous communication with the administrators of the program (Herrera and Paras, 1983; Debertin and Schrader, 1992; Woods et al., 1996; Szorenyi et al., 1998; Iwahara et al., 2002; dos Santos et al., 2004; Oropesa et al., 2005). Most importantly, the infrastructure for delivering a timely response to the participants must be improved in order to rapidly identify difficulties in measurements and offer timely guidance for improvements to be implemented.

Conclusions

A blind proficiency test was conducted to evaluate the performance of nuclear medicine facilities in making dose calibrator measurements. The study was conducted by NIST in collaboration with the NANP, a commercial radioisotope manufacturer and 11 nuclear medicine facilities. Test-sample geometries were chosen to represent typical geometries used in preparing and dispensing the radiopharmaceutical ^{90}Y -ZEVALIN®. All test samples were returned to NIST for activity verification and certification. All reported values were within the $\pm 20\%$ conformance limits published by the US NRC for defining therapeutic dose misadministration. On the other hand, 20% of reported values fell outside of the $\pm 10\%$ content limits specified by USP for ^{90}Y -ZEVALIN®. An identifiable negative bias was revealed for measurements of ^{90}Y in the syringe (-4%) and reaction vial (-6%) geometries. Participants indicated that calibration instructions were provided by the radiopharmaceutical manufacturer, but details for the precise method for determination of dial setting (at individual sites) was not obtained. The average bias of the reported results (RV and TS) fall within acceptable limits (NRC and USP). All participants reported that quality control radioactivity standard sources (^{137}Cs and ^{57}Co) were measured prior to measurements performed for this test. Reporting forms indicated that quality-control acceptance criteria were met in all cases. Based on these results, no relationship can be established between the accuracy of ^{90}Y radioactivity determinations (in the measurement geometries of the test) and the results of system performance tests conducted prior to measurements. Instructions provided for the NRQMP0305 performance test were prescriptive. It is possible that unintended bias may have been introduced due to instructed-deviations from normal operating procedures of the participants. Future tests are to include a more detailed questionnaire that will enable the organizers to evaluate more effectively the difference between routine procedures and performance testing sample measurements.

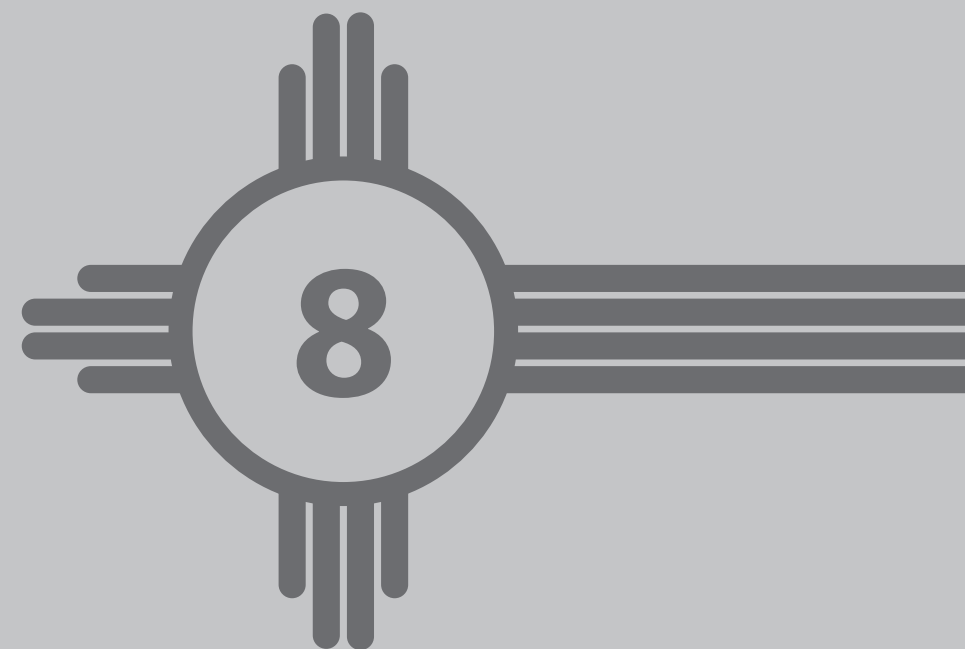
This performance test can be considered a guide, within which the value of an ongoing measurement assurance program for nuclear medicine pharmacies and clinics can be evaluated. Within this context, clearly improvements can be made to the accuracy and precision of measurements conducted in these facilities. An ongoing measurement assurance program, whereby measurement performance of facilities is monitored on an ongoing basis (e.g., quarterly), may provide the necessary feedback for laboratories to maintain accurate calibrations for the radionuclides and measurement geometries performed in their labs. On the other hand, for such a program to be effective, the responsiveness of the administering organization must be rapid.

References

1. Allen, B., Raja, C., Rizvi, S., et al. 2004. Targeted alpha therapy for cancer. *Phys. Med. Biol.* 49 (16), 3703-12.
2. Calhoun, J.M., 1987b. Radioactivity calibrations with the 4p gamma ionization chamber and other radioactivity calibration capabilities. NBS Special Publication 250-10. National Bureau of Standards. Library of Congress catalog No. 87-619870.
3. Cavallo L.M., Golas, D.B., Mann, W.B., 1979. The traceability program for radiopharmaceuticals at the National Bureau of Standards. *Atomic Energy*. July-October, 55-57.
4. Connors, J.M., 2005. Radioimmunotherapy — a hot new treatment for lymphoma. *N Engl J Med.*, Feb 3, 352 (5), 496-498.
5. Debertin, K., Schrader, H., 1992. Intercomparisons for quality assurance of activity measurements with radionuclide calibrators. *Nucl. Instr. Meth.*, A312, 241-245.
6. dos Santos, J.A., Iwahara, A., de Oliveira, A.E., et al. 2004. National intercomparison program for radiopharmaceutical activity measurements. *Appl. Rad. Iso.*, 60, 523-527.
7. ENSDF, 2005. Evaluated Nuclear Structure Data File, www.nndc.bnl.gov/nndc/nudat. United States Department of Energy National Nuclear Data Center, Brookhaven National Laboratory, Upton, NY, US.
8. Filliben, J.J., 1975. The probability plot correlation coefficient test for normality. *Technometrics*, 17 (1), 111-117.
9. Golas, D.B., 1982. Traceability programs for nuclear medicine. In: *Proceedings of a meeting on traceability for ionizing radiation measurements. National Bureau Standards Special Publication 609*. Library of Congress catalog No. 81-600197, 99-110.
10. Golas, D.B., Calhoun, J.M., 1983. US National Bureau of Standards Atomic Industrial Forum Radioactivity Measurements Assurance Program. *Int. J. Nucl. Med. Biol.*, 10 (2/3), 163-168.
11. Golas, D.B., 1998. NIST Radiopharmaceutical Standard Reference Materials and the NEI/NIST Radiopharmaceutical Measurement Assurance Program. *Appl. Rad. Iso.*, 49 (4):329-334.
12. Herrera, N.E., Paras, P., 1983. Q-Series. The College of American Pathologists Surveillance of activity (dose) calibrators. *Int. J. Nucl. Med. Biol.*, 10 (1-2), 107-110.
13. ISO, International Standards Organization. 1995. Guide to the expression of uncertainty in measurement. ISO, Geneva, Switzerland. ISBN 92-67-101188-9.
14. Iwahara, A., de Oliveira, A.E., Tauhata, L., et al. 2002. Performance of dose calibrators in Brazilian hospitals for activity measurements. *Appl. Rad. Iso.*, 56, 361-367.
15. Kossert, K., Schrader, H., 2004. Activity standardization by liquid scintillation counting and half-life measurements of ^{90}Y . *Appl. Rad. Iso.*, 60, 741-749.
16. Kowalsky, R.J., Johnston, R.E., Chan, F.H., 1977. Dose calibrator performance and quality control. *J. Nuc. Med. Tech.*, 5 (1), 35-40.
17. Maloney, D.G., Press, O.W., 1998. New treatments for non-Hodgkins lymphoma: monoclonal antibodies. *Oncology*, Oct., 12 (10), 63-76.
18. NCRP, 1985. Measurement assurance, standards, traceability and the statement of uncertainty. *A Handbook of Radioactivity Measurements Procedures. NCRP Report No 58*. ISBN: 0-913392-71-5., 332-349.
19. NRC, 2005. US Nuclear Regulatory Commission, Code of Federal Regulations, Medical Use of Byproduct Material, 10 CFR (Part 35), 562-609.
20. Oropesa, P., Hernandez, A.T., Serra, R., Varela, C., 2005. Comparisons of activity measurements with radionuclide calibrators — A tool for quality assessment and improvement in nuclear medicine. *Appl. Rad. Iso.*, 63, 493-503.

21. Szorenyi, A., Vagvilgyi, J., Zsinka, A., 1998. Experiences of fifteen years on metrological supervision of radionuclide calibrators used in nuclear medicine. *Appl. Rad. Iso.*, 49 (9-11), 1459-1461.
22. Taylor, B.N., Kuyatt, C.E., 1994. Guidelines for evaluating and expressing the uncertainty of NIST measurement results. NIST Technical Note 1297.
23. Thieme, K., Beinlich, U., Fritz, E., 2004. Transfer standard for beta decay radionuclides in radiotherapy. *Appl. Rad. Iso.*, 60, 519-522.
24. USP, 2005. United States Pharmacopoeia. Yttrium Y-90 ibritumomab tiuxetan injection; *USP28*, Official Monograph, 2044-2045.
25. Witzig, T.E., White, C.A., Gordon, L.I., Wiseman, G.A., Emmanoulides, C., Murray, J.L., Lister, J., Multani, P.S., 2003. Safety of Yttrium-90 Ibritumomab Tiuxetan Radioimmunotherapy for relapse low-grade, follicular, or transformed Non-Hodgkin's lymphoma. *J. Clin. Onc.*, April, 21 (7), 1263-1270.
26. Woods, M.J., Keightley, J.D., Ciocanel, M., 1996. Intercomparison of ^{67}Ga solution sources in UK hospitals. National Physical Laboratory Report CIRA(EXT)012. National Physical Laboratory, Centre for Ionizing Radiation, Teddington, UK.
27. Zimmerman, B.E., Cessna, J.T., Millican, M.A., 2004. Experimental determination of calibration settings for plastic syringes containing solutions of ^{90}Y using commercial dose calibrators. *App. Rad. Iso.*, 60, 511-517.

Summary and conclusions



Summary

As a result of the tremendous advances in our understanding of molecular biology, genomics, and proteomics, efforts to apply these advances to personalized molecular medicine have greatly increased. In turn, these advances have fueled a growing emergence of targeted molecular imaging and therapy using radioligands. In order to harness the tremendous promise of these applications, increased efforts are necessary to more effectively translate novel probes from pre-clinical to clinical applications. The work presented herein, describes novel strategies to improve targeted molecular imaging and therapy. Through careful deconstruction of the ligand-radionuclide-imaging application trilogy, each component may be optimized to produce a net gain in safety and efficacy. Thus, examination of the complex system can be more easily and thoroughly examined by reduction to accounts of the individual constituents or components. The aim of the studies described in this thesis was to apply novel strategies to optimize molecular imaging and radionuclide therapy.

Chapter 2 describes several novel approaches designed to affect targeted therapy using high-LET (linear energy transfer) radionuclides. The high-LET α -particle emitter ^{213}Bi -DOTATOC was shown to be significantly more potent than the lower-LET β -particle emitter ^{177}Lu -DOTATOC in vitro due to the high-LET alpha emission and enhanced effects on mitotic and apoptotic cell killing. At equivalent radiation absorbed doses, ^{213}Bi -DOTATOC was 3-4-fold more therapeutically effective than low-LET ^{177}Lu -DOTATOC in killing pancreatic adenocarcinoma cells in vitro due to its higher relative biological effectiveness (RBE). In vivo, ^{213}Bi -DOTATOC demonstrated dose-related antiproliferative effects without significant renal toxicity, and no other acute or chronic toxicity.

Radiation absorbed dose estimates predict that ^{213}Bi -DOTATOC is capable of delivering clinically useful anti-proliferative and tumoricidal doses of radiation to SSTR-expressing tumors without radiation-induced toxicity to non-target organs. This is markedly different than the dose-limiting radiation-induced toxicity observed following PRRT with ^{90}Y -, ^{111}In -, and ^{177}Lu -DOTATOC. Thus, ^{213}Bi -DOTATOC remains the most promising targeted therapeutic radiopharmaceutical agent for PRRT of sstr-expressing tumors and warrants further evaluation in the treatment of neuroendocrine tumors. These studies demonstrate the superior safety and efficacy of high-LET ^{213}Bi -DOTATOC.

Chapter 3 describes strategies to enhance PRRT of SSTR-expressing tumors using gemcitabine to up-regulate SSTR expression and to act as a radiosensitizer through cell cycle modulation. In tumor cells treated with gemcitabine for 4 days, followed by 4 days of recovery and additional growth, the uptake of ^{177}Lu -DOTATOC was 1.5-3 times higher than untreated control cells. The combination of gemcitabine and SSTR-targeted PRRT is a strategy that resulted in the delivery of higher doses of the radioligand to the target. The observed response to gemcitabine exposure also suggests that further optimization may be possible through chronotherapy, to align PRRT with the maximum SSTR expression following gemcitabine treatment.

Chapter 4 describes efforts to target leukocyte function-associated antigen-1 (LFA-1), an important integrin cell-surface receptor expressed on leukocytes that bind to intracellular adhesion molecule-1 (ICAM-1) on antigen-presenting cells and functions as an adhesion molecule. LFA-1 is the first to bind T-cells to antigen-presenting cells. The restricted expression of LFA-1 and its pivotal role in inflammation and immune diseases has created great interest in LFA-1 as a target of drug therapy. This has also provided opportunities for targeted molecular imaging and therapy using the LFA-1 targeted radioligand DOTA-butylamino-NorBIRT.

Chapter 5 describes the preclinical development of a novel, estrogen receptor-targeted estradiol derivative for imaging breast and endometrial cancers. This work reports a new structural class of neutral tridentate $^{99\text{m}}\text{Tc}$ -(I)-estradiol-pyridin-2-yl hydrazine derivatives that demonstrate high affinity for GPR30, an atypical estrogen-like receptor expressed in many cancers. This novel GPR30-targeted radioligand showed receptor-mediated uptake in human breast adenocarcinoma MCF-7 tumors and in biodistribution studies. However, the poor lipophilicity indicates that further structural modifications are needed to optimize these compounds to improve their utility in molecular imaging and therapy.

The development of novel imaging strategies to evaluate pulmonary drug delivery are presented in Chapter 6. In these studies, novel 3D topographic image analysis techniques were developed to allow quantitative assessment of aerosol deposition using small-animal SPECT/CT imaging. These methods were subsequently validated in rats and mice, and then translated to humans. These optimized and validated quantitative techniques allowed SPECT/CT imaging in asthmatic patients to clearly demonstrate the decreased peripheral airway deposition. Increased oropharyngeal deposition of fluticasone/salmeterol HFA was a result of its larger particle size, while the smaller particle size of HFA beclomethasone allowed a greater proportion of lung deposition with a concomitant decrease in oropharyngeal deposition. This demonstrates that pharmacokinetics predisposes pharmacodynamics. In other words, drugs must reach their intended target tissues in order to impart their desired effect. This is a particularly operative precept in targeted molecular imaging and therapy.

Chapter 7 describes efforts to optimize the measurement of ^{90}Y -radiopharmaceuticals used in targeted therapy. The importance of accurate and reproducible radioactivity measurement techniques cannot be overestimated as one attempts to understand the dose response of PRRT. Acknowledging that both safety and efficacy are linked to dose, one thereby accepts that sound measurement techniques are paramount to advancing our understanding of the dose response and optimizing patient outcomes following PRRT.

Future outlook

The future of targeted molecular imaging and therapy appears very promising. The continued advancement of proteomics and pharmacogenomics usher in a new era in drug discovery and development. Theranostics have arrived.

The ability to effect alpha therapy using ^{213}Bi conjugated to SSTR-targeting peptides appears very promising. The demonstrated safety and efficacy are compelling. However, the extremely limited amount of the ^{225}Ac parent radionuclide currently available now limits the clinical evaluation of all ^{213}Bi -labeled radioligands. Several groups in Europe, Russia, and the US are proposing new production methods aimed at improving the availability of ^{225}Ac . As of this writing, the lack of availability of ^{225}Ac poses a frank barrier to the development of ^{213}Bi -DOTATOC, an otherwise very promising therapy.

The future of GPR30-targeted ligands for molecular imaging and radionuclide therapy is also a mixture of promise and defeat. The initial radioligand described in this work proved highly lipophilic and unsuitable for in vivo molecular imaging. The expression of the GPR30 target receptor is restricted to intracellular and intranuclear domains. This presents great challenges to in vivo administration for molecular imaging and radionuclide therapy. Further work is underway to develop targeted ligands capable of crossing the cell membrane to reach these intracellular receptors.

The most promising ligand among those discussed in this thesis appears to be DOTA-butylamino-NorBIRT targeting LFA-1 expression. This novel small-molecule has demonstrated high specificity for LFA-1 expression and very rapid clearance. This molecular imaging agent shows great promise in imaging sites of occult infection, inflammation, and immune cell trafficking. Studies are now underway evaluating ^{68}Ga -DOTA-butylamino-NorBIRT for PET imaging in a wide variety of small-animal models of disease. The results of our initial experience with ^{111}In - and ^{213}Bi -DOTA-butylamino-NorBIRT for SPECT molecular imaging and therapy have resulted in two issued patents. Several additional patent applications are currently under examination, which limits the ability to discuss in greater detail herein.

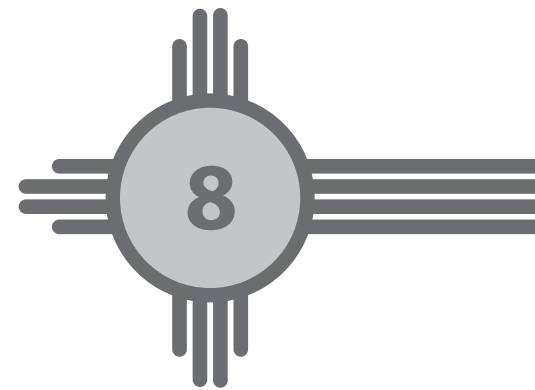
The future of molecular imaging to aid in the evaluation of novel drug formulations is also very bright. Understanding that pharmacokinetics predisposed pharmacodynamics and off-target toxicities, many are interested in the more precise delivery of drugs. This desire to modify and understand drug delivery requires a new toolbox, one in which non-invasive molecular imaging using radioligands has demonstrated great promise. Building upon our studies evaluating pulmonary drug delivery, we are now working on several novel aerosolized and dry powdered formulations of drugs and vaccines. The ability to administer vaccines via intranasal or pulmonary delivery is very exciting. The World Health Organization has expressed their belief that non-needle based vaccinations have the power to greatly improve public health, particularly in developing countries where the fear of needles sometimes outweighs the fear of communicable diseases.

Efforts to improve the fundamental measurement of radioactivity are critical to understanding dose-related effects of targeted radionuclide therapy. The difficulties in measuring radioactivity has caused the amount of radioactivity administered to be under and over estimated. This, in turn, has led to both under and over treatment of patients with radionuclide therapies. In order to fully understand the dose-related safety and efficacy of targeted radionuclide therapy, the measurement techniques employed in the clinical setting must be improved. The same is also true of clinical molecular imaging which is now becoming more quantitative, and increasingly reliant upon sound measurement techniques. If, for example, the standardized-uptake value (SUV) of a PET radioligand is believed to have prognostic value, then the uncertainty of the measurement of the administered radioactivity must be minimized, well characterized, and more routinely understood.

Conclusions

The novel strategies to optimize targeted molecular imaging and therapy described in this thesis are based upon the careful deconstruction of the ligand-radionuclide-imaging application trilogy, allowing each component to be examined and optimized to produce a net gain in safety and efficacy. This reductionist approach demonstrates that more focused interventions are capable of producing more discrete and likely better results. This work demonstrates that the systematic examination of the components of this complex system continue to identify opportunities to advance our understanding of targeted radioligands for molecular imaging and therapy and to improve patient outcomes.

Samenvatting



Door de ontwikkelingen in moleculaire biologie, genomics en proteomics zijn toepassingen ervan in de zogenaamde “personalized” moleculaire geneeskunde sterk toegenomen. Deze vooruitgang heeft ook de groei van moleculaire beeldvorming en therapie met behulp van radioliganden gestimuleerd. Dit proefschrift beschrijft nieuwe strategieën om gerichte en specifieke moleculaire beeldvorming en therapie te verbeteren.

Hoofdstuk 2 beschrijft een aantal nieuw ontwikkelde benaderingen om gerichte therapie met behulp van high-LET (hoge lineaire energieoverdracht) radionucliden te verbeteren. De high-LET alfa-deeltjes emitter ^{213}Bi -DOTATOC bleek beduidend effectiever dan de lagere-LET beta-deeltjes emitter ^{177}Lu -DOTATOC in in vitro studies. Bij dezelfde geabsorbeerde dosis bleek ^{213}Bi -DOTATOC 3-4x meer therapeutisch effectief dan ^{177}Lu -DOTATOC in pancreas-adenocarcinoom-cellen in kweek. In vivo induceerde ^{213}Bi -DOTATOC dosisgerelateerde anti-proliferatieve effecten zonder significante renale toxiciteit of andere acute of chronische toxiciteit. Deze studies tonen dus de superieure veiligheid en werkzaamheid van high-LET ^{213}Bi -DOTATOC. Hoofdstuk 3 beschrijft strategieën om radionuclide therapie-effecten in receptor-positieve (SSTR) tumoren te verhogen door middel van gemcitabine. In tumorcellen die behandeld waren met gemcitabine gedurende 4 dagen, gevolgd door 4 dagen van herstel en groei, bleek de opname van ^{177}Lu -DOTATOC 1,5-3x hoger dan die in onbehandelde controlecellen (die dus geen gemcitabinebehandeling hadden gekregen). De combinatie van gemcitabine en SSTR-gerichte therapie heeft geresulteerd in de afgifte van hogere doses van radioactiviteit aan de tumorcel.

Hoofdstuk 4 beschrijft onderzoek aan leukocytfunctie-geassocieerd antigeen-1 (LFA-1), dit is een belangrijke receptor op T-leukocyten die binden aan adhesiemolecuul-1 (ICAM-1) op antigeenpresenterende cellen. De selectieve expressie van LFA-1 en de centrale rol in ontstekings- en immuunziekten heeft grote interesse voor LFA-1 als doel tijdens therapie middels medicatie gewekt. Dit heeft ook mogelijkheden gecreëerd voor gerichte moleculaire beeldvorming en therapie met behulp van het tegen LFA-1 gerichte DOTA-butylamino-NorBIRT.

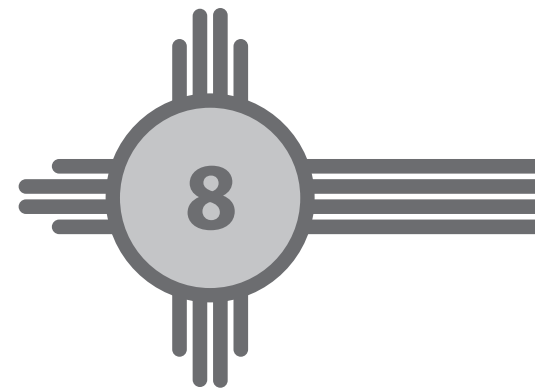
Hoofdstuk 5 beschrijft de preklinische ontwikkeling van een nieuw oestrogeen receptor-gericht estradiolderivaat voor beeldvorming van borst- en endometriumkankers. Nieuwe $^{99\text{m}}\text{Tc}$ (I)-estradiol-pyridin-2-yl hydrazine derivaten die een hoge affiniteit tonen voor GPR30, een receptor aanwezig in vele kankersoorten, zijn onderzocht. Een geselecteerd radioligand toonde receptor-gemedieerde opnames in humane MCF-7 tumoren en in biodistributiestudies. Verdere structurele aanpassingen zijn nodig om deze verbindingen te optimaliseren.

Onderzoek naar nieuwe beeldvormingsstrategieën voor pulmonale geneesmiddelafgifte wordt gepresenteerd in Hoofdstuk 6. Nieuwe 3D-topografische beeldanalysetechnieken zijn ontwikkeld om kwantitatieve beoordeling van aerosoldepositie middels SPECT / CT-beeldvorming in kleine dieren mogelijk te maken. Deze methoden zijn gevalideerd in

ratten en muizen en vertaald naar de humane situatie. Deze geoptimaliseerde en gevalideerde technieken toonden duidelijk een verminderde depositie in de perifere luchtwegen in astmapatiënten; dit onderzoek toont mogelijkheden om te onderzoeken of medicatie het beoogde weefsel kan bereiken, zodat het gewenste effect gesorteerd kan worden.

Hoofdstuk 7 beschrijft onderzoek met als doel de optimalisatie van ^{90}Y -radiofarmacameetingen in gerichte radionuclidentherapie. Het belang van nauwkeurige en reproduceerbare radioactiviteit-meettechnieken kan niet worden overschat als het gaat om een beter begrip van dosis-gerelateerde therapie-effecten. De veiligheid en werkzaamheid van een radioligand zijn beide afhankelijk van de dosis, daaruit volgt dat accurate meettechnieken cruciaal zijn bij het optimaliseren van radionuclidentherapie.

PhD portfolio



Summary of PhD training and teaching

Name PhD student: Jeffrey P. Norenberg
 Erasmus MC Department: Nuclear Medicine
 Research School: Molecular Medicine

PhD Period: 1-10-2010 - 29-5-2013
 Promoters: Prof. M. De Jong, Prof. E.P. Krenning
 Co-promotor: Dr. W.A.P. Breeman
 Supervisor: Prof. M. de Jong

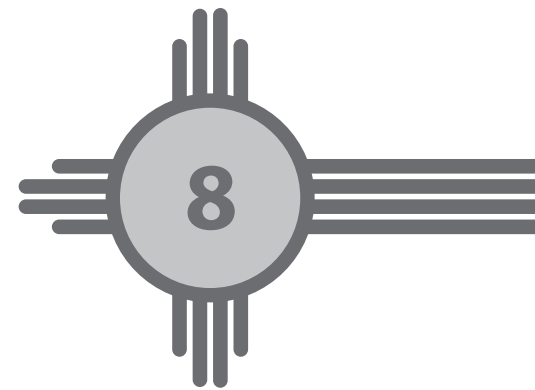
Courses:	Year	Hours
Hands-On Training PK/PD Using WinNonlin Professional 3.3	2009	32
Human Research Subject Assurances Training	2010	8
	2011	8
	2012	8
Radiopharmaceutical Internal Dosimetry Assessment Certification	2009	40
U.S. Food and Drug Administration Clinical Investigator Training Program	2011	32
Subtotal		128
Teaching:	Year	Hours
Medical Decision Making and Diagnostic Reasoning	2011	4
	2012	4
Medical Imaging Drugs and Adjuvants	2011	6
	2012	6
Use and Safety of Contrast Agents for CT and MRI	2009	2
	2010	2
	2011	2
	2014	2
Imaging Cancer	2010	2
	2011	2
	2012	2
Radiation Dose in Medicine	2011	1
	2012	1

U.S. Food and Drug Administration Clinical Investigator Training	2012	6
	2013	6
Subtotal		48
Study Sections and Grant Review Activities	Year	Hours
Natural Sciences and Engineering Research Council of Canada, Collaborative Health Research Projects Program	2012	24
Canadian Institutes of Health Research, Networks of Centres of Excellence	2010	16
	2011	16
Congressionally Directed Mandated Research Programs - American Institute of Biological Sciences	2005	16
	2006	16
	2008	16
Subtotal		104
Editorial Activities	Year	Hours
Editor		
<i>UNM COP Continuing Education Courses for Nuclear Pharmacists and Nuclear Medicine Professionals</i>	2008	32
	2009	32
	2010	32
	2011	32
	2012	32
	2013	12
Editorial Boards		
<i>Molecular Imaging</i>	2010	8
	2011	8
	2012	8
	2013	4
<i>Pharmacy Practice News</i>	2008	4
	2009	4
	2010	4
	2011	4
	2012	4
	2013	4
Subtotal		224

Peer-review Activities	Year	Hours
<i>Cancer Research</i>	2010	2
	2012	2
<i>Clinical Cancer Research</i>	2009	2
	2010	2
	2012	2
<i>Drug Safety</i>	2010	2
<i>European Journal of Nuclear Medicine and Molecular Imaging</i>	2007	2
	2009	2
	2011	2
	2012	2
<i>Imaging Economics</i>	2009	2
Journal of Nuclear Medicine	2008	8
	2009	8
	2010	8
	2011	8
	2012	8
	2013	6
<i>Molecular Imaging</i>	2010	6
	2011	6
	2012	6
	2013	6
<i>Molecular Pharmaceutics</i>	2009	6
	2012	6
<i>Nuclear Medicine and Biology</i>	2008	2
	2009	2
	2011	2
	2012	2
Subtotal		112
Invited Lectures	Year	Hours
Probe Validation Using Small-Animal Imaging. Society of Nuclear Medicine Mid-Winter Meeting	2009	1
Molecular Imaging In Drug Development Using High Resolution NanoSPECT/CT. 4th Annual Imaging in Clinical & Pre-clinical Drug Development Conference	2009	1

From the Laboratory Bench To The Patient's Bedside: Advancing Cancer Diagnosis And Treatment Using Radiopharmaceuticals. University of New Mexico Health Sciences Center	2009	1
Current Good Manufacturing Practices (cGMP's) for PET Drugs. 32 nd Annual High Country Nuclear Medicine Conference	2011	1
Subtotal		4
Total		620

Acknowledgements



This work would not have been possible without the generous support of many, only some of whom are mentioned here. I am sincerely grateful to each and everyone who contributed to this work, and to my personal and professional development.

I am grateful to Prof. Marion de Jong for her kind assistance and repeated urging to complete the PhD process. She has been very generous to offer constructive and critical feedback that has consistently improved the quality and impact of the research. It is because of her remarkably steady force and support that this work has been realized.

I am also sincerely grateful to Prof.dr. Eric Krenning for his unwavering support over the last 15 years, since our collaborations first began. In 1998 when Prof.dr. Larry Kvols asked me to support the 90Y-Octreother trial at UNM, I soon thereafter met Prof.dr. Eric Krenning. This also introduced me to somatostatin-receptor biology and neuroendocrine cancers that turned out to be among the most fortuitous events in my life, leading to both great professional achievement and much personal satisfaction. His keen scientific mind together with his generous and warm spirit have been a true inspiration to me throughout the many years it has taken to complete this work. I am sincerely grateful to know Prof.dr. Krenning and his family.

Special thanks to Professor/Dr. Larry Kvols for bringing me into the world of neuroendocrine cancer and somatostatin-receptor targeted ligands. His work to advance the treatment of patients with neuroendocrine cancers has inspired many, including me. While Prof.dr. Kvols at the University of New Mexico (UNM), he also took a personal interest in my professional development, guiding me through my early years as a faculty member. His introduction to Prof. dr. Krenning subsequently brought Dr. Boudewijn Krenning and Dr. Inge Konings to work in my laboratories at UNM for one year. This collaboration was itself a great success and even now, many years later, continue to drive many further studies to improve the treatment of patients with somatostatin-receptor expressing neuroendocrine tumors. It is really not possible to thank Boudewijn and Inge enough for the hard work and curiosity they brought to this work. Their efforts were substantial, and showed great devotion and commitment. I was very fortunate to have had the opportunity to work alongside them at the genesis of the work that has become this thesis. I am also very fortunate to have spent many sunny days with my wife Renée-Claude, Boudewijn, and Inge away from the labs enjoying the beauty of New Mexico. We were also together with them during a rare, and very memorable snowstorm in Las Vegas, Nevada.

Thanks to Dr. Wouter Breeman for the many discussions of receptor biology, pharmacology, radiochemistry, and scientific exploration. His passion for, and knowledge of these subjects is remarkable, and is only exceeded by his passion for, and knowledge of wine. I have also had the good fortune to mix science and pleasure with Wout and his wife Lieneke at several congresses, which brings to me a deeper appreciation for them both.

Thank you to the members of the Thesis Inner committee, Prof.dr. Theo Visser, Prof.dr. de Herder and Prof.dr. Fred Verzijlbergen for their continued support throughout thesis process and the transition in departmental leadership.

I am also very thankful for the generous support and guidance of many collaborators. Chief among them is Professor/Dr. Robert W. Atcher who first introduced me to alpha emitters and the concept of high linear-energy transfer radionuclide therapy. Through his help, I have been introduced to a field of science and community of researchers that I very likely would not have otherwise known. There are many others whose kind assistance and support enabled this work including: Dr. Martin Brechbiel, Dr. Kayhan Garmestani, and Paul Plascjak at the National Institutes of Health; Profess/Dr. Richard Larson for his work of small molecules targeting leukocyte function-associated antigen-1 (LFA1); Drs. Jacob McDonald, Philip Kuehl, and Chet Leach for their work imaging pulmonary drug delivery; Professor/Dr. Larry Sklar whose support led to funding to establish the Keck-UNM Small-Imaging Resource (KUSAIR); Amit Ahuja, Tapan Nayak, and Rahul Poria who were graduate students that contributed to this work; and the many other pharmacy and graduate students who have worked in my laboratories.

I am very thankful for the direction and support Dr. Jack Hoppin has provided to establish KUSAIR as a world-class small-animal imaging facility. His knowledge of math and imaging physics, together with his keen sense of inquiry have moved me in directions that I would not have imagined possible. Jack's ability to realize the enhanced image analysis algorithms and tools that together we have envisioned continues to bring great rewards.

I am also deeply indebted to the kind assistance and material support provided by many other scientists at Erasmus. Special thanks to Dr. HFF "Bert" Bernard for sharing his wealth of knowledge regarding animal models; Dr. Mark Konijnenberg for his help with dosimetry, and particularly models of radiation absorbed dose from high-LET alpha-emitters.

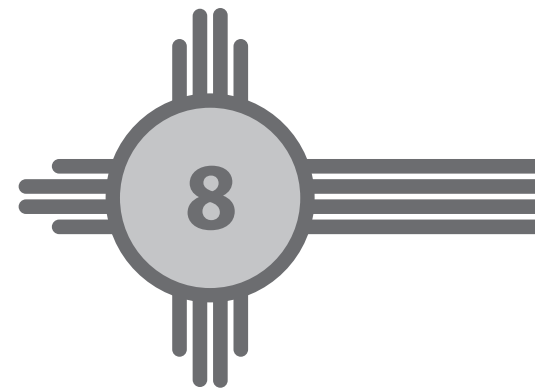
I also must thank my faculty colleagues at the UNM College of Pharmacy for their support to help make it possible for me to complete this work. Many times, these colleagues have been called upon to do a little more at UNM to enable me to pursue this work. Thanks to Tamara Anderson who managed all things related to my laboratories. Her amazing commitment and attention to the details have kept this research enterprise working the last 13 years. I am also thankful for the unwavering support of my department chairs Dr. Mark Holdsworth and Dr. Matthew Borrego; and my former Deans Prof.dr. William Hadley, Prof.dr. John Pieper; and the current Dean Prof.dr. Lynda Welage.

I am very fortunate to have been raised by parents, grandparents, and an extended family who loved and cared for me, always. Their love and guidance helped me to learn the meaning of hard work, the value of family and friends, and the rewards that come from leading a principle-centered life. Their everyday examples of lives lived with integrity, honesty, and sincerity

continue to be a rich reserve from which I draw great strength. Deepest thanks to my parents Bob and Joan Norenberg, and to my grandparents Louie and Sarah Jensen. I simply wouldn't be the person I am without their love.

Finally, and most importantly, I am very fortunate to know the love of family. Deepest thanks to my wife, Renée-Claude who continues to amaze me with her patience and kind support throughout our hectic life together. Special thanks to Coralie and Sophia for being such extraordinary children! I relish the time we spend together. Your love of the outdoors, skiing, swimming, dance, and an active lifestyle are among my greatest assets as I grow old. I am so very thankful for the texture and color you bring to my life each day. Together, we have made many special memories and I wish only that we can continue to love and support one another.

Curriculum vitae



Jeffrey Paul Norenberg was born on November 10, 1962 in Wahoo, Nebraska, USA. He graduated from Wahoo High School in 1981. He then began studies leading to the Bachelor of Science in Life Sciences (Biology) at the University of Nebraska in 1986. In 1987 he entered the University of New Mexico where he completed the Bachelor of Science in Pharmacy in 1990 and Master of Science in Pharmaceutical Sciences (Radiopharmacy) in 1991. In 1990 and 1991, he also completed post-graduate training in nuclear pharmacy and PET radiochemistry at the National Institutes of Health in Bethesda, Maryland, USA while serving in the US Public Health Service. From 1991-1993, he served as a Radiology Lecturer and Director of Nuclear Pharmacy Services at Tufts School of Medicine and New England Medical Center Hospitals in Boston, Massachusetts.

In 1993 he joined the Radiopharmaceutical Sciences faculty of the University of New Mexico College of Pharmacy. He was appointed the Director of Radiopharmaceutical Sciences Program in 1998, where he continues to serve. In 1999, he was made an Associate Member of Medical Staff of the University of New Mexico Health Sciences Center. In 2006, he was appointed as the Director of the Keck-UNM Small-Animal Imaging Resources at the University of New Mexico Health Sciences Center. In 2009, he was promoted to the rank of Professor.

Professor Norenberg's work in the discovery and development of radiopharmaceuticals for molecular imaging and therapy have resulted in more than 100 scholarly works and garnered over \$13,000,000 in extramural funding for basic and translational research. He has been awarded two patents for novel leukocyte-associated antigen-1 (LFA-1) targeted ligands for molecular imaging and therapy.

Dr. Norenberg is a Board Certified Nuclear Pharmacist and a fellow in the American Society of Health-System Pharmacists and the American Pharmacists Association. He serves on the Boards of Directors of the Society of Nuclear Medicine and Molecular imaging, the Education and Research Foundation for Nuclear Medicine and Molecular Imaging, and the American Board of Science in Nuclear Medicine. He is a delegate to the United States Pharmacopeia Convention.

Since 2002, he has also served as the Chairman and Executive Director of the National Association of Nuclear Pharmacies, a trade association representing 500 commercial nuclear pharmacies in the US.

Jeff is the fortunate husband of Renée-Claude Mercier and the proud father of Coralie (2003) and Sophia (2006).